UNIVERSITÀ
DEGLI STUDI
DI PADOVA

UNIVERSITÀ DEGLI STUDI DI PADOVA

DEPARTMENT OF MANAGEMENT AND ENGINEERING

PH.D. SCHOOL IN MECHATRONICS AND PRODUCT INNOVATION ENGINEERING

Curriculum: MECHANICS OF MATERIALS

Cycle: XXXI

MULTISCALE MODELING OF SHORT FIBER-REINFORCED THERMOPLASTICS UNDER FATIGUE LOADING

Thesis written with the financial contribution of Robert Bosch GmbH (Germany)

Coordinator: Ch.ma Prof.ssa Daria Battini

Supervisor: Ch.mo Prof. Marino Quaresimin

Ph.D. Student: RICCARDO PIETROGRANDE

UNIVERSITÀ
DEGLI STUDI
DI PADOVA

UNIVERSITÀ DEGLI STUDI DI PADOVA

DIPARTIMENTO DI TECNICA E GESTIONE DEI SISTEMI INDUSTRIALI

SCUOLA DI DOTTORATO IN INGEGNERIA MECCATRONICA E DELL'INNOVAZIONE MECCANICA DEL PRODOTTO

Curriculum: MECCANICA DEI MATERIALI

Ciclo: XXXI

MODELLAZIONE MULTISCALA DEL COMPORTAMENTO A FATICA DI COMPOSITI TERMOPLASTICI RINFORZATI CON FIBRE CORTE

Tesi redatta con il contributo finanziario di Robert Bosch GmbH (Germania)

Coordinatrice: Ch.ma Prof.ssa Daria Battini

Relatore: Ch.mo Prof. Marino Quaresimin

Dottorando: RICCARDO PIETROGRANDE

Table of contents

Abstract

The present work falls within a wider framework concerning the prediction of the mechanical response of short glass fiber-reinforced thermoplastics (SFRT), which are commonly employed in the automotive industry to reduce the overall weight of the components.

More in detail, the main objective of the thesis is to develop a fatigue criterion for predicting the effect of different factors affecting the fatigue strength of such materials. In this interest, the influence of the composite complex morphology (local fiber orientation and fiber content) and of notches giving rise to stress concentrations is taken into account.

In the present thesis, an experimental activity related to plain and notched specimens is firstly presented. In this context, data resulting from computed tomography (CT) analyses are shown. The latter serve to evaluate the specimens' fiber orientation distributions, which are quantified by means of fiber orientation tensors (FOT). Furthermore, fatigue test data on the considered coupons, in the absence and in the presence of notches (with radii of 0.1 mm, 0.2 mm, 2 mm and 5 mm), are presented for different fiber orientations and weight fractions (15 wt%, 25 wt%, 35 wt% and 50 wt%).

Secondly, being aware of the fact that the onset of a macroscopic crack is driven by the evolution of damage at the matrix level, a multiscale fatigue model relying on matrix stress distributions is presented.

The calculation of the matrix stress cumulative distribution functions is achieved by formulating an analytical numerical pseudo-grain approach (i) permitting to avoid the generation, mesh and solution of complex microstructures, but only relying on the solution of simple unidirectional cells. The pseudo-grain method is subsequently included in the formulation of a fatigue criterion, for plain (ii), at first, and for notched specimens (iii), subsequently.

The proposed fatigue criterion is eventually validated with a bulk of experimental data, partially presented in this work. Namely, fiber orientation tensors are used to properly assign the anisotropic elastic properties to the developed numerical models and the presented fatigue data are employed to assess the efficacy of the model in terms of fatigue strength prediction.

Sommario

Questa tesi di dottorato di ricerca si inserisce all'interno di un quadro più ampio relativo alla previsione del comportamento meccanico di materie termoplastiche rinforzate con fibre corte di vetro. Tali materiali compositi sono spesso impiegati nell'industria automobilistica per ridurre il peso complessivo della componentistica coinvolta.

L'obbiettivo principale di questo lavoro è legato alla necessità di sviluppare criteri di cedimento che prevedano l'influenza di diversi fattori sulla resistenza a fatica di tali materiali. In particolar modo, si è scelto di focalizzarsi sull'effetto della morfologia (orientazione locale e contenuto di fibre) e della presenza di intagli, che a loro volta danno luogo a concentrazioni tensionali.

In questa tesi viene presentata innanzitutto l'attività sperimentale svolta. Ovvero si riportano dati relativi ad analisi ottenute tramite tomografia computerizzata (CT). Quest'ultima ha il ruolo di fornire informazioni sulle distribuzioni locali dell'orientazione delle fibre, le quali vengono quantificate tramite il tensore di orientazione delle fibre (FOT). Inoltre, si presentano dati relativi al comportamento a fatica di provini con e senza intagli (di raggio pari a 0.1 mm, 0.2 mm, 2 mm e 5 mm), considerando contemporaneamente l'effetto dell'orientazione delle fibre e delle loro frazioni di peso (15 wt%, 25 wt%, 35 wt% e 50 wt%).

In secondo luogo, consapevoli del fatto che l'origine di cricche macroscopiche può essere imputata all'evoluzione del danneggiamento nella matrice, si propone un modello multiscala per la previsione della vita a fatica di tali compositi, basandosi sul calcolo delle distribuzioni tensionali locali.

Il calcolo delle funzioni cumulate delle tensioni matriciali è ottenuto tramite la formulazione di un approccio analitico-numerico di tipo pseudo-grain (i). Quest'ultimo permette quindi di evitare la generazione, mesh e risoluzione di microstrutture complesse e di ottenere i risultati desiderati tramite semplici modelli numerici unidirezionali. Tale approccio viene poi inserito nella formulazione di un criterio di fatica per provini lisci (ii) e intagliati (iii).

Il criterio proposto è poi validato con un numero consistente di dati sperimentali, parte dei quali è presentata in questo lavoro. In particolare, i tensori di orientazione delle fibre sono impiegati per assegnare le proprietà elastiche anisotrope ai modelli numerici. I dati di fatica sono invece utilizzati per verificare l'efficacia del modello in termini di previsione della resistenza a fatica di provini lisci e intagliati.

Acknowledgments

Coming to the end of these three years of Ph.D., I feel to thank many people who have contributed to enrich me personally and professionally.

I am very grateful to my academic supervisor Prof. Marino Quaresimin who guided me in pursuing my doctoral goals in a scientific way with his precious and pragmatic advices.

I would also like to thank my Bosch tutor, Matthias De Monte. With him, I had the pleasure to weekly discuss with great interest about my research topics and concretely define the short- and long-term goals that I had to reach.

Thanks to my friend and Mentor Paolo Andrea Carraro who inspired me in my research activity since my Master thesis and was always willing to have proficient scientific discussions with me.

A great thank goes also to Prof. Michele Zappalorto, who provided me with various inputs, crucial for the development of my work, mainly during my last Ph.D. year.

I big thank goes to all my Ph.D. colleagues (current and ex) of the office at the DTG, Lucio Maragoni, Elisa Novello, Amir Ghorbani, Francesco Panozzo and Giacomo Modenato. With them, I have shared a very good time.

I also thank my doctoral colleagues at Bosch: Larissa Kutscha, Patrick Hessman, Artur Kochanke, Susanne Kugler and many others. We had different opportunities to spend time at work sharing ideas, but we also had many chances to pleasantly hang out, in front of a fresh beer.

A particular thank goes to my Bosch Ph.D. colleague and friend Dominik Naake, who really helped me in many occasions of working life and not only. We had many chances to exchange our dining experiences and to strengthen our friendship.

I am also very grateful to my friend and Bosch Ph.D. colleague Besher Baradi, with whom I have always worked in tune.

I also thank my friends and colleagues Camilo Cruz and Harnoor Saini for the great days spent together.

Thanks also to my friend and predecessor Enrico Belmonte. He has always been willing to share precious ideas with me, useful for my research activity.
I am grateful to my group-leader and to my department-leader at Bosch, Kurt Hornberger and Martin Giersbeck, with whom I have always interfaced in a professional, but, at the same time, friendly manner.
A great thank goes to the entire CR/APP2 group: Egon Moosbrugger, Andreas Wilmes, Robert Wieland, Vivien and Valerie Le Baube, Jan-Martin Kaiser, Armin Kech, Cedric Feuillette, Stefan Büchler, Volker Klostermann, Jürgen Willing, Fabian Welschinger, Ana Rodriguez and Philipp Weißgraeber. I really enjoyed the time with them in the office as well as the after-work activities.
A big thank to the Bosch (Elke and Andrea) and university (Tania) secretaries. They have always helped me to put a lot of paperwork in order.
I am of course grateful to my parents Andrea and Paola and to my sister Clara, who have never had doubts on my professional and life choices and always supported me.
Last but not the least, a huge thank goes to my beloved girlfriend Giada. Since almost eight years, she has been following me unconditionally, with patience, in my crazy decisions and has been continuously encouraging me.

Introduction and outline

The use of fiber reinforced polymers (FRP) provides today an alternative to the commonly diffused materials, such as metal, aluminum and wood. The role of FRPs is to contribute to the enhancement of the lightweight of the part of interest, without affecting negatively the required material properties (e.g. mechanical strength, stiffness, resistance to chemicals, thermal or electrical insulation). In fact, the efficacy of using FRPs derives from the advantage of possessing different properties that cannot be usually found in one single material. In this interest, fibers contribute to improve the composite mechanical properties, while the polymeric matrix is by nature a low-density material, favoring in turn weight savings.

This topic is of particular interest for the automotive industry due to different aspects. One reason related to the component's weight reduction is certainly connected to the improvement of the car performances. On the other hand, the main motivation can be attributed to the necessity of decreasing the gas emissions. In 1992, the Kyoto protocol committed the state parties to reduce the emissions of greenhouse gases, such as Carbon dioxide (CO_2) that has been significantly increasing in the last decades (Fig. I.1). The CO_2 is mainly released by fossil fuels and industrial processes (Fig. I.2).

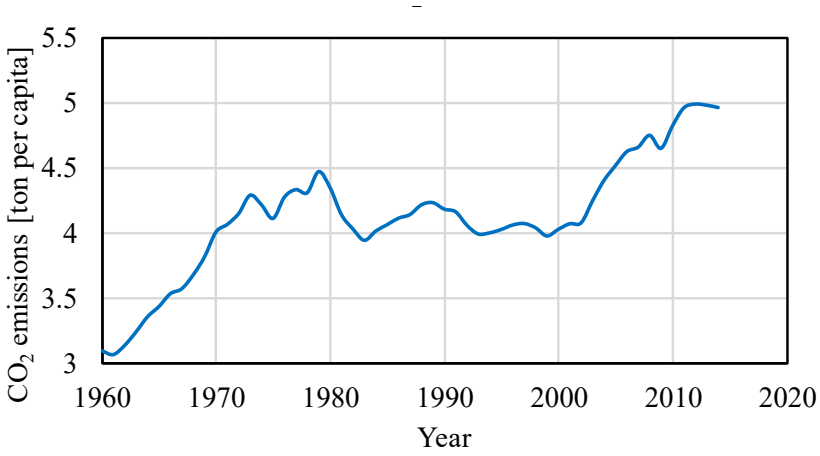

Figure I.1. CO_2 global emissions' trend (WEB1).

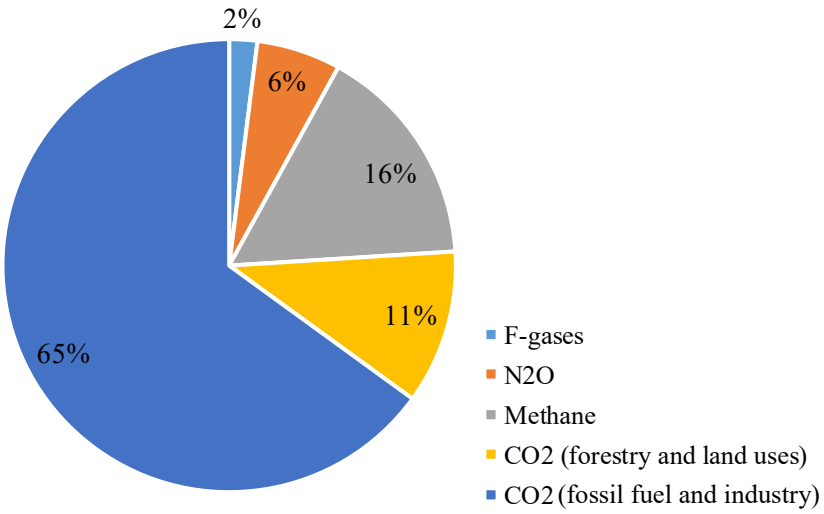

Figure I.2. Global greenhouse gas emissions statistics (WEB1).

In particular, the thesis work has been developed in collaboration with the Plastic Engineering Department of the research division of Robert Bosch GmbH (Germany). The company has demonstrated to be very active in the research field related to the use of short fiber-reinforced thermoplastics, which are nowadays part of the automotive components and constitute an essential contribute to the car weight reduction.

To better understand the framework which the thesis work falls in, the simulation chain usually adopted for the fatigue lifetime prediction of SFRTs is depicted in Fig. I.3. Referring to an actual component undergoing cyclic loadings (i), the composite morphology is characterized by spatially varying fiber orientation distributions. For this reason, it is common practice to firstly perform process simulation analyses (ii) to estimate the local fiber orientations, which are quantified by means of a second-order fiber orientation tensor (FOT). This type of simulation makes use of inputs that must be accurately chosen to have an optimal prediction of the FOTs, i.e. fiber aspect ratio (A_R), fiber diameter (d_f), fiber volume fraction (v_f) and other process parameters, such as pressure, temperature etc. Once FOT components are computed, the elastic properties that have to be assigned to the structural model can be calculated by means of homogenization schemes (iii). The required inputs for this step are fiber parameters, FOTs and the constituents' elastic properties. A homogenized model subjected to ex-

ternal loads (F) can now be numerically solved (iv) and the stress/strain field read. Eventually, the fatigue failure criterion must be applied to the solved model and the predicted life of the part of interest can be evaluated (v).

By reference to Fig. I.3, the scope of the Ph.D. work can be represented by the aforementioned point (v). Namely, the main goal consists in the development of a reliable and robust fatigue criterion for the prediction of the fatigue strength of short fiber-reinforced thermoplastics (SFRT). Since such materials are often in contact with dangerous liquids, the present work aims at developing models for the prediction of the fatigue lifetime up to crack initiation, in order to avoid possible leakage phenomena due to the crack propagation phase.

In comparison to the world of continuous fiber-reinforced composites, in the literature only few works proposed damage-based criteria for predicting the fatigue response of SFRTs.

Short fiber reinforced-thermoplastics are characterized by extremely complex morphologies as a consequence of the fiber arrangement induced by the production process (injection molding). The latter influences significantly the local material fatigue strength, but there is is still a lack of models enabling to take into account the actual spatially varying fiber arrangement. Therefore, among all possible factors affecting the fatigue response of SFRTs, the effect of the fiber content (identified as fiber volume fraction or weight fraction) and of the local fiber orientation distribution are taken into account in the present work.

Additionally, due to the non-brittle nature of the thermoplastic matrix, this type of composite is sensitive to the presence of notches and, therefore, a model also capable of accounting for stress concentrations induced by notches is proposed.

The fatigue damage occurring in the material while cyclically loaded is by nature a hierarchical process and can be mainly attributed to the formation of micro-scale cracks in the matrix. For this reason, a multiscale model is hereby proposed, which aims at predicting the formation of a macroscopic crack, based on the matrix stress distributions assumed to be responsible for the evolution of the damage at the micro-scale, among fibers.

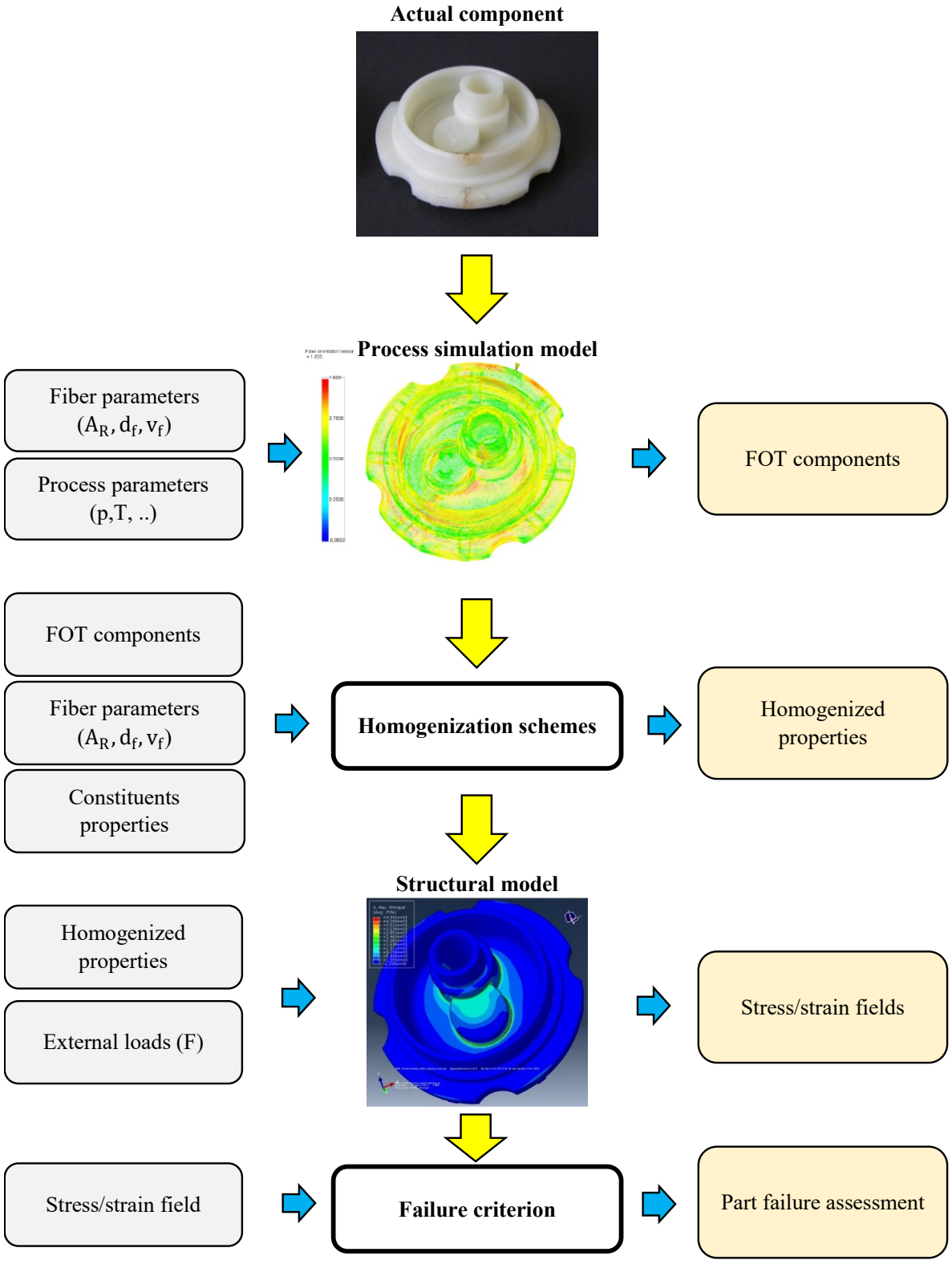

Figure I.3. Schematic simulation chain for failure assessment of real parts.

The thesis work can be subdivided into two major activities:

a) Experimental activity: studies on the morphology and fatigue behavior of short glass fiber-reinforced polyamides 6.6.
b) Modeling activity: development of multiscale fatigue criteria accounting for the effect of fiber orientation, fiber volume fraction and notch geometry.

The thesis chapters are presented here below:

- Chapter 1 is dedicated to provide a broad overview of the mechanical behavior (static and fatigue) of short fiber-reinforced thermoplastics, focusing on different factors affecting it.
- Chapter 2 presents the carried out and employed experimental data, quantifying the variation of the fiber orientation tensor components by means of the X-ray computed tomography (CT). Furthermore, experimental fatigue data are presented for plain and notched SFRT specimens.
- Chapter 3 deals with the formulation and validation of a numerical analytical pseudo-grain method, which enables the computation of the matrix stress distributions of a complex microstructure, without generating and solving onerous models with misaligned fibers.
- Chapter 4 makes use of the model presented in chapter 3 for the development and validation of a multiscale criterion aiming at predicting the effect of fiber orientation and volume fraction on the fatigue strength of SFRT plain specimens.
- Chapter 5 applies the model proposed in chapter 4 to notched specimens and includes the effect of notch geometry among the factors affecting the fatigue strength of SFRTs.

A schematic overview of the structure of the work is depicted in Fig. I.4. It can be seen that chapter 2 contains blocks *Fiber orientation analyses on specimens* and *Fatigue tests on specimens*, while chapter 3 corresponds to block *Model for matrix stress distribution*, chapter 4 to *Fatigue model in the absence of notches* and chapter 5 to *Fatigue model in the presence of notches*.

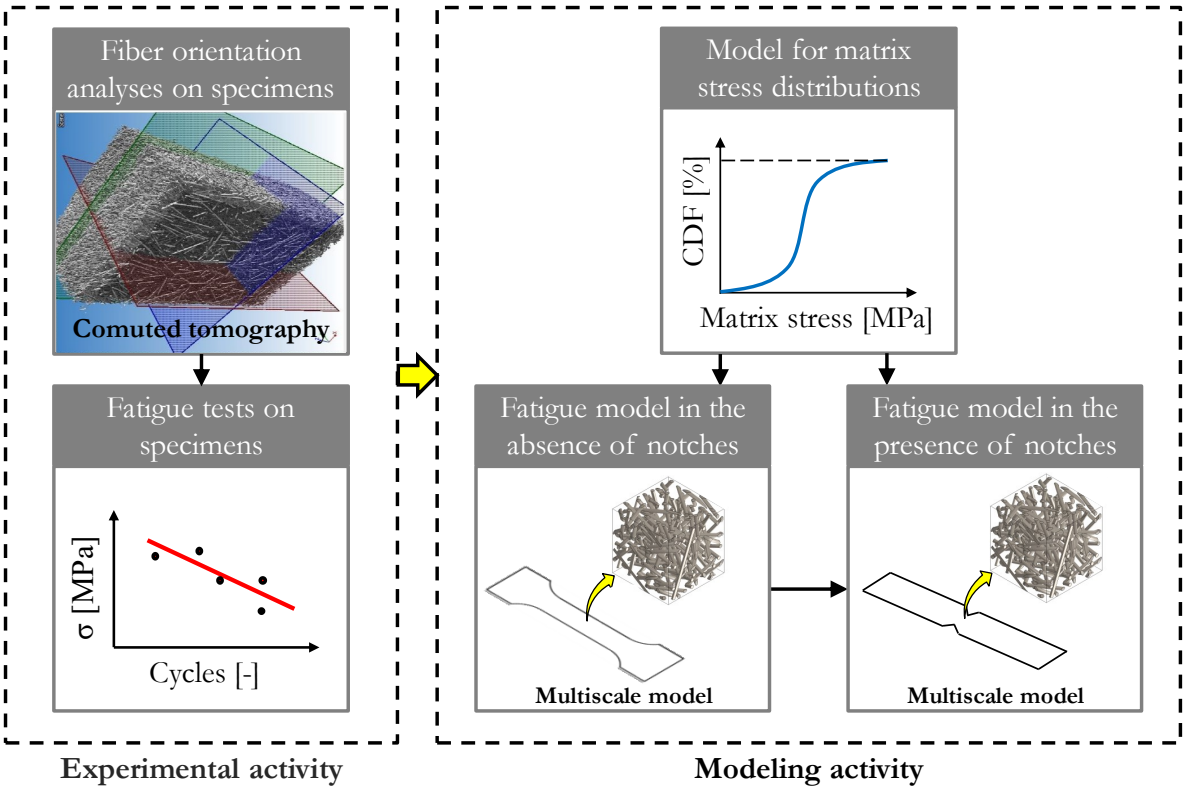

Figure I.4. Structure of the thesis' work.

Chapter 1

Fundamentals and preliminary remarks

1.1 Composite materials

By definition, a composite material (TSA80, BIE16) is made of two or more constituents having significantly different mechanical properties. These materials can be classified according to the following main categories:

- Ceramic matrix composites (CMC);
- Metal matrix composites (MMC);
- Fiber-reinforced plastics (FRP).

The first listed group finds its application in those products undergoing very high temperatures, but still requiring lightweights. This is, for instance, the case of brake disks, rocket nozzles, etc. Nevertheless, this type of matrix is normally reinforced with carbon, silicon carbide alumina of mullite fibers, which in turns help the material improve its mechanical properties (fracture toughness) in comparison with the neat matrix.

The second mentioned group of composites are characterized by a metallic matrix. The latter must additionally have a low specific weight in order to guarantee efficient performance in the automotive industries and in other fields of application. Light metal alloys are rarely used for this application, but the union with other reinforcements (continuous, long and short fibers, particles, etc.) can significantly enhance the mechanical properties. In this interest, short fibers are the most commonly used fillers, also due to the advantages deriving from the production process, contrary to the use of long/continuous fibers.

The last mentioned type of composite consists in fiber-reinforced plastics. This kind of composite is widely used in the aerospace, wind energy and automotive industry. The main reason of adopting such composites comes from the need of significantly reducing the weight of the entire product. The plastic matrix is usually a thermoplastic or a thermoset. The employed

fibers can be made of glass, carbon or aramid and they are essential to improve the overall material stiffness and strength. Also in this case, fibers can be continuous or discontinuous (long or short), depending on the order of magnitude of the filler with respect the part size. Due to their geometrical nature (long and narrow), fibers cannot resist to shear or compression loads and, therefore, the production process (thence, the fiber orientation) must be optimized as much as possible to maximize the composite strength under well-defined loads.

1.2 Short fiber-reinforced thermoplastics

In this work, only short fiber-reinforced polymers will be adopted to validate the proposed fatigue criteria. In particular, two-phase-composites will be considered, namely those composed of a thermoplastic matrix and short glass fibers. In this section, more details related to the used materials will be provided, giving a brief overview on the chemical and mechanical properties of such composites.

1.2.1 Matrix

As mentioned above, the employed matrix of the composite is a polyamide 6.6, namely a thermoplastic polymer. Thermoplastics differ from thermosets for various aspects. The latter can be solidified only once through a chemical reaction that makes the molecules cross-link. On the other hand, thermoplastic materials are remeltable and this enables their storage in the form of small pallets (GOO07).
The polyamide 6.6, which is also called nylon 6.6, is obtained by polycondensation of hexamethylendediamine and apidic acid. The structural unit (i.e. monomer) of this material is depicted in Fig. 1.1.

$$– CO – [CH_2]_4 – CO – NH – [CH_2]_6 – NH –$$

Figure 1.1. Structural unit of the polyamide 6.6 (OSS12).

This type of thermoplastic is characterized by a semi-crystalline structure (Fig. 1.2), i.e. some molecules are aligned with their neighbor and the rest presents an amorphous structure. For the sake of clarity, in an amorphous polymer, molecules are randomly arranged.

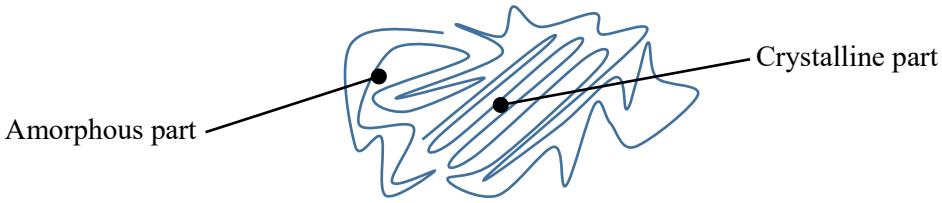

Figure 1.2. Schematic representation of a semi-crystalline structure.

Concerning the mechanical behavior of the polyamide 6.6, an example is reported in Fig. 1.3, where the material clearly shows a ductile behavior and sensitivity to the load rate.

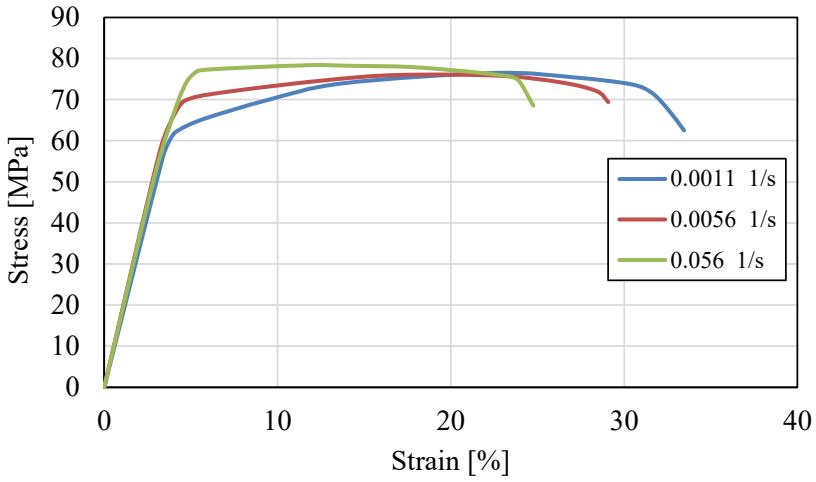

Figure 1.3. Tensile response of PA66 for different strain rates (MOU06).

With regard to other properties relevant to the modeling activity (formalized later), the reader can refer to Tab. 1.1.

Table 1.1. Properties of a PA66 material (BAS1).

Density [kg/m³]	**Young's modulus** [MPa]	**Poisson's ratio** [-]
1130	3000	0.39

1.2.2 Filler

Different types of fillers, in particular fibers, might be used to reinforce the thermoplastic matrix (e.g. steel, glass, carbon and natural fibers). Especially, in this work short fibers have been employed. It has been reported by many authors that such fillers get broken during the production process and their length is significantly reduced and can be described by means of a fiber-length distribution (FU00, FU01, MOR15, HAS12, KÖP13, MAS16, LEE18).
The SFRTs adopted in this work contain short E-glass fibers. Typical values for the fiber properties that will be used in the next chapters are reported in Tab. 1.2.

Table 1.2. Glass fibers' properties.

Density [kg/m³]	**Young's modulus** [MPa]	**Poisson's ratio** [-]
2540	72000	0.22

1.2.3 Useful parameters

Some parameters that will be used later on are hereby described.

Fiber aspect ratio:
Referring to short fibers, their geometry is normally described as a cylinder, as it is depicted in Fig. 1.4.

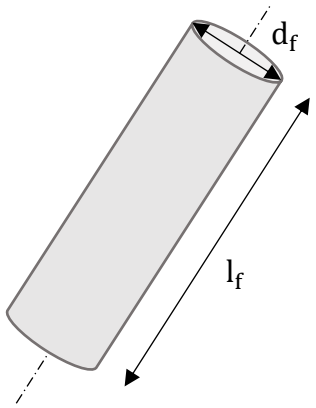

Figure 1.4. Schematic representation of a short fiber and significant dimensions.

In Fig. 1.4, symbols l_f and d_f denote the fiber's length and diamater. These two paramters can also be combined and the fiber aspect ratio (A_r) can be defined thus:

$$A_r = \frac{l_f}{d_f} \tag{1.1}$$

Fiber volume fraction:

While talking about composite materials, terms fiber volume fraction (v_f) and fiber weight fraction (ω_f) are commonly adopted to quantify the content of fibers inside the composite. The correlation between ω_f and v_f reads:

$$\omega_f = \frac{\rho_f v_f}{\rho_f v_f + \rho_m (1 - v_f)} \tag{1.2}$$

where subscripts f and m respectively denote fibers and matrix and symbols ω, v and ρ indicate the constituent's weight fraction, volume fraction and density.

As it will be discussed in detail later on, this entity has a significant influence on the composite mechanical properties.

Fiber orientation tensor:

While modeling short glass fiber-reinforced polymers, the involved constituents may be normally considered as isotropic, but the union of matrix and fillers (i.e. short fibers) usually gives rise to an intrinsic composite anisotropy, which makes the material mechanical response depend on the applied load direction.

Nevertheless, the anisotropy of such materials generally varies within the considered part. The local material anisotropic response is a consequence of the complex arrangement that fibers assume while settling inside the mold. In particular, the anisotropy can beattributed to the orientation of fibers or, rather, to their orientation distribution. It is common practice to derive the latter from the fiber orientation tensors (FOT) that can be estimated numerically

(i.e. by means of process simulations) of experimentally (through optical observations or computed tomography).

The formulation of the FOT has been extensively treated in the work of Advani and Tucker in 1987 (ADV87) to describe and predict the fiber orientation distributions in composite materials. More precisely, the authors dealt with the placement of short stiff fibers while being carried by the flow of a viscous material.

In ADV87, the formulation of the FOT for the orientation state estimation of a generic point is provided and the single fiber is ideally modelled as a rigid cylinder, the orientation of which is described by two angles (ϕ and θ) identifying a unit vector $\mathbf{p}$, as Fig. 1.5 shows. The fiber orientation tensor has been subsequently used by many other authors (ADV87, DOG05, DOG06) for describing the orientation assumed by short fibers and developing failure criteria. According to Fig. 1.5, the expressions of the vector $\mathbf{p}$ components (p_x, p_y, p_z) is:

$$\begin{aligned} p_x &= \sin\theta\ \cos\phi \\ p_y &= \sin\theta\ \sin\phi \\ p_z &= \cos\theta \end{aligned} \tag{1.3}$$

The FOT will be used in this work to compute the fiber orientation probability density function (FOPDF) denoted by $\psi(\theta, \phi)$ or equivalently by $\psi(\mathbf{p})$. The latter expresses the probability (P) of finding a fiber within a sufficiently small interval described by a predefined vector $\mathbf{p}_k$, according to the following equation:

$$P(\mathbf{p}_k < \mathbf{p} < \mathbf{p}_k + d\mathbf{p}) = \psi(\mathbf{p}_k)d\mathbf{p} \tag{1.4}$$

As it will be detailed later on, the FOPDF can be expressed as a function of the second and the forth order FOT, respectively indicated by $\mathbf{A}$ and $\mathbb{A}$ according to Eq. (1.5).

$$\psi(\mathbf{p}) \approx f(\mathbf{A}, \mathbb{A}) \tag{1.5}$$

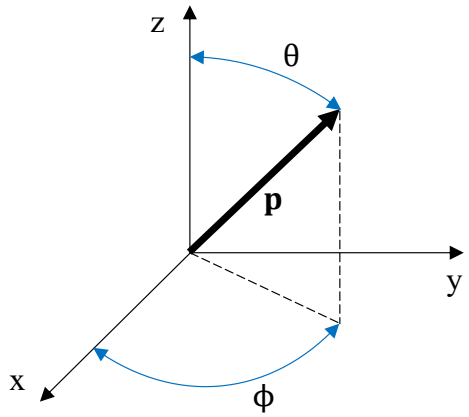

Figure 1.5. Unit vector and its describing angles.

As it can be read in ADV87, Eq. (1.5) can be expressed as a Fourier series expansion and reduces the information concerning the fiber orientation to the identification of a scalar value, i.e. $\psi(\mathbf{p})$.

Only the second-order tensor is often available and the estimation of $\mathbb{A}$ will be performed by means of the *closure approximation* expressions provided in ADV87, which permits the formulation of the fourth-order FOT as a function of the second-order one. However, the expressions of $\mathbf{A}$ and $\mathbb{A}$ read:

$$A_{ij} = \oint p_i \, p_j \, \psi(\mathbf{p}) \, d\mathbf{p} \tag{1.6}$$

$$A_{ijkl} = \oint p_i \, p_j \, p_k \, p_l \, \psi(\mathbf{p}) \, d\mathbf{p} \tag{1.7}$$

where A_{ij} and A_{ijkl} respectively denote $\mathbf{A}$ and $\mathbb{A}$ by means of the Einstein's notation and p_i is a generic component of the unit vector $\mathbf{p}$.

Some characteristics of the second-order FOT are additionally expressed by means of the following equalities:

$$\begin{aligned} &A_{ij} = A_{ji} \\ &0 < A_{ii} < 1 \quad \text{and} \quad \textstyle\sum_x^z A_{ii} = 1 \qquad \forall i \ \text{in} \ [x,y,z] \\ &-\tfrac{1}{2} < A_{ij} < -\tfrac{1}{2} \qquad \forall i,j \ \text{in} \ [x,y,z] \quad \text{with} \quad i \neq j \end{aligned} \tag{1.8}$$

Eq. (1.6) and (1.7) are valid in ideal situations in which angles θ and ϕ have no discontinuities while ranging, respectively, within $[0, \pi]$ and $[0, 2\pi]$. Indeed, while dealing with discrete fiber orientations, the second-order FOT is computed by means of the following equation:

$$A_{ij} = \frac{1}{N} \sum_{k=0}^{N} p_{i,k}\, p_{j,k} \tag{1.9}$$

where $p_{i,k}$ can is obtained by substituting θ_k and ϕ_k in Eq. (1.3). Term N of Eq. (1.9) denotes the amount of fibers enclosed in the observation volume. Therefore, the formulation of term $p_{i,k}\, p_{j,k}$ yields:

$$p_{i,k}\, p_{j,k} = \begin{bmatrix} \sin^2\theta_k \cos^2\phi_k & \sin^2\theta_k \cos\phi_k \sin\phi_k & \sin\theta_k \cos\phi_k \sin\phi_k \\ \sin^2\theta_k \cos\phi_k \sin\phi_k & \sin^2\theta_k \sin^2\phi_k & \sin\theta_k \cos\phi_k \sin\phi_k \\ \sin\theta_k \cos\phi_k \sin\phi_k & \sin\theta_k \cos\phi_k \sin\phi_k & \cos^2\theta_k \end{bmatrix} \tag{1.10}$$

1.3 Injection molding process

The injection molding (ROS12, BIR13, WEB2) is a process commonly adopted for the production of plastic parts and, in particular, has been used for the fabrication of all SFRT specimens that will be presented in this work.

In the practice, this process is used for producing thin-walled parts that might be characterized by complex shapes, generally difficult to achieve with other methods. Furthermore, injection molding guarantees excellent fine details and very high production rates.

1.3.1 Machine modules

The part production requires: the injection molding machine, the raw plastic material (in this case, the short glass fiber-reinforced thermoplastic) and the mold.
A schematic representation of the injection molding machine is reported in Fig. 1.6.

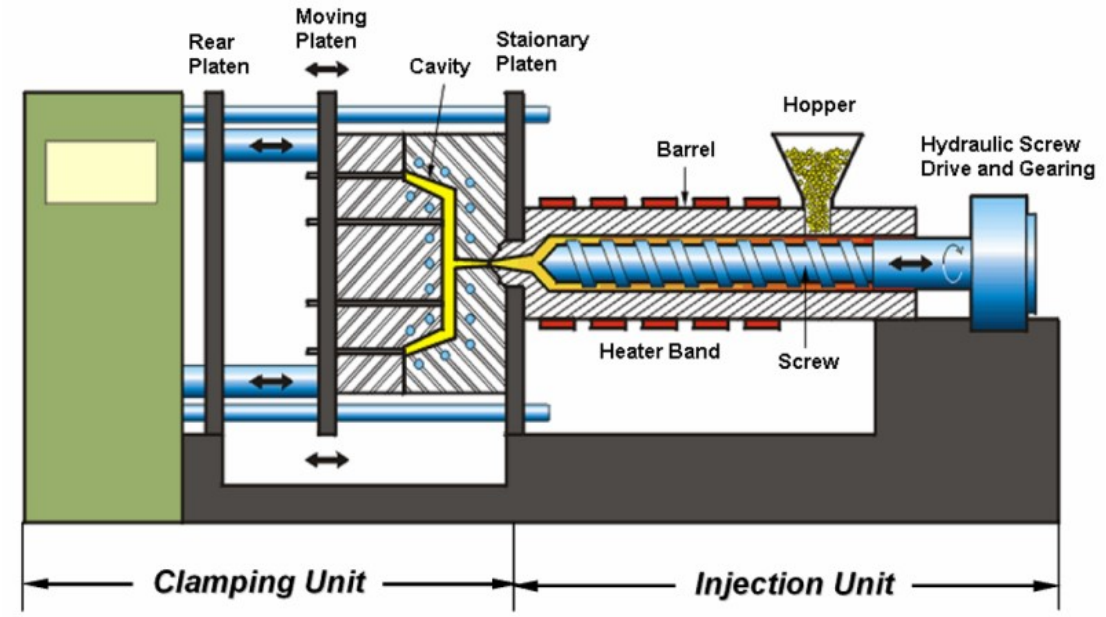

Figure 1.6. Schematic scheme of an injection molding machine (PAT06).

The latter can be schematically subdivided into two units:

- *Injection unit*: the raw material is introduced into the barrel by means of the hopper. Inside the barrel, a reciprocating screw rotates and slides, making the material advance forward. In parallel, the heating generated externally, together with the friction and the pressure produced among the screw grooves, makes the material melt.
- *Clamping unit*: in this unit, a half of the mold (front) is fixed to a stationary large plate, called platen. The rear half of the mold is instead connected to a moving platen, which enables the extraction of the part once the injection is over. A clamping motor drive controls the positioning of the moving platen.

1.3.2 Process phases

The phases, which this process method is composed of, can be summarized as follows:

1. *Clamping*: the mold has to be secured to the clamping system. Both halves of the mold are connected to the clamps, but only one is allowed to slide while the other is fixed. The system is normally controlled by a hydraulic system.
2. *Injection*: the material (in the form of pellets) is fed into the injection unit and is molten thanks to the very high temperature and pressure.
3. *Cooling*: as the material gets in contact with the mold walls, this step begins and the part starts to assume the desired shape. Shrinkage deformations are also possible because of this stage and they can be less visible whether the material is efficiently packed.
4. *Ejection*: one half of the mold is firstly ejected and the produced part is pushed out of the front half of the mold.
5. *Post-processing:* some excess material that have solidified during the process can be eventually removed.

1.4 Computed tomography

The term tomography (KRE17) refers to a technique that allows the gathering, in a non-destructive way, of sectional images of an entire body part that can be passed through by a certain radiation. This methodology is adopted in different fields, such as radiology, biology, material science (LAP16), etc.

The conventional computed tomography (CT) makes use of the X-rays for scanning the part of interest. The beam source (or alternatively the object) moves in multiple directions during the exposure time of the observation and enables to obtain images of the inside of the analyzed volume. The geometry reconstruction relies on the mathematical principle that an infinite amount of projections permits to entirely replicate an object geometry (HSI09). This step

usually takes place in a software collecting data from the analyses. Eventually, a post-process can be performed to carry out three-dimensional images and to extract useful information.
A schematic representation of a CT machine is depicted in Fig. 1.7.

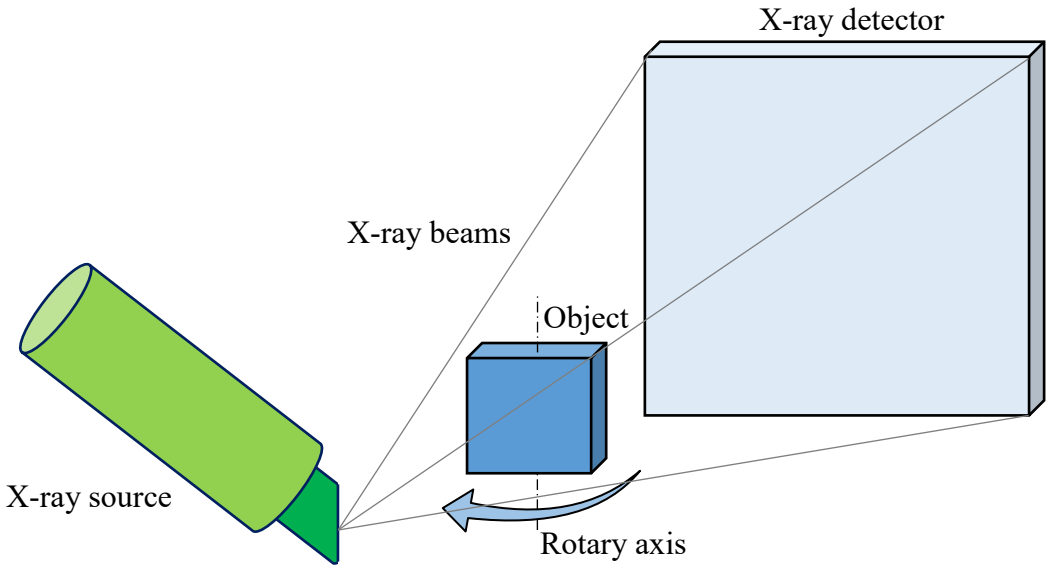

Figure 1.7. Schematic representation of a CT scan.

Concerning the working principle of the CT, the X-rays are emitted by a tube (source) and hit the detector positioned on the other side of the object. This operation is repeated from different angulations of the part in order to have a fully 3D image. As the geometry is elaborated with the software, it is discretized in small voxels, each of them containing a grey-scale value. The latter depends on the absorption properties of the investigated constituents and, by properly choosing a grey-scale threshold, the different phases can be thus separated.
In particular, this work deals with SFRTs, where fibers and matrix possess different X-ray absorption properties, this leading to a clear graphical separation of the constituents. Once the CT data are transferred to the post-processing software, it is possible to extract some local information, i.e. fiber orientation tensor, fiber volume fraction, etc.
Referring to SFRTs, the CT has been adopted in this work for evaluating the FOT variation within volumes considered as critical in terms of fatigue resistance of the component. In order to evaluate the FOTs, a volume discretization in elements has to be performed with the software, as it is schematically shown in Fig. 1.8.

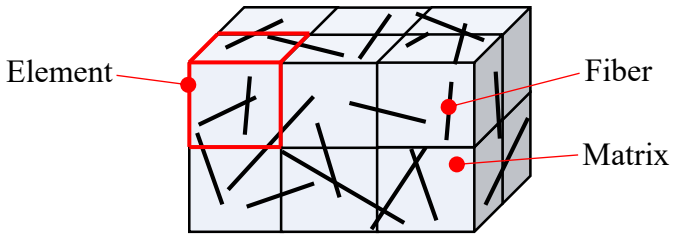

Figure 1.8. Schematic representation of a volume discretization for CT analyses.

As the grid schematically shown in Fig. 1.8 is created, the evaluation of the fiber orientation tensor is now possible for each element.

1.5 Quasi-static behavior of SFRTs

This section aims at the giving an overview on the quasi-static behavior (σ-ε curves), as well as the elastic properties, of short fiber reinforced thermoplastics. Similarly to those SFRTs undergoing fatigue loading, such composites yield different responses depending on the parameters characterizing the material and the external factors to which it is subjected.
The effect of fiber volume fraction, fiber orientation, temperature and moisture will be hereinafter briefly discussed.

1.5.1 Fiber volume fraction

The choice of the fiber volume fraction while creating a SFRT part plays an important role with regard to the material mechanical response while subjected to mechanical loadings. In the literature, different authors have investigated how the fiber content affects the quasi-static behavior of SFRTs. It can be generally stated that, by increasing the amount of fillers (i.e. fibers), the composite ultimate tensile strength (UTS) is enhanced. The same observation can be furthermore done for the elastic response of the tested material.
It must be remarked that the fiber volume fraction can be directly correlated to the fiber weight fraction, once the constituents' density is available.

Fu et al. (FU00) focused on the effect of fiber volume fraction on the quasi-static response of a polypropylene (PP) reinforced with short glass fibers Fig. 1.9.

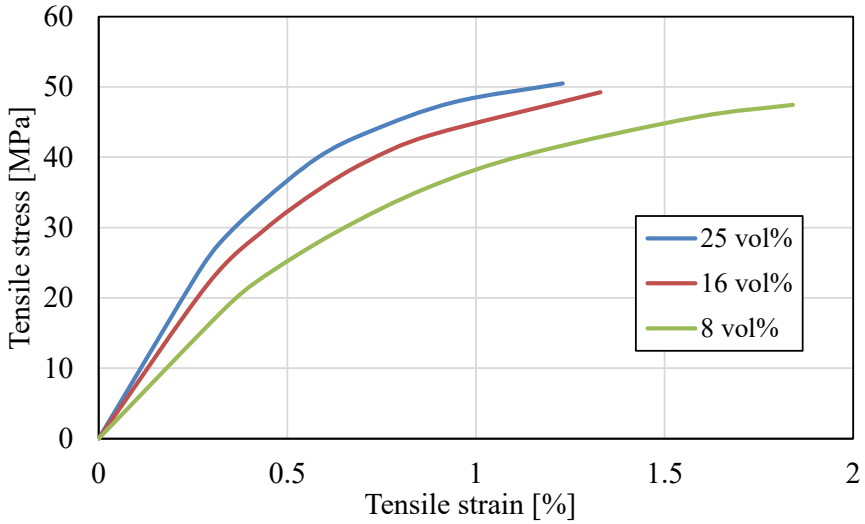

Figure 1.9. Quasi-static curves for a PP reinforced with short glass fibers (FU00).

By focusing on the effect of fiber volume fraction on UTS (Fig. 1.10a) and on the tensile elastic response (Fig. 1.10b) of the material, an improvement in terms of mechanical properties can be observed.

Further details related to this PP matrix composite can be found in FU00.

In the present work, fatigue criteria for SFRTs will be later proposed and formulated and, in particular, all proposed and used data refer to short fiber-reinforced polyamides 6.6 (PA66).

In Fig. 1.11, the UTS and elastic modulus variations are reported for short fiber composites with PA66 matrix.

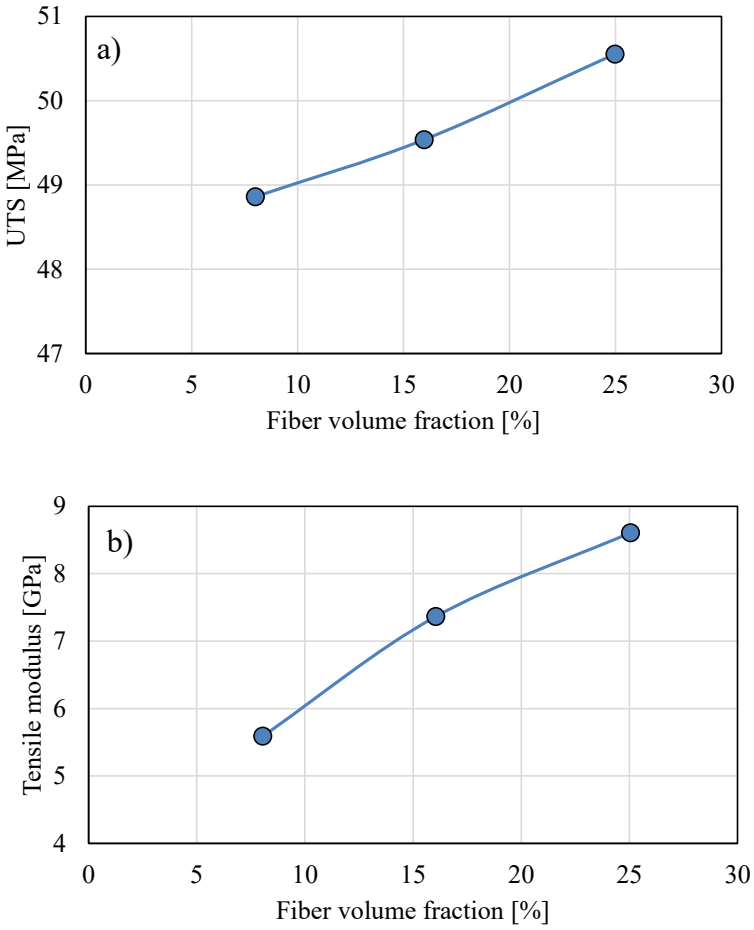

Figure 1.10. UTS (a) and tensile modulus (b) vs. fiber volume fraction for a short glass fiber-reinforced PP (FU00).

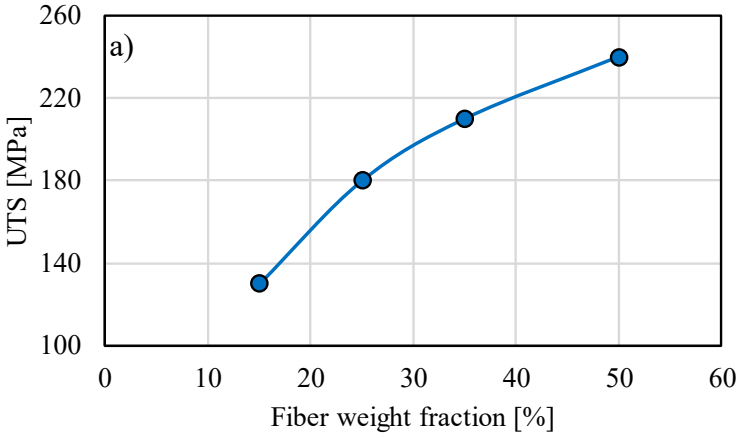

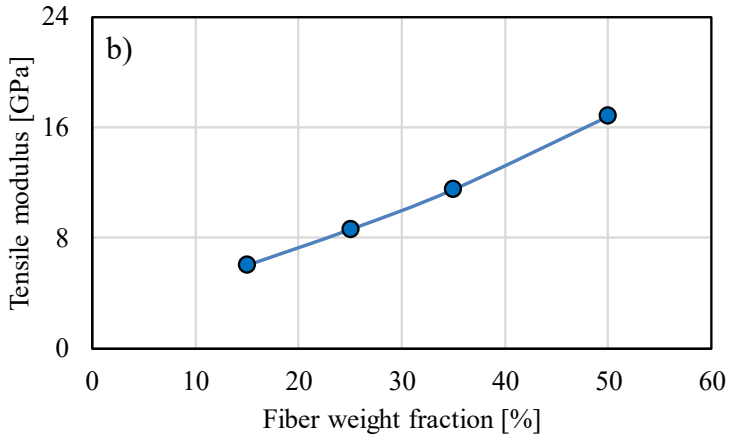

Figure 1.11. UTS (a) and tensile modulus (b) vs. fiber volume fraction for a short glass fiber-reinforced PA66 (BAS2, BAS3, BAS4, BAS5).

1.5.2 Fiber orientation

Dealing with short fibers, their orientation is an issue that many authors face while trying to properly describe the mechanical behavior of SFRTs. In this paragraph, the actual local fiber orientation variation is not taken into account, but, rather, the angle at which specimens have been extracted from injection-molded plates. Because of the material anisotropy induced by fibers, the composite mechanical properties reveal to depend on the extraction angle, identified by angle θ.

De Monte et al. (DEM10) investigated the variation of the UTS (Fig. 1.12a) and tensile modulus (Fig. 1.12b) for a polyamide 6.6 reinforced with the 35 wt% of fibers (PA66-GF35).

From Fig. 1.12 it is clear that the specimens do not possess perfectly aligned fibers that are oriented with the extraction angle. Indeed, a different mechanical behavior is encountered for different thicknesses, this meaning, in turn, that fibers are differently oriented with the three different specimen geometries. For this reason, more effort will be put on the investigation of the actual fiber orientation within the next chapters.

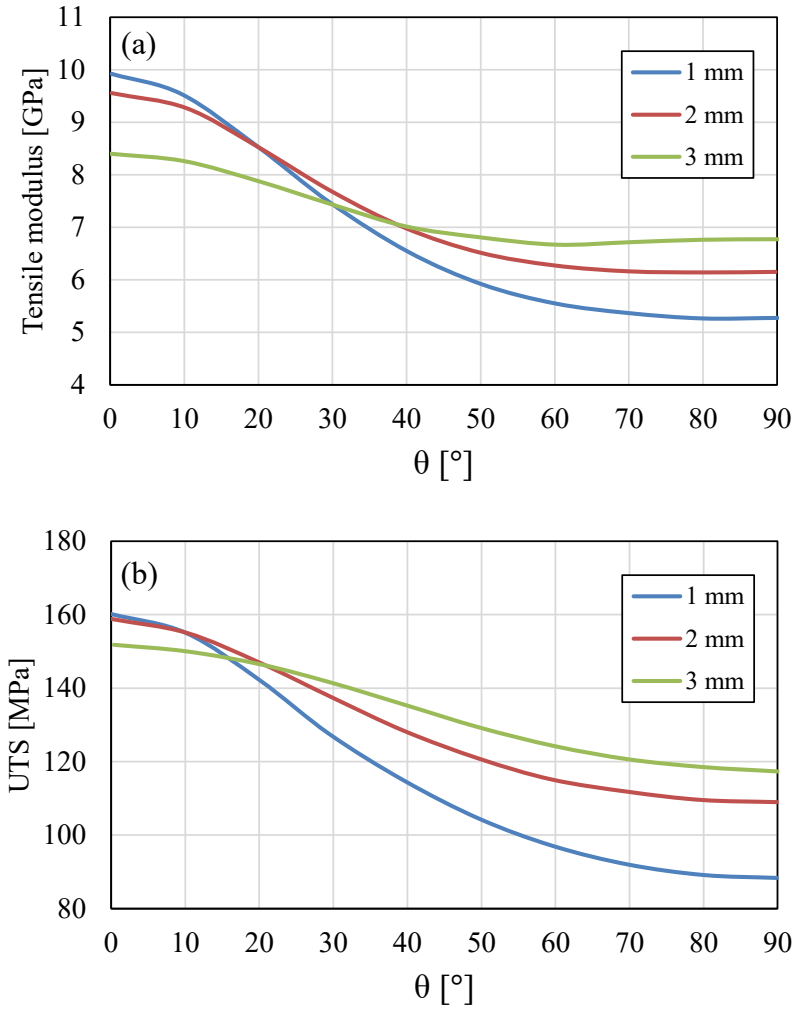

Figure 1.12. Regression of tensile modulus (a) and UTS (b) variation as a function of the specimen extraction angle, for three different thicknesses.

1.5.3 Temperature

The effect of temperature on the mechanical behavior of such materials cannot be neglected. Also in this case, test results for different temperature have been reported by different authors.

Once again, in DEM10 data points carried out at 130°C are reported for different extraction angles in case of a PA66-GF35. Furthermore, after summarizing data of BAS4, the effect of temperature on the quasi-static response of such materials tested at different temperatures is shown in Fig. 1.13.

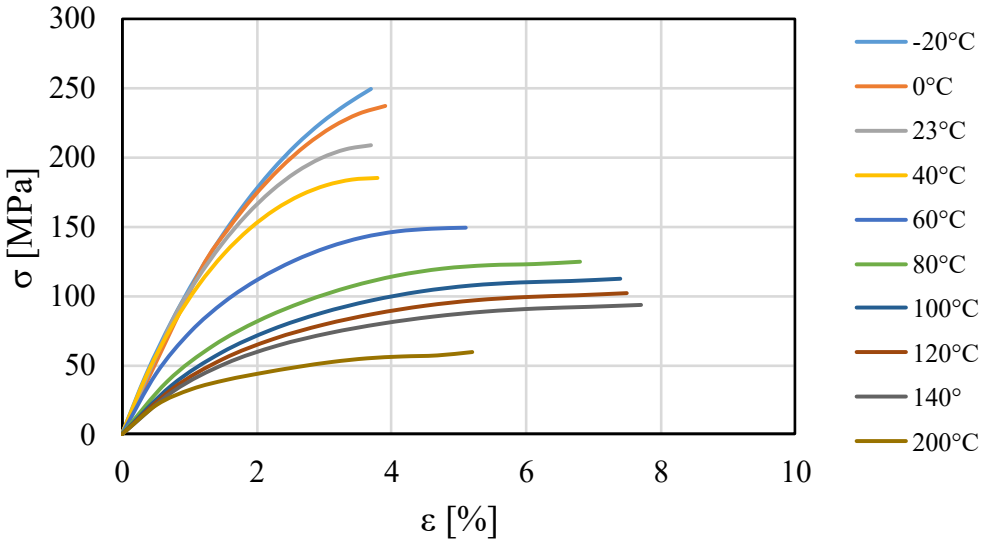

Figure 1.13. Quasi-static tensile curves for a PA66-GF35 at different temperatures.

1.5.4 Moisture

As reported in different works, the mechanical properties of thermoplastics may be affected by the humidity absorbed by the composite matrix (BAS90, MOH94, ISH94, LYO98, PAN07, HAS12, ARI13). Fig. 1.14 reports the differences in terms of UTS and tensile modulus for a PA66-GF35, both for dry-as-molded and conditioned (i.e. after humidity absorption) specimens. Thence, it can be stated that the presence of water in the matrix significantly affects the composite properties, decreasing the material strength and making it more compliant with respect to the dry-as-molded state.

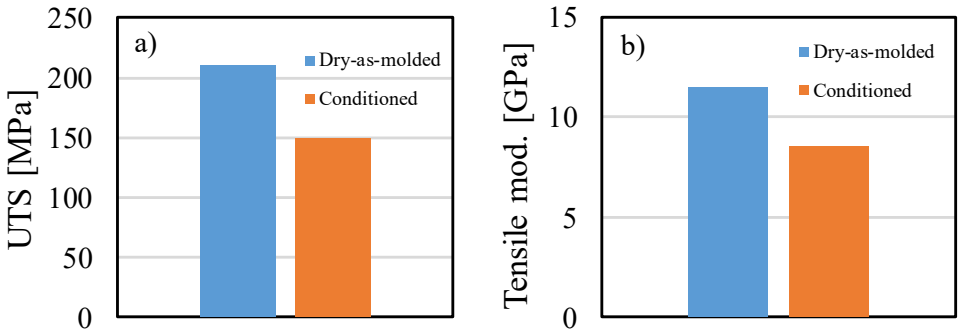

Figure 1.14. UTS (a) and tensile modulus (b) for a dry-as-molded and conditioned PA66-GF35.

1.6 Fatigue behavior of SFRTs

The principal causes affecting the fatigue life of short fiber reinforced thermoplastics are hereby presented and discussed. Namely, the effects of the following factors/parameters will be treated:

- Fiber volume fraction;
- Fiber orientation;
- Temperature;
- Humidity;
- Mean stress;
- Frequency;
- Notch geometry.

1.6.1 Preliminary remarks

Before focusing on the fatigue response of SFRTs, some preliminary remarks concerning the basic concepts of the fatigue theory are hereby recalled.

Fatigue data can be normally reported with different plot types, but in this work only Wöhler-curves will be treated. The latter, can also be named S-N curve and are generally displayed in a bi-logarithmic scale. Referring to Fig. 1.15, the x axis consists in the number of cycles N spent up to a desired moment of the part fatigue lifetime. Namely, either cycles up to crack initiation either up to failure will be discussed later on.

On the other hand, the y axis corresponds to the nominal stress applied to the specimen of interest. As shown in Fig. 1.15, in the literature either the stress amplitude or the maximum applied stress can be used for the parts' design. The meaning of these two types of stresses can be better understood by referring to Fig. 1.16, where a schematic constant amplitude load history is depicted.

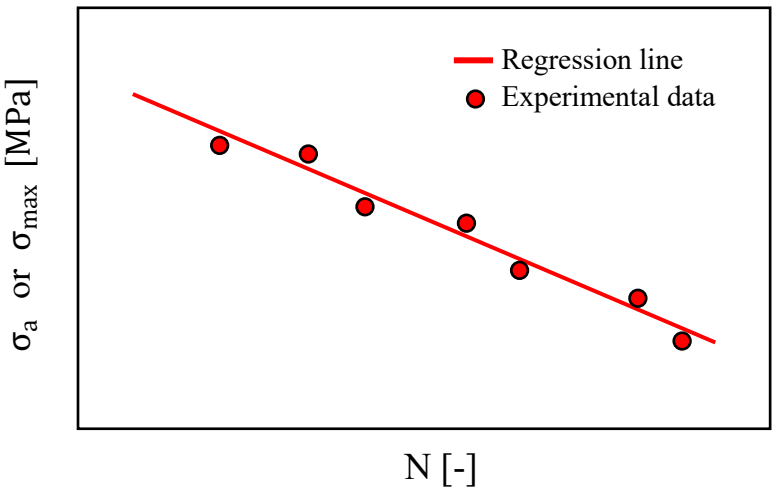

Figure 1.15. Schematic example of Wöhler-curve in bi-logarithmic scale.

Referring to Fig. 1.16, the load ratio (R) of a generic applied cyclic load is defined as follows:

$$R = \frac{\sigma_{min}}{\sigma_{min}} \tag{1.11}$$

As it is clear from Fig. 1.16, symbols σ_a, σ_{min}, σ_{max} and σ_m respectively denote the amplitude, the maximum, the minimum and the mean value of the stress-time curve.

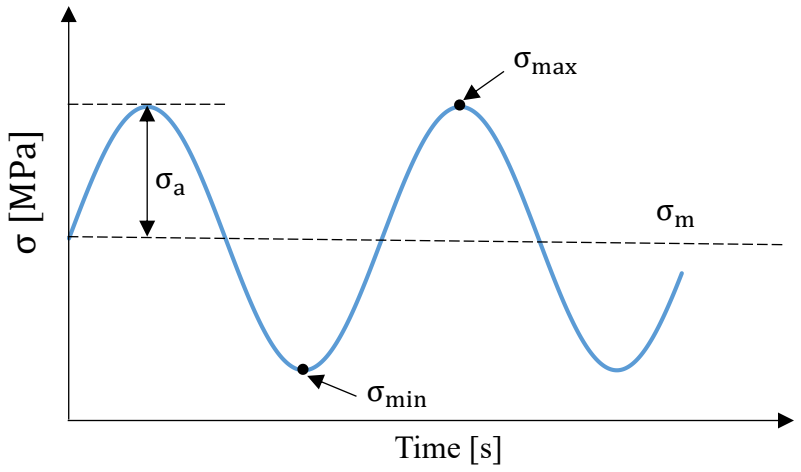

Figure 1.16. Schematic representation of a constant amplitude cyclic load history.

1.6.2 Fiber volume fraction

As anticipated in case of quasi-static loadings, the amount of fillers is crucial to determine the mechanical properties of SFRTs. This statement is also valid for parts or specimens undergoing mechanical fatigue loadings.

It must be additionally highlighted that the effect of fiber volume fraction and orientation on the fatigue strength of such materials cannot be separated a-priori and, therefore, the trends of the fatigue strengths reported in this paragraph must not be considered as always valid. The aim of this section is indeed to give a qualitative overview about the effect of fiber content on the fatigue strength of SFRTs. However, chapter 2 will show how the fatigue strength of 90°-oriented specimens is not very sensitive to the fiber volume fraction.

Only few works in the literature has dealt with the effect of the filler content on the fatigue strength of a SFRT. For example, Zago et al. (ZAG01) investigated the effect of fiber content (30 wt% and 50 wt%) for short glass and carbon fiber reinforced thermoplastics showing an enhancement of the mechanical properties by increasing the amount of fillers.

Belmonte et al. (BEL17) studied the influence of fiber volume fraction on the fatigue life of a short glass fiber-reinforced PA66. Neglecting the fiber orientation differences among the analyzed specimens, the authors of BEL17 showed that a significant strength increase is observed by sequentially considering PA66-GF15, PA6625 and PA66-GF3. Only a slight improvement of the fatigue properties can be seen when moving to the PA66-GF50. Since the authors dealt with sharply notched specimens, they also quantified the cycles to crack initiation and to failure. Focusing on the lifetime spent up to 10^5 cycles, the fatigue strength values (referred to the crack initiation phase) can be plotted as in Fig. 1.17. More details regarding the used geometries and test conditions can be furthermore found in BEL17.

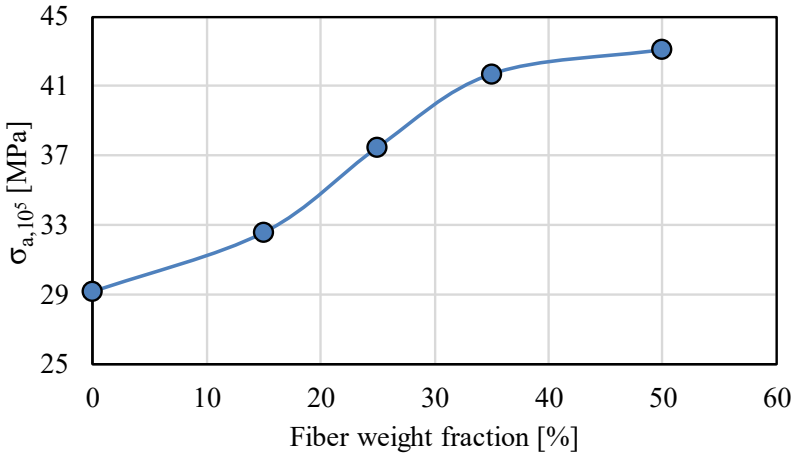

Figure 1.17. Effect of short glass fiber content on the fatigue strength of a PA66 (BEL17).

1.6.3 Fiber orientation

The effect of fiber the orientation on the fatigue life of SFRTs would require detailed studies at the micro-scale, since the fiber cannot be considered as perfectly aligned along one common direction. Nevertheless, different authors have quantified the fatigue strength of SFRT plain specimens, stating that not only the extraction angle influences the fatigue behavior of such materials, but also the profile of the through-the-thickness fiber orientation tensor too (BER07, DEM10, KLI11, LUN13, TAN14, ARI14, JAI16).

Bernasconi at al. (BER07) employed a PA6-GF30 for investigating the effect of the extraction angle on a plain specimen. They decided to cut coupons at four different angles, showing that, as expected, the fatigue strength of the treated SFRT is highly sensitive to the extraction angle and, therefore, to the fiber orientation. The obtained regression values for the material fatigue strength chosen at 10^5 cycles (specimen failure) are summarized in Fig. 1.18. In the latter, a neat decrease of the specimen fatigue strength is observed. This is a consequence of the fact that fibers have a good degree of alignment within the skin layers of the specimen, as it is shown in BER07.

Differently from BER07, De Monte et al. (DEM10) investigated the effect of the plate thickness and, implicitly, of the fiber orientation along the thickness direction. The authors observed that, by increasing the thickness, a lower sensitivity to the extraction angle is encountered.

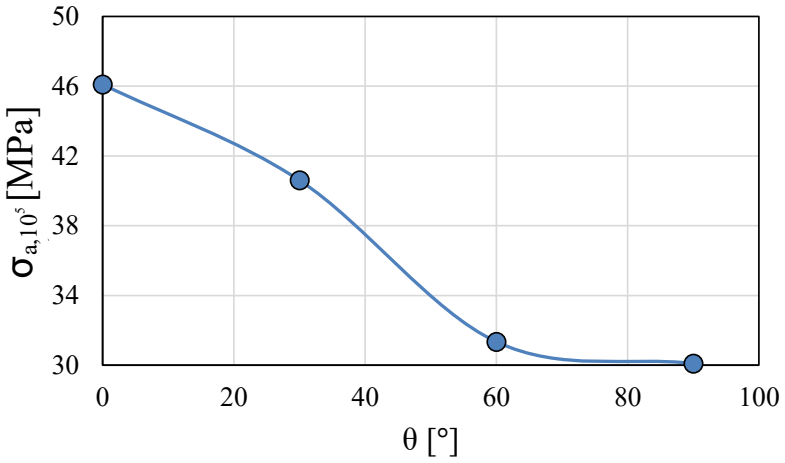

Figure 1.18. Effect of extraction angle (θ) on the fatigue life of a PA6-GF30 (BER07).

In this context, Fig. 1.19 reports the differences in terms of fatigue strength for a 1 mm and a 3 mm thickness specimen as a function of the cut-out angle.

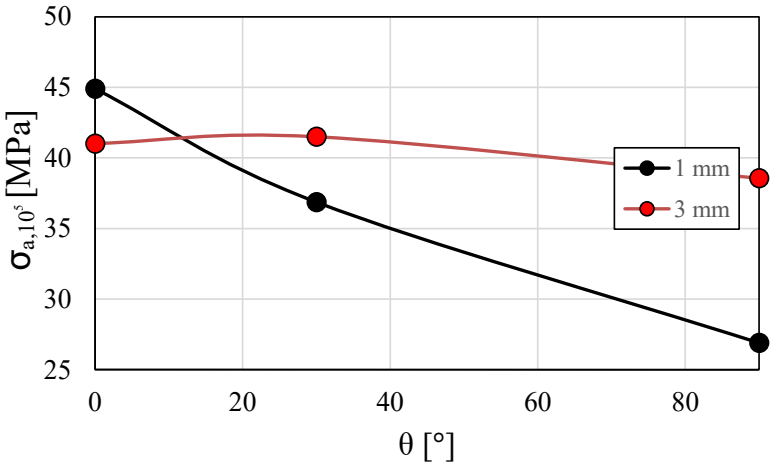

Figure 1.19. Effect of extraction angle (θ) on the fatigue life of a PA66-GF35 (DEM10).

1.6.4 Temperature

Also the effect of temperature on the fatigue behavior of SFRTs has been often treated in the literature showing that, by significantly increasing the service temperature, the material becomes more compliant and less resistant.

As an example of the fatigue behavior of a PA66-GF30 undergoing high temperatures, Eftekhari and Fatemi (EFT16) reported data shown in Fig. 1.20 for temperatures of 85° and 120°C.

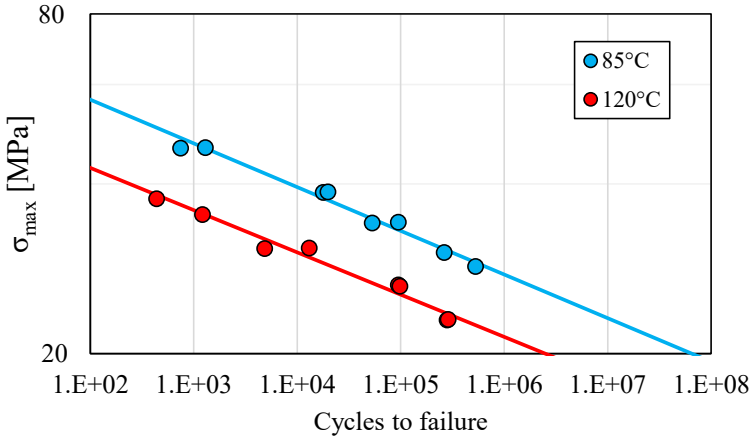

Figure 1.20. Fatigue behavior of a PA66-GF30 at different temperatures (EFT16).

With regard to the specimens of Fig. 1.19, the effect of temperature is also reported in (DEM10) and shown in Fig. 1.21.

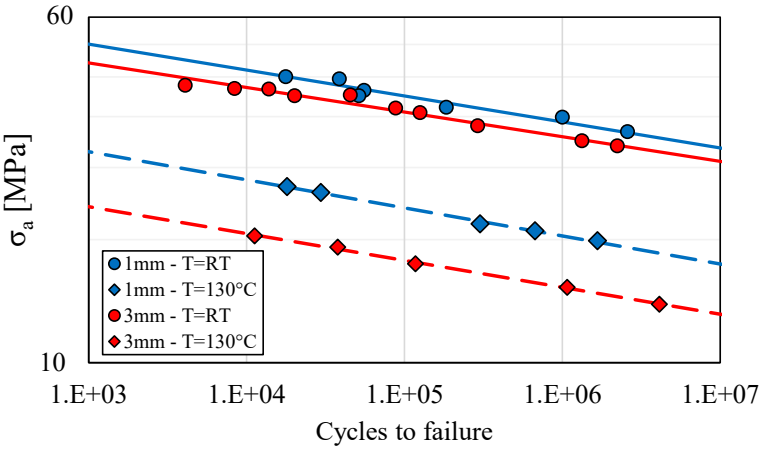

Figure 1.21. Fatigue behavior of a PA66-GF35 at different temperatures (DEM10).

1.6.5 Moisture

Similarly to the effect of temperature on the fatigue repose of SFRTs, as the composite absorbs water and, thence, the matrix cannot be considered dry anymore, a change in terms of fatigue strength occurs (HOP92, BAR07, MOR15_2, FAT15).

In MOR15_2, fatigue curves have been obtained for a PA6-GF30 in both dry and wet conditions. These data are reported in Fig. 1.22 and show how the presence of water within the composite thermoplastic matrix reduce the fatigue strength of the composite.

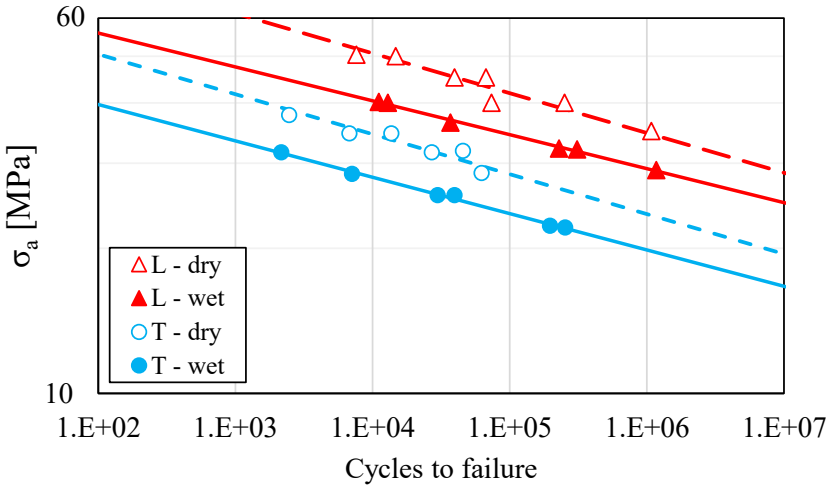

Figure 1.22. Moisture effect on the fatigue behavior of a PA6-GF30 extracted longitudinally (L) and transversally (T) from injection-molded plates (MOR15_2).

1.6.6 Mean stress

Another parameter affecting the fatigue lifetime duration of SFRTs can be attributed to the mean stress at which tests are performed (MAL04, SON08, KLI11, KRA16, EFT16, KAW17).

In their work, Mallick and Zhou (MAL04) performed fatigue curves at different load ratios for tension-tension tests.

Fig. 1.23 shows that the higher the load ratio is, the lower the fatigue strength is.

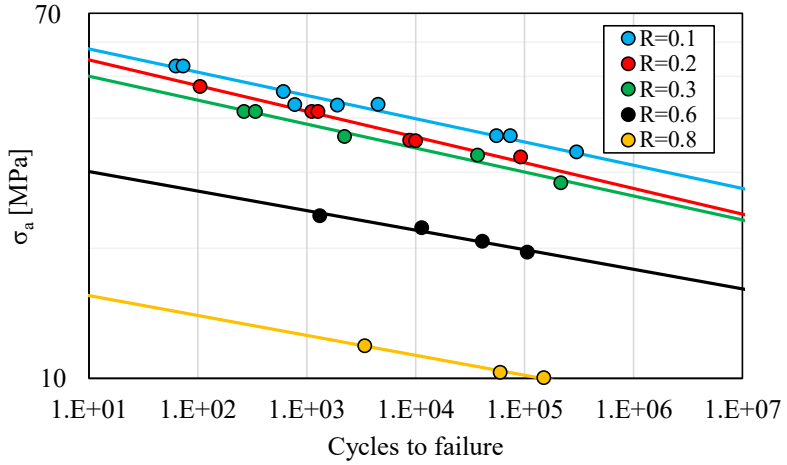

Figure 1.23. Effect of load ratio on the fatigue response of a PA66-GF30 (MAL04).

1.6.7 Frequency

In the work of Eftekhari and Fatemi (EFT16), some investigations on the effect of loading frequencies are provided (Fig. 1.24). The authors quantified the cycles spent up to failure for a chosen load, after performing tests at different frequencies. For instance, they observed that in case of a short fiber-reinforced polypropylene (PP-GF30), the amount of cycles up to failure increases while increasing the test frequency until a certain value, after which self-heating effects becomes predominant with respect to the beneficial frequency effect.

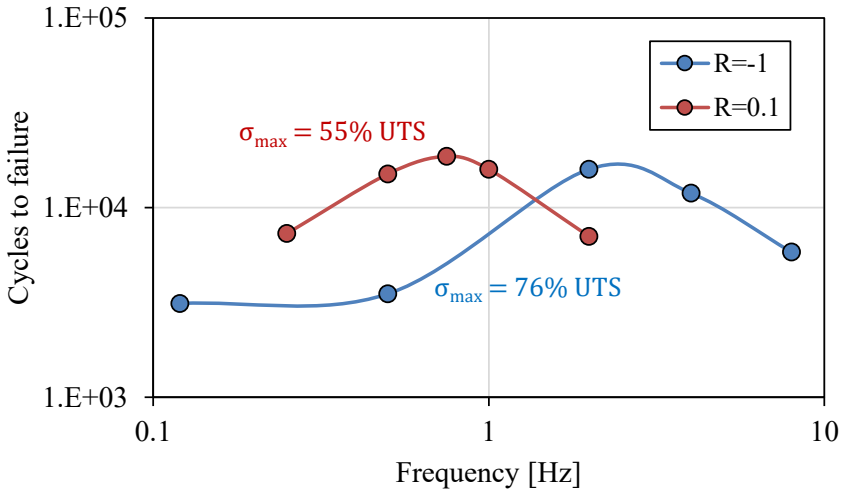

Figure 1.24. Fatigue cycles to failure vs. load frequency for a PP-GF30 (EFT16).

1.6.8 Notch geometry

SFRT materials are often employed thanks to the possibility of filling complex cavities during the injection molding process. Mold geometries might give rise to strong geometrical variations which in turns can be identified as notches contributing to local stress concentrations.

The effect of notches on the fatigue behavior of SFRPs has not been widely covered in the literature yet. The definition of the notch geometry and the creation of it is a crucial stage, since the local fiber orientation is strongly affected by the notch generation method. In this context, Belmonte et al. (BEL16, BEL17. BEL17_2) and Bernasconi et al. (BER15) innovatively proposed to include the notch geometry in the mold, without machining it. Indeed, they demonstrated how local fiber orientation does not appear similar to the one obtained in injection-molded plates.

In the work of Zhou and Mallick (ZHO06), notches were obtained by drilling holes of different sizes at the mid-length of a plain specimen. The authors showed how the fatigue strength of PA66-GF33 is lowered by increasing the holes diameter (Fig. 1.25).

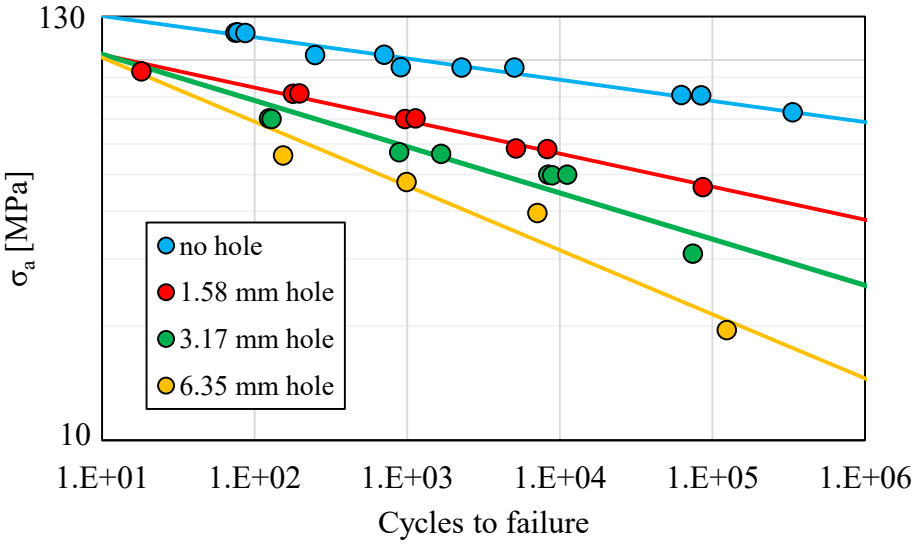

Figure 1.25. Effect of hole-size on the fatigue response of a PA66-GF33 (ZHO06).

For the sake of completeness, the fatigue curves are also reported in case a sharply notch was obtained by means of a metallic slit generating a 0.2 mm radius notch (BEL17_2). The comparison with a plain specimen is therefore shown in Fig. 1.26.

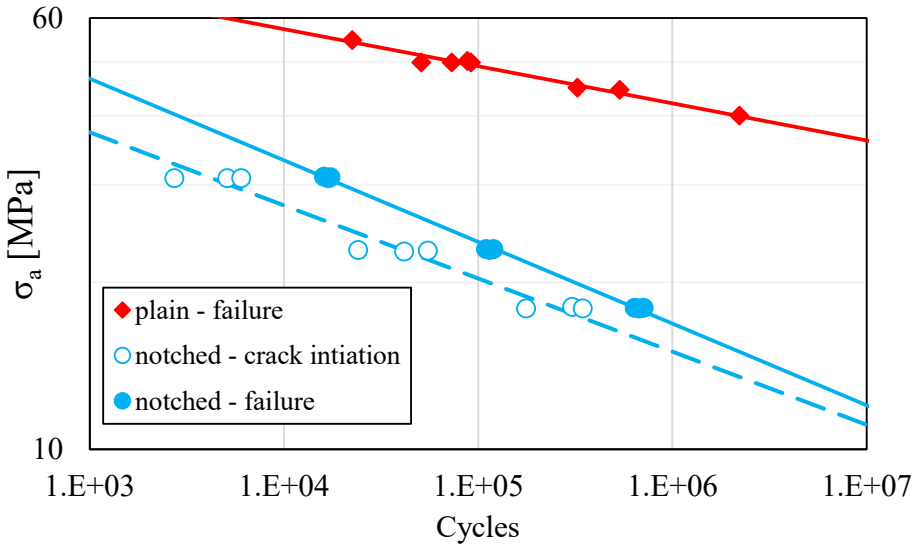

Figure 1.26. Fatigue curves for a plain and a sharply notched PA66-GF35 (BEL17_2).

Chapter 2

Materials and experiments

2.1 Introduction

The aim of the present chapter is to present new experimental data enabling a comprehensive characterization of the considered materials (short glass fiber-reinforced thermoplastics) and to supply further information related to the analyzed microstructures (local fiber orientation distributions) at the most critical sites. The attention is mainly focused on the effect of fiber volume fraction and fiber orientation on the fatigue life of plain and notched specimens made of a polyamide 6.6 (PA66) reinforced with short glass fibers. Additionally, fatigue tests on coupons in the presence of notches (sharp and mild) are presented in order to evaluate the effect of the notch geometry, combined to the intrinsic material anisotropy.

Furthermore, computed tomography (CT) scans have been performed for most of the presented specimens and, additionally, the fiber orientation tensors (FOT) have been evaluated for some of them, the fatigue data of which are already present in the literature. This has been done in order to provide the developed fatigue models with the proper inputs (FOTs and fatigue S-N curves) in order to robustly verify the applicability of the fatigue criteria that will be treated within the next chapters, either for plain either for notched coupons,.

It has been observed and stated by different authors (DEM10, BER07, ARI14) that short fiber-reinforced composites possess anisotropic properties, which in turn cannot be generally considered uniform along the three directions of the Cartesian reference system within an injection-molded specimen (BEL17) or plate. Thence, analyses on the locally varying fiber distributions are needed to properly build up finite element (FE) models capable of predicting the fatigue strength of the considered geometries.

Differently from continuous fiber-reinforced polymers, where the fiber orientation reconstruction reveals to be sufficiently straightforward thanks to the ease of setting the fiber orientations within the plies of the produced specimens, in case of SFRTs the injection molding process increases the difficulty of controlling the local fiber orientations at the most critical sites (e.g. close to strong geometrical variations). As a matter of fact, not only the molds' geometry might affect the local fiber placement, and therefore the part's fatigue strength, but also the process parameters (e.g. pressure and temperature) play an important role in the fiber orientation predictability.

In the literature, the correlation between the fatigue response of SFRTs and the fibers' orientation has been not deeply investigated yet. Indeed, only a few works showing the fatigue behavior of such materials associated to studies on the actual microstructures are available. In this context, Bernasconi et al. (BER15) investigated the effect of V-notch radius size and local fiber orientation of a glass fiber reinforced polyamide 6 (PA6-GF30). Furthermore, they optically observed the cross sectional area and quantified the FOT components variation.

De Monte et al. (DEM10_3) dealt with injection-molded tubes (PA66-GF35) undergoing multiaxial external fatigue loadings. The authors also performed 2D analyses on the net section and evaluated the first component of the FOT. They found a non-negligible fiber orientation gradient along the specimen thickness. The authors of DEM10 performed process simulations, as well, which revealed to be too optimistic in terms of fiber alignment. Furthermore, in DEM10 the effect of temperature, load ratio and applied biaxiality ratio was investigated by performing S-N curves.

In BEL17, the specimen characterization has been performed in the presence of sharp notches. In particular, the authors aimed at quantifying the effect of the filler content on the fatigue strength of the proposed specimens geometries. Similarly to BER15, the authors innovatively did not created the notch geometry by machining injected plates, but inserted a metallic slit during the molding process in order to emulate a real part fabrication. They also gave an insight about the local fiber arrangement at the notch root, pointing out that a fiber orientation distribution gradient might be normally encountered along the 3D directions in such a scenario.

Nevertheless, many works in the literature rely on qualitative analyses of the microstructure or on the fiber orientations carried out by performing process simulations. As previously

mentioned, in order provide the developed models with reliable inputs, fatigue data and FOTs (obtained with CT scans) of plain and notches specimens are hereby presented.
One more remark concerns the number of cycles employed for displaying S-N curves. In this context, the present work aims at providing a fatigue criterion enabling the specimens' life-time prediction up to crack initiation. According to (BEL17_2), plain coupons do not normally undergo extended crack propagation phases because of the absence of stress concentrations that usually localize the crack initiation within limited volumes. For the previously mentioned reasons, the number of cycles up to failure will be employed in the absence of notches. On the other hand, while considering notched specimens, depending on the notch radius and the specimen size, the crack onset phase might interest only a reduced percentage of the material life.
According the previous observations, the following data will be presented in this chapter:

- FOT components evaluation by means of the X-ray computed tomography;
- Fatigue curves up to failure in the absence of notches;
- Fatigue curves up to crack initiation in the presence of notches.

2.2 Specimens' geometry

Different specimen geometries will be hereinafter involved to verify the robustness of the fatigue criterion that will be detailed within the next chapters. In this interest, not always the same coupons' geometry is considered. Indeed, the fatigue strength and the fibers' orientation of specimens characterized by different thicknesses (1 mm, 2 mm and 3 mm), lengths (80 mm and 250 mm) and notch radii (0.1 mm, 0.2 mm, 2.0 mm and 5 mm) are investigated.
Nevertheless, all data here presented and those obtained from the literature are characterized by the same constituents, i.e. a PA66 matrix reinforced with a certain fiber weight fraction (GF15, GF25, GF35 and GF50). No particular attention is given to the possible local fiber volume fraction variations, since the proposed fatigue models will assume a uniform distribution of the fiber content within the analyzed part.

The effect of the material anisotropy is also of particular concern. Therefore, in different occasions, the influence of the angle between the main flow direction (MFD) and the loading direction is accounted for. In fact, specimens nominally oriented at 0°, 30° and 90° are also used for the sake of completeness.

The geometries of specimens, as well as of the injection-molded plates, are described below. With regard to the specimens extracted form plates, it must be highlighted that only one coupon is obtained from each plate by means of the end mill process (cylindrical tool) and the specimen lateral surfaces have not been polished after the extraction.

2.2.1 Plain specimens

In this section, an overview of the considered plain specimens is given. The location at which CT scans have been performed is moreover marked by means of blue dots. Eventually, symbol t will be used in this chapter to denote the thickness of the geometry of interest.

Firstly, the dimensions of the specimens presented by De Monte et al. (DEM10_2) are reported in Fig. 2.1. The reason why such a geometry is depicted is due to the fact that values of the significant FOTs will be presented later on. This geometry is furthermore denoted in this work by P/A, meaning P plain and indicating A the type of geometry.

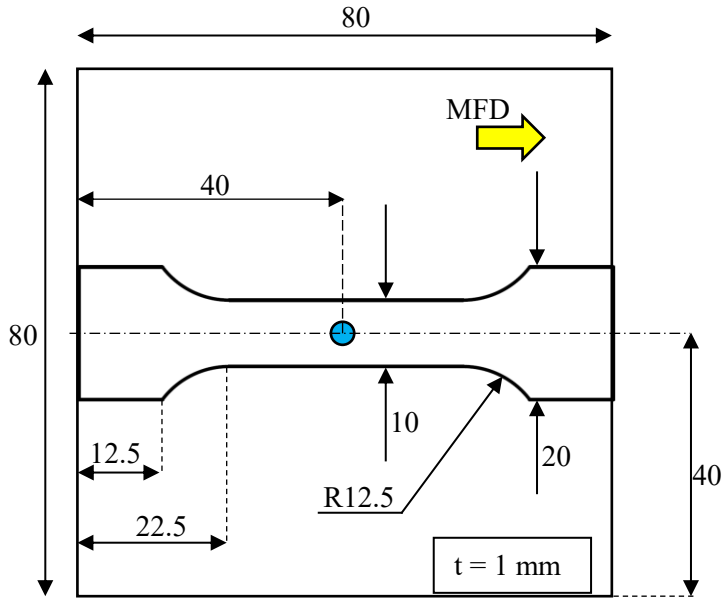

Figure 2.1. Geometry P/A (DEM10_2). Specimen and plate dimensions.

More details related to the coupons of Fig. 2.1 can be found in DEM10_2.

The next geometry called P/B has been extracted from a plate, the size of which is 120x80x2 mm^3.

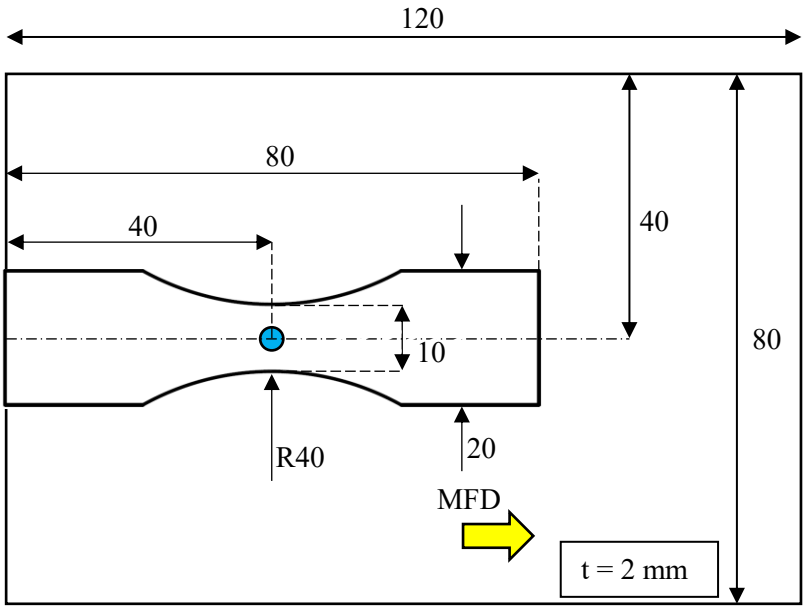

Figure 2.2. Gemetry P/B. Specimen and plate dimensions.

The reason of choosing such a geometry is due to the fact that more control related to the crack onset site was required. Indeed, it was demonstrated by De Monte et al. (DEM08) that geometry P/A might have the cracks arising at the different locations along the gauge length. On the other hand, specimens P/B always yield cracks at the smallest cross-sectional area.

The third adopted plain geometry (P/C) is shown in Fig. 2.3. Contrary to the previous ones, the latter has been obtained without machining plates. In fact, the mold corresponds to the coupon and the only performed mechanical finish served to remove the injection gate.

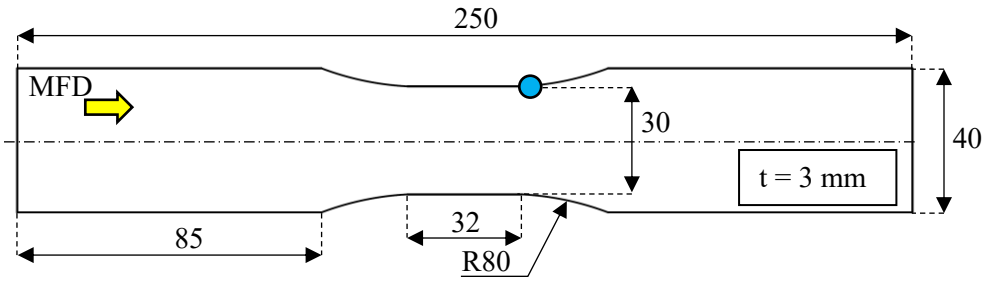

Figure 2.3. Geometry P/C. Specimen dimensions.

2.2.2 Notched specimens

Beside tests on plain specimens, coupons in the presence of notches will be also taken into account. The reason of this choice derives from the fact that real SFRT parts produced in the industry are mostly characterized by sudden geometrical variations raising strong stress concentrations. Later, a model for the prediction of the notch effect on the fatigue life of SFRTs will be presented. In order to extensively validate the given approach, data related to the FOTs will be reported in this paragraph.

The first employed geometry consists in a V-notched specimen machined out of the plates of the same series as the one depicted in Fig. 2.2. The specimen dimensions are therefore shown in Fig. 2.4.

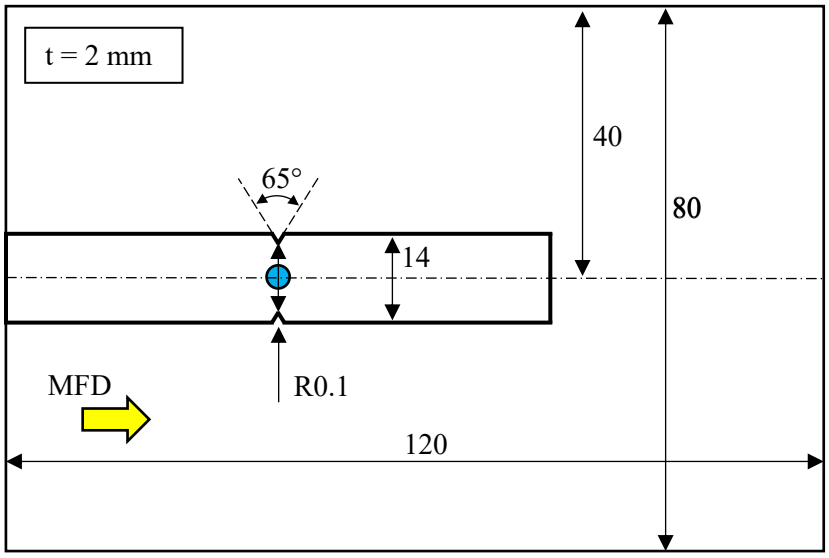

Figure 2.4. Geometry N/A. Specimen and plate dimensions.

The specimen type shown in Fig. 2.4 has been chosen to have a good control of the FOTs characterizing the coupon. Namely, less variability with regard to the fiber orientation within the most critical volumes, i.e. the region surrounding the notch tip, is induced by machining the notch shape. Thus, while assigning the elastic properties to the model, less effort can be put in this activity.

On the other hand, to complete the cases of study, a scenario in which the FOT at the notch root strongly depend on the material flow hitting a preexisting notch is required The notch is shaped during the injection molding process by means of a metallic slit inserted into the mold. According to the work of (BEL17_2), fatigue data presented by the authors will be adopted. In this interest, the FOTs have been evaluated by means of the X-ray computed tomography. Specimen geometry N/B is furthermore shown in Fig. 2.5.

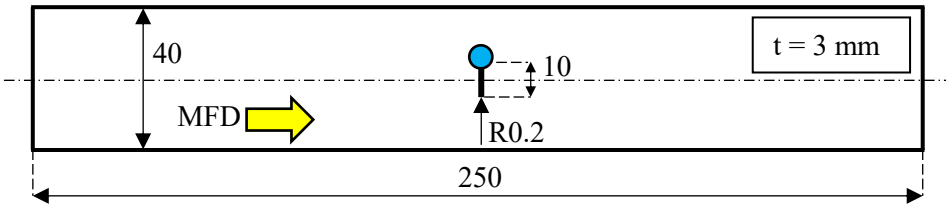

Figure 2.5. Geometry N/B (BEL17_2). Specimen dimensions.

The previous coupons (N/A and N/B) can be classified as sharply notched specimens. Hence, the validation of a robust fatigue criterion requires mild notches as well, in order to understand whether the proposed model actually takes into account the notch geometry. Accordingly, the dimensions of a mild notched coupon, denominated N/C, are reported in Fig. 2.6.

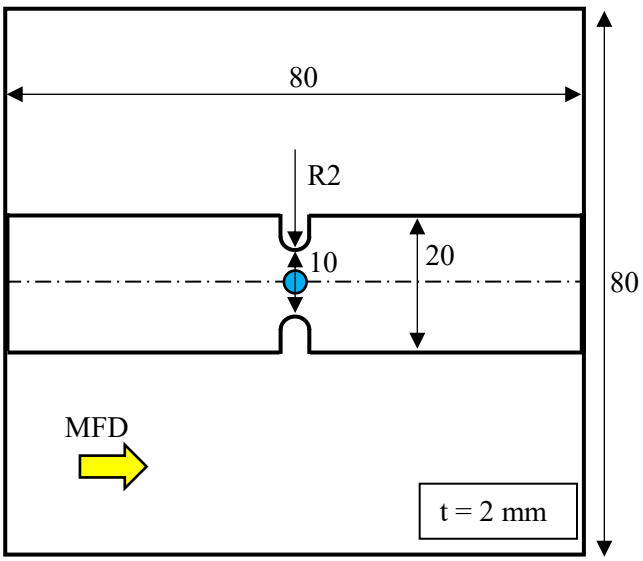

Figure 2.6. Geometry N/C. Specimen and plate dimensions.

Eventually, the notch geometry of specimen N/D (Fig. 2.7) has been obtained with a circular metallic insert. Therefore, fibers tend to settle according to the deviated material flow during the injection molding process.

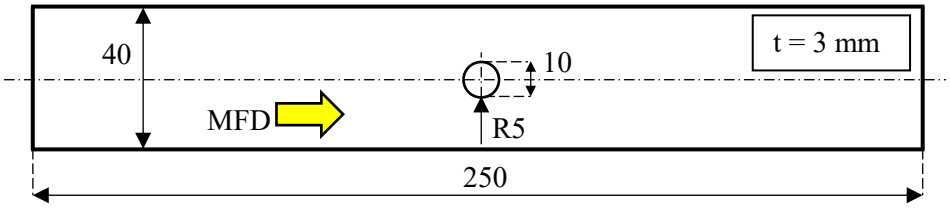

Figure 2.7. Geometry N/D. Specimen dimensions (DEM08).

It must be noticed that Fig. 2.7 has no blue dot at the notch tip. Indeed, no CT scans have been performed and only FOT data resulting from Moldflow® simulations will be used. This can be justified by the notch shape. Indeed, no strong geometrical variations are induced by the large notch radius (i.e. 5 mm) and the material flow can be assumed not to undergo particular out-of-plane perturbations, whereas the same observations cannot be done for geometry N/B. The central slot of the latter gives rise to an instable material flow that is expected not to be captured through process simulations efficiently.
It is additionally remarked that the considered specimens are characterized by different sizes and notch shapes. Therefore, in order to develop reliable fatigue criteria to predict the specimen failure, proper information related to the fibers' orientation must be chosen. In this interest, the following paragraph report data of the FOTs evaluated for the previously described geometries.

2.3 X-ray computed tomography analyses

In this paragraph, results concerning the evaluation of the FOTs at the critical specimen locations are presented and discussed. Fiber orientation tensors have been obtained by performing CT scans at the sites of interest.

The choice of the analyzed volumes is a crucial operation for the model development process. In fact, the assignment of the elastic properties to the elements of the FE mesh highly affects the resulting stress fields, which in turn are responsible for defining the proper stress component controlling the fatigue damage. Indeed, as it will be shown within the next paragraphs, FOTs are normally used as inputs for analytical homogenization schemes for the estimation of the elastic properties of an entire FE model.

All CT analyses here presented have been performed in collaboration with the CR/ANA department of Robert Bosch GmbH. A *phoenix v|tome|x m* machine by the firm GE Sensing & Inspection Technologies has been used to evaluate the FOTs within the analyzed parts, the resolution of which is nominally beyond down to < 1 μm.

2.3.1 Results

In this section, the FOTs resulting from CT analyses on the specimens/plates that have been previously shown will be presented and discussed. All FOTs reported in this section have been evaluated by means of the orientation analysis module of the software VG Studio Max. The latter makes use of the grey-scale values resulting from the analysis of the part of interest. Indeed, thanks to their nature, fibers possess a stronger image contrast with respect to the matrix, enabling the software to distinguish whether the analyzed voxels belong to fibers or matrix. Once a grey-scale threshold is chosen by the operator, an average FOT can be evaluated for each grid element, according to Fig. 1.8.

Before reporting CT data, it must be remarked that two different FOT evaluation techniques are here adopted, depending on the specimen nature. Namely, in case of coupons extracted from injection-molded plates, only the FOT variation along the through-the-thickness direction is taken into account. Diversely, whether the notch is obtained by means of a metallic insert, a finer discretization of the observed area has to be performed in order to better capture the FOT components' gradient along the three directions of the reference Cartesian system.

For the sake of completeness, the settings that have been used for the CT machine are listed in Tab. 2.1

It must be furthermore remarked that geometries P/A and N/A have been obtained from the same series of plates and, therefore, the same CT data will be employed for both.

By reference to Tab. 2.1, the voxel stands for the resolution of the carried out analysis. These values can be considered acceptable for the case of SFRTs, since the smallest dimension of a fiber, i.e. its diameter, is around 10 μm. On the other hand, if fiber geometry reconstruction had to be performed, a higher resolution would be needed.

Table 2.1. Adopted CT scan settings.

Geometry	**Voxel size** [μm]	**Tension** [kV]	**Tube current** [μA]	**Exposure time** [ms]
P/A and N/A	2.0	80	225	333
P/B	2.3	80	225	333
P/C	2.4	80	225	333
N/B	2.4	80	225	333
N/C	2.9	80	225	333

Nonetheless, it is worth mentioning that the reached resolution, i.e. voxel dimension, does not correspond to the machine nominal one. This is a consequence of the size of the investigated volume extracted from the plates/specimens. Indeed, the bigger the observed part is, lower the resolution is.

As already said, CT data, expressed terms of FOTs, have been evaluated at the sites highlighted with a blue dot in sections 2.2.1 and 2.2.2. Since not only one fiber volume fraction has been generally tested, more CT scans have been therefore performed with regard to one plate geometry, but for different filler contents. Some coupons have been additionally extracted transversally to the main flow direction of the plate. There, no further analyses would be required, but the FOT components can be simply rotated mathematically.

As mentioned above, in case of CT scans on plates, the FOT evaluation takes place along the through-the-thickness direction. The latter is normally discretized and a certain amount of layers are identified. By way of example, Fig. 2.8b reports the image reconstruction of a typical CT scan and Fig. 2.8a**,** 2.8c and 2.8d represent the discretization that might be done along the thickness direction.

For the sake of clarity, be the following notation used to identify the reference systems:

- x = main flow direction;
- y = plate/specimen width;
- z = through-the-thickness direction.

The first presented fiber orientation data concern geometry P/A of Fig. 2.1 and the analyzed material is a PA66-GF35. The FOT evaluation has been done choosing 15 layers along the thickness direction. The resulting FOT components are plotted in Fig. 2.9.

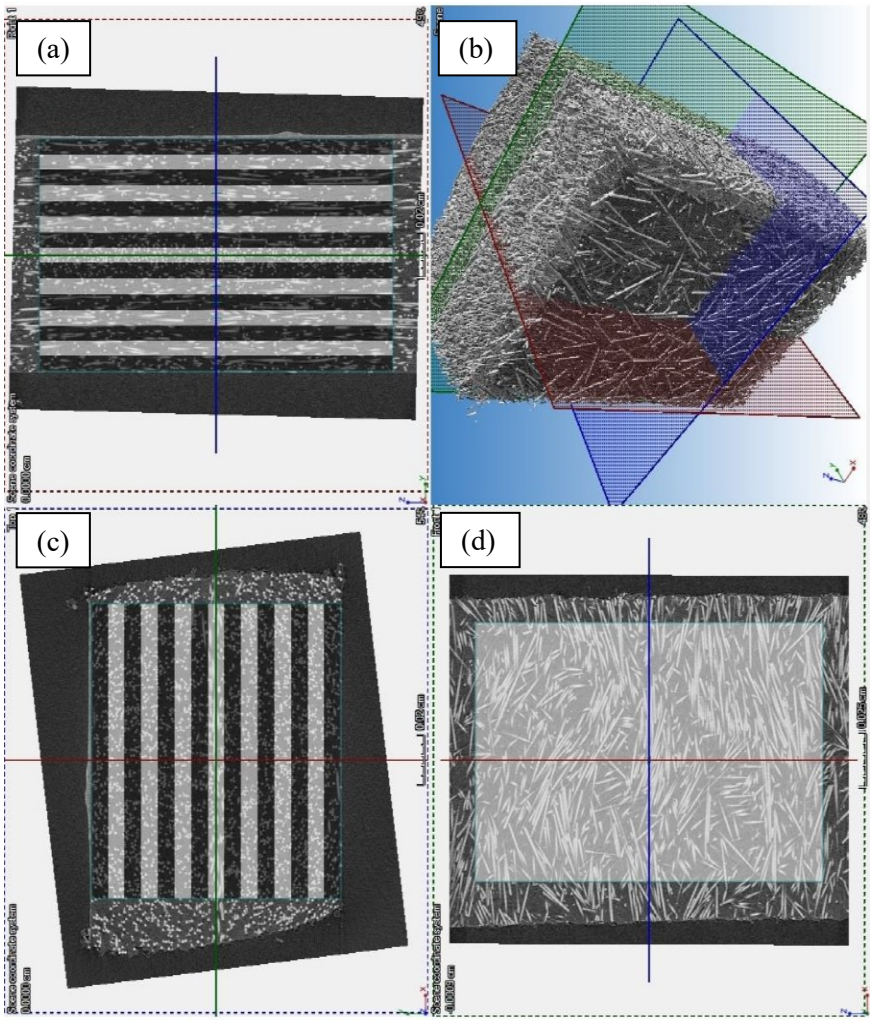

Figure 2.8. Example of CT grid placement for analyses on plates.

Without paying attention to the out-of-plane FOT component (a_{zz}), Fig. 2.9 presents the skin-core effect, which is typical for injection-molded plates. Indeed, by observing the xx and yy components, it can be quantitatively stated that fibers possess a better alignment within the

regions close to the upper and lower model faces and roughly a transversal orientation within the central layers.

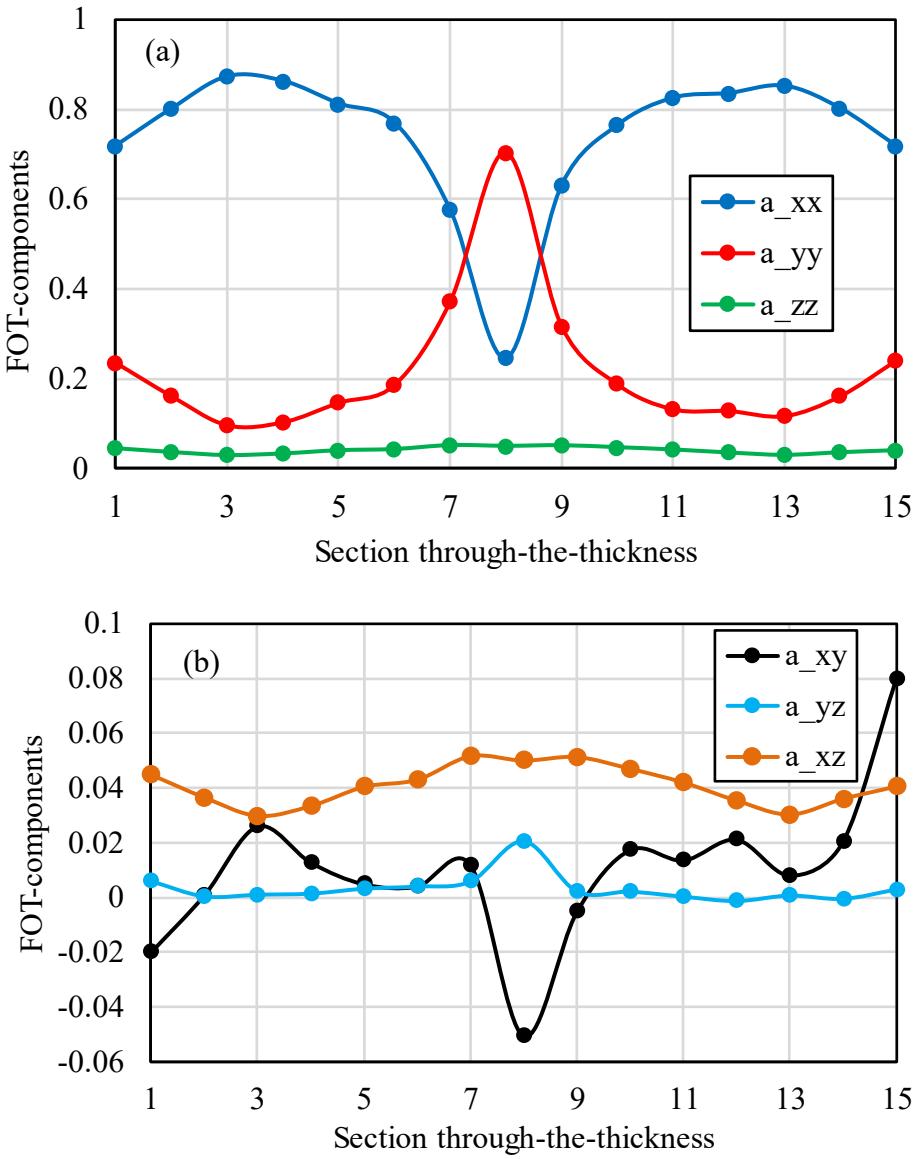

Figure 2.9. FOT components for a plate of geometry P/A (PA66-GF35). Diagonal (a) and out-of-diagonal (b) components.

The same observations can be done for the plates of Fig. 2.2 and 2.4. This time, not only one fiber volume fraction is considered, indeed, fatigue tests to investigate the effect of fiber volume fraction will be shown later on. Similarly to Fig. 2.9, a discretization of 15 layers

through-the-thickness has been kept here too. The FOT components evaluated for this plate geometry are therefore reported in Fig. 2.10, 2.11, 2.12 and 2.13, respectively for PA66-GF15, PA66-GF25, PA66-GF35 and PA66-GF50. Here again, the typical skin-core effect is encountered. By observing the differences among the investigated fiber weight fractions and focusing on the a_{xx} components, an improvement in terms of fiber alignment can be observed within the skin-layers. On the other hand, the PA66-GF50 plate is characterized by a core-layer that is much wider than the other plates.

It must be furthermore noticed that the zz component of the fiber orientations tensors shown until now might be also neglected during the modeling process, due to its low values.

Similar analyses have been carried out for geometry P/C of Fig. 2.3. Having the latter dimensions much bigger than to the previous geometries, more details concerning the crack onset critical site will be given.

Indeed, no measurement has been performed in the center of the gauge length of the specimens, but FOT components estimation has been carried out at the specimen shoulder, as highlighted by the blue dot in Fig. 2.5.

Observing the FOT profiles through-the-thickness of specimens with geometry N/C (Fig. 2.14-2.17), a better fiber alignment at the critical site is encountered. The reason of it may be attributed to the fact that the CT analyses have been performed close to the mold wall, which in turn induces a stronger surface tension allowing fibers to settle predominantly along the MFD.

Additionally, the value of a_{xx} becomes more uniform along the thickness direction by increasing the fiber volume fraction.

In the presence of notches, the use of information deriving from CT scans are hereinafter treated in a different manner. Especially, the presented results and considerations are valid for those notches obtained by inserting metallic slits into the mold while fabricated.

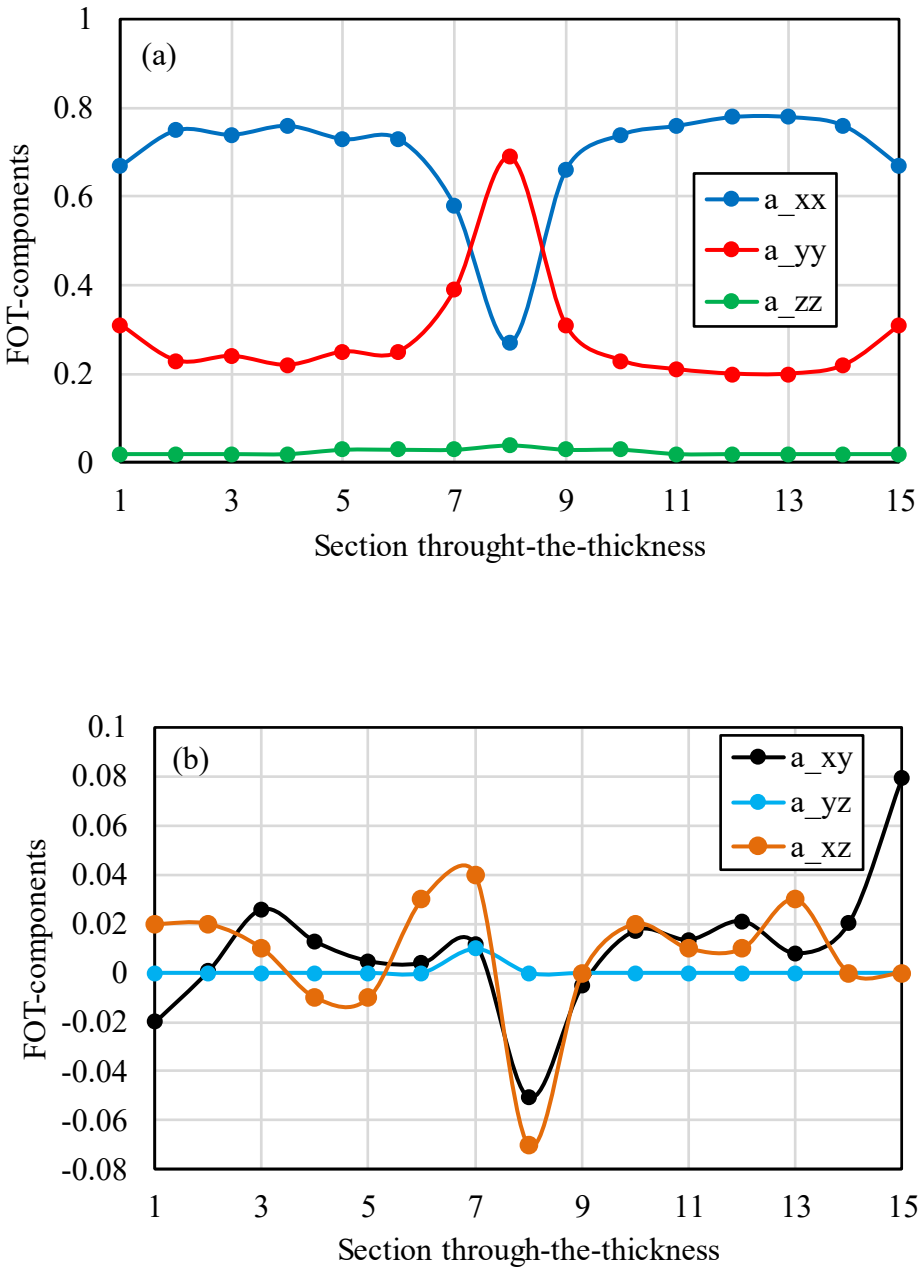

Figure 2.10. FOT components for a plate of geometry P/B and N/A (PA66-GF15). Diagonal (a) and out-of-diagonal (b) components.

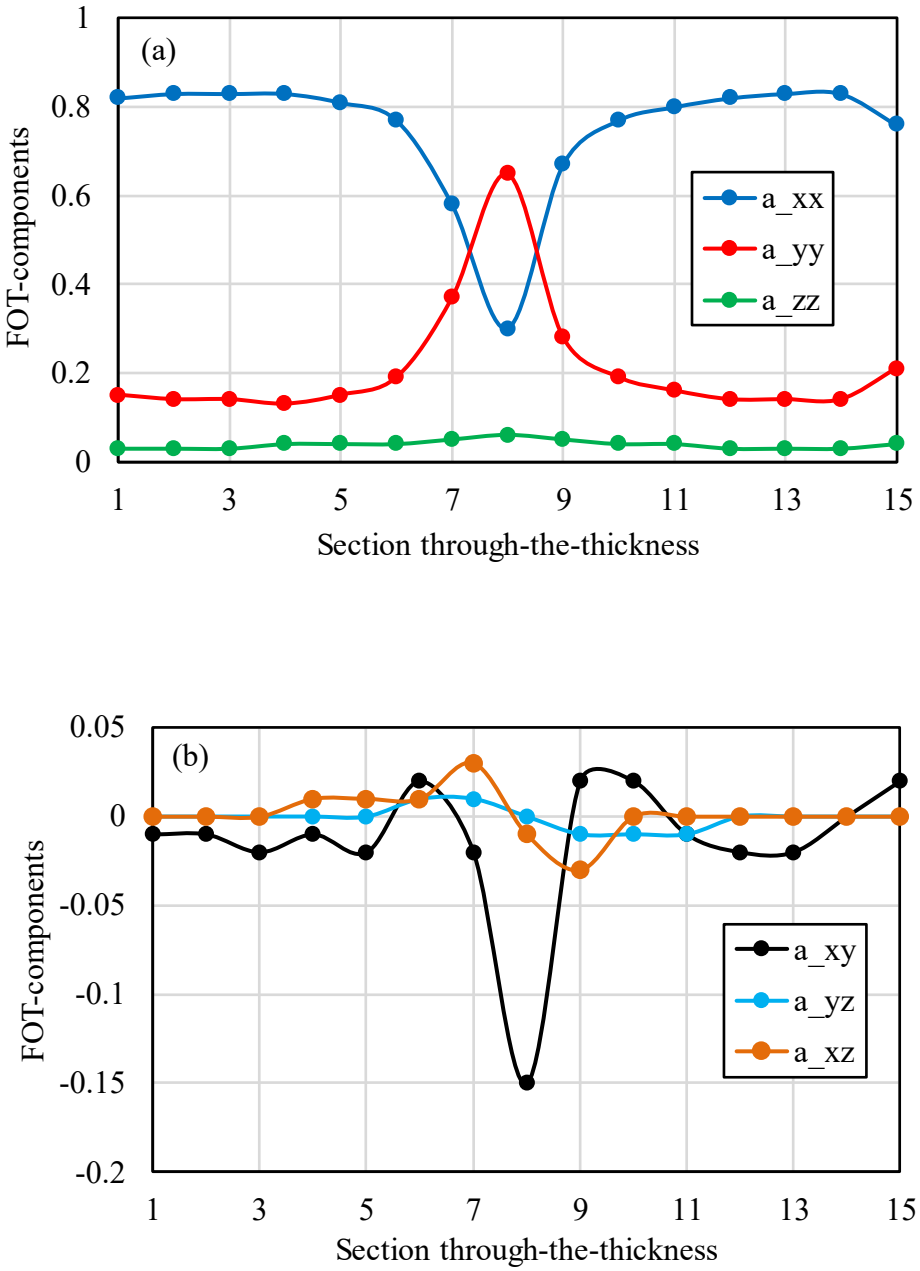

Figure 2.11. FOT components for a plate of geometry P/B and N/A (PA66-GF25). Diagonal (a) and out-of-diagonal (b) components.

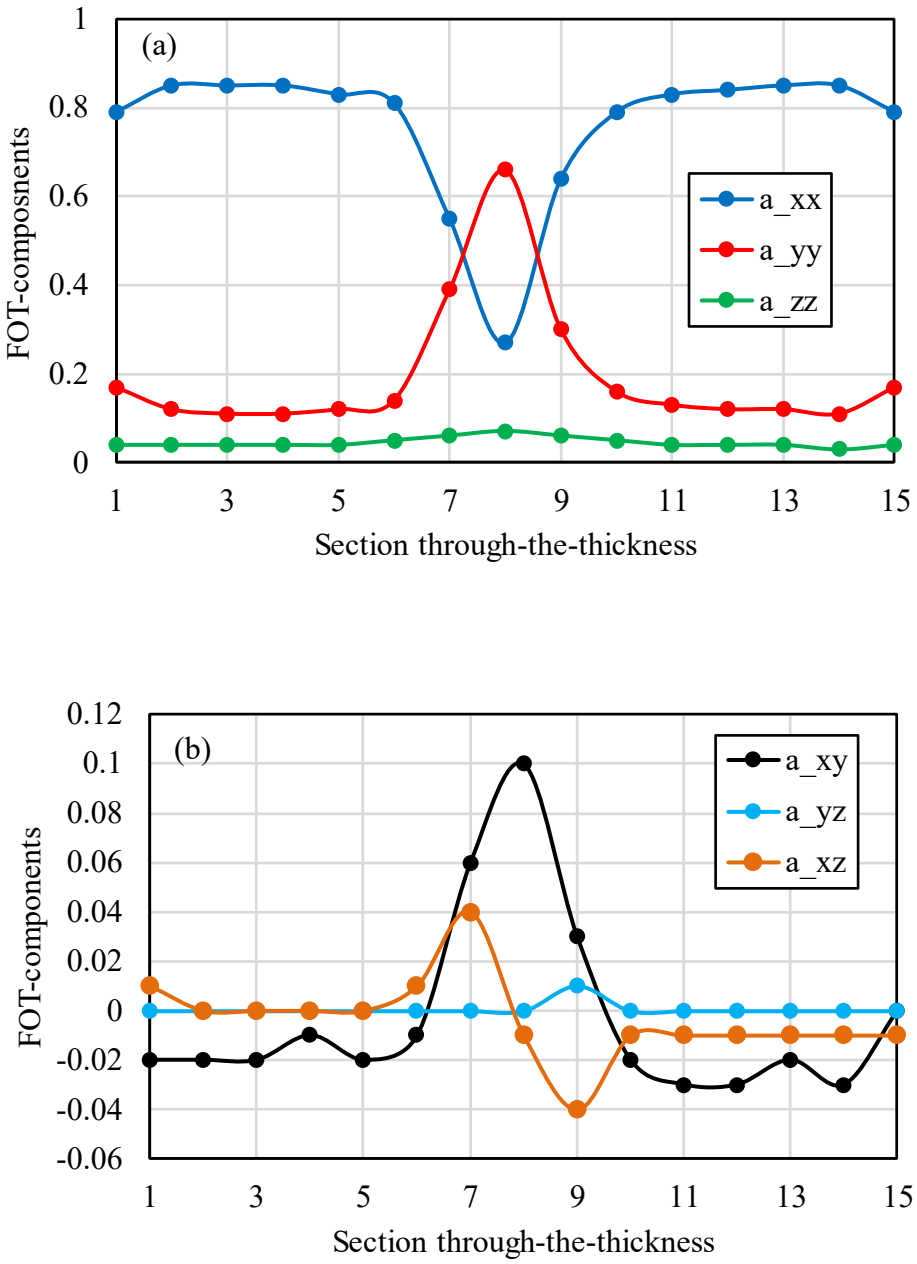

Figure 2.12. FOT components for a plate of geometry P/B and N/A (PA66-GF35). Diagonal (a) and out-of-diagonal (b) components.

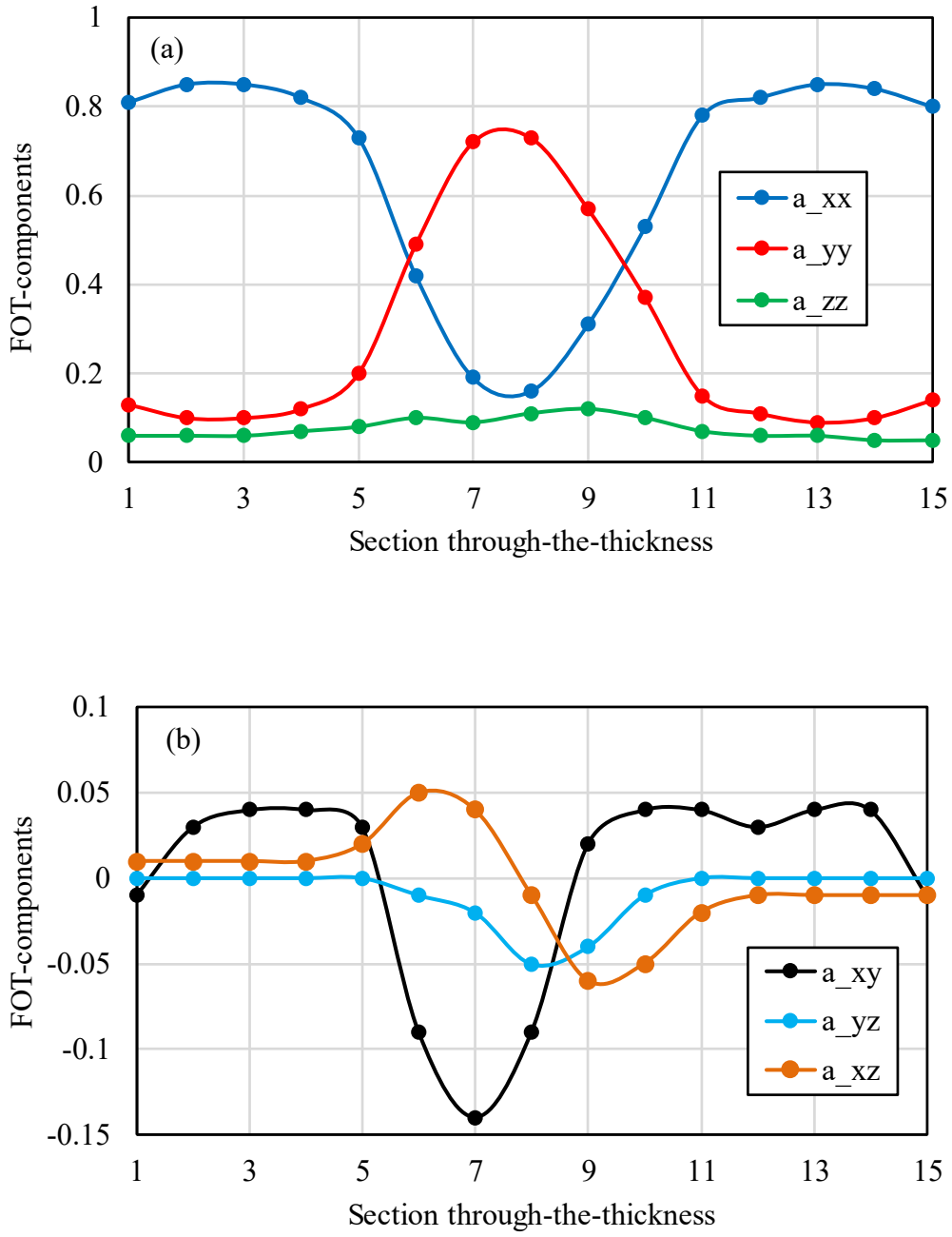

Figure 2.13. FOT components for a plate of geometry P/B and N/A (PA66-GF50). Diagonal (a) and out-of-diagonal (b) components.

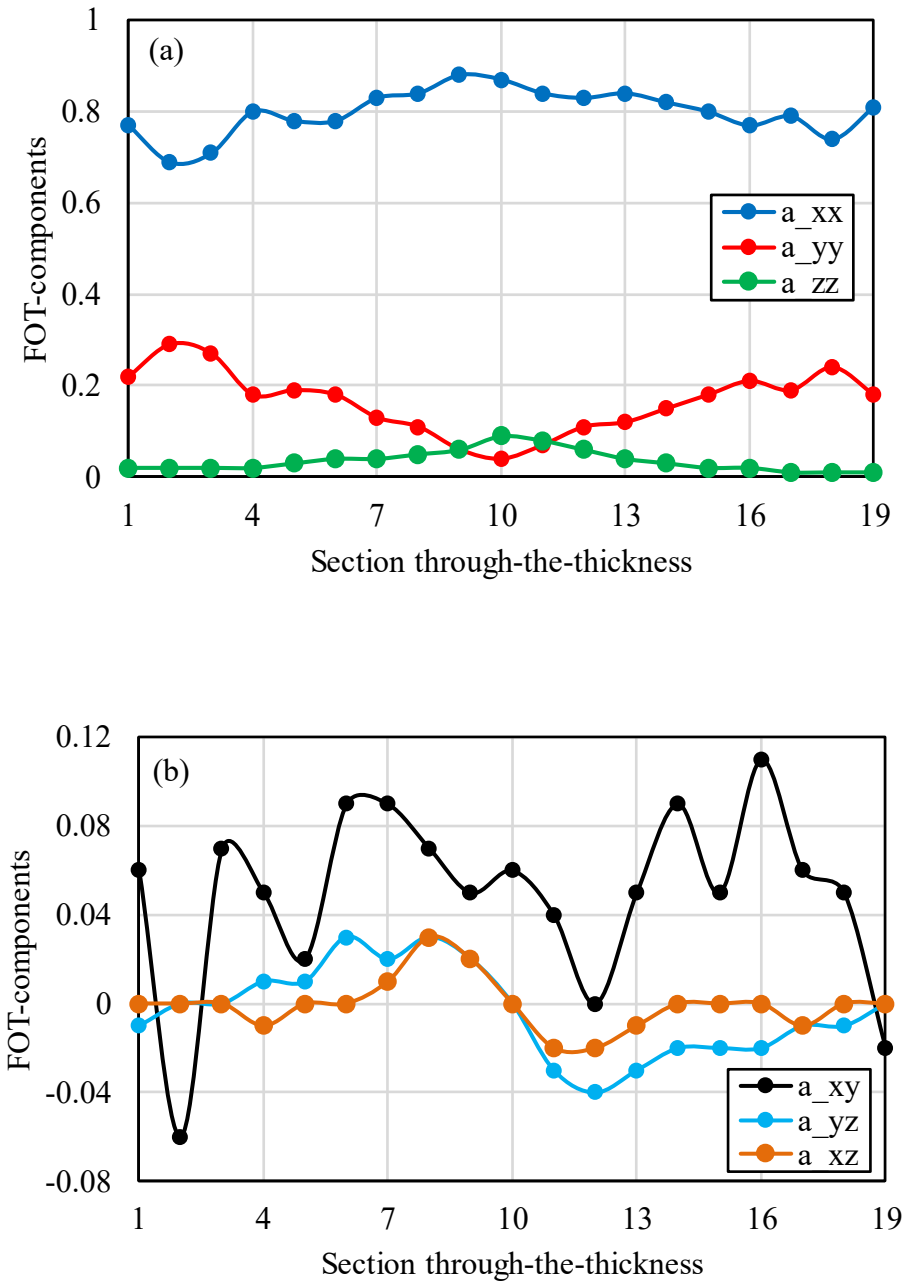

Figure 2.14. FOT components for a plate of geometry P/C (PA66-GF15). Diagonal (a) and out-of-diagonal (b) components.

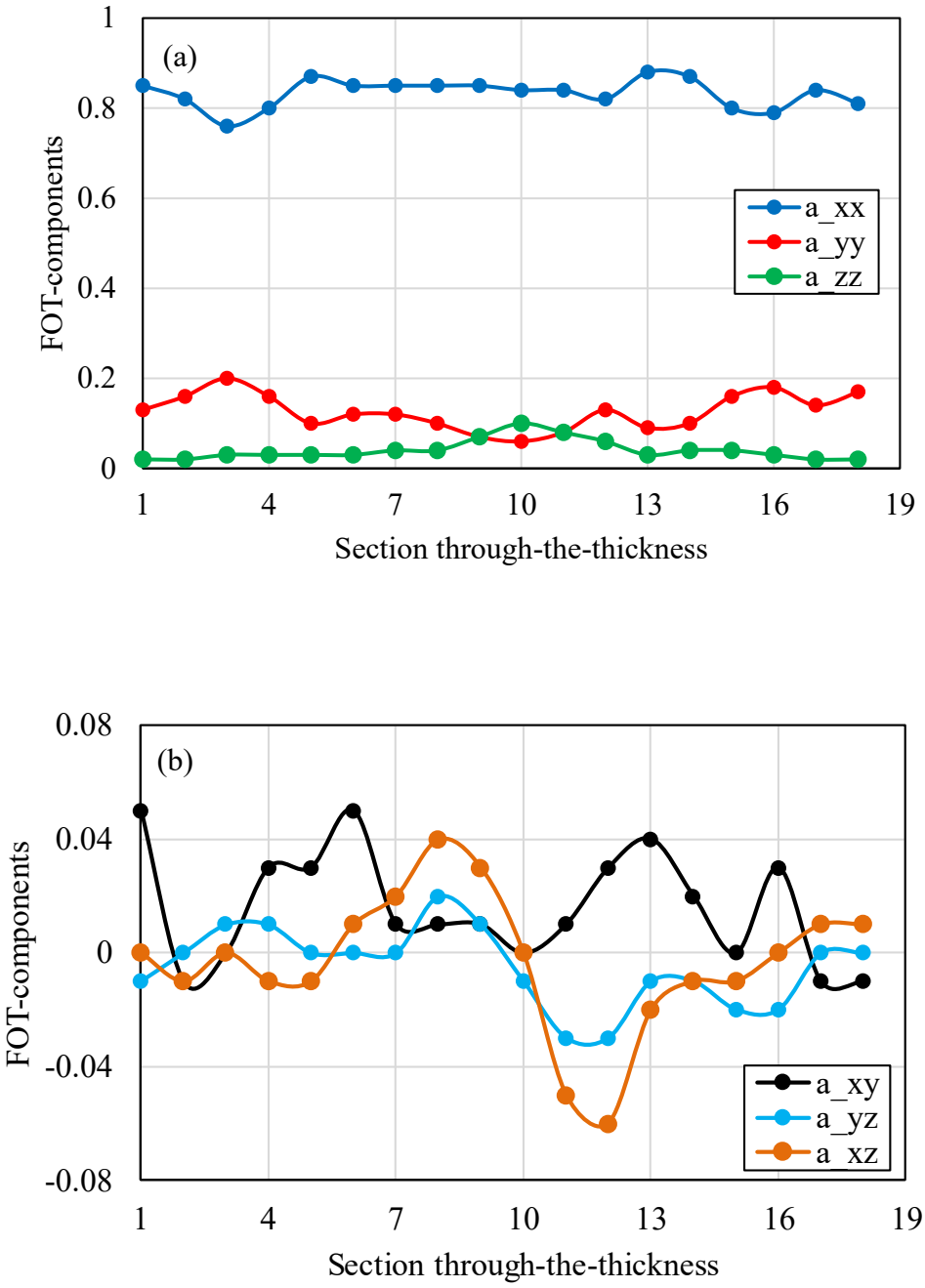

Figure 2.15. FOT components for a plate of geometry P/C (PA66-GF25). Diagonal (a) and out-of-diagonal (b) components.

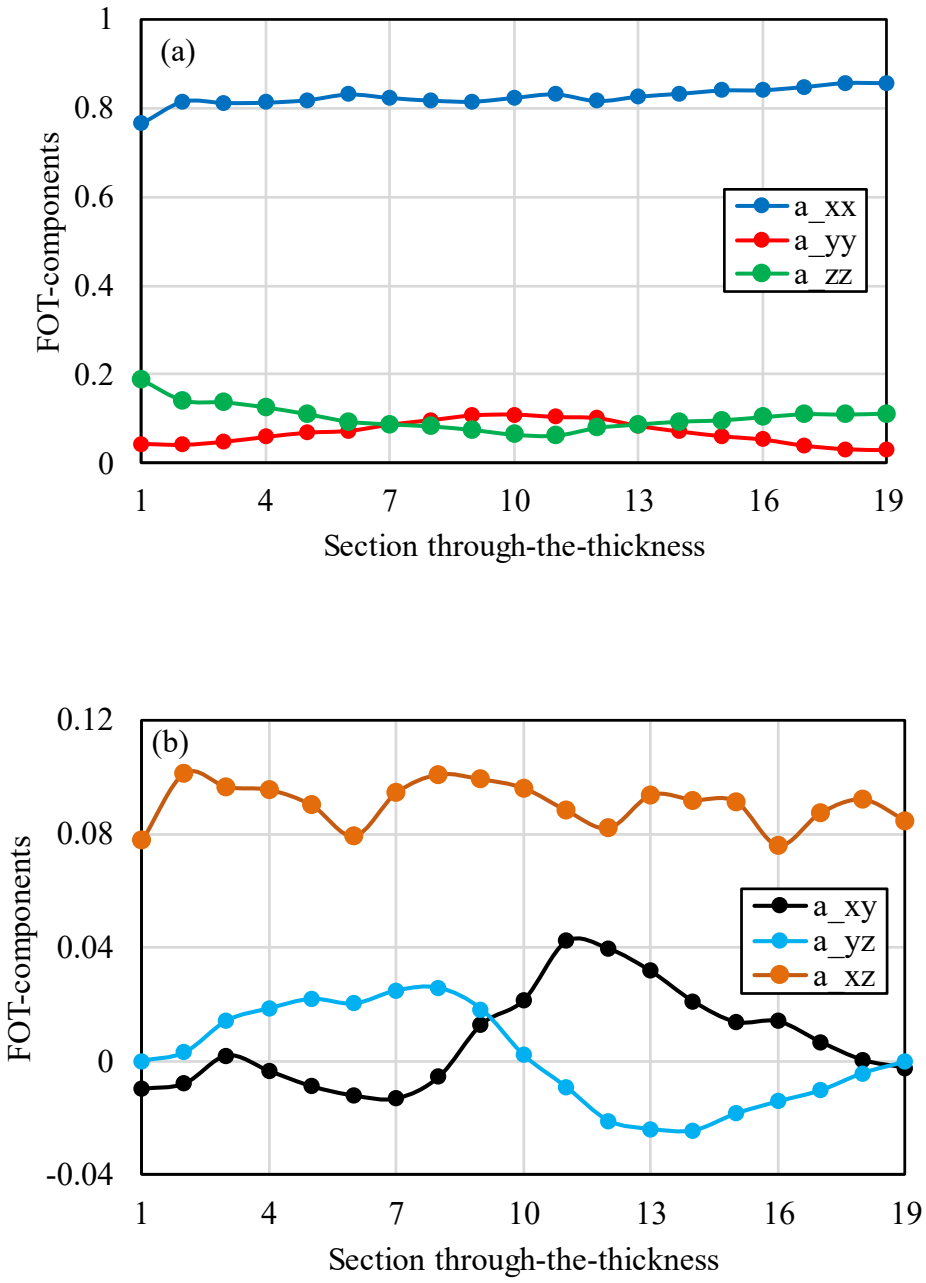

Figure 2.16. FOT components for a plate of geometry P/C (PA66-GF35). Diagonal (a) and out-of-diagonal (b) components.

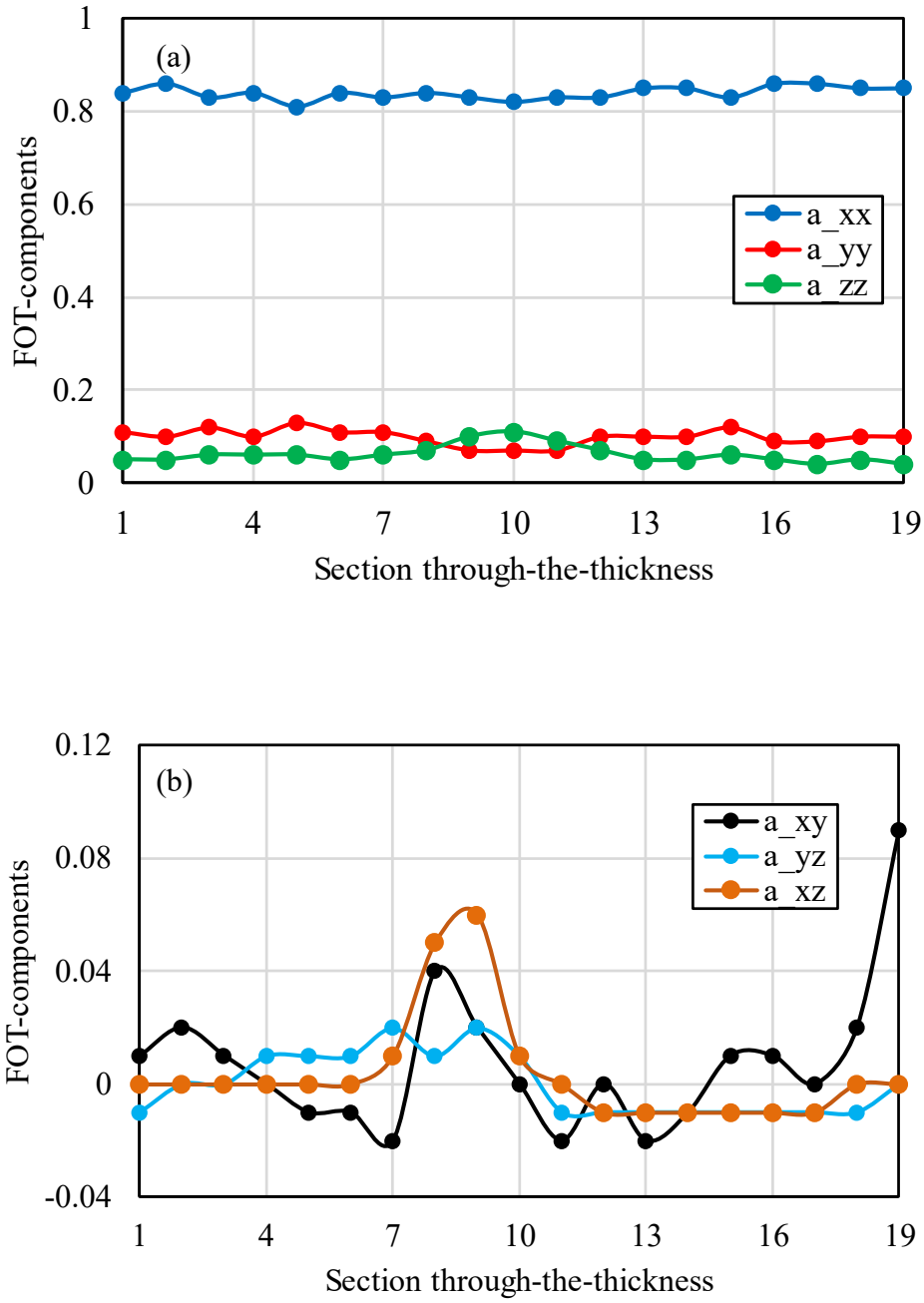

Figure 2.17. FOT components for a plate of geometry P/C (PA66-GF50). Diagonal (a) and out-of-diagonal (b) components.

Until now, only FOTs based on a layered discretization through-the-thickness have been presented. In the presence of metallic slits, the material flow is subjected to strong perturbations on the xy plane. Therefore, a fully 3D analysis of the FOTs around the notch tip is needed. The software and the method procedure employed for such an operation are the same as those used until now. The only difference consists in defining a finer grid of observation elements, within each an average FOT is estimated by means of the grey-scale values of the analyzed volumes.

In order to optimally read the FOTs, cubic elements of 80 μm^3 are adopted. This choice resulted to be a crucial step and difficult to achieve. Indeed, the following observations can be done:

a) The smaller the grid-element size is, the higher the risk of reading volume with no fibers is;
b) The bigger the grid-element size is, the more difficult to properly describe the notch edge shape is.

The risk of point a) to occur is more likely in case of low fiber volume fractions because of the reduced amount of fibers within the analyzed volumes.

In Fig. 2.18 an image acquisition obtained with the CT is shown. After importing all grey-scale data, an observation grid has been placed at the notch root region, as it is shown in Fig. 2.19.

With regard to geometry N/B, in this section only results concerning PA66-GF15, PA66-GF25 and PA66-GF50 will be shown and discussed, although the validation of the model that will be described later on will also involve the PA66-GF35. More details related to the latter can be however found in the work of Belmonte et al. (BEL17) who performed fatigue tests on specimens of Fig. 2.5 too.

Because of the large amount of data that have been stored with the CT method applied to geometry N/B, only one layer of the specimen thickness will be shown in Fig. 2.20-2.22 to have an idea of the main differences in terms of FOTs between specimens with different fiber volume fractions. The corresponding out-of-diagonal FOT components are reported in the appendix A.

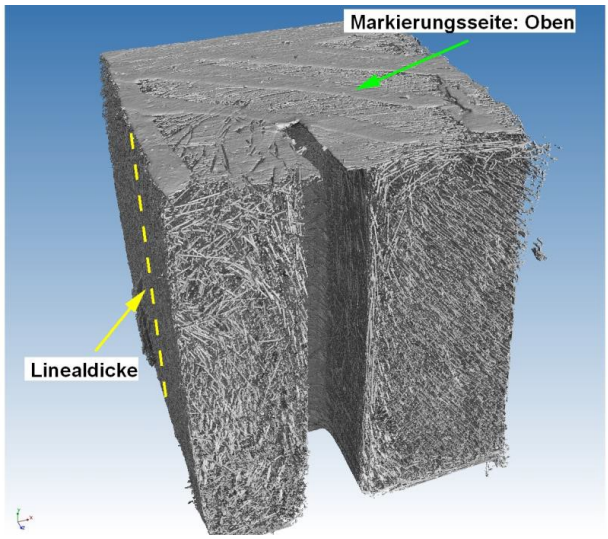

Figure 2.18. Notch detail of geometry N/B for a PA66-GF25. Image reconstructed by means of computed tomography.

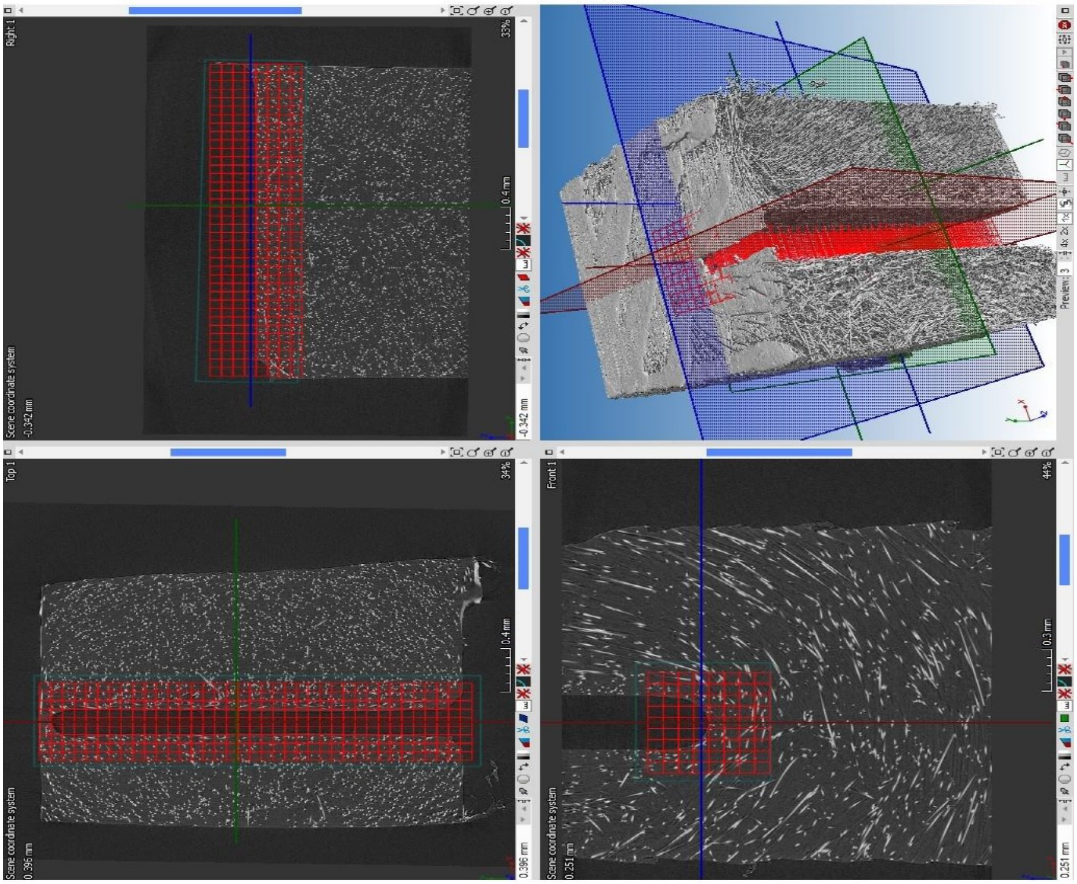

Figure 2.19. Grid placement for CT analyses. Specimen N/B made of PA66-GF25.

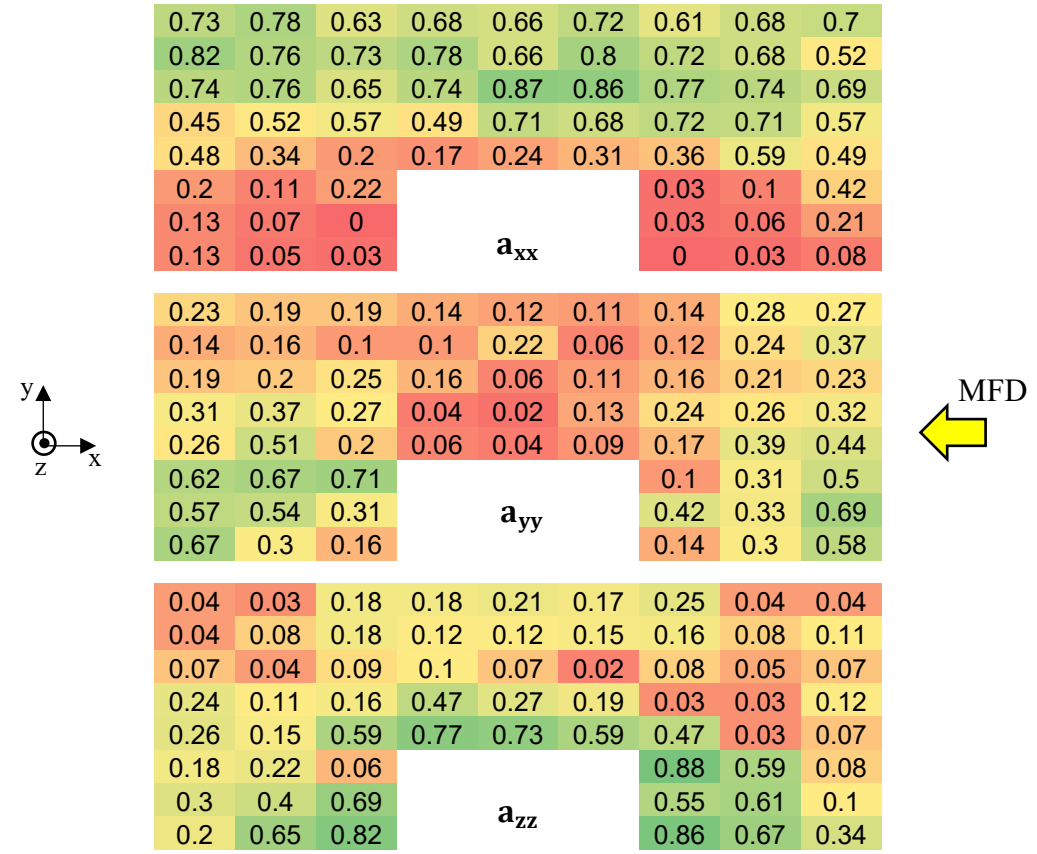

Figure 2.20. FOT components around the notch of specimen N/B made of PA66-GF15.

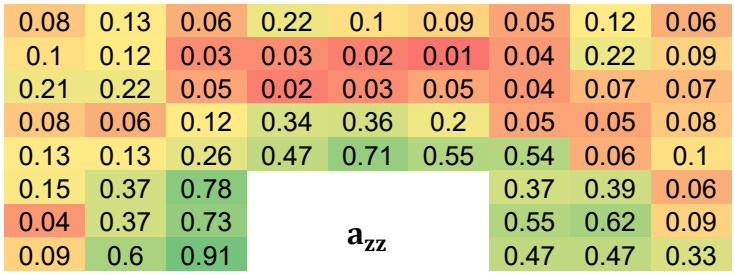

Figure 2.21. FOT components around the notch of specimen N/B made of PA66-GF25.

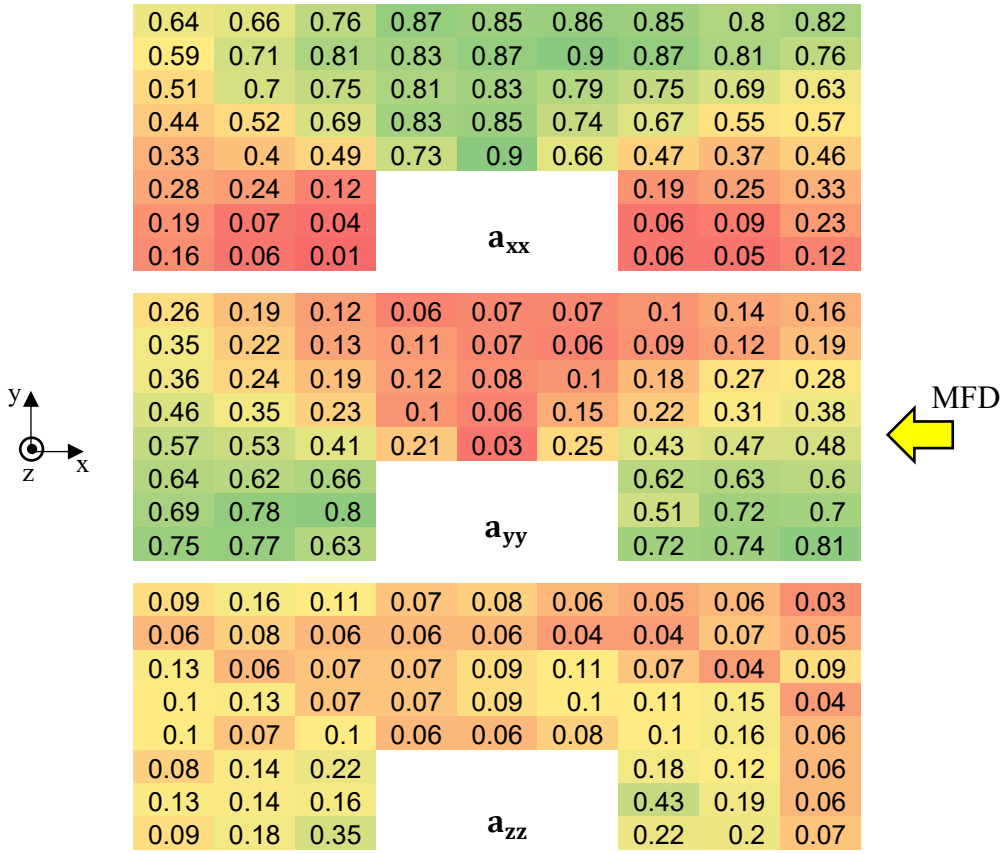

Figure 2.22. FOT components around the notch of specimen N/B made of PA66-GF50.

Paying attention to the FOT components of Fig. 2.20- 2.22 it can be noticed that specimens with the 15 wt% and 25 wt% of fibers have qualitatively similar profiles. Indeed, the regions in front of the tip are characterized by large values of the xx component, but zooming on the notch profile the zz component tends to increase at expense of a_{xx}. This means in turn that fibers preferentially settle along the through-the-thickness direction at the notch tip. This

actually agrees with the studies of Belmonte et al. (BEL17_2), who performed several microscopies at the notch root of the N/B specimen for the fiber volume fractions that are here taken into account. Nonetheless, the FOT yy component seems to be relatively lower, this implying that fibers are not likely to be oriented along the specimen-width direction.
Instead, Fig. 2.22 shows that for a PA66-GF50 fibers are better aligned with the main flow direction. In fact, higher values of the xx component of the FOT are encountered at the notch tip. Furthermore, the notch edges perpendicular to the MDF are characterized by large yy components. This highlights the main difference between this fiber volume fraction and the previous two. Namely, when the material is highly filled with short fibers, the latter keep their in-plane arrangement. Instead, by increasing the fiber volume fraction, fibers deviated along the specimen thickness while hitting the notch edges.
During the modeling activity, the complete three-dimensional grid will be used to properly assign the elastic constants to the generated models, while in this chapter only one layer of elements isolated along the z axis has been shown for the sake of clarity.

2.4 Experimental fatigue data

In this section, fatigue data for short glass fiber-reinforced polyamides 6.6 are presented and discussed.
Not all data that will be used for the validation of the proposed fatigue criteria are hereby shown, since part of them have been taken from the literature. The latter will be however reported within the next chapters for the sake of completeness while applying the developed fatigue models.
All data hereinafter presented and discussed have been performed with a load ratio equal to 0 (R = 0) and at room temperature (RT). Therefore, no effect of temperature and mean stress has been investigated, in order to preferentially focus on the fatigue strength variations deriving from local fiber orientation distribution and fiber volume fraction.

2.4.1 Plain specimens

Fatigue curves for plain specimens of type P/B are firstly presented, the dimensions of which are reported in Fig. 2.2. The tested coupons have been cut out of injection-molded plates, transversally to the main flow direction. The investigated fiber weight fractions are those of PA66-GF15, PA66-GF25, PA66-GF35 and PA66-GF50. These experiments have been done at the fatigue laboratory of the CR/APP2 department of Robert Bosch GmbH in Germany and are plotted in Fig. 2.23.

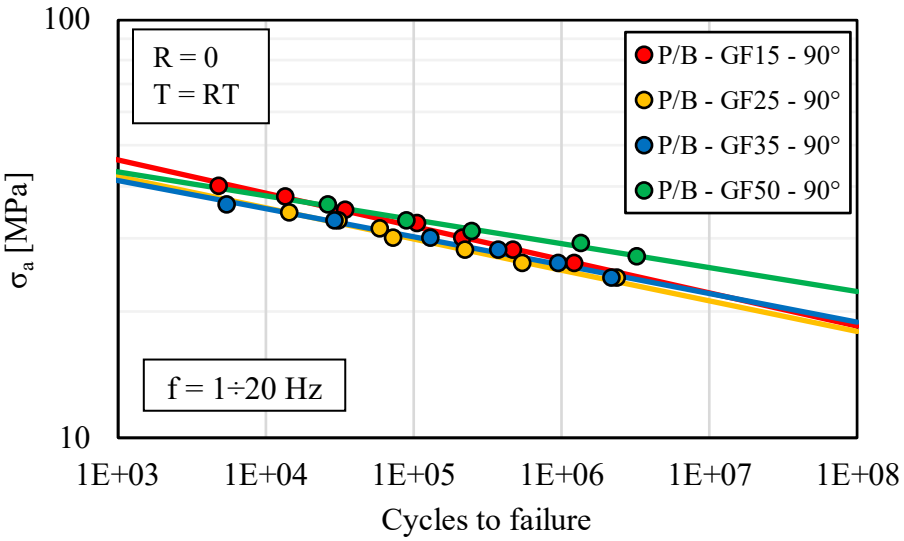

Figure 2.23. Fatigue data for geometry P/B, transversally extracted from plates.

Fatigue tests (6 tested specimens per curve) of Fig. 2.23 have done by means of a testing machine with a 25 kN load cell. Differently from BEL17 where all specimens were injected longitudinally, no significant difference among all fiber volume fractions' strength is observed. This might be a consequence of the fact that fibers are mainly oriented transversally to the load direction. Indeed, they are not expected to efficiently carry the load while cyclically stressed. Therefore, being the load bearing capability mainly attributed to the matrix, no particular differences between the plotted S-N curves of Fig. 2.23 is encountered. On the other hand, by referring to the FOTs of Fig. 2.13, a significant improvement of the fatigue strength of the PA66-GF50 (geometry P/B) would be expected since the core layer is much

wider than the other fiber volume fractions. Contrary, in Fig. 2.23 it can be observed that all fatigue curves lie very close to each other. This might be a consequence of the fact that, by increasing the amount of fibers within a specimen extracted at 90°, the fibers themselves would play a role of matrix stress concentrators when transversal to the load. This would limit therefore the beneficial effect of load-bearing capacity normally encountered with fibers oriented along the load direction. Therefore, it might be assumed that the possible fatigue strength enhancement caused by the large core layer could be weakened by the presence of zones with fibers oriented transversally to the loading direction, because of high local matrix stresses caused by such a large fiber content (50 wt%).

The second proposed set of fatigue data has been carried out for plain specimens of type P/C. As mentioned above, these coupons have not been machined out of plates, but the specimen geometry corresponds to the mold shape.

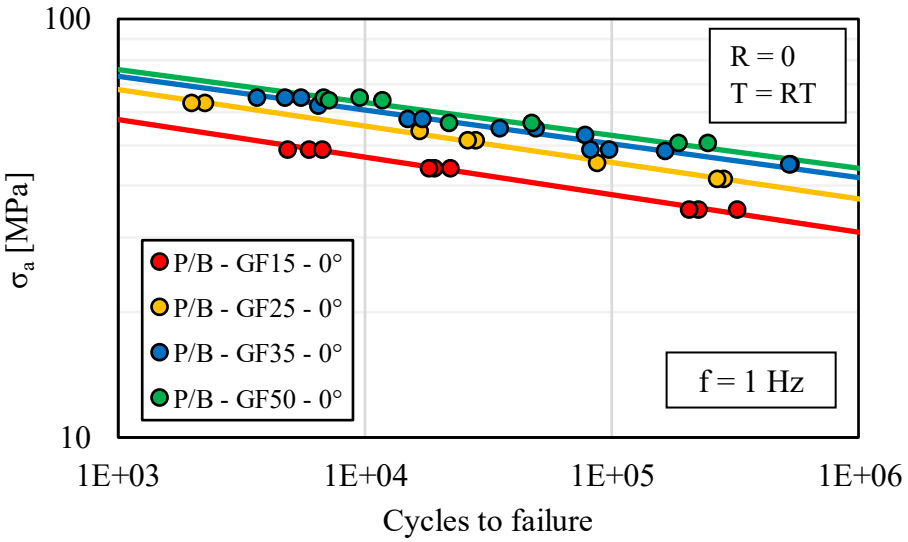

Figure 2.24. Fatigue data for geometry P/C, longitudinally injected.

Once again, the effect of fiber content on the fatigue behavior of SFRTs has been investigated in Fig. 2.24. In this case, 9 specimens have been tested for the PA66-GF15, 8 for the PA66-GF25, 12 for the PA66-GF35 and 8 for the PA66-GF50. The trend of the fatigue strength reveals to be different from the former fatigue data of Fig. 2.23. Indeed, a clear difference of the relative fatigue strength for the PA66-GF15 can be observed.

Nonetheless, it must be kept in mind that the two presented series of fatigue data cannot be compared straightforwardly, since specimens have been produced with different methods and the through-the-thickness values of the FOT components possess different profiles, as it is clear from Fig. 2.10-2.13 and Fig. 2.14-1.17.

2.4.2 Notched specimens

In order to comprehensively capture the effect of the notch geometry, beside the effect of fiber volume fraction and local fiber orientation, tests on sharply and mildly notched specimens have been performed.

Belmonte et al. (BEL17), who tested specimens of type N/B, observed that the crack propagation phase within SFRTs is generally not negligible in the presence of sharp notches. Since fatigue criteria up to crack initiation will be later proposed, it is essential to estimate the number of cycles up to crack onset in order to get rid of the cycles interested by the crack propagation phase.

Firstly, type N/A coupons are hereby considered and discussed. As reported within the previous paragraphs, these geometries have been obtained by machining injection-molded plates. The crack initiation system has been set up at the fatigue laboratory of Robert Bosch GmbH (CR/APP2) and it is depicted in Fig. 2.25.

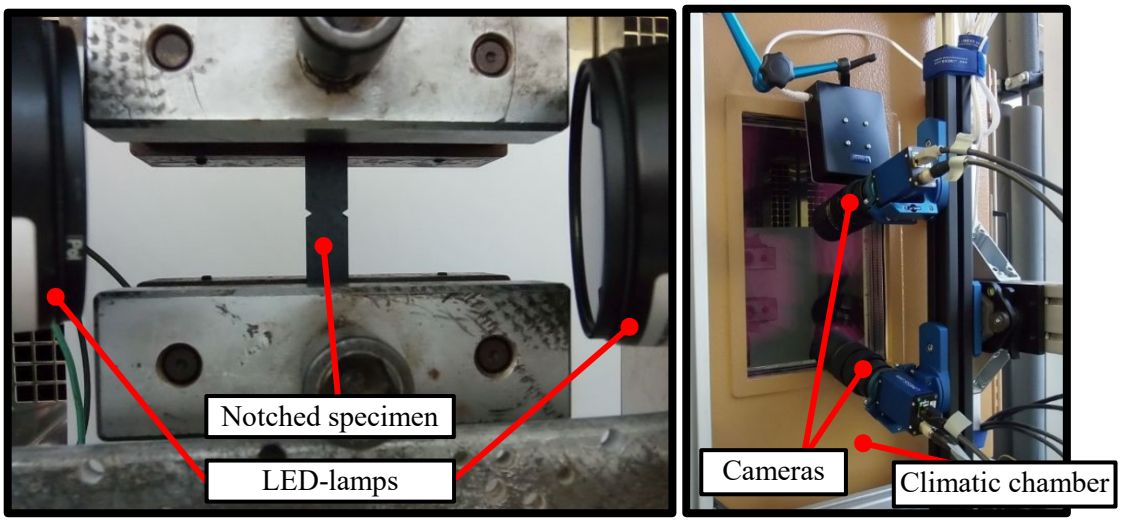

Figure 2.25. Experimental set-up for fatigue tests and crack detection at Bosch.

Two LED lamps have been placed in front of the tested specimen in order to light the crack up, as it arises. The use of such lamps revealed to make the temperature raise on the specimen surface and, therefore, all tests have been performed within a controlled temperature chamber (23°C) in order to avoid self-heating phenomena that might deteriorate the material mechanical properties. Additionally, two 5 megapixel cameras have been placed in front of the chamber to detect the crack initiating and growing.

For some of the tested specimens, scanning electron microscopies (SEM) have been done to calibrate the crack detection system. In order to be consistent with the crack lengths detected in BEL17, crack lengths of 0-0.5 mm must be detected. In this context, Fig. 2.26 shows the notch of a N/A specimen reinforced with the 15 wt% of fibers, in the presence of a crack.

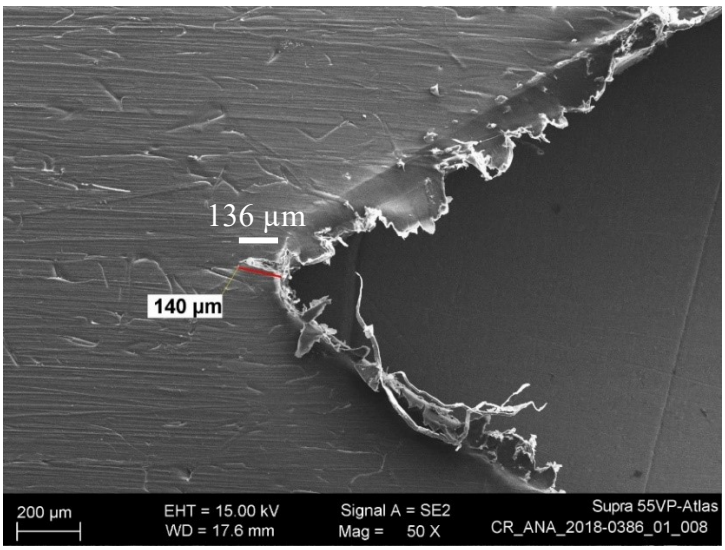

Figure 2.26. SEM acquisition at the notch tip of geometry N/A made of PA66-GF15, extracted at 90° from a plate.

The same site has been furthermore observed by means of the system in Fig. 2.25, as it is shown in Fig. 2.26. In Fig. 2.27, the difference between a close (a) and an open (b) crack is visible. In Fig. 2.27b, the lighted up crack is the same as Fig. 2.25**,** but this time with an applied external load of 0.54 kN. The latter has been chosen because corresponding to the maximum applied stress of the fatigue test.

From Fig. 2.27b, it is clear that the detection of an existing crack would be a difficult operation with no applied load. Therefore, the use of lamps, combined with the external applied load, enables a visible crack detection resolving lengths smaller than 0.5 mm.
The presented experimental set-up has been adopted for performing fatigue tests on specimens of type N/A. The considered specimens are characterized by different fiber contents (15 wt%, 35 wt% and 50 wt%) and have been cut out at 0° and 90° with respect to the MFD of plate of Fig. 2.2.

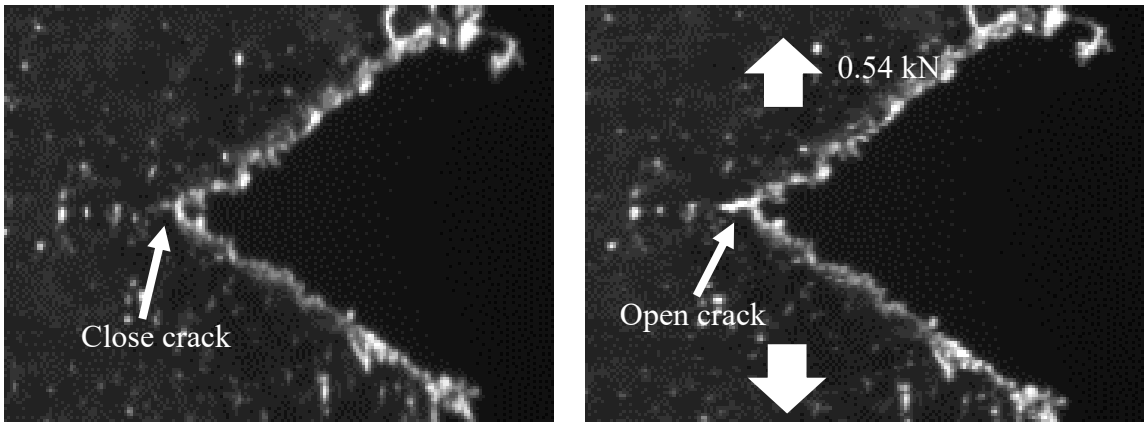

Figure 2.27. Example of close and open crack detected with the optical system at Bosch.

By referring to Fig. 2.26 and 2.27, it must be highlighted that the visible material irregularities are not always present on the analyzed images and they only consist in flashes (on the specimen's upper surface) that have remained after the milling process. Therefore, they must not be intended as representative for the notch surface roughness. In this context, no further studies have been carried in this work to investigate the effect of the notch roughness on the fatigue strength of the geometry of interest. On the other hand, poor surface qualities are expected to reduce the specimen strength.
The resulting fatigue data are plotted in Fig. 2.28 and 2.29, respectively for 0°- and 90°-oriented specimens. These fatigue points have been carried out on a servo-hydraulic testing machine with a 10 kN load cell. With referece to Fig. 2.28, 8 specimens for the PA66-GF15 have been tested, 8 for the PA66-GF35 and 5 for the PA66-GF50. Concerning Fig. 2.29, 8 specimens for the PA66-GF15 have been employed, 5 for the PA66-GF35 and 8 for the PA66-GF50.

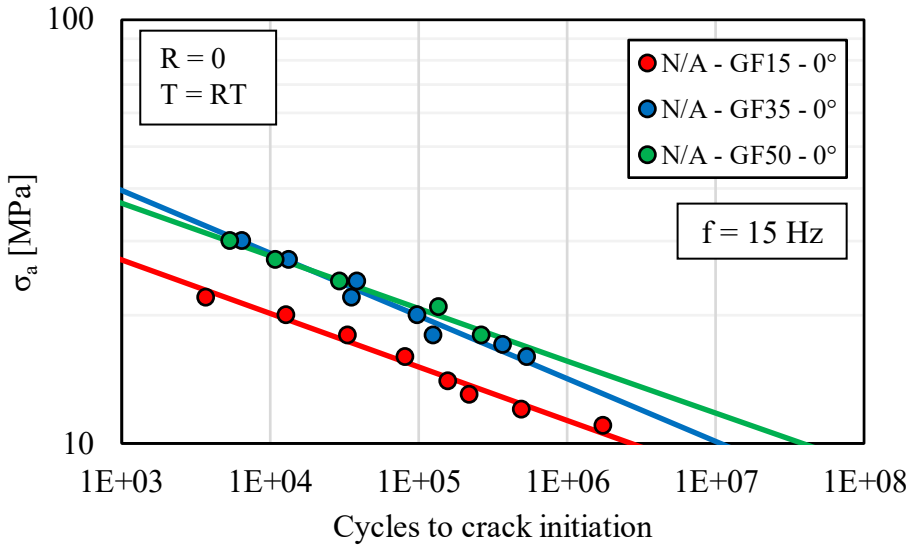

Figure 2.28. Fatigue data for geometry N/A, longitudinally extracted from plates.

With regard to mild notches, fatigue data obtained with specimens of Fig. 2.6 will be employed within the next paragraphs. In WIL16, the authors report data up to failure of this specimen type without evaluating the amount of cycles required for the crack initiation phase of geometry N/C.

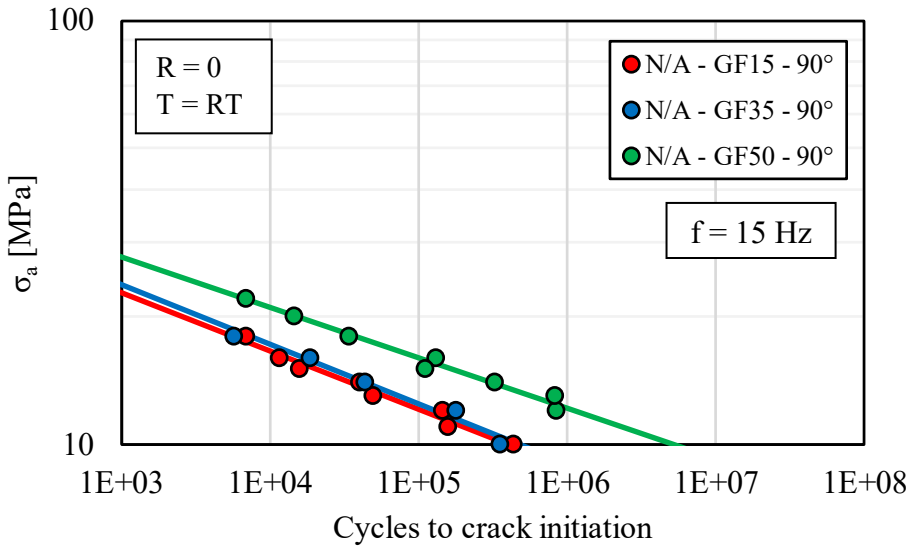

Figure 2.29. Fatigue data for geometry N/A, longitudinally extracted from plates.

The latter was extracted at 0° with respect to the MFD and it was made of PA66-GF35. The percentage of the lifetime of the mildly notched specimen N/C spent for the crack initiation and propagation phases has been quantified at the fatigue laboratory of DTG at the University of Padova. The experimental set-up can be observed in Fig. 2.30. It can be seen that two extensions have been used in order to create room for the lamp positioning. An example of propagating crack is reported in Fig. 2.31.

The obtained comparison between fatigue data up to crack initiation and failure are reported in Fig. 2.32 for a PA66-GF35 extracted at 0° from the plate, according to Fig. 2.6.

Relying on Fig. 2.32, it can be easily stated that the crack propagation phase of the N/C specimen can be neglected, as it will be done within the next chapters while applying the proposed fatigue criteria.

Eventually, fatigue data for the notched specimen N/D (DEM08) of Fig. 2.7 are reported in Fig. 2.33, which will be used to validate the proposed fatigue model for notched specimens, also performing process simulation on it to have an estimation of the local fiber orientation tensors at the notch root. In this case, 12 specimens have been tested.

Experimental data have been obtained up to failure without quantifying the crack initiation phase. Because of the large notch radius characterizing geometry N/D and being aware of the negligible crack propagation phase of specimen N/C, only data up to failure will be treated for geometry N/D.

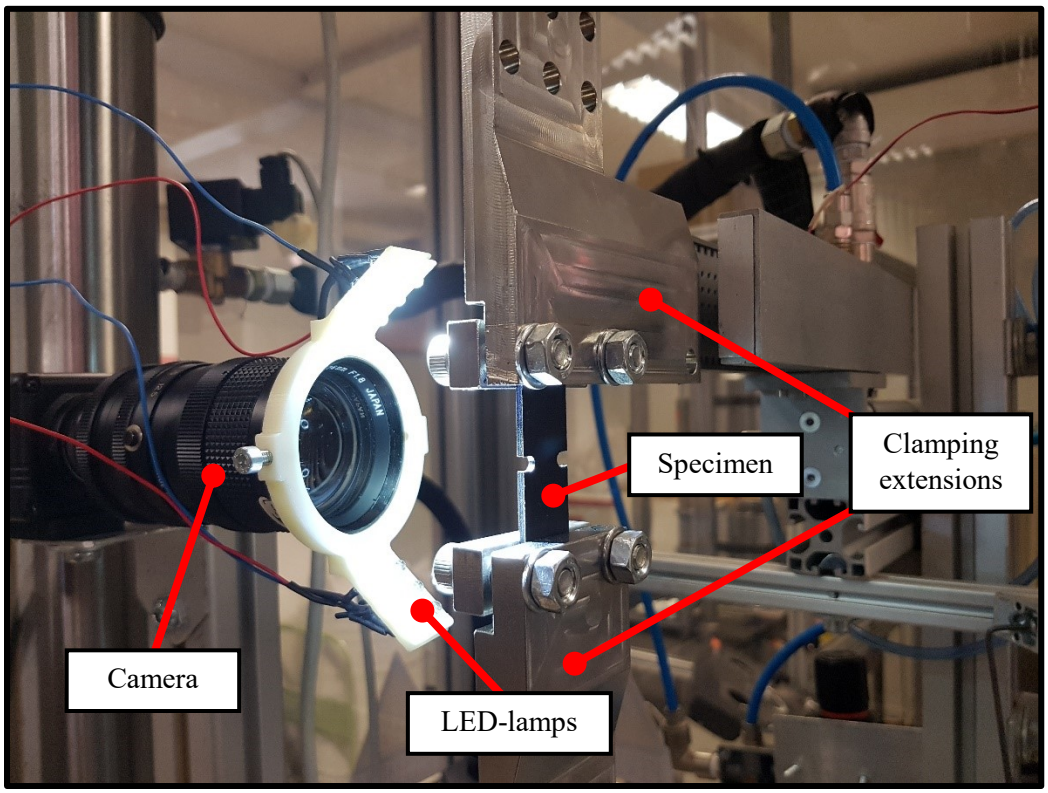

Figure 2.30. Experimental set-up for fatigue test and crack detection at the DTG laboratory of the University of Padova.

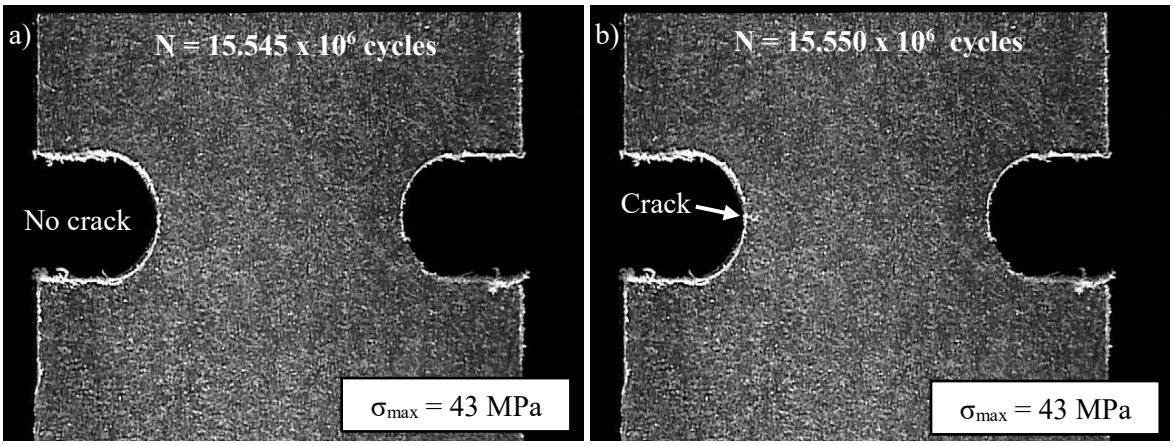

Figure 2.31. Example of crack detection at the DTG laboratory of the University of Padova. Geometry N/C made of PA66-GF35.

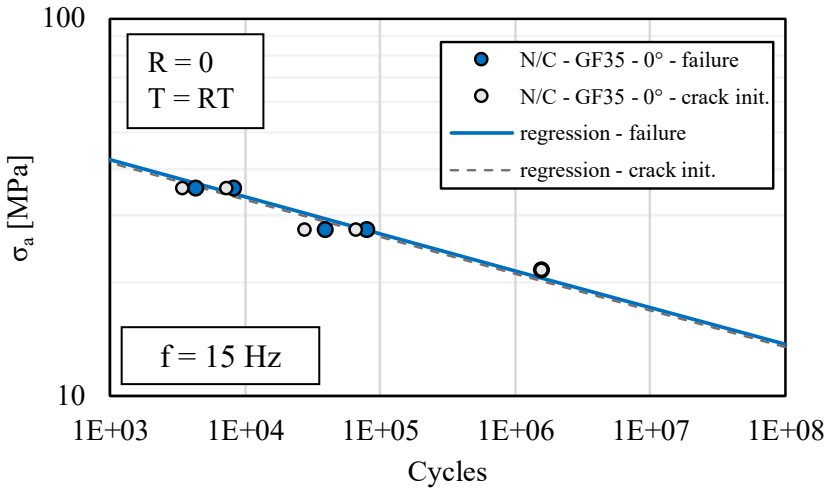

Figure 2.32. Comparison between crack initiation and propagation cycles for geometry N/C made of PA66-GF35 with a 0° cut-out angle.

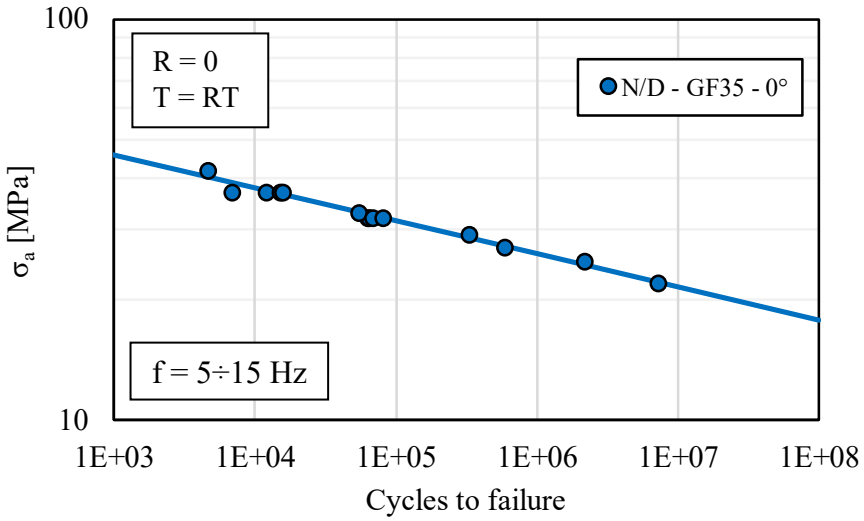

Figure 2.33. Fatigue data for geometry N/D, longitudinally injected (DEM08).

2.5 Conclusions

The present chapter is the result of several experimental activities that have been done to provide the fatigue model of the next chapters with the proper inputs.

Some data that will be employed are already available in the literature and they have been integrated with the already present ones in order to supply reliable information in terms of fiber orientation distribution and fatigue behavior of a certain type of specimen. The experimental activity has taken place on two different levels: on one hand, analyses of the local fiber orientation tensors have been done and, on the other hand, fatigue curves, i.e. S-N data, have been carried out.

Firstly, FOT data resulting from injection-molded plates have been presented, which show the typical skin-core effect along the through-the-thickness direction. Secondly, a similar display method has been adopted for the case of plain specimens that have been longitudinally injected and not extracted from plates. In this case, a different FOT profile has been observed, yielding a better fiber alignment with respect to the MFD.

Subsequently, FOTs have been evaluated also in case of notched coupons, the notch of which was shaped during the injection molding process by placing a metallic slit in the mold. This time, more complex fiber orientations have been encountered because of the flow perturbation caused by the metallic insert.

Furthermore, fatigue tests have been performed for plain and notched specimens, investigating the effect of fiber volume fraction, local fiber orientation distribution in the presence and in the absence of notches.

While treating plain specimens, it has been assumed that no crack propagation phase takes place, namely as the crack initiates, the failure of the specimen suddenly occurs.

Referring to notched specimens, the difference between the amount of cycles spent up to crack onset and up to failure cannot be neglected. In this interest, an optical system has been set-up in collaboration with Robert Bosch GmbH to detect the early stages of the crack initiation, in order to have a better estimation of the amount of fatigue cycles spent until a first crack appears. Eventually, a study on the estimation of the fatigue life up to crack initiation for a mild notch has been carried out at the University of Padova (DTG), concluding that the propagation phase, here, is not relevant.

Chapter 3

Pseudo-grain approach for matrix stress distributions

3.1 Introduction

In the present chapter, an innovative method enabling the computation of the matrix stress distributions (PIE18) of short fiber microstructures is presented. This approach will be later on embedded in the fatigue models proposed within the next chapters.

SFRP parts generally undergo a wide variety of loading and environmental conditions and, therefore, extensive and expensive testing campaigns are necessary to characterize the material behavior (DEM10_2, DEM10_3, SCH14). To decrease the development cost of SFRP parts and achieve a more optimized design, reliable failure criteria are necessary to predict the damage initiation and evolution and the final failure under static and fatigue loadings. It is important to mention that the damage evolution in SFRPs is, by nature, a multiscale and hierarchical process (BEL17, BEL17_2, HOR97) that can be predicted on the basis of the local stresses in the constituents, which are strongly dependent on the microstructure. In support of this statement, several works report the fundamental role of the matrix in the micro-scale damage initiation and evolution in composite materials under cyclic loadings (BEL17_2, HOR97, QUA16, CAR14, KAB06, LAR18).

On the other hand, the development of criteria for predicting the crack initiation (BEL17_2, HOR97, QUA16, CAR14, KAB06) and the failure (JAI16, KLI11, KAM11, ARI14, JAI16_2) of SFRPs usually has to face different issues related to the microstructure for the analysis of the local stresses in the matrix (TIA14, TIA15, SCH17). In this regard, the adoption of the representative volume element (RVE) strategy consisting in the generation of an equivalent microstructure has gained a widespread usage. This technique has been widely used by different authors aiming at describing the properties of the investigated materials

(TIA14, TIA15, SCH17, PON15). As short fibers are employed, the following problems might arise:

- The achievement of the desired fiber volume fraction (v_f) requires the implementation of complex algorithms for fibers' placement within the model. From several works it can be deduced that fiber volume fractions that are typical of commercial materials are generally difficult to achieve for common fiber aspect ratios (> 15).

  In case of short fibers, the fiber volume fraction is not the only requirement for the RVE generation. In fact, also a given fiber orientation tensor (FOT) (ADV90, ADV90_2, ADV87, MOO11, GOL17) has to be achieved, which is mostly non-uniform within a specimen or a part (BEL17_2, KLI11, ARI14, BER07, FOS14, DEA17). Nevertheless, a recent work by Schneider (SCH17) provides a procedure for generating RVEs filled with high fiber volume fractions, e.g. up to 60%, simultaneously fulfilling the required FOT;
- Once the problem of the geometry generation is overcome, the meshing activity may be an issue due to the internal complexity of the geometry. In fact, as a consequence of the misaligned fibers' placement, locations where inclined fibers are cut by the RVE edges might be very difficult to mesh. In any case, given the large amount of elements involved, the computational cost in solving such RVEs could be very high;
- In addition, boundary conditions for these FE models can be rather complex. Indeed, Nguyen and coauthors (NGU12) highlight that, concerning the classical application of periodic boundary conditions (PBCs), a periodic mesh should be, in principle, guaranteed, this representing another issue considering the complex geometries involved. In NGU12, an enhanced method for applying PBCs in the presence of a non-periodic mesh is therefore formulated.

The present work aims at providing an innovative approach for the computation of the elastic stress distributions within the matrix of a SFRP, without going through the generation of complex FE models with misaligned fibers. This would make the stress analysis faster and more efficient, allowing to get results with a lower computational cost for the exact v_f and FOT investigated . This has been achieved by adopting a pseudo-grain (PG) approach, which

has been extensively employed in the literature by several authors with the objective of computing the homogenized macro-scale properties of FRPs (see, among the others, Refs. KAM11, MÜL15, CAM90, DOG05, DOG06, JAI13, NOT14, MOR15_3 and the references reported therein). The aforementioned approach consists in the subdivision of a complex microstructure in a set of PGs, having constant features in terms of spatial orientation, fiber diameter and fiber length. The final properties are therefore computed by analytically averaging the grains properties through a certain weight that can be identified based on the fiber orientation probability function.

In the work of Camacho et al. (CAM90), a two step-homogenization method was proposed for computing the thermo-elastic properties of a composite material for a given microstructure.

Pierard et al. (PIE04) successfully investigated the applicability of the pseudo-grain method for computing the stiffness tensor of complex microstructures.

Müller et al. (MÜL15) gathered different homogenization models and compared the elastic properties derived from the solution of numerical models to the ones obtained from the analytical models, including a two-step homogenization formulation according to the PG approach.

Within the framework of materials reinforced with non-spherical and misaligned inclusions, Doghri and Tinel (DOG05) proposed to reproduce the macroscopic elasto-plastic behavior of composites with the aid of a PG approach. Later, the same authors have extended the proposed methodology to the case of linear thermo-elastic and rate-independent inelastic matrices (DOG06).

Jain at el. (JAI13) focused on the computation of the average stresses within the matrix and the inclusions of SFRPs by adopting a Mori-Tanaka pseudo-grain (MTPG) approach.

Kammoun et al. (KAM11) made use of a PG methodology to formulate the so-called “first pseudo-grain failure model” in analogy to the “first ply failure model”, widely used for continuous fiber-reinforced laminates. Similarly, an approach developed by Notta-Cuvier et al. (NOT14) proposed the use of pseudo-grains for the prediction of the macroscopic elasto-plastic behavior of SFRPs under quasi-static loadings, including its dependency on the local anisotropic damage that occurs within the matrix of the composite.

The approaches listed above rely on two-step methodologies, in which the single PG has to be firstly homogenized through analytical schemes and, secondly, the properties resulting from the first stage have to be combined in order to reproduce the macro-scale behavior of the composite. However, with respect to the literature, in the present work the pseudo-grain method is used with a different and innovative approach, aiming to compute the local stress fields in the matrix, rather than the homogenized composite properties or the average matrix stresses. In fact, the approach presented here aims at reproducing the entire elastic stress distribution within the matrix of a generic microstructure, to serve as an input for fatigue failure criteria based on the local stresses in the matrix (chapters 4 and 5). The choice of focusing on the elastic stress fields is justified by the fact that the mechanisms leading to fatigue crack initiation, at least below the matrix T_g, were found to be of a brittle type (BEL16, BEL17, BEL17_2), the load levels being quite low with respect to those leading to the static failure. In particular, the matrix stress-cumulative distribution function (S-CDF) relevant to a given microstructure will be obtained by weighting the S-CDFs resulting from unidirectional PGs, solved with the finite element method (FEM). The proposed methodology, which represents a novelty with respect to the literature, is therefore characterized by the following advantages:

- The generation and numerical solution of complex RVEs with misaligned fibers is now avoided. Indeed, only unidirectional volume elements, of which the generation and solution is much easier, are adopted;
- The meshing operation is not anymore hindered by the complexity of the fibers placement. Unidirectional models are, furthermore, relatively small and require a lower amount of finite elements with respect to complex microstructures;
- Thanks to the simple geometry of the unidirectional models, a periodic mesh is easier to be achieved with respect to RVEs with misaligned fibers.

With the presented methodology, the local matrix stress fields can be obtained avoiding the generation of complex microstructures and the numerical effort is reduced to the generation and solution of unidirectional cells (pseudo-grains).

In the following sections, a description of the proposed approach will be provided, detailing the stages related to the recovery of the orientation probability density function (OPDF) of the fibers from a second-order FOT (ADV90, ADV90_2, ADV87, DOG05, DOG06,

CHU02, DRA07) and describing the pseudo-grain approach for computing the stress distributions in the matrix. Eventually, the results obtained from several analyses carried out on RVEs filled with misaligned fibers will be reported in order to validate the efficacy of the new PG methodology.

In order to extensively validate the proposed methodology, the cumulative distribution function of different stress components, i.e. local hydrostatic stress (LHS) , local maximum principal stress (LMPS) (CAR14) and von Mises stress (σ_{VM}), will be computed through the PG approach. As a validation, the results will be then compared to the CDFs deriving from reference microstructures with misaligned fibers.

3.2 Analytical preliminaries

In this section, a few details related to the symbols that will be encountered within the next paragraphs are provided to better understand the notation adopted. Furthermore, information concerning the common method for calculating the fiber orientation probability density function, having the FOT available, will be given.

3.2.1 Notation

In this section, information related to the notation adopted throughout this paper is provided. With regard to tensor-symbols, vectors and second-order tensors are denoted by lowercase and uppercase bold letters (e.g. $\mathbf{p}$ and $\mathbf{A}$). An exception is made for stress and strain second-order tensors, the symbolism of which is characterized by lowercase and bold Greek letters, such as $\boldsymbol{\sigma}$ and $\boldsymbol{\varepsilon}$. Fourth-order tensors are instead indicated with double-struck letters, e.g. $\mathbb{A}$. The linear mapping of a second-order tensor by a fourth-order tensor is denoted by $\mathbb{A} : \mathbf{A}$, whereas the scalar products between second- and fourth-order tensors are respectively identified by $\mathbf{A} : \mathbf{A}$ and $\mathbb{A} : \mathbb{A}$. According to the work of Müller et al. (MÜL15), considering a generic fourth-order tensor $\mathbb{D}$, the symbol $\square$ can be better explained through Eq. (3.1):

$$\mathbb{D} = \mathbf{A} \square \mathbf{A} = A_{ik}A_{jl}e_i \otimes e_j \otimes e_k \otimes e_l = D_{ijkl}e_i \otimes e_j \otimes e_k \otimes e_l \tag{3.1}$$

where e_i is a generic base of the space and $\otimes$ represents the dyadic product.
The superscript T_R is used to indicate the right transposition operation, such that $A_{ijkl}^{T_R} = A_{ijlk}$.
Symbols $\det(\cdot)$, $\mathrm{dev}(\cdot)$, and $\mathrm{diag}(\cdot)$, indicate the determinat, deviatoric part and diagonal components of a generic second-order tensor.
Symbol $\cup$ is employed to denote the union among a collection of sets.
Throughout this work, $\mathbb{C}_f$ and $\mathbb{C}_m$ will be adopted to indicate the stiffness tensors attributed to fibers and matrix of the considered composite.

3.2.2 Definition of the orientation probability density function

As already mentioned in the, the thesis work deals with short fiber-reinforced polymers. Indeed, the microstructure is identified through $\omega = \omega_m \cup \omega_f$ (MÜL15), ω_m and ω_f being respectively the domains corresponding to matrix and fibers. Within a reference volume ω, fibers are commonly described through the orientation probability density function (OPDF) $\psi(\mathbf{p})$. As widely discussed in the work of Advani and Tucker (ADV87), the OPDF describes the probability of finding a fiber having its orientation unit vector $\mathbf{p}$ within the interval between $\mathbf{p}$ and $\mathbf{p} + d\mathbf{p}$. According to Fig. 3.1, the aforementioned vector can also be described by means of its polar coordinates identified by angles ϕ and θ.
A normalized OPDF is considered and the following identity has to be fulfilled:

$$\oint_{\omega} \psi(\mathbf{p}) d\mathbf{p} = 1 \tag{3.2}$$

where

$$d\mathbf{p} = \sin\theta \, d\theta \, d\phi \tag{3.3}$$

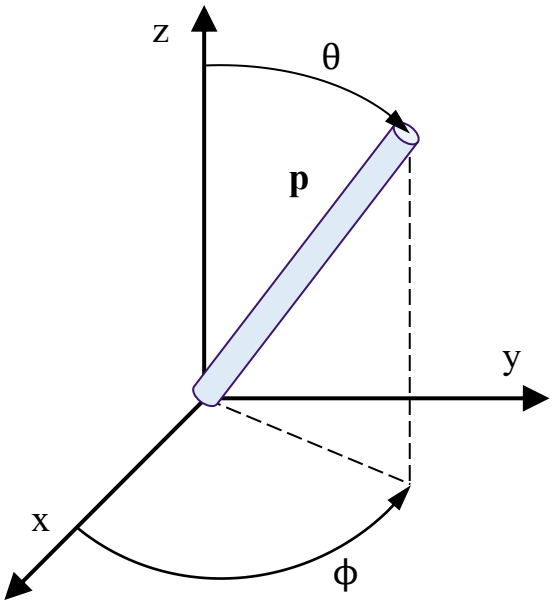

Figure 3.1. Unit vector in the global reference system and its polar coordinates.

Due to the symmetric nature of $\mathbf{p}$ with respect to the origin of the three-dimensional Cartesian system, the equality $\psi(\mathbf{p}) = \psi(-\mathbf{p})$ has to be valid.

In the present thesis, it is assumed that all the fibers of a generic microstructure possess the same diameter d, length l and therefore aspect ratio $A_R = l/d$. Referring to the different works (MÜL15, CAM90, PIE04, DOG05, DOG06, JAI13, NOT14) that has dealt with the application of the PG approach, the domain ω can be subdivided into other domains ω_k, which are the so-called pseudo-grains, as it is shown in Fig. 3.2.

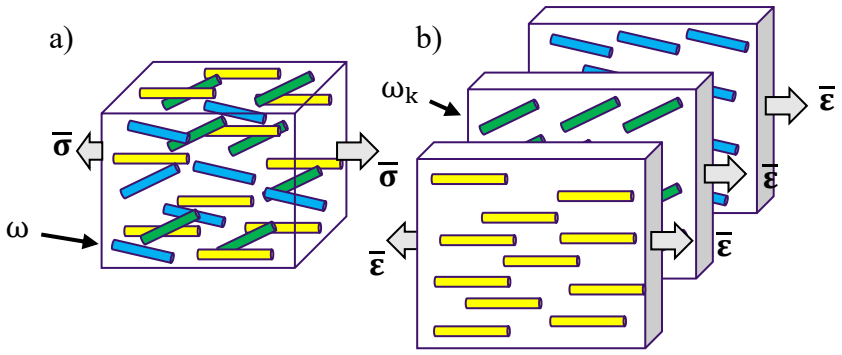

Figure 3.2. Schematization of a real microstructure (a) and discretization in pseudo-grains (b), each characterized by a weight α_k and subjected to Voigt boundary conditions.

The domain of the OPDF can be therefore discretized into K orientations and each PG is assumed to contain fibers with the same orientation, which will be denoted by the vector $\mathbf{p}_k$ from here on. The fiber volume fraction of each PG, evaluated with respect to ω_k, equals v_f which in turn denotes the fiber volume fraction of the entire microstructure.
According to the work of Pierard et al. (PIE04), a Voigt formulation is assumed for combining the properties of PGs and the computation of a generic property f_ω (e.g. stiffness tensor, matrix's and fibers' average stress tensor, etc.) of the entire domain ω reads:

$$f_\omega = \sum_{k=1}^{K} f_{\omega_k} \alpha_k \tag{3.4}$$

where α_k is a weight factor, which, according to Eq. (3.3), is defined as follows:

$$\alpha_k = \psi(\mathbf{p})\, \Delta\mathbf{p}_k = \psi(\phi_k, \theta_k) \sin\theta_k\, \Delta\phi_k \Delta\theta_k \tag{3.5}$$

3.2.3 Recovery of the OPDF

In the literature, many authors have proposed methodologies for reconstructing the OPDF. Advani e Tucker (ADV87) described a detailed formulation for an approximate calculation of the OPDF by using the second- and fourth-order FOTs, respectively denoted with $\mathbf{A}$ and $\mathbb{A}$.

$$\mathbf{A} = \oint \mathbf{p} \otimes \mathbf{p}\, \psi(\mathbf{p})\, d\mathbf{p} \tag{3.6}$$

$$\mathbb{A} = \oint \mathbf{p} \otimes \mathbf{p} \otimes \mathbf{p} \otimes \mathbf{p}\, \psi(\mathbf{p})\, d\mathbf{p} \tag{3.7}$$

Typically, only the second-order FOT is available from analyses on real parts, carried out by means of the X-ray computed tomography (CT). Then, the generic fourth-order FOT can be recovered by means of the so-called *closure approximations* (ADV87).
The formulation adopted in this work is that by Doghri and Tinel (DOG06), who re-wrote in a tensor-notation the expressions discussed in ADV87. The authors illustrated that, only in case of perfectly randomly oriented or aligned inclusions, an exact expression for $\mathbb{A}$ is possible. Respectively, the formulations for the reconstruction of the fourth-order FOTs for these two exemplar cases are designated as *linear closure* ($\mathbb{A}^{l}$) and *quadratic closure* ($\mathbb{A}^{q}$) (DOG06):

$$\begin{aligned}\mathbb{A}^{l} = {} & a_1 \mathbf{I}^{s} \otimes \mathbf{I}^{s} + 2(a_1 - b_1)\mathbb{I}^{s} + a_1(\mathbf{I}^{s} \otimes \mathbf{A} + \mathbf{A} \otimes \mathbf{I}^{s}) \\ & + 2b_1[\mathbb{I}(A + \mathbf{I}^{s}) - \mathbb{I}(\mathbf{A})]\end{aligned} \tag{3.8}$$

where $\mathbb{I}(\mathbf{A})$ can be re-written as follows:

$$\mathbb{I}(\mathbf{A}) = \frac{1}{2}[(\mathbf{A} \square \mathbf{A}) + (\mathbf{A} \square \mathbf{A})^{T_R}] \tag{3.9}$$

according to Eq. (3.1).
In Eq. (3.8), $\mathbf{I}^{s}$ and $\mathbb{I}^{s}$ are symmetric identity tensors and the values of coefficients a_1 and b_1 are reported in (ADV87).
When fibers are fully aligned, the *quadratic closure* can be expressed as follows:

$$\mathbb{A}^{q}(\mathbf{A}) = \mathbf{A} \otimes \mathbf{A} \tag{3.10}$$

In case of misaligned fibers, the orientation of which is neither isotropic nor unidirectional, a hybrid formulation of the fourth-order FOT (*closure approximation*) was proposed by Advani and Tucker (ADV87) and, according to (DOG06), it reads:

$$\mathbb{A}^{h} = (1 - a)\mathbb{A}^{l}(\mathbf{A}) + a\mathbb{A}^{q}(\mathbf{A}) \qquad \text{with} \qquad a = 1 - b\,\det(\mathbf{A}) \tag{3.11}$$

Parameter b of Eq. (3.11) can be found in (DOG06).

Once that $\mathbf{A}$ and $\mathbb{A}^{h}$ are available, it is possible to calculate the OPDF. Referring to the work of Doghri et al. (DOG06), the final formulation of $\psi(\mathbf{p}_k)$, evaluated along a generic orientation vector $\mathbf{p}_k$, is expressed through the following formulation:

$$\psi(\mathbf{p}_k) \approx \psi_1 + \psi_2 \mathbf{B}(\mathbf{A}) : \mathbf{F}(\mathbf{p}_k) + \psi_3 \mathbb{B}(\mathbf{A}) :: \mathbb{F}(\mathbf{p}_k) \tag{3.12}$$

3.3 Development of the proposed procedure

3.3.1 Description of the approach

The PG approach has been frequently adopted, in the literature, for the computation of macro-scale properties of a composite by mathematically combining the results derived from the solution of homogenized grains (see, among the others, MÜL15, CAM90, PIE04, DOG05, DOG06, JAI13) which, in principle, can be solved analytically (PIE04) or numerically (KAM14). Conversely, in the present work, the PG approach is adopted for the efficient computation of the local stress fields in the matrix, without focusing on the macroscopic elastic properties or the average stresses in the constituents.

In this frame, the single pseudo-grain becomes a unidirectional cell composed of few short fibers, which undergoes periodic boundary conditions and can be easily generated and solved by means of commercial FE codes. The choice of solving numerically (with the FE method) the pseudo-grain allows the computation of the complete matrix stress distribution within the single grain. Indeed, the field f_ω of Eq. (3.4) that will be computed is the inverse of the matrix stress-cumulative distribution function denoted by $F(\sigma_{ij})$. From an implementation point of view, after computing the discrete x values (stress values for predefined CDF values) of the single pseudo-grain, the latter are combined according to Eq. (3.4). Particularly, the matrix

stress-CDFs of the LMPS, LHS and von Mises stress (σ_{VM}) will be considered here and they are indicated with $F(LMPS)$, $F(LHS)$ and $F(\sigma_{VM})$.

The starting inputs for the application of the proposed methodology are v_f, the fiber aspect ratio A_R, $\mathbf{A}$ and a generic external macro-scale stress state $\overline{\boldsymbol{\sigma}}$ that is applied to the composite. The first step of the procedure consists in the discretization, into K sub-domains, of the unit-sphere on the surface of which the OPDF is defined: namely, vectors $\mathbf{p}_k$ with k belonging to $[1, K]$ have to be defined (K was chosen equal to 482 in the present work, high enough to provide a fine discretization). The unit vector $\mathbf{p}_k$ can be actually expressed as follows:

$$\mathbf{p}_k = (\sin\theta_k \cos\phi_k, \sin\theta_k \sin\phi_k, \cos\phi_k) \tag{3.13}$$

and therefore a discretization based on the angles of Eq. (3.13) can be established, such that $\phi_k \in [0,2\pi]$ and $\theta_k \in [0,\pi]$.

At this point, the values of $\psi(\mathbf{p}_k)$, for all integers within the interval $[1, K]$, can be computed according to Eq. (3.12). It is reminded that each index k corresponds to a PG, i.e. a FE model with fully aligned fibers, identified by its domain ω_k. Subsequently, the external stress state is transferred to each ω_k (the characteristics of which are reported within the next paragraphs) that can be numerically solved. The resulting matrix stress fields (e.g. LMPS, LHS and σ_{VM}) of each PG can be carried out and, accordingly, the S-CDFs is calculated. Eventually, Eq. (3.4) is applied to the stress values of the cumulative distribution functions of the pseudo-grains and the S-CDFs for the desired microstructure are found.

For the sake of clarity, all the steps for the computation of a generic stress component CDF are schematically reported in the flow-chart in Fig. 3.3.

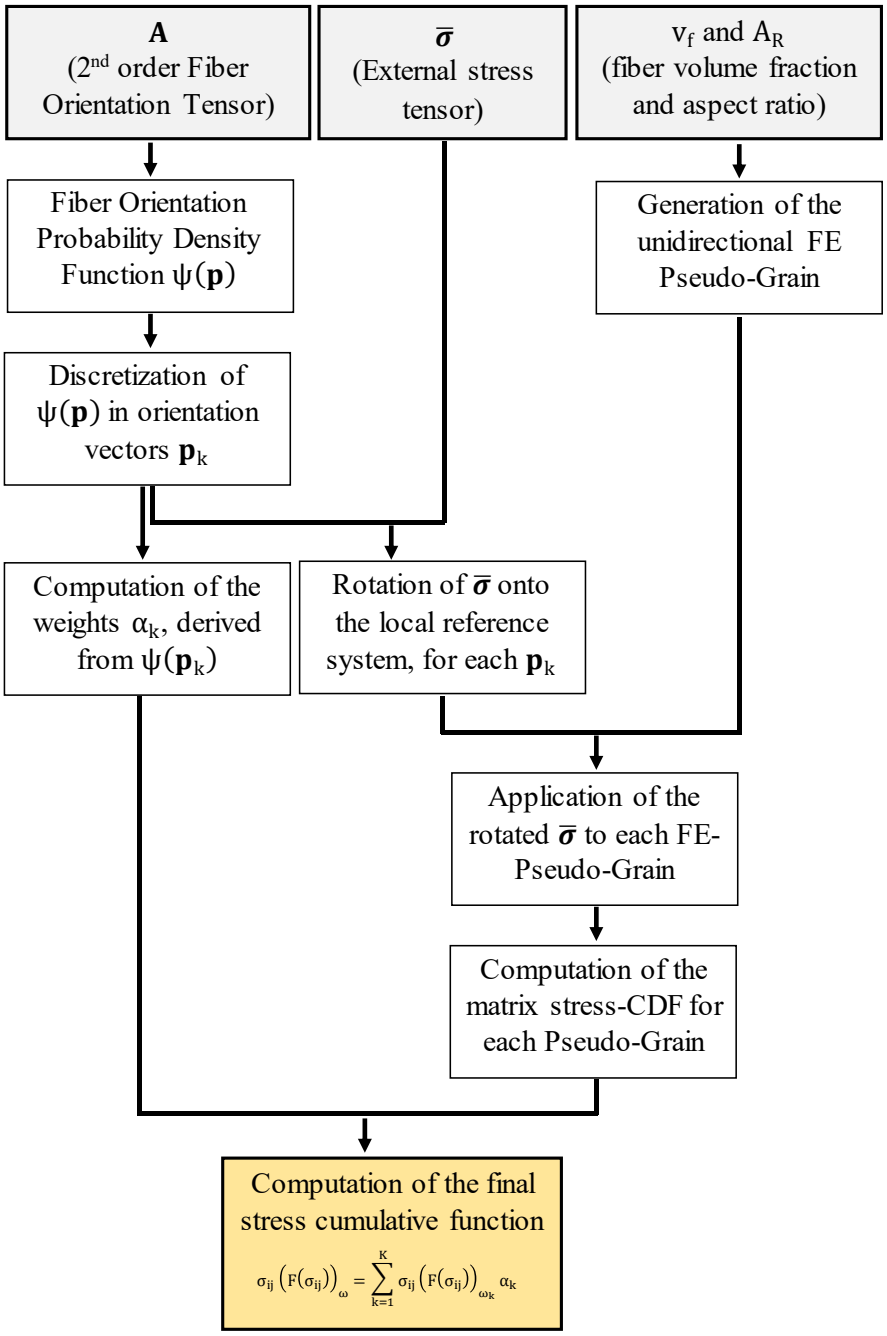

Figure 3.3. Flow-chart for the application of the proposed PG approach.

3.3.2 Pseudo-grain boundary conditions

As already mentioned, it is assumed that all the fibers of the microstructure are characterized by the same aspect ratio A_R and diameter d. Regarding the generation of the geometry of the PGs, it is sufficient to create only one unidirectional FE model (Fig. 3.4).

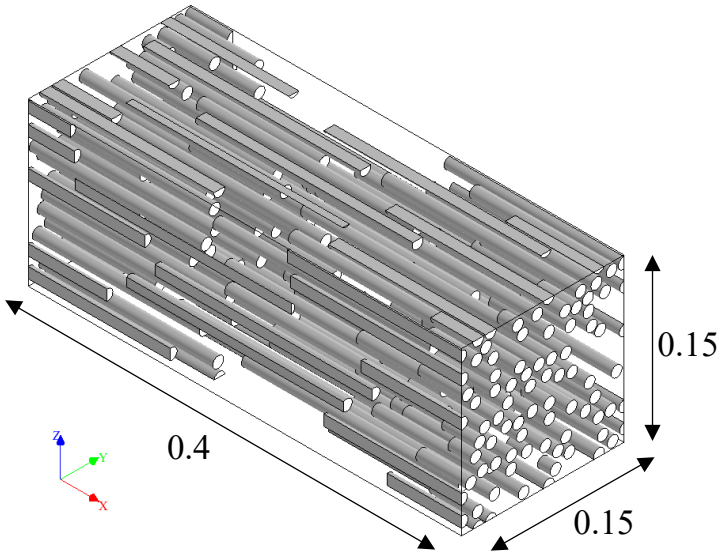

Figure 3.4. Example of unidirectional pseudo-grain generated with Digimat® (fiber volume fraction is set to 20%).

The grains can be therefore distinguished from each other only relying on the applied boundary conditions that depend on the grain orientation. In this work, the UD models have been created with the software Digimat®, which makes use of an algorithm that follows a random and uniform placement of inclusions (DIG18).

Boundary conditions need to be applied to the unidirectional FE model, representative of each domain ω_k, oriented along a vector $\mathbf{p}_k$ (Fig. 3.5). For this purpose, a Voigt formulation is adopted, which means that each pseudo-grain is subjected to the same external strain state $\bar{\boldsymbol{\varepsilon}}$ (Fig. 3.2), that can be easily derived by the following equation:

$$\bar{\boldsymbol{\varepsilon}} = \mathbb{C}_{\omega}^{-1} : \bar{\boldsymbol{\sigma}} \tag{3.14}$$

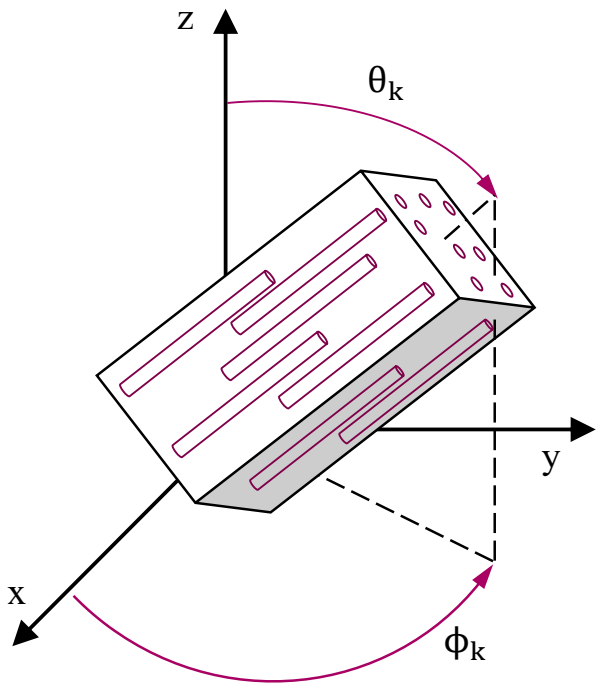

Figure 3.5. Schematic representation of a FE pseudo-grain rotated along a generic orientation vector $\mathbf{p}_k$.

In Eq. (3.14), $\mathbb{C}_\omega$ is the fourth-order stiffness matrix corresponding to domain , which is calculated by replacing f_{ω_k} in Eq. (3.4) with the stiffness tensor $\mathbb{C}_{\omega_k}$ of the single UD model:

$$\mathbb{C}_\omega = \sum_{k=1}^{K} \mathbb{C}_{\omega_k} \alpha_{\omega_k} \tag{3.15}$$

The term $\mathbb{C}_{\omega_k}$ is the stiffness tensor of each PG obtained from FE analyses. Eq. (3.15) must be computed adopting the same base system for both terms $\mathbb{C}_\omega$ and $\mathbb{C}_{\omega_k}$.

First, the external strain tensor can be expressed with bases belonging to the global reference system, as follows:

$$\bar{\boldsymbol{\varepsilon}} = \bar{\varepsilon}^g_{mn} e^g_m \otimes e^g_n \tag{3.16}$$

$\bar{\varepsilon}^{g}_{mn}$ being the external strain components in the global reference system and $\{e^{g}_{i}\}$ the corresponding global base system.

Then, to determine the boundary conditions for each pseudo-grain, a base transformation of Eq. (3.16), from $\{e^{g}_{i}\}$ to $\{e^{l_k}_{i}\}$, the latter denoting the local base system for the k-th PG, must be performed. Therefore, the external strain tensor also reads:

$$\bar{\boldsymbol{\varepsilon}} = \bar{\varepsilon}^{g}_{mn} Q_{im} Q_{jn} e^{l_k}_{i} \otimes e^{l_k}_{j} = \bar{\varepsilon}^{l_k}_{ij} e^{l_k}_{i} \otimes e^{l_k}_{j} \tag{3.17}$$

where $\bar{\varepsilon}^{l_k}_{ij} = \bar{\varepsilon}^{g}_{mn} Q_{im} Q_{jn}$ identifies the external strain components that must be applied to each pseudo-grain. $Q_{im}$and Q_{jn} are the components of a generic second-order rotation tensor $\mathbf{Q}$, of which the formulation is:

$$\mathbf{Q}(\mathbf{n}, \alpha) = \mathbf{n} \otimes \mathbf{n} + \cos\alpha\,(\mathbf{I} - \mathbf{n} \otimes \mathbf{n}) - \sin\alpha\,\mathbf{R} \cdot \mathbf{n} \tag{3.18}$$

In Eq. (3.18), symbols $\mathbf{n}$, α and $\mathbf{R}$ denote, respectively, a unit vector corresponding to the rotation axis, the rotation angle and the Ricci's tensor. According to Eq. (3.18), for a generic ω_k, terms Q_{im} and Q_{jn} of Eq. (3.18) can be recovered after performing the two subsequent rotations identified by tensors $\mathbf{Q}\left([0,0,1], -\phi_k\right)$ and $\mathbf{Q}([1,0,0], \theta_k - \pi/2)$.

For easiness of implementation, the boundary conditions for each pseudo-grain are applied in the form of stresses, which can be computed as:

$$\boldsymbol{\sigma}^{BC}_{\omega_k} = \mathbb{C}_{\omega_k} : \bar{\boldsymbol{\varepsilon}} \tag{3.19}$$

Therefore, symbol $\boldsymbol{\sigma}^{BC}_{\omega_k}$ denotes the stress tensor that must be applied to the single PG and the superscript BC stands for boundary condition.

3.3.3 Numerical implementation

According to Eq. (3.4), a certain amount K of solutions of the UD model, characterized by the proper PBCs, should be performed. However, it is reminded here that this work aims at calculating the local elastic stress fields within the matrix, these being useful for predicting the high cycle fatigue crack initiation through proper criteria (chapters 4 and 5). Therefore, the constitutive law of the phases is assumed as linear-elastic and, subsequently, the numerical solution of any applied stress state can be carried out by linearly combining the solutions of six uniaxial load cases, each representing the application of one single component of the stress tensor. To this end, the formulation of the stress tensor $\boldsymbol{\sigma}_{\omega_k}(\mathbf{x})$ evaluated at a defined coordinate-vector $\mathbf{x}$ within ω_k reads:

$$\boldsymbol{\sigma}_{\omega_k}(\mathbf{x}) = \sum_{i=x}^{z}\sum_{j=x}^{z} \overline{\sigma}_{ij}\, \boldsymbol{\sigma}^{ij}_{\omega_k}(\mathbf{x}) \tag{3.20}$$

In Eq. (3.20), $\boldsymbol{\sigma}^{ij}_{\omega_k}$ denotes the full stress tensor at a generic coordinate vector $\mathbf{x}$ in case the k-th PG undergoes a stress state where only the external stress component $\overline{\sigma}_{ij}$ is equal to 1 MPa and the others are set to 0 MPa. For a better understanding, terms of Eq. (3.20) are reported, as an example, in Fig. 3.6, in case i = j = x.

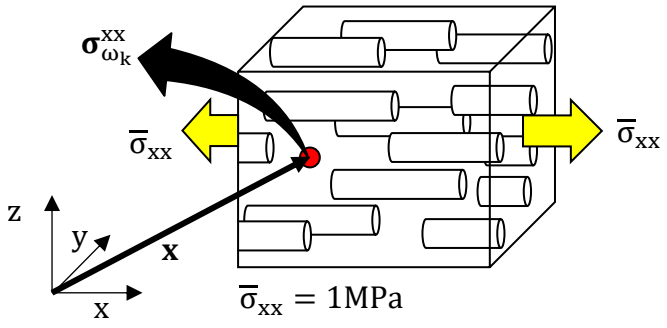

Figure 3.6. Graphical visualization of the terms in Eq. (3.20), in case (i, j) = (x, y).

After computing the complete stress field within the matrix of the UD grain, the stress values of the CDFs $F_{\omega_k}(\mathrm{LMPS})$, $F_{\omega_k}(\mathrm{LHS})$ and $F_{\omega_k}(\sigma_{\mathrm{VM}})$ can be calculated and combined, according to Eq. (3.4). With this approach, the computation of the elastic stress-cumulative function of misaligned short fiber microstructures can be carried out without relying on the generation and solution of complex microstructures.

The entire procedure for the calculation of the matrix stress-CDF is eventually summarized in the following steps:

1) Generation and meshing of a UD pseudo-grain;
2) Application of the six unit stress cases to the UD pseudo-grain;
3) Discretization of the unit sphere into K directions $\mathbf{p}_k$, with $k = 1, \dots, K$;
4) Calculation of the global stress state relevant to each PG, according to its orientation, by adopting a Voigt approach;
5) Computation of the entire linear elastic stress fields within the matrix of each PG by combining the results coming from the six uniaxial load cases, according to the stress state defined at point 4, according to Eq. (3.20);
6) Computation of the cumulative matrix stress distribution for each pseudo-grain;
7) Computation of the average cumulative stress distribution (along the stress axis) over all PG cells according to Eq. (3.4), each of them weighted by means of the fiber orientation probability evaluated along the single PG direction.

Eventually, it is worth mentioning that, from the conceptual point of view, the proposed approach could be applied also in case of non-linear or inelastic behavior of the constituents. In such a case, the UD pseudo-grains with different orientations discretizing the entire 3D space (482 divisions were chosen in this work), should be solved through separated FE models with proper boundary conditions depending on the grain orientation. Once this is done, the results can be combined to obtain the final matrix stress-CDF as in Eq. (3.4) and Fig. 3.3. However, in this case the proposed approach, though still possible, would not be efficient as it requires 482 non-linear FE analyses.

The efficiency of the proposed approach lies, indeed, in the computation of the matrix stress field of each pseudo-grain by performing a linear combination of the stress fields of six uni-axial load cases, as highlighted in Eq. (3.20). This is possible only for a linear elastic behavior of the constituents.

3.4 Results and discussions

In this section, a validation of the proposed method for the computation of the cumulative distribution function of the matrix stress fields in short-fiber RVEs is carried out. For this purpose, different volume elements with misaligned fibers have been generated and their actual S-CDFs, computed within the matrix, have been compared to the ones obtained with the proposed methodology.

3.4.1 Reference microstructures

The generation of the microstructures for validating the proposed approach has been performed by means of a non-commercial software developed by the Fraunhofer Institute ITWM, which makes use of the algorithm described in SCH17. With such tool, the desired FOT and fiber volume fraction can be efficiently reached. Furthermore, due the complexity of the reference microstructures, it has been decided not to generate a conventional mesh, but to voxelize the entire model (voxel size of 1 μm^3). The complexity of the mesh activity is therefore avoided. In order to better discretize the considered microstructure, the dimension of the single voxel has been set to 1µm. All reference cells have been subsequently solved with a fast Fourier transform (FFT) based solver (WEB3).

In order to validate the proposed PG approach, which has been developed to compute the matrix stress distributions, the reference microstructures listed in Tab. 3.1 have been analyzed. According to the software settings, only cubic cells have been generated and the edges' length was set to 300µm. Fibers have been modeled as cylinders with flat tips. As reported in Tab. 3.1, some parameters have been varied, i.e. different fiber aspect ratios, fiber volume

fractions (20%, 22%, 25%) and FOTs have been adopted. The fiber diameter has been kept equal to 10 µm for all analyses, as it is indicated in Tab. 3.1.

Table 3.1. Geometrical features of the reference models with misaligned fibers.

No.	v_f [%]	A_R	d [µm]	Cell size [mm³]	Amount of voxels	Amount of fibers	diag(**A**)
1	20	20	10	0.30 x 0.30 x 0.30	$27x10^6$	250	(0.7, 0.2, 0.1)
2	20	15	10	0.30 x 0.30 x 0.30	$27x10^6$	250	(0.7, 0.2, 0.1)
3	20	20	10	0.30 x 0.30 x 0.30	$27x10^6$	250	(0.5, 0.4, 0.1)
4	20	20	10	0.30 x 0.30 x 0.30	$27x10^6$	250	(0.33, 0.33, 0.34)
5	20	25	10	0.30 x 0.30 x 0.30	$27x10^6$	250	(0.7, 0.2, 0.1)
6	22	20	10	0.30 x 0.30 x 0.30	$27x10^6$	275	(0.7, 0.2, 0.1)
7	25	20	10	0.30 x 0.30 x 0.30	$27x10^6$	313	(0.7, 0.2, 0.1)

As an example, microstructure 1 is shown in Fig. 3.7. For the sake of representation, the fiber coordinates, which have been generated with the algorithm described in (SCH17), have been imported in Digimat® and used to generate the microstructure.

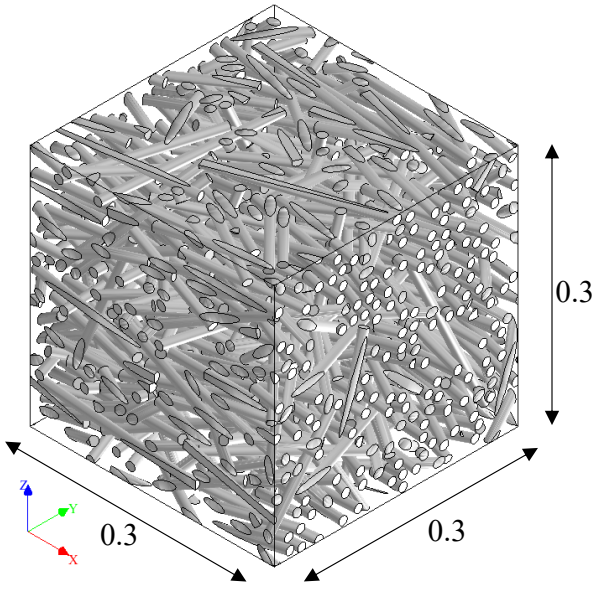

Figure 3.7. Example of complex microstructure (microstructure 1 of Tab. 3.1).

The reference microstructures with misaligned fibers undergo PBCs (appendix B) and a unit external stress has been applied. The latter has been rotated by 0°, 45° and 90° around the z axis, starting from the x axis of the global reference system (Fig. 3.7).
The properties assumed for the constituents are listed in Tab 3.2.

Table 3.2. Reasonable elastic constants of matrix (subscript m) and fibers (subscript f): tensile modulus E and Poisson's ratio ν.

$\mathbf{E_m}$ [MPa]	$\boldsymbol{\nu_m}$ [-]	$\mathbf{E_f}$ [MPa]	$\boldsymbol{\nu_f}$ [-]
3000	0.39	72000	0.22

3.4.2 Convergence study

The application of the pseudo-grain approach requires the use of the numerical results deriving from the solution of unidirectional cells.
In this section, a convergence study related to the choice of the PG cell size is reported. In this interest, two unidirectional FE cells has been generated, having their fiber volume fraction equal to 20%, according to the values reported in Tab 3.1. The cell sizes listed in Tab 3.3 have been investigated and an external unit stress has been rotated by 0°, 45° and 90° around the z axis (Fig. 3.4). The CDFs related to the matrix von Mises stress are plotted in Fig. 3.8, showing a good agreement between the two investigated cell sizes. The maximum relative error, evaluated along the horizontal axis, is lower than 10%, this allowing the usage of the UD cell (0.4x0.15x0.15 mm^3) for the current application.

Table 3.3. Considered microstructures for cell size convergence studies.

No.	$\mathbf{v_f}$ [%]	$\mathbf{A_R}$	d [μm]	Cell size [mm^3]	Amount of elements	Cell type
1	20	20.0	10.0	0.40 x 0.15 x 0.15	$0.7x10^6$	Unidirectional
2	20	20.0	10.0	0.40 x 0.30 x 0.30	$2.6x10^6$	Unidirectional

The average element size (edge length) adopted for microstructures 1 and 2 of Tab. 3.3 is 4μm and the amount of fibers in the cells are respectively 83 and 333.

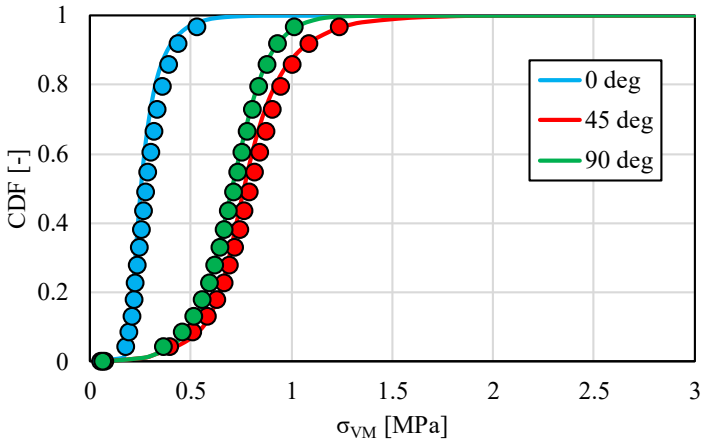

Figure 3.8. Convergence study: comparison of matrix von Mises-CFDs for microstructures of Tab. 3.3 (solid line for no. 1 and symbols for no.2).

3.4.3 Validation of the approach

As mentioned above, the computation of the matrix elastic stress distributions within the pseudo-grain cells can be performed by computing the matrix stress fields under six load cases. This has been achieved by meshing the UD geometry with the software Hypermesh® and by solving it with the FE software Abaqus®. According to the Abaqus® notation, C3D10 elements (quadric thetraedric) have been adopted.

In Fig. 3.9, the CDF of LHS, LMPS and σ_{VM} within the matrix are reported for microstructure 1, whereas only the CDF of the von Mises stress is shown for the other microstructures in Fig. 3.10, for the sake of brevity. The results obtained with the misaligned RVEs are compared to those obtained with the proposed PG methodology. For all the analyses, the unidirectional cell size has always been set to 0.40 x 0.15 x 0.15 mm^3, sufficient to get converged results for the matrix stress distributions.

It can be observed that, in case of microstructures 3 and 4 of Tab. 3.1, the cumulative distribution functions for different orientations of the global load are very close to each other (Fig. 3.10b and 3.10c). Indeed, the first two entries of the FOT diagonal of microstructure 3 are

close to each other, reproducing with a good approximation a planar isotropic fiber orientation distribution. A similar observation can be done for microstructure 4, where the FOT is almost three-dimensionally isotropic. As a consequence, the stress distribution, in these two cases, is not dependent on the load orientation angle on the xy plane.

From Fig. 3.9 and 3.10 it is clear that the PG approach reproduces very well the CDFs of LMPS, LHS and σ_{VM} as the maximum relative error with respect to the results obtained by solving the geometries of Tab. 3.1 is never higher than 10%.

As a concluding remark, it has to be highlighted that the problems that could arise because of the microstructure generation and solution are now overcome by adopting the proposed approach. Indeed, the PG methodology requires the generation of unidirectional FE models, in which high volume fractions ($\geq 15\%$) can be easily reached and the FOT is defined a-priori as an input to the approach. The use of such UD models makes the meshing activity easier with respect to FE geometries with misaligned fibers because of the absence of sharp edges on the model faces, which might arise as a consequence of fibers non-parallel to the model outer surfaces. This accelerates the meshing procedure and, eventually, the time needed for solving the model is not anymore hindered or slowed down by the presence of large mesh refinements around sharp edges. Finally, the proposed approach allows to compute the matrix elastic stress distribution without using complex fiber generation algorithms and with relatively low computational costs.

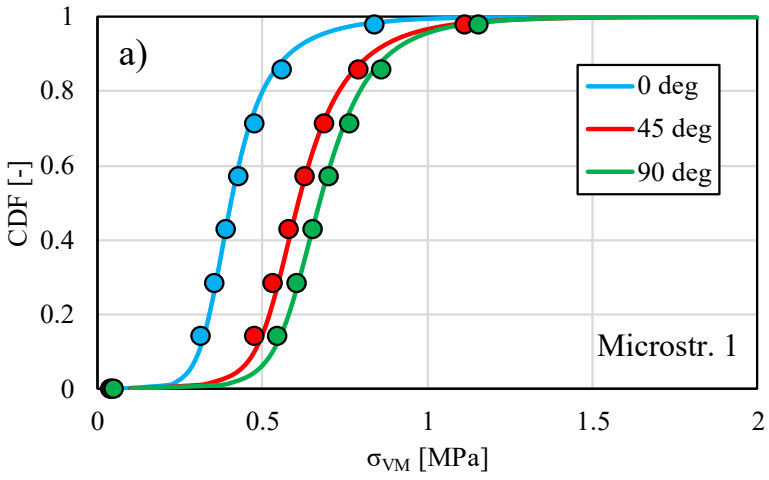

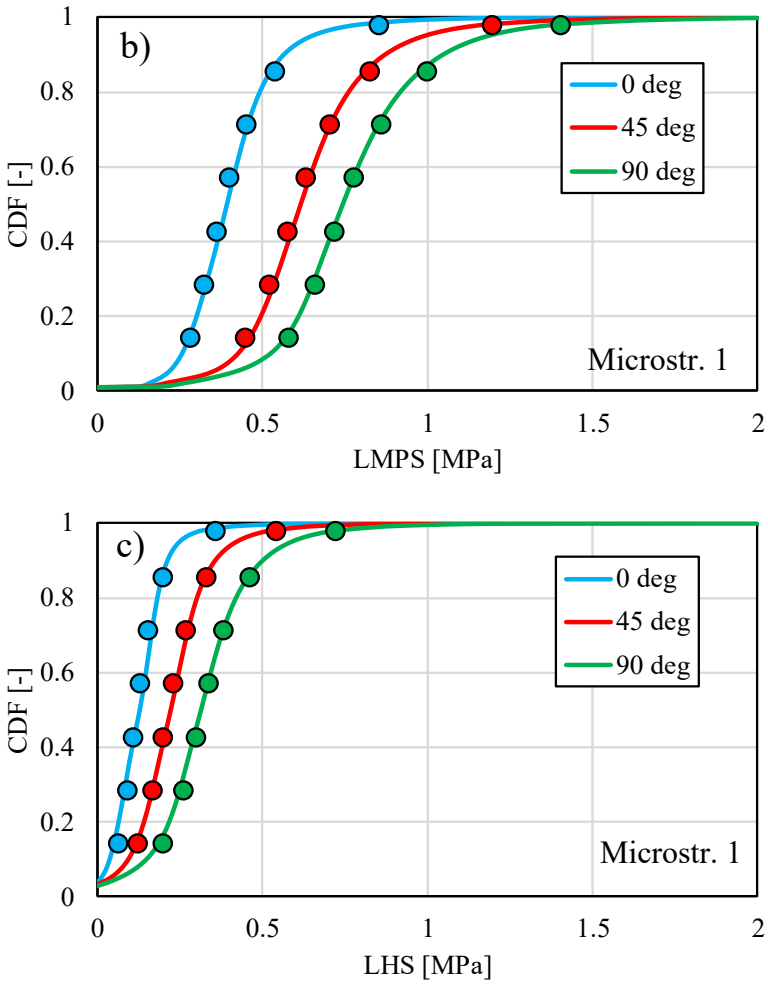

Figure 3.9. Validations of the PG approach for microstructure 1. Solid lines: PG, symbols: RVE.

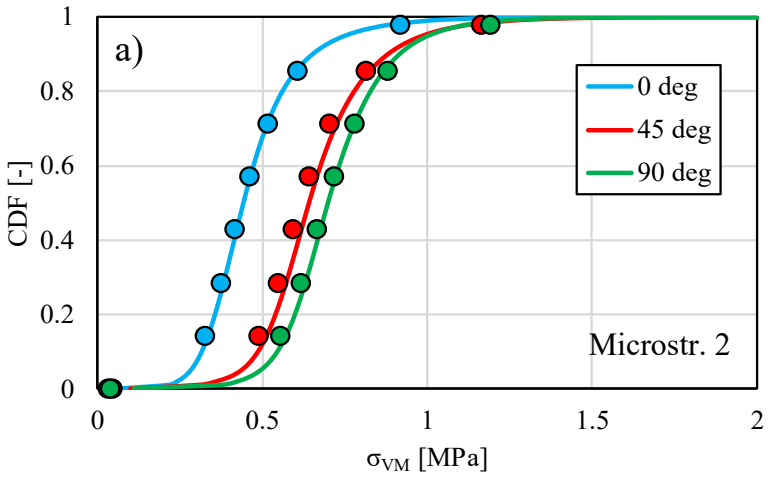

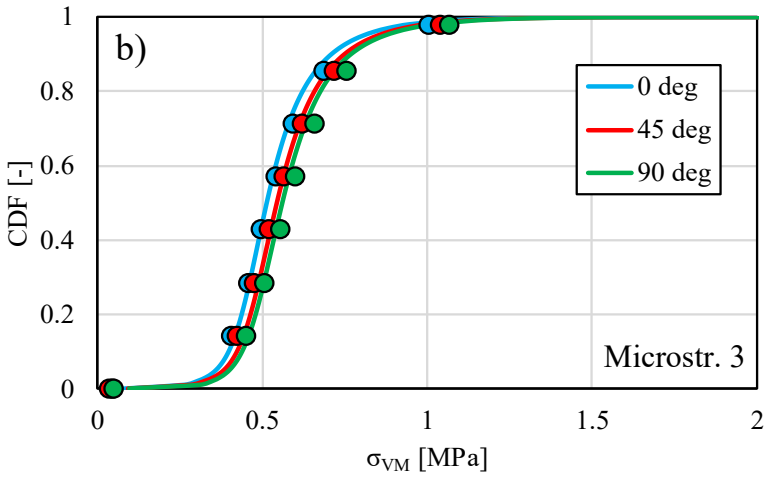
b)
0 deg
45 deg
90 deg
Microstr. 3
CDF [-]
σ_{VM} [MPa]
0
0.2
0.4
0.6
0.8
1
0.5
1.5
2

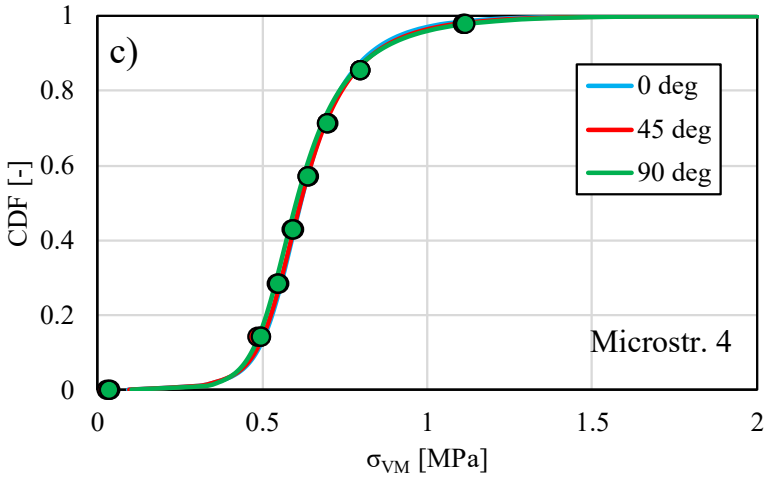
c)
0 deg
45 deg
90 deg
Microstr. 4
CDF [-]
σ_{VM} [MPa]
0
0.2
0.4
0.6
0.8
1
0.5
1.5
2

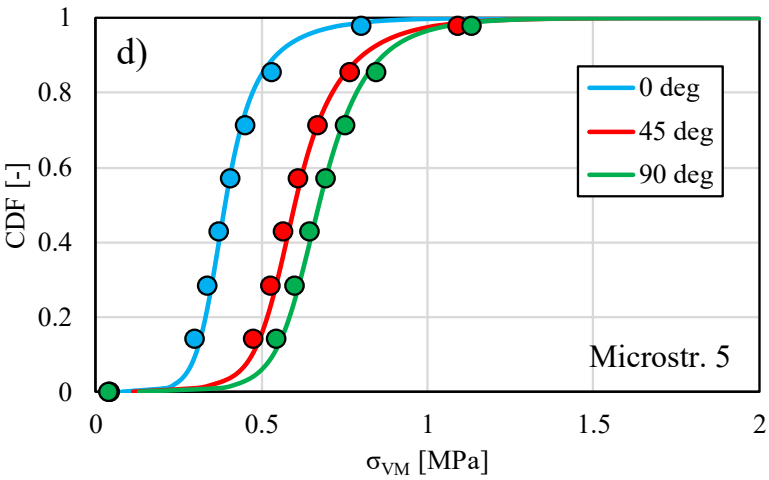
d)
0 deg
45 deg
90 deg
Microstr. 5
CDF [-]
σ_{VM} [MPa]
0
0.2
0.4
0.6
0.8
1
0.5
1.5
2

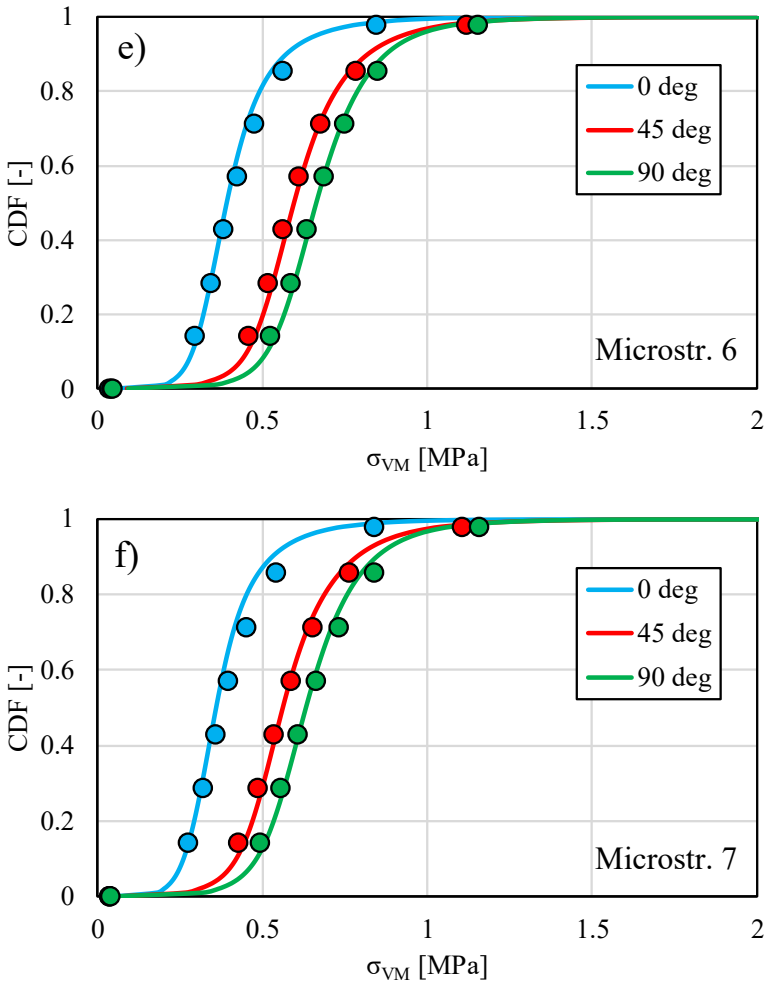

Figure 3.10. Validations of the PG approach for microstructure 2-7. Solid lines: PG, symbols: RVE.

It is furthermore worth highlighting that the adopted elastic modulus (3000 MPa) can be considered as typical for dry-as-molded materials. On the other hand, the matrix phase of real SFRT parts can present a certain concentration of absorbed water as a consequence of the humidity of the surrounding environment. Nevertheless, by lowering the matrix elastic modulus by two thirds (thus reproducing a matrix with a relative humidity of 50%), no significant variation in the PG formulation (cell size at convergence) is expected. This would be a consequence of the fact that both in case of dry and conditioned SFRTs, the matrix elastic modulus still results to be one order of magnitude smaller than the fibers' one. Accordingly, Fig.

3.11 shows the capability of the proposed approach and PG size of reproducing the matrix von Mises stress CDF for microstructure 1 of Tab. 3.1.

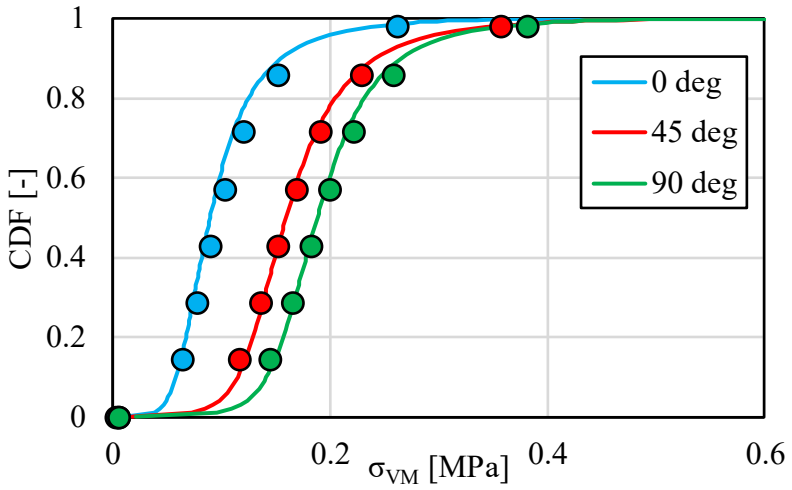

Figure 3.11. Validations of the PG approach for microstructure 1. Solid lines: PG, symbols: RVE. The matrix elastic modulus has been set to 1000 MPa.

3.5 Conclusions

In the present chapter, an innovative procedure for computing the cumulative distribution function of different local stress components within the matrix of a generic microstructure with misaligned short fibers has been formulated.

A framework based on the application of the pseudo-grain methodology combined to the generation and solution of single UD grains through the finite element method has been proposed.

The efficacy of the present approach consists in the capability of overcoming issues related to the generation, meshing and solution of a classical volume element filled with a high fraction of misaligned short fibers.

Eventually, the cumulative distribution functions of the local maximum principal stress, local hydrostatic stress and von Mises stress within the matrix of different microstructures with misaligned fibers have been computed and employed to validate the proposed approach.

A good agreement between the results obtained from the reference microstructures and the pseudo-grain model has been obtained.

As it will be better within the next chapters, the proposed PG methodology will be later used to formulated multiscale fatigue criteria based on the definition of matrix effective stresses. In fact, the latter will be formulated on the basis of the matrix stress distributions.

Furthermore, some considerations regarding the choice of the threshold of the matrix stress cumulative functions can be found in the appendix D.

Concluding, It has been numerically verified that while dealing with the energetic matrix contributes (deviatoric and hydrostatic), the deviatoric part results to be 3-4 orders of magnitude higher than the hydrostatic one. Therefore, within the next paragraphs, the computation of the matrix Beltrami stress (the use of which will be discussed later on) distributions will be also possible by only considering the matrix von Mises stress distributions, after performing some algebraic manipulations.

Chapter 4

Fatigue model for plain specimens

4.1 Introduction

In this chapter, the pseudo-grain approach for computing the matrix stress distribution, presented in chapter 3, is integrated in a multiscale model for the prediction of the fatigue strength of specimens in the absence of notches. Data on plain specimens presented in chapter 2 are furthermore employed to validate the proposed criterion.

The lightness and the good mechanical properties of short fiber reinforced thermoplastics (SFRTs) have encouraged a widespread employment of such materials within the automotive industry. This is the case, for example, of under-the-hood-components (e.g. fuel-rails), which commonly undergo repeated mechanical loads. As a consequence, the need of reliable methods for designing those parts against fatigue failure has become more and more relevant.

The fatigue lifetime of SFRTs is generally determined by several parameters such as the load application (load ratio, stress amplitude), the fiber geometry (length and diameter) and the fiber spatial distribution (fiber orientation and volume fraction).

Accordingly, a comprehensive material characterization typically requires a large bulk of experimental tests. Therefore, robust fatigue models are needed to restrict the experimental effort and the inferred costs.

The present work falls within this framework. It aims to provide a model for predicting the fatigue life to crack initiation of SFRTs. In particular, the effect of the fiber volume fraction (v_f) and fiber orientation distribution (FOD) will be accounted for. The latter, which may be non-uniform within a single specimen or component (BER07, DEM10_2, JAI16_2, KLI11, LUN13, LUN13_2, ARI14, KRA16, BER15, MOR17), is usually described by means of a second-order fiber orientation tensor (FOT) (ADV87).

The fatigue strength of such materials is highly sensitive to the local fiber orientation distributions. In this context, many authors have conducted studies on the effect of the angle between the loading direction and the main flow direction (MFD).

An exhaustive literature review on the fatigue response of SFRTs was carried out by Mortazavian and Fatemi (MOR15_3) and the effect of material anisotropy was emphasized. The authors showed that it is caused both by the FOD non-uniformity within the part and the specimen cut-out angle, meant as the orientation of the load with respect to the injection direction (MOR17).

Bernasconi and coworkers (BER15) investigated the fatigue response of notched specimens that were longitudinally or laterally injected. They evaluated the FOD through the specimen thickness by adopting an optical method at the notched cross section. Thus, they demonstrated how the fatigue strength could depend on the FOT profile of each specimen.

Additionally, the matrix stress multiaxiality influencing the fatigue behavior of SFRTs also depends on the amount of fibers, namely on the material fiber volume fraction. The effect of the latter has not been widely investigated in the literature yet.

Nevertheless, in 2017 Belmonte and coauthors (BEL17_2) tested, under cyclic uniaxial loads, sharply notched specimens with a v_f ranging from 0% (unreinforced polymer) to 50% in weight. They obtained S-N curves correlating the nominal applied stress to the life to crack initiation and final failure, showing a strengthening effect as the v_f was increased.

In the literature are furthermore present fatigue failure criteria that mainly aim to capture the effect of the material anisotropy induced by the fiber orientation onto the material fatigue behavior.

A broad overview of the existing fatigue models until 2015 was also provided in (MOR15_3).

Additionally, in their work (WIL15) Wilmes and Hornberger proposed a criterion for predicting the effect of the local material anisotropy onto the fatigue strength of a polyamide 6.6 reinforced with the 35 wt% of fibers (PA66-GF35). The authors formulated a numerical scalar indicator called *fiber-share*, which takes into account the local material anisotropy deriving from the FOT. Thanks to this, tests on specimens extracted from injected plates along two different angles (0° and 90°) are needed to calibrate the model and to predict the fatigue life of a SFRT composite with a generic FOT profile and loading direction. Furthermore, in

WIL15 the authors made use of the process simulation software Moldflow® to compute the FOTs within the injected plates and, subsequently, within the considered specimens.

In 2016, Jain et al. (JAI16) formulated a master S-N curve approach for the fatigue life prediction of SFRTs. The FOTs assigned to the material were evaluated through process simulations (KLIM11) or derived from the first entry of the second-order FOT measured through optical 2D analyses (DEM10). The authors formulated an approach in which the fatigue strength of the considered specimens can be related to the simulated material quasi-static laws.

In another recent work, Krairi and coauthors (KRA11) proposed a multiscale model for predicting the high-cycle fatigue life of a PA66-GF30, including the effect of the material anisotropy. The tested plain dumbbells were cut out at 0°, 45° and 90° with respect to the main flow direction (MFD). Regarding the properties' assignment, the average second-order FOT, evaluated through the thickness, was adopted. The formulated criterion attributes the fatigue progressive damage to matrix weak spots obeying a viscoelasic-viscoplasic law including damage.

On the other hand, the effect of the v_f on the fatigue strength of SFRTs has not been widely treated in the literature yet.

In such a complex scenario, where the material behavior is influenced by several material and geometrical/morphological features, a reliable crack initiation model has to be based on the damage mechanisms occurring during the fatigue life.

In addition, the evolution of damage within SFRTs under cyclic loads is by nature a multiscale and hierarchical process. Indeed, it has been shown that the initiation of a fatigue crack in a SFRT is the result of the accumulation of damage at the microscopic scale, occurring mainly in the matrix surrounding the fibers (BEL17, BEL17_2). Accordingly, the crack onset can be identified as a matrix-driven phenomenon (HOR97, BEL17, BEL17_2).

Horst and Spoormaker described in HOR97 the damage phases that follow one another during the fatigue life of a PA6-GF30, in both cases conditioned and dry-as-molded states. They highlighted that matrix damage form at fiber tips and subsequently at fiber walls. This gives rise to bridging cracks from fiber to fiber. All observations were carried out by cryogenically fracturing the damaged material and analyzing the exposed surface by means of a scanning electron microscope (SEM).

De Monte et al. (DEM10_3) also performed SEM analyses on failed PA66-GF35 flat and tubular plain coupons. They paid attention to the crack nucleation zones and observed that the damage affects the thermoplastic matrix, determining fibers' debonding and pull-out.
In a paper of Arif and coauthors (ARI14), a study on the correlation between local fiber orientation and matrix damage was carried out, conducting micro-computed tomography (μCT) analyses on cyclically loaded PA66-GF30 materials. They observed that the damage evolution is mainly governed by the formation and growth of voids, identified as fiber-matrix debonding.
Eventually, Belmonte and coworkers (BEL17_2) inspected the crack onset site in plain specimens made of PA66-GF35 and found a clear ductile rupture within the matrix. Furthermore, zooming on the fibers' wall, no neat matrix detachment from fibers could be encountered.
In light of this, it is important to mention that most of the fatigue models developed for SFRTs in the literature do not focus on the matrix damage at the microscale and are typically formulated at the macroscale level, i.e. based on macro-scale stress fields. In addition, none of the models available at present is capable of accounting, at the same time, for the influence of the FOD, the load orientation and the fiber volume fraction. In this context, the present work aims at developing a fatigue crack initiation criterion for SFRTs, based on the micro-scale stress fields in the matrix, computed for the actual material microstructure. Thanks to the stress distribution resolved at the micro-scale level (within the matrix), it will be possible to formulate an effective stress component enabling the prediction of the whole composite fatigue strength. This means that the macroscopic fatigue response of the treated materials will be linked to the aforementioned effective stress (σ_{eff}) component, which, in turn, has to be considered as responsible for the microscopic matrix fatigue damage, the evolution of which brings to the appearance of a macroscopic crack.
The criterion is validated against new and already existing experimental data on PA66-GF15, PA66-GF25, PA66-GF35 and PA66-GF50, showing a very good agreement and the capability of accounting for the load orientation, the FOD and the fiber volume fraction.

4.3 Fatigue criterion definition

In this section, the formulation of a fatigue criterion based on the identification of a matrix stress component considered as responsible for the initiation of a macroscopic crack interesting the overall composite is provided. In particular, the aforementioned stress is obtained by means of an effective stress (σ_{eff}) calculated within the matrix (microscale) and considered as responsible for the microscopic matrix fatigue damage evolution, bringing, in turn, to the onset of a visible macro-crack. This falls within the formulation of a multiscale criterion which describes the composite fatigue response on the basis of the local matrix strength identified by the formulated effective stress. This agrees furthermore with the experimental observations previously discussed, stating that the composite fatigue damage mainly occurs within the matrix, i.e. among fibers.

The novelty of the present work consists in identifying the previously discussed σ_{eff} by means of the elastic stress field, which the composite matrix undergoes, or rather thanks to the matrix stress distributions. The choice of using the stress distribution lies in the fact that the introduced effective stress can be computed within the most stressed regions of the matrix phase. It is indeed reasonable assuming that, considering the stress field of a certain matrix stress component, the upper tail of its distribution control the matrix fatigue damage evolution. As a matter of fact, the latter is representative for the most stressed regions that can be identified within the matrix. It is therefore decided to formulate the effective stress as the average value of a certain matrix stress component, computed within the matrix phase region corresponding to the stress distribution upper tail.

To sum up, the concept of effective stress allows to bridge the macroscopic crack initiation and the local matrix fatigue damage by means of the formulation of such a matrix stress component controlling in turn the fatigue strength of the whole composite.

Eventually, since only plain specimens will be considered within this chapter and no significant stress gradients are present, the maximum value of the carried out effective stress ($\sigma_{eff,max}$) encountered within the plain specimen model will be used to predict the fatigue strength of the whole composite.

Furthermore, the matrix of the composite is normally subjected to a strong stress multiaxiality as a consequence of the local fibers' arrangements and of the fiber geometry. Indeed, the cylindrical shape of fibers, combined with their tip, strongly perturbs the local matrix stress field.

In order to capture the aforementioned effects, it is hereby proposed to compute the fatigue damage driving force (σ_{eff}) from the distributions of the Beltrami stress calculated at the matrix level. This stress component is nothing but the expression, in terms of stress, of the total strain energy density computed within the matrix and it reads:

$$\sigma_{B,m} = \sqrt{W_{tot,m} \cdot E_m} \tag{4.1}$$

Terms $W_{tot,m}$ and E_m of Eq. (4.1) respectively denote the total strain energy density and the Young's modulus. Subscript m indicates furthermore that the terms refer to the constituent matrix.

Symbol $W_{tot,m}$ can also be expressed as follows:

$$W_{tot,m} = W_{dev,m} + W_{dil,m} \tag{4.2}$$

According to Eq. (4.2), the total strain energy density can be normally split into two energetic contributions, namely a deviatoric ($W_{dev,m}$) and a dilatational ($W_{dil,m}$) part. The deviatoric strain energy density can be reformulated by means of the matrix von Mises stress:

$$W_{dev,m} = \frac{1 + \nu_m}{3E_m} \sigma_{VM}^2 \tag{4.3}$$

while the dilatational, or alternatively hydrostatic, term of Eq. (4.2) can be formulated as a function of the first invariant $I_{1,m}$ of the matrix stress tensor:

$$W_{dil,m} = \frac{1 - 2\nu_m}{6E_m} I_{1,m}^2 \tag{4.4}$$

where symbol ν_m stands for the Poisson's ratio of the matrix and $I_{1,m}$ can be expressed as a function of the matrix hydrostatic stress:

$$I_{1,m} = \sigma_{xx,m} + \sigma_{yy,m} + \sigma_{zz,m} = 3\,\sigma_{H,m} \tag{4.5}$$

In Eq. (4.5), terms $\sigma_{xx,m}$, $\sigma_{yy,m}$ and $\sigma_{zz,m}$ respectively denote the diagonal stress components of a generic matrix stress tensor and $\sigma_{H,m}$ the matrix hydrostatic stress.

As it will be widely discussed later on, the plain specimen geometry will be simplified and reproduced with the RVE technique. In particular, a model layered along the thickness direction will be proposed and for each layer the computation of the Beltrami stress distribution will be possible by means of the pseudo-grain approach (chapter 3).

It is furthermore assumed that the crack initiation interesting the whole specimen can be attributed to the most critical layer, namely to the one characterized by the highest values of matrix Beltrami stresses, which can be identified by considering the cumulative stress distribution functions.

As proved by Belmonte et al. (BEL17, BEL17_2), the micro-scale damage process that leads to the initiation of a technical crack is not a point phenomenon. Conversely, it involves a finite matrix volume that can be defined as a process zone, which is typically confined within the matrix regions surrounding the fibers. Based on numerical simulations (Fig. 4.1) and on (BEL16), it can be easily stated that the right tail of the stress distributions (e.g. CDF higher than 90 %) are associated to the matrix portion surrounding the fibers. On the other hand, the same matrix regions correspond to the critical volumes in which the damage initiates and evolves during the fatigue life (BEL16, BEL17, BEL17_2, ARI14). As a consequence, the effective stress (σ_{eff}) proposed in the present chapter, is equal to the average value of the Beltrami stress, calculated within a matrix volume corresponding to a given percentage $V_{c\%}$ of the matrix subjected to the highest values of the Beltrami stress, as schematically shown in Fig. 4.2. The choice of the critical volume $V_{c\%}$ has to be such that the matrix regions

included are those where the damage actually occurs, i.e. those surrounding the fibers. As an example, the Beltrami stress field for an RVE with misaligned fibers under a unit tensile stress along direction x is shown in Fig. 4.1, where the most critical 10% of the matrix is isolated. It can be seen that the volume involved is always surrounding the fibers, suggesting that a $V_{c\%}$ equal to 10% or similar can be a reasonable choice.

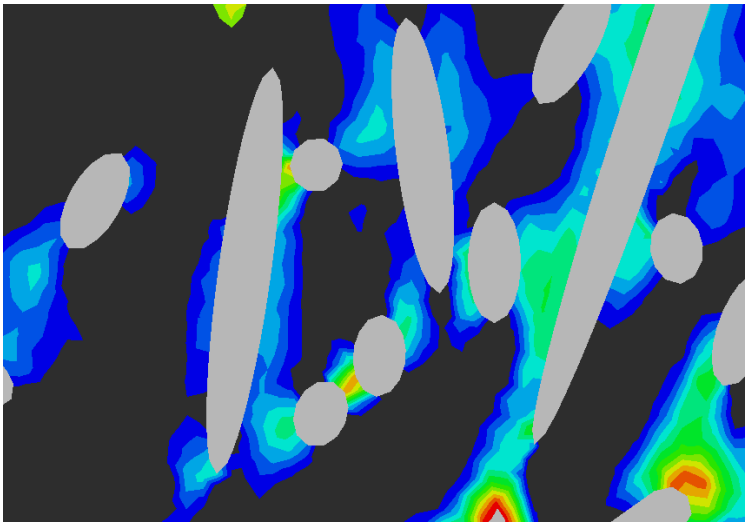

Figure 4.1. Example of $V_{c\%}$ corresponding to the 10%.

Fig. 4.2 schematically shows the isolation of the $V_{c\%}$ by setting a threshold of the cumulative distribution function of the matrix Beltrami stress.

For calculating σ_{eff} as the average value of the local Beltrami stress within a matrix volume defined by a CDF% equal to $(100 - V_{c\%})$, the probability density function (PDF) must be obtained from the derivative of the CDF. In case of the Beltrami stress, it reads:

$$\mathrm{PDF}(\sigma_{B,m}) = \frac{d\left(\mathrm{CDF}(\sigma_{B,m})\right)}{d(\sigma_{B,m})} \tag{4.6}$$

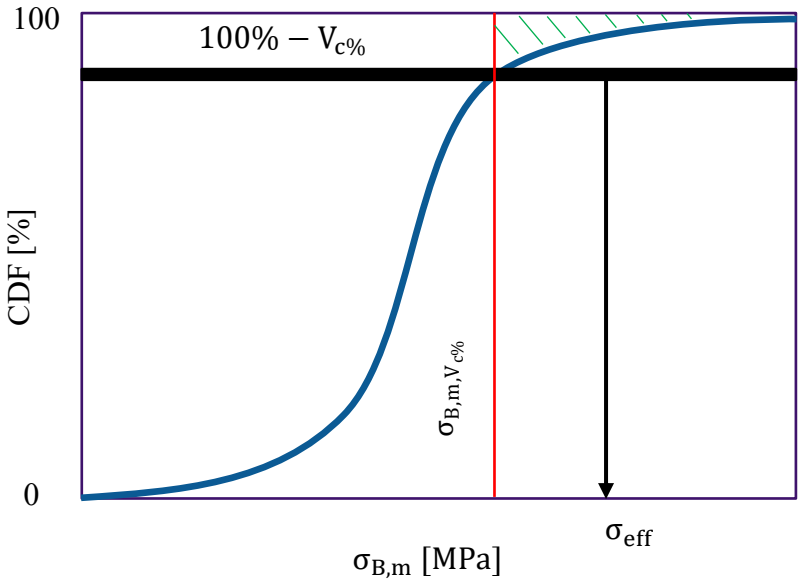

Figure 4.2. Schematic representation of effective stress computation from a CDF threshold.

As already mentioned, the effective stress is computed as the average value of the Beltrami stresses corresponding to the distribution tail. Indeed, as it is schematically depicted in Fig. 4.2, once the distribution tail is identified by means of the threshold ($100 - V_{c\%}$) of the CDF, the mean value of $\sigma_{B,m}$ can be calculated by means of the following expression:

$$\sigma_{eff} = \frac{1}{\int_{\sigma_{B,m,V_{c\%}}}^{+\infty} \mathrm{PDF}(\sigma_{B,m})\, \mathrm{d}(\sigma_{B,m})} \int_{\sigma_{B,m,V_{c\%}}}^{+\infty} \sigma_{B,m} \cdot \mathrm{PDF}(\sigma_{B,m})\, \mathrm{d}(\sigma_{B,m}) \tag{4.7}$$

Eq. (4.7) represents, therefore, the mean value of the Beltrami stress carried at the right tail of the distribution (dashed region). To better understand the expression of Eq. (4.7), it is additionally remarked that the integration domain is identified by the $\sigma_{B,m}$ variable, as indicated by the differential symbol $\mathrm{d}(\sigma_{B,m})$.

Nonetheless, the choice of $V_{c\%}$ will be discussed within the next paragraphs.

4.2 Multiscale model

In this section, the fatigue crack initiation model, accounting for the combined effect of the local FOD and the fiber volume fraction within SFRTs is presented. It has already been discussed that the initiation of a macro-crack (meant as a visible technical crack propagating in the material) is driven by the damage evolving within the thermoplastic matrix, among the fibers. As a consequence, it is reasonable to identify, as the driving force for crack initiation, a local stress parameter calculated at the micro-scale in the matrix. For this reason, a multiscale model is required to compute the micro-scale stress fields in the matrix and link them to the macro-scale stresses. The choice of the effective stress (σ_{eff}) to be adopted as a driving force will be discussed later on. As it will be detailed within the next paragraphs, the computation of such a stress component identified as responsible for the crack initiation within the modeled specimen geometry will be based on the matrix stress distributions. As already reported in the introduction of the present chapter, σ_{eff} will be computed by means of the matrix stress field, or better by using the stress distribution to which the composite matrix phase undergoes. It will be therefore possible to explain and describe the composite fatigue strength (associated with the onset of a crack at the macro-scale) by means of such a local parameter computed at the matrix level. This implicitly means that the macroscopic crack onset is controlled by the stress state present at the matrix level and, therefore, by the matrix damage mechanisms themselves.

In the following, a multiscale strategy is presented, to be used for the computation of the microscale stress fields in the matrix. In particular, a two-scales strategy is here adopted, as schematically shown in Fig. 4.3. Therefore, the multiscale model has the following characteristics:

- At the macro-scale, the material is considered as homogeneous and anisotropic. In particular, the modeled geometry can be discretized into a number of sub-layers. Each of them is characterized by a uniform in-plane FOT. Concerning the through-the-thickness direction, a varying FOT is assigned, according to the experimental data obtained by means of CT scans. It is furthermore worth highlighting that no actual

specimen geometry will be modeled, but a RVE technique will be employed as it will be detailed later on;

- At the micro-scale, fibers and matrix are modeled as separated phases. At this scale, heterogeneous RVEs can be generated, fulfilling the required FOT and v_f. The desired microstructure can be normally generated by using conventional algorithms for placing fibers within a cell. The latter is an operation that usually has to face different problems related to the model generation, mesh and solution. For this reason, in the present work the pseudo-grain methodology proposed in chapter 3 and PIE18 will be used, since the final aim of the micro-model solution is to carry out the matrix stress distributions.

For the calculation of the elastic properties of the macro-models, the path from the micro- to the macro-scale has to be followed, by using analytical (PIE4) or numerical homogenization techniques by means of Finite Element (FE) analyses on the micro-scale RVE.

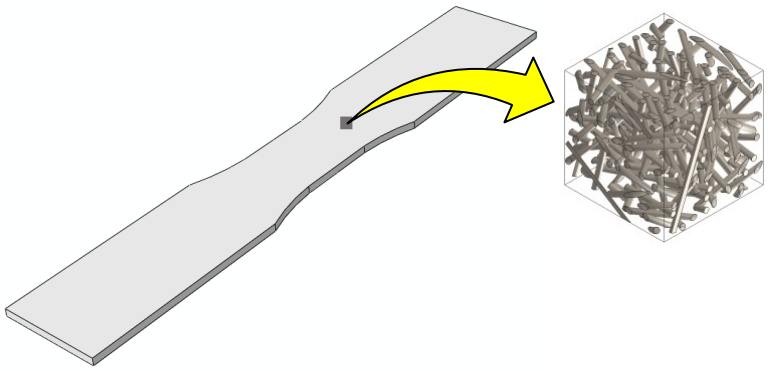

Figure 4.3. Schematic representation of multiscale modeling.

For the computation of the local stress fields in the matrix, the opposite path is taken, according to the following steps:

1) FE solution of the macro-scale model with homogenized elastic properties under prescribed displacement and/or load boundary conditions, for the calculation of the complete macro-scale stress field, namely the homogenized stress tensor within each layer;

2) FE solution of the heterogeneous microstructure representative of each sub-layer, subjected to boundary conditions simulating the stress field in the relevant sub-layers. As already mentioned, the use of the pseudo-grain approach (PIE18) is suggested for the calculation of the local stress fields in the matrix, this being more efficient than the generation and solution of actual RVEs with misaligned fibers.

Once the micro-scale stress distributions are calculated, the damage driving force parameter can be identified as the maximum value of the effective stress field, i.e. $\sigma_{eff,max}$. The latter can be eventually used to plot crack initiation $\sigma_{eff,max}$-N curves. The workflow for the computation of the micro-scale effective stress responsible for the fatigue damage evolution at the micro-scale, by way of the pseudo-grain application, is shown in the flowchart of Fig. 4.4. Further details on the construction and solution of the macro- and micro-scale models are given within the next sections.

It has to be furthermore pointed out that, since only linear analyses will be carried out, only one simulation for each specimen geometry is needed. Indeed, as it is shown in Fig. 4.4, instead of considering all stresses describing the nominal S-N curve, one normalized external load (i.e. a unit nominal stress) can be applied to the macro-model. Be therefore $\overline{\sigma}_{eff,max}$ the most critical effective stress computed for an external applied unit nominal stress.

Once all fatigue data are displayed in terms of $\sigma_{eff,max}$, whether fatigue points collapse within a narrow scatter band, the robustness of the proposed fatigue criterion is demonstrated. The expression of fatigue curves as a function of the most critical effective stress can be done according to the following equation:

$$\sigma_{eff,max} = \sigma_a \cdot \overline{\sigma}_{eff,max} \tag{4.8}$$

where symbol σ_a denotes the nominal stress amplitude used for displaying Wöhler-curves. Eq. (4.8) is moreover based on the assumption that all fatigue curves are lines parallel to each other, whether displayed through a bi-logarithmic scale.

Observing Fig. 4.4., it must be pointed out that information related to the external load direction and the used fiber orientation tensors are connected to each other. Hence, in order to avoid mistakes, it is suggested to refer the FOT components' reference system to the one

related to the injection-molded geometries. From now on, the following axis conventions will be adopted:

- x direction: main flow direction;
- y direction: specimen/plate width direction;
- z direction: through-the-thickness direction.

4.2.1 Macro-scale model

As revealed by CT analyses or process simulations (KLI11), the FOTs within a generic component might be characterized by a large variability along the three space coordinates. However, for plain flat specimens, as those considered for the practical application in the present work, a significant variability of the FOT is obtained along the through-the-thickness direction only. This phenomenon is typically observed in specimens that have been extracted from injection-molded plates. Therefore, in the specimen plane, the FOT variations can be considered as negligible.

As schematically shown in Fig. 4.5, the thickness of the specimen is discretized into a number of sub-layer, each of them having a uniform FOT that varies, layer by layer, according to the trend given by CT measurements or process simulations.

Once again, no FOT variation is considered along x and y, but only along z. Accordingly, the homogenized macro-model is characterized by the actual thickness of the corresponding specimen. As already mentioned, the model depicted in Fig. 4.5 is meant to undergo a unit external load, the direction of which lays on the xy plane, letting the upper and lower faces unconstrained. This can be done by applying mixed periodic boundary conditions (PBC) to the cell of Fig. 4.5. More details regarding the implementation of the PBCs are reported in appendix B**.** The equations expressing the deformation of faces/edges/vertices are written in terms of nodal displacements, i.e. nodes belonging to opposite faces move in the same manner and their relative displacements are expressed by the equations themselves.

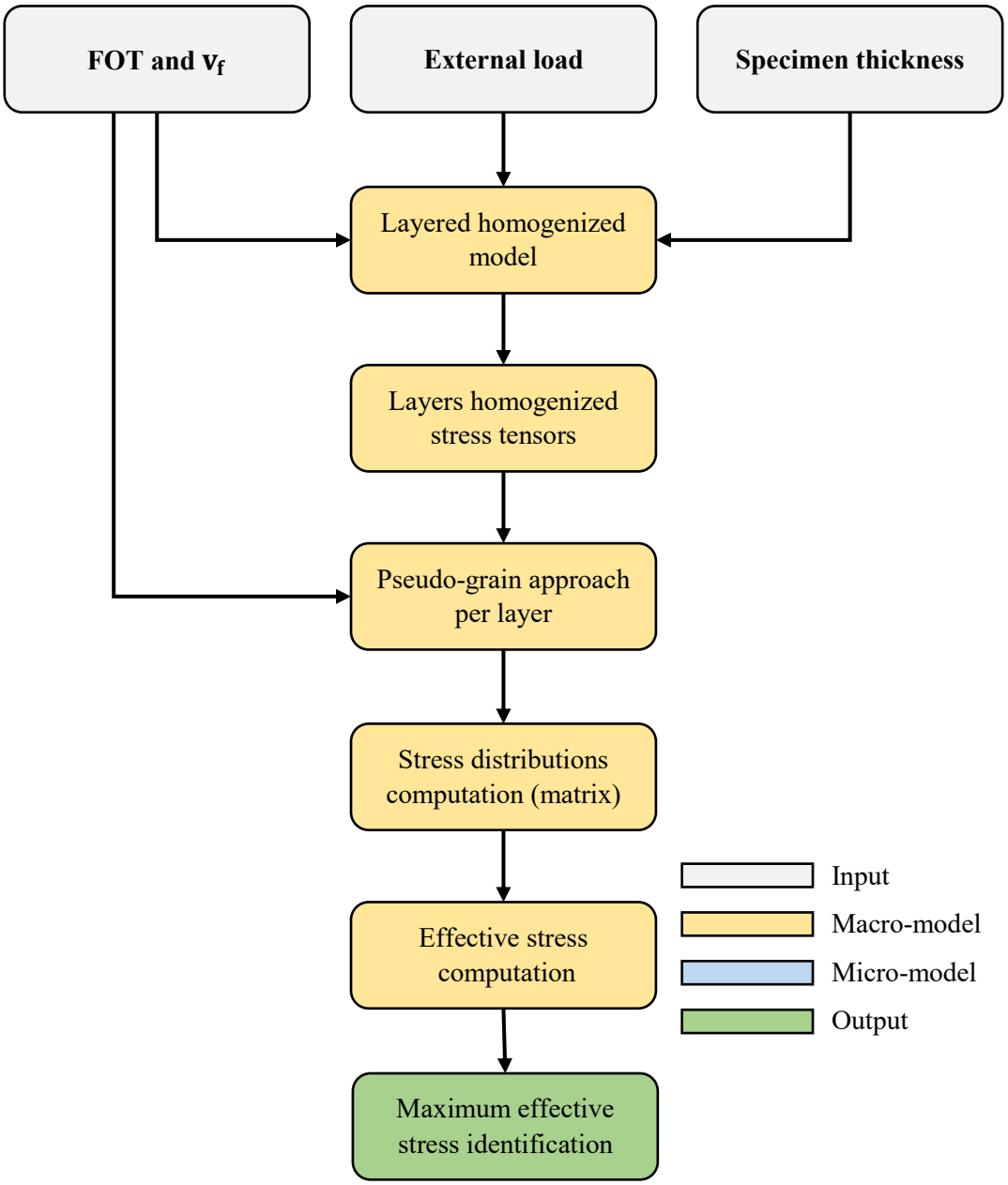

Figure 4.4. Flow-chart for computing the fatigue effective stress of a generic SFRT plain specimen.

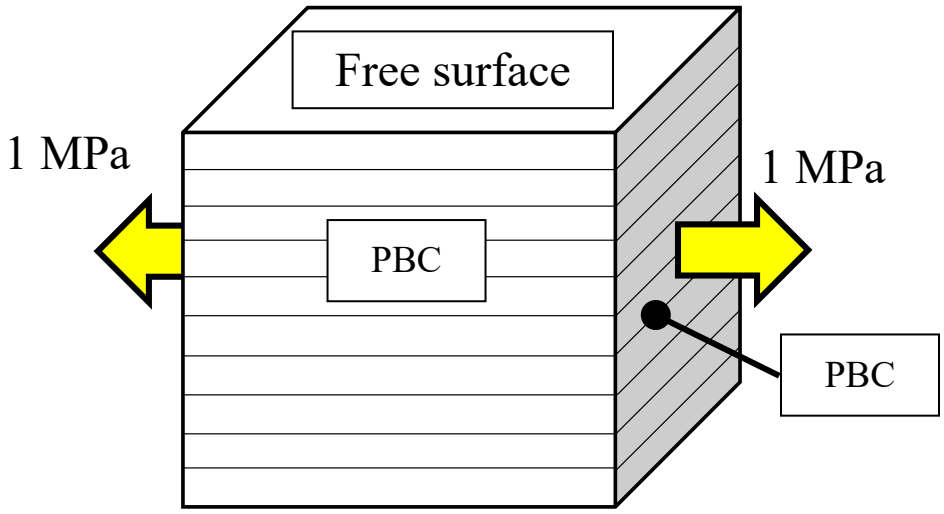

Figure 4.5. Example of layered macro-scale model for plain specimens.

The external stress tensor $\boldsymbol{\sigma}_{\text{ext}}$, which the model undergo, can be converted to an external strain tensor by means of the Hook's law:

$$\boldsymbol{\varepsilon}_{\text{ext}} = \mathbb{C}_{\text{macro}} : \boldsymbol{\sigma}_{\text{ext}} \tag{4.9}$$

where term $\mathbb{C}_{\text{macro}}$ identifies the stiffness tensor of the homogenized cell of Fig. 4.5, which can be numerically evaluated from the macro-model.

The proper elastic constants must be assigned to each sub-layer of the macro-scale model. In the present chapter, this is done by means of two-steps homogenization schemes (DOG06, MÜL15, PIE04, OGI17) that permit the computation of the stiffness matrix as a function of the FOT and v_f. As widely reported in the literature, this method is articulated in the following two steps:

i) Computation of the stiffness matrix for the so-called pseudo grains (PG), which are unidirectional cells oriented along discretized spatial directions;

ii) Computation of the final stiffness tensor components by averaging the previous UD stiffness matrices, weighted by the fiber orientation probability density function (FO-PDF) evaluated along the predefined orientations.

Regarding step i), the above mentioned spatial directions can be hereby identified by angles θ_u and ϕ_u, as it is shown in Fig. 4.6.

Therefore, the stiffness tensor components of the PG schematically represented in Fig. 4.6 must be computed for discrete angles.

Each PG is characterized by aligned fibers and its fiber volume fraction matches that of the material. The generation and solution of the single PG is hereby achieved by means of the finite element (FE) method, according to (PIE18). The reason why such a technique is adopted stems from the fact the same unidirectional FE model will be used later on for the computation of the micromechanical stress distributions within the composite matrix, as proposed by the authors (PIE18).

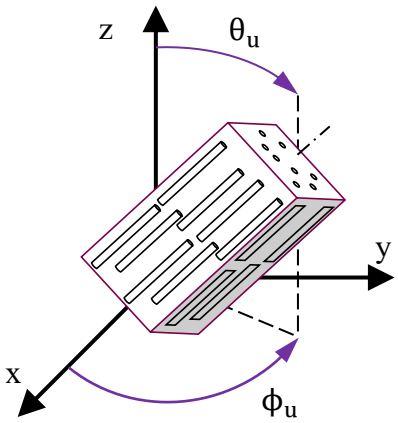

Figure 4.6. Schematic representation of a pseudo-grain rotated along its unit vector described by two angles (PIE18).

The components of the fourth-order stiffness tensor $\mathbb{C}_{PG}$ of the single PG can be derived once that two subsequent rotations of the global stiffness components are performed:

$$\begin{aligned}\mathbb{C}_{PG} &= C^{\phi}_{PG,mnop} e^{\phi}_m \otimes e^{\phi}_n \otimes e^{\phi}_o \otimes e^{\phi}_p \\ &= C^{l}_{PG,qrst} Q^{l}_{mq} Q^{l}_{nr} Q^{l}_{os} Q^{l}_{pt} e^{\phi}_m \otimes e^{\phi}_n \otimes e^{\phi}_o \otimes e^{\phi}_p\end{aligned} \tag{4.10}$$

$$\begin{aligned}\mathbb{C}_{PG} &= C^{g}_{PG,ijkl} e^{g}_i \otimes e^{g}_j \otimes e^{g}_k \otimes e^{g}_l = \\ &= C^{\phi}_{PG,mnop} Q^{\phi}_{im} Q^{\phi}_{jn} Q^{\phi}_{ko} Q^{\phi}_{lp} e^{g}_i \otimes e^{g}_j \otimes e^{g}_k \otimes e^{g}_l\end{aligned} \tag{4.11}$$

Therefore, combining Eq. (4.10) and (4.11), the $\mathbb{C}_{PG}$ components expressed in the global reference system read:

$$C^{g}_{PG,ijkl} = C^{l}_{PG,qrst} Q^{\phi}_{im} Q^{\phi}_{jn} Q^{\phi}_{ko} Q^{\phi}_{lp} Q^{l}_{mq} Q^{l}_{nr} Q^{l}_{os} Q^{l}_{pt} \tag{4.12}$$

Terms Q_{ij} indicate the components of the second-order rotation tensor $\mathbb{Q}(\mathbf{n}, \alpha)$, the expression of which is reported in the first chapter and in (PIE18). Symbols **n** and α respectively denote the axis (unit vector) and the angle of each rotation. Referring to Eq. (4.10)-(4.12), bases $\{e^{g}_{i}\}$ and $\{e^{l}_{i}\}$ stand for the global and the pseudo-grain coordinate systems and $\{e^{\phi}_{i}\}$ represents the bases of an intermediate coordinate system. The latter refers to the first of the two rotations that must be performed to migrate from the global to the pseudo-grain local reference system. The required coordinate system transformations are the followings:

- ϕ-rotation of $\{e^{g}_{i}\}$ around $[0,0,1]^{g}$. Thence, $\{e^{\phi}_{i}\}$ is obtained;
- $\left(\frac{\pi}{2} - \theta\right)$-rotation of $\{e^{\phi}_{i}\}$ around $[1,0,0]^{\phi}$.

Concerning the step ii), the computation of the stiffness tensor $\mathbb{C}_{layer}$ components can be performed for each sub-layer of the model and the equation reads:

$$\mathbb{C}_{layer} = \sum_{u=1}^{U} \mathbb{C}_{PG,u}\, \psi(\mathbf{p}_u)\, \Delta\mathbf{p}_u \tag{4.13}$$

In Eq. (4.13), $\psi(\mathbf{p_u})$ denotes the fiber orientation probability density function (FO-PDF), which is recovered from the FOT resorting to the equations of Advani and Tacker (ADV87). Symbol $\mathbf{p_u}$ is the unit orientation vector along witch the u-th pseudo-grain is rotated, as depicted in Fig. 4.6. Eventually, U quantifies the amount of PGs derived from the discretization of angles θ and ϕ.

Once the elastic constants of each layer are carried out, they can be assigned to the homogenized model of Fig. 4.5**.** The latter, that undergoes periodic boundary conditions emulating an external unit stress state, can be now solved. Eventually, the stress states read from the

solved macro-model can be employed as loads that must be applied to the micro-model that will be detailed in the next paragraph.

In order to better understand the complete workflow that has to be performed to achieve the layers' stress tensor, the reader may refer to Fig. 4.7, in which information concerning the involved software is also provided. Therefore, the latter reports the steps that have to be followed in order to obtain the Abaqus® output file (.odb), in which the solution information is stored.

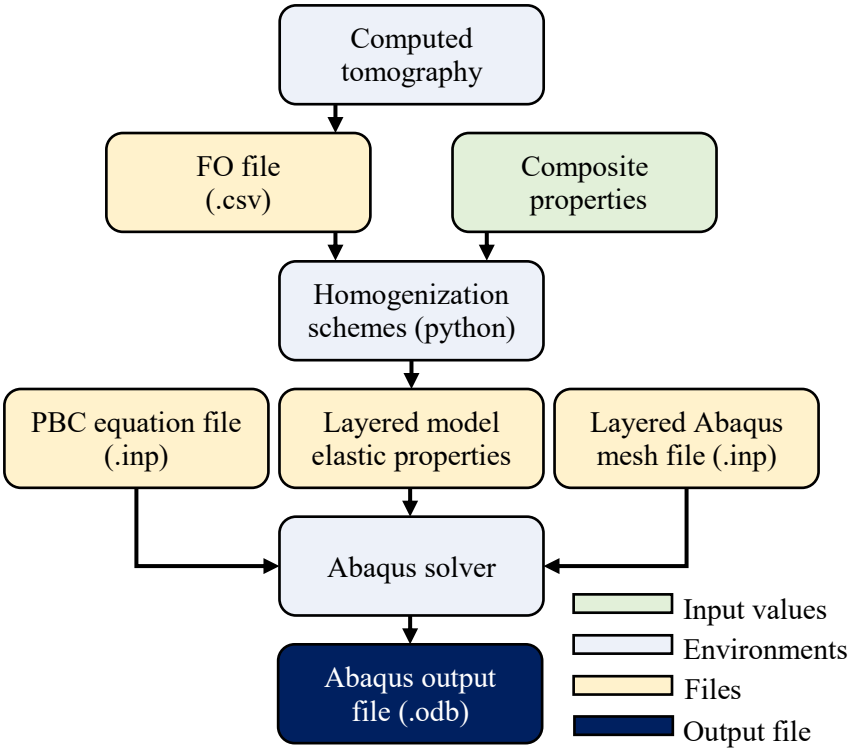

Figure 4.7. Macro-scale model solution workflow for plain specimens.

4.2.2 Micro-scale model

In this section, the steps that must be followed to obtain the matrix stress distributions of the macro-model layers are covered. As already said, the pseudo-grain methodology shall replace the generation and solution of a generic cell made of misaligned fibers and matrix.

As mentioned above, the matrix stress distribution of each layer is obtained by adopting the pseudo-grain approach presented in the chapter 3 and in PIE18.

The procedure to compute the stress distribution within the matrix of a generic microstructure corresponding to each sub-layer of Fig. 4.5 is the following:

- Identification of the FOT, fiber volume fraction and layer stress tensor of the macro-model (the v_f is assumed to be equal to the nominal fiber volume fraction of the entire composite);
- Generation of a unidirectional model (pseudo-grain) to which PBC must be applied. According to PIE18, the cell size is set to 0.4x0.15x0.15 mm^3, being 0.4 mm the dimension along fibers' direction. v_f corresponds to the nominal value;
- Computation of the Fiber Orientation Probability Density Function (FO-PDF) as a function of FOT, as explained in ADV87;
- Discretization of the angles of Fig. 4.6 and rotation of the pseudo-grain along all the unit vectors;
- Application of the same external strain tensor (chapter 3 and PIE18) to each PG (i.e. Voigt boundary condition) and solution. The cumulative density function is now computed for each PG;
- Computation of the desired matrix stress-CDF through the linear combination of pseudo-grain CDFs, by weighting them through the FO-PDF.

With this procedure, it is now possible to compute the cumulative distribution function (CDF) of any stress component within the matrix, without facing the multiple problems that may arise while generating, meshing and solving complex RVEs with misaligned fibers.

The pseudo-grain procedure has been implemented in Python and the computation of the matrix stress distribution of each layer can be achieved by referring to the flowchart of Fig. 3.3 and using the computed layers' stresses as inputs.

A schematic application of the workflow for computing $\sigma_{eff,max}$ is shown in Fig. 4.8. According to latter, once σ_{eff} is calculated for all layers of the macro-model (Fig. 4.5), the highest value among them is adopted as damage driving force parameter and used to plot the $\sigma_{eff,max}$-N curves to crack initiation, according to Eq. (4.8).

To sum up, the homogenized and anisotropic macro-model is firstly solved and, secondly, the layer FOT and stress tensor are adopted as input to the pseudo-grain method. The latter yields the Beltrami stress distribution of each layer and, after computing the effective stresses

of the whole layered model, the most critical value ($\sigma_{eff,max}$) can be individuated as used to re-express the fatigue nominal S-N curves. The effectiveness of the fatigue criterion would be then demonstrated in case all data fell within a narrow scatter band.

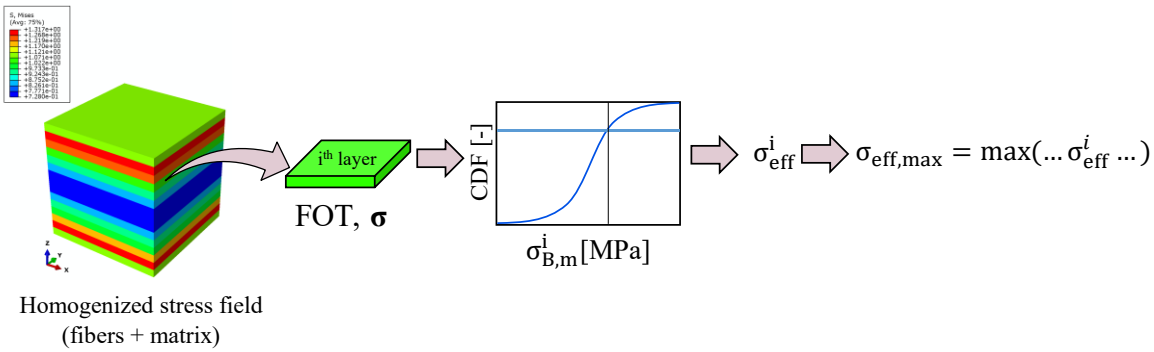

Figure 4.8. Schematic workflow of the multiscale model application to plain specimens.

Later on, data corresponding to different critical volumes will be shown and discussed.

4.4 Case studies

In this paragraph, more details related to the type of specimens that will be used for the validation of the proposed criterion are provided.

In chapter 2, a wide overview on the experimental tests that have been performed for this work have been presented.

It has already been mentioned that the application of the proposed fatigue model for plain specimens requires reliable information concerning the FOT estimated through-the-thickness and the corresponding fatigue S-N curves for the sake of validation. Not only data reported in chapter 2 will be used, but also some of them have been taken from the literature. A comprehensive overview of the used FOT and fatigue data is reported in Tab. 4.1.

Referring to Tab. 4.1, the adopted specimens' nomenclature recalls the one used in chapter 2 to identify the specimen geometry. An identification number has been furthermore added to differentiate specimens characterized by different cut-out angles or fiber volume fractions.

Table 4.1. List of employed plain specimens.

Name	Geometry	Material	FO	Mold	Machined	T	R	Source
P/A1	P/A	PA66-GF35	0°	80x80x1 mm³	✓	RT	0	DEM10_2
P/A2	P/A	PA66-GF35	30°	80x80x1 mm³	✓	RT	0	DEM10_2
P/A3	P/A	PA66-GF35	90°	80x80x1 mm³	✓	RT	0	DEM10_2
P/B1	P/B	PA66-GF15	90°	120x80x2 mm³	✓	RT	0	Chap. 2
P/B2	P/B	PA66-GF25	90°	120x80x2 mm³	✓	RT	0	Chap. 2
P/B3	P/B	PA66-GF35	90°	120x80x2 mm³	✓	RT	0	Chap. 2
P/B4	P/B	PA66-GF50	90°	120x80x2 mm³	✓	RT	0	Chap. 2
P/C1	P/C	PA66-GF15	0°	250x40x3 mm³	✗	RT	0	Chap. 2
P/C2	P/C	PA66-GF25	0°	250x40x3 mm³	✗	RT	0	Chap. 2
P/C3	P/C	PA66-GF35	0°	250x40x3 mm³	✗	RT	0	Chap. 2
P/C4	P/C	PA66-GF50	0°	250x40x3 mm³	✗	RT	0	Chap. 2

It must be pointed out that symbol FO of Tab. 4.1 denotes the extraction angle of a specimen with respect to the main flow direction. Symbol T indicates the temperature at which tests have been performed and, in particular, it can been seen that all of them have been carried out at room temperature (RT) and R denotes the load ratio, in this work kept equal to 0.

It is also highlighted that the considered specimens possess different geometrical characteristics and the efficiency of the proposed model relies on the choice of the proper FOTs.

The employed fiber orientation tensors are those reported in chapter 2. Concerning the through-the-thickness discretization of the model shown in Fig. 4.5, the original one obtained from the CT observations has been kept.

It must be highlighted that all fatigue data presented in Tab. 4.1 correspond to the lifetime of the specimens up to failure. Nevertheless, no significant crack propagation phases were observed during the tests on plain specimens, as it is stated also in BEL17. This implies that the fatigue curves can be interpreted as crack initiation data.

One more observation can be made concerning the application of the proposed model to specimens characterized by different extraction angles (Tab. 4.1). In case the out-of-diagonal components of the FOTs were neglected, significant errors could arise whether the specimens were extracted at 30° with respect to the MFD. This would be caused by the fact that a de-coupling between the diagonal and deviatoric components of the stress tensor could not be assumed anymore as valid, due to the strong anisotropy of the specimen layers. In this work, instead, the complete FOTs are involved for the computation of the homogenized stiffness tensors of model of Fig. 4.5 and the possible shear-coupling effects are taken into account for all different extraction angles. Therefore, models of specimens extracted at different angles are treated in the same manner.
Nevertheless, the proposed fatigue model does not take into account the actual gradient of the FOT components along the gauge length. More accurate models might be developed by reproducing the specimen actual geometry and by adopting higher order (fourth-order) FOTs for the estimation of the elastic properties.

4.5 Results and discussion

For what concerns fiber and matrix, the properties of both constituents have been reported in Tab. 4.2.

Table 4.2. Fiber and matrix properties for a short glass fiber-reinforced PA66.

$\mathbf{d_f}$ [μm]	$\mathbf{l_f}$ [μm]	$\mathbf{E_f}$ [MPa]	$\boldsymbol{\nu_f}$ [-]	$\mathbf{E_m}$ [MPa]	$\boldsymbol{\nu_m}$ [-]
10	275	72000	0.22	3000	0.39

In Tab. 4.2, the subscripts f and m respectively refer to fiber and matrix. Symbols d, l, E and ν denote diameter, length, Young's module and Poisson's ratio. According to Tab. 4.2, both constituents have been assumed to be isotropic.
Furthermore, the fiber volume fractions assigned to each material are listed in Tab. 4.3.

Table 4.3. Fiber volume fractions for the examined short glass fiber-reinforced PA66.

Material	PA66-GF15	PA66-GF25	PA66-GF35	PA66-GF50
$\mathbf{v_f}$ [%]	8	14	20	28

As already mentioned, concerning the homogenized model generation, the same discretization as the ones shown in chapter 2 is kept (each data-point in the FOT plots corresponds to a layer). As already said, the FOT components are expressed in the global reference systems of Fig. 4.6. Therefore, the unit external stress is rotated according to the cut-out angle, whether the specimens are extracted from plates. In case of geometry P/D, no rotation is required.

According to the flow-chart reported in Fig. 4.4, the effective stress, intended as driving force responsible for the fatigue damage, has been computed for each specimen, which in turn depends on the FOTs derived through CT scans and on the v_f. It has been widely discussed about the choice of evaluating such a mean stress component in a critical region surrounding the fibers. This has been achieved by setting different CFD thresholds (i.e. $V_{c\%}$) and computing σ_{eff}.

Eventually, the T_σ values are summarized in Tab. 4.4 for different CDF thresholds. It can be seen that the values of the scatter index do not exceed 1.30 for different values of $V_{c\%}$, this implying the robustness of the proposed criterion.

Table 4.4. Scatter indices of fatigue data after model application to plain specimens.

$\mathbf{V_{c\%}}$	10%	8%	6%	4%	2%
$\mathbf{T_\sigma}$	1.29	1.29	1.25	1.25	1.27

The fatigue data points expressed, firstly, in terms of nominal stress (Fig. 4.9) then of $\sigma_{eff,max}$ for different values of $V_{c\%}$% are shown in Fig. 4.10, in which the upper and lower solid lines respectively delimit a confidence interval between the 10% and 90% of probability of survival.

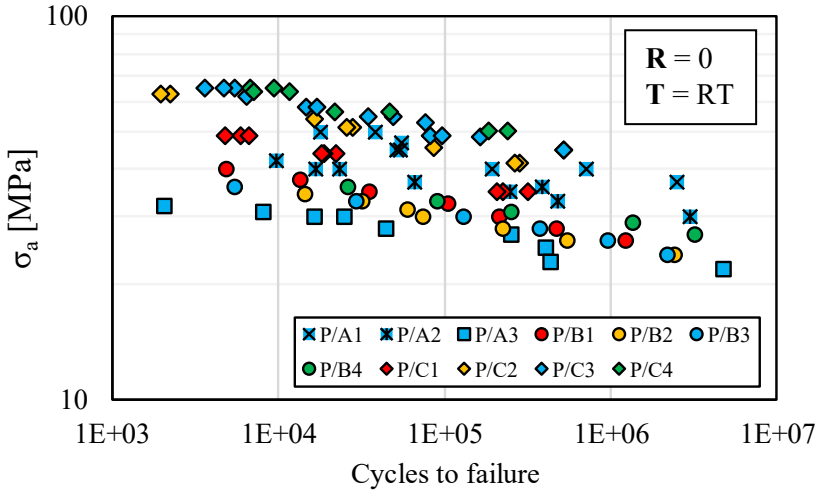

Figure 4.9. Fatigue data for plain specimens, expressed in terms of nominal stress.

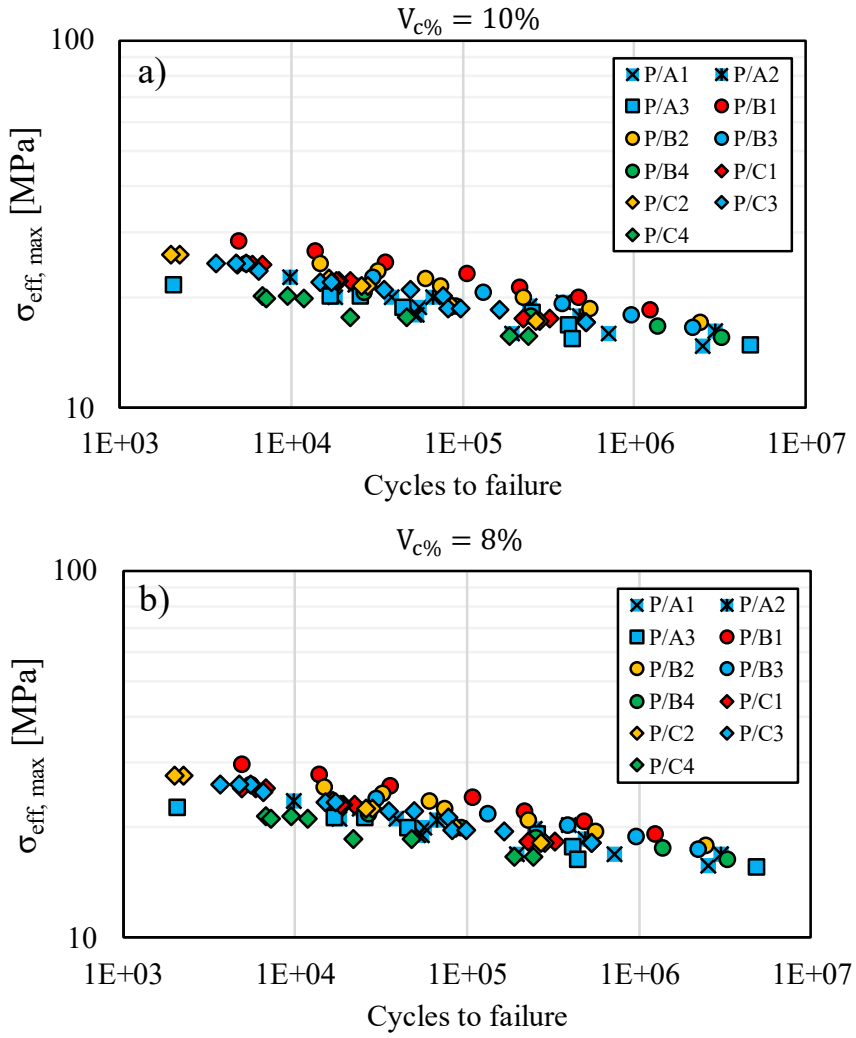

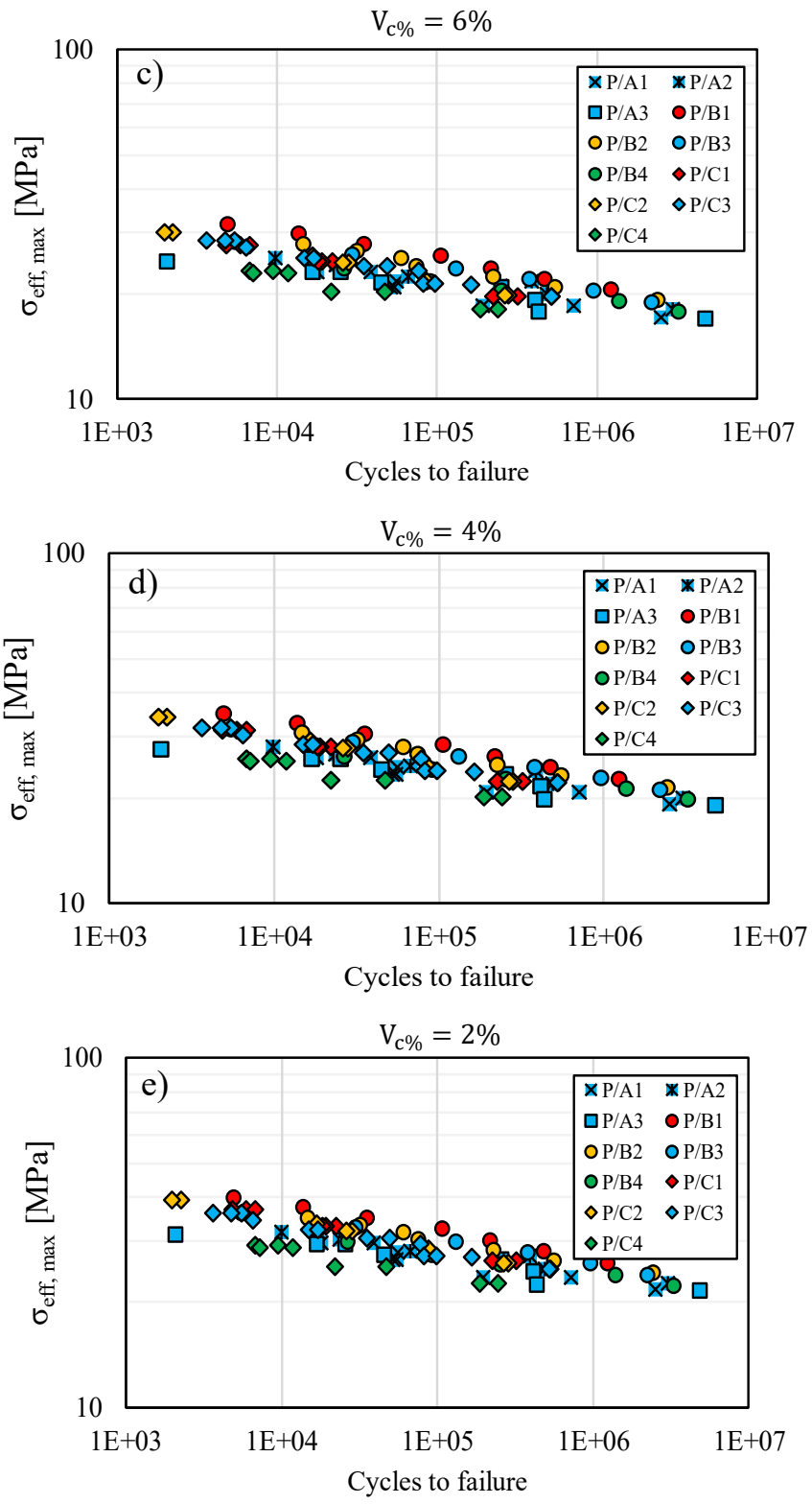

Figure 4.10. Fatigue data of plain specimens, expressed in terms of effective stress for different values of $V_{c\%}$.

The outcome of the proposed criterion consists in the possibility of choosing different values of $V_{c\%}$ in order to identify critical regions surrounding the fibers.
It is worth mentioning that the proposed criterion was specifically conceived for plain specimens, in which the macro-scale stress field is uniform or nearly uniform, so that a point-criterion can be adopted at the macro-scale (the macro-scale material point with the highest σ_{eff} values controls the crack initiation). In the presence of high stress gradients, caused by severe notches for instance, the present multiscale approach must be combined with a methodology to account for the effect of stress concentrations, as it will be done in chapter 5.
Eventually, it is also worth mentioning that specimens listed in Tab. 4.1 and used for the sake of validation are generically characterized by different geometries. Indeed, different specimen thicknesses (1 mm, 2 mm and 3 mm) and different shoulder radii (R12.5, R40 and R80) have been employed. Nonetheless, the application of the proposed approach revealed to be efficient for all specimens, even taking into account the effect of the local fiber orientation distributions and of the fiber volume fractions. Therefore, it can be stated that, as long as no strong geometrical variation is present, a simplified approach as the one presented in this chapter can be adopted with a good approximation, without paying attention to the actual specimen shape and dimensions.

4.5.1 Considerations on the critical section

Before concluding, it is worth making some considerations concerning the critical through-the-thickness section assumed to be responsible for the initiation of a macroscopic crack within plain specimens characterized by the skin-core effect. Fig. 4.11 reports the computed effective stresses (with $V_{c\%} = 10\%$) for geometry N/A, evaluated for each layer of the homogenized model (Fig. 4.5). The external applied stress is 1 MPa and therefore the effective stress is hereby denoted by $\overline{\sigma}_{eff}$.

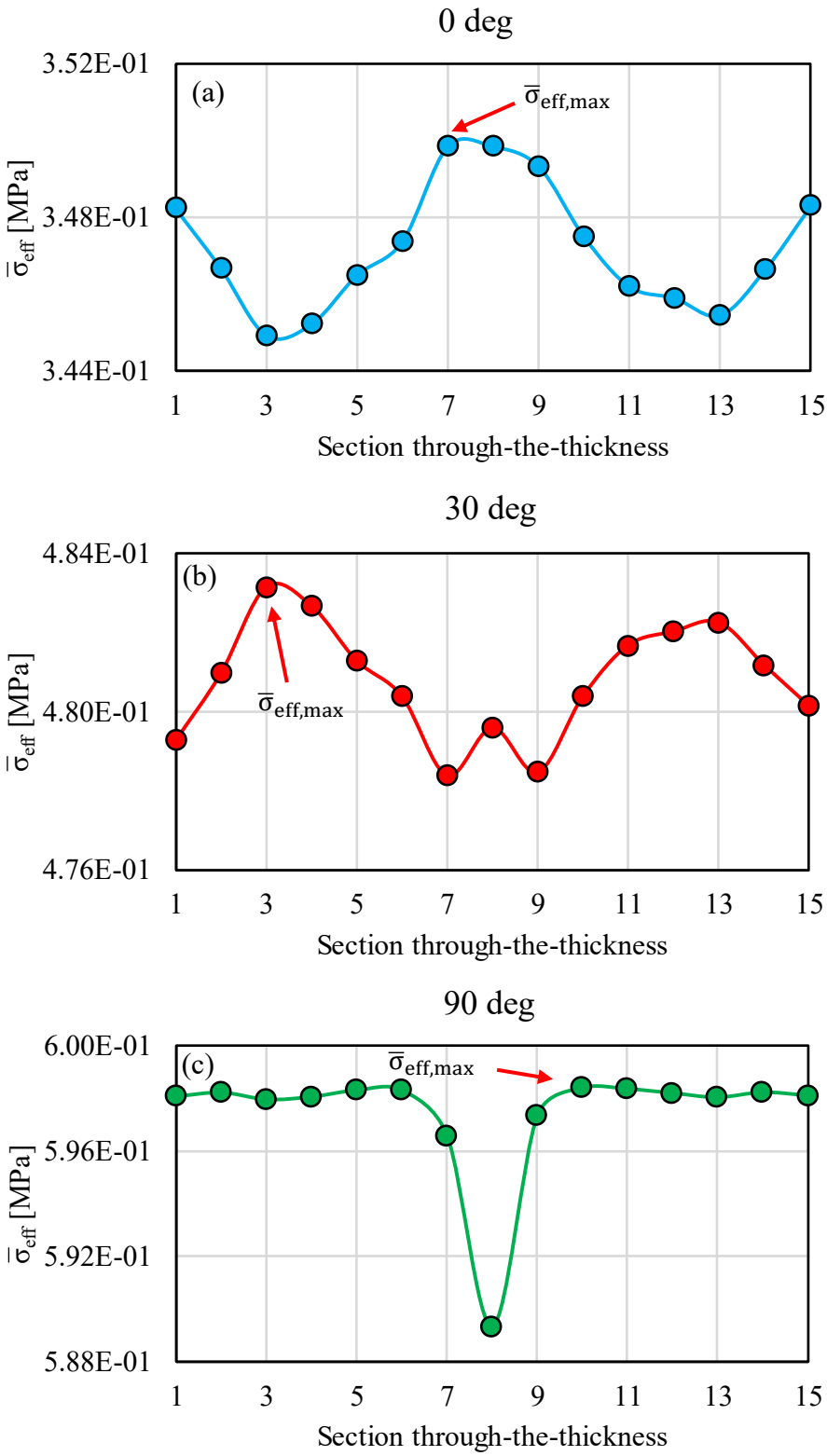

Figure 4.11. Through-the-thickness effective stress ($V_{c\%} = 10\%$) for geometry N/A, evaluated for three cut-out angles: 0° (a), 30° (b) and 90° (c). The external stress has been set to 1MPa.

In Fig. 4.11, the maximum value of the effective stress is highlighted. The latter identifies therefore the section in which the crack caused by the fatigue loading is supposed to start. Nonetheless, by observing the scale of the y axis, it can be stated that the obtained maximum effective stress can be considered approximately constant along the thickness direction. Therefore, relying on the σ_{eff} values resulting from the model application, it can be observed that the crack onset layer cannot be identified with absolute certainty.

4.6. Conclusions

In the present chapter, a multiscale model has been proposed to predict the effect of local fiber orientation, load direction and fiber volume fraction on the cycles to fatigue crack initiation in SFRT plain specimens. Based on the experimental observations, it has been possible to state that the fatigue damage mainly occurs within the matrix surrounding fibers. Due to the strong mulitaxiality that characterizes the specimen damage zones, a criterion based on the matrix stress distributions has been developed in order to carry out the fatigue damage driving force. It was possible to identify an effective stress responsible for the micro-scale damage accumulation by means of the Beltrami stress distribution within the matrix. The identification of the matrix critical regions has been performed by setting thresholds of the stress-cumulative density function within the matrix. Being the generation and solution of equivalent microstructures still a time consuming operation, the pseudo-grain approach proposed in chapter 3 has been employed for computing the matrix stress-CDFs. A bulk of experimental data (CT scans and fatigue curves) has been herein presented and used for validating the proposed fatigue criterion.

The proposed approach enables the prediction of the lifetime duration of plain specimens characterized by generic through-the-thickness FOT profiles, fiber volume fractions and external loads. This is done by computing a scalar fatigue parameter (effective stress) at the matrix level of the composite.

The efficacy and the robustness of the model have been demonstrated by obtaining low-scattered fatigue data for different Beltrami-CDF thresholds, once fatigue data for different materials have been displayed in terms of maximum matrix effective stress over the specimen thickness.

It is furthermore worth remarking that the proposed fatigue criterion cannot implicitly account for the effect of the fatigue mean stress. In case the proposed method were applied to different load ratios, it would be recommended to adopt the formulated fatigue criterion within each set of data characterized by the same load ratio. Empirical methodologies may also been applied later on to correlate the computed effective stress and the mean stress (e.g. MAL04) in order to predict the fatigue strength for various load ratios.

The proposed approach has been validated for dry-as-molded materials. In case of conditioned specimens, in the first place, the proposed model might be used only by changing (lowering) the elastic modulus of the thermoplastic matrix. On the other hand, the humid matrix results to be more ductile and the damage mechanisms interesting SFRT part might be different. Therefore, the proposed criterion might not be able to capture the previously discussed effects and further criterion modifications would be required.

Chapter 5

Fatigue model for notched specimens

5.1 Introduction

In this chapter, the fatigue criterion proposed for plain specimens in chapter 4 is extended to notched specimens and fatigue data reported in chapter 2 are used for validating the proposed fatigue model.

Because of the complex geometries characterizing the components' shape, some part sites become critical as a consequence of the presence of notches that may not be avoided. It is well known that notches consist in local strong geometry variation to which a part strength reduction is often attributed. In this work, only the fatigue strength of SFRTs will be treated. In this context, the aim of the present section can be outlined. Namely, a fatigue criterion simultaneously accounting for following effects is hereby presented and validated:

- Local fiber orientation distribution;
- Fiber volume fraction;
- Notch geometry.

In the literature, only a few works have dealt with the combined effects of the aforementioned parameters influencing the fatigue strength of the material and in most cases they have faced them separately.

It must be remarked that many works in the literature has stated that a perfect control of the fiber orientation during the injection molding process is not possible and a fiber orientation gradient is normally encountered within SFRT parts (DEM10, DEM10_2, DEM10_3, ZHO04, MOR15, BER06, BER12, ROL16, ROL18, BEL17, KLI11).

With regard to the presence of notches, a comprehensive study has been carried out by Belmonte et al. (BEL17), who created notched specimens made of polyamide 6.6 (PA66) reinforced with different fiber weight fractions (15wt%, 25wt%, 35wt% and 50%wt). Contrary

to most of the works, where notches are obtained by machining plates, the authors of BEL17 decided to insert a sharp slit into the mold, thus resulting in the "natural" formation of a notch. Additionally, in BEL17 the effect of fiber volume fraction onto the local fiber orientation distribution around the notch edges was analyzed thee-dimensionally, showing in average an enhancement of the fiber alignment along the main flow direction (MFD) by increasing the fiber content.

Moreover, Bernasconi et al. (BER15), created notched specimens without machining the notch geometry. In fact, they modeled a double V-notch mold and filled it with a PA6-GF30, longitudinally and laterally. The authors performed optical analyses at the net cross-section, quantifying the thickness average fiber orientation by means of the computed average angle cosines. In this interest, they observed that moving from notch to notch along the specimen width-direction, a relevant fiber longitudinal alignment could be detected nearby the notch tips.

With regard to the effect of fiber orientation onto the fatigue life of SFRTs, many authors have produced specimens extracted at different angles (BER07, DEM10_2) or directly injected from different gate locations (BER15) and then tested them under fatigue loading. All authors showed a neat decrease of the fatigue load bearing capability while reducing the fiber alignment with respect to the loading direction.

With reference to the effect of fiber content onto the strength of SFRTs, only few works have deeply dealt with it. In BEL17, the author carried out fatigue curves for sharply notched specimens, showing how the fatigue specimens' fatigue strength is enhanced by increasing the amount of fillers (i.e. fibers). In particular, the authors of BEL17 experimentally estimated the difference between crack initiation and propagation phases. Besides, they observed that the higher the fiber volume fraction is the lower the crack propagation rate is.

Concerning the effect of notch geometry, different authors have experimentally quantified the influence of the notch radius onto the fatigue strength. In BER15, Bernasconi et al. performed S-N curves for longitudinally and transversally injected specimens, having 0.5 mm, 1.0 mm and 2.0 mm radii and demonstrating how, respectively, the specimen becomes less resistant. The authors also highlight that the crack initiation phase is reduced while enlarging

the notch radius. Once again, the fatigue strength drop (tests performed up to specimen failure) of a PA66-GF33 specimen was shown by Zhou and Mallick (MAL04), who obtained circular notches by drilling holes with decreasing radii.

At this point, it must be remarked that SFRTs are often in contact with dangerous liquids (e.g. fuel in SON08) and possible leakages should be avoided. To this aim, the need of developing a fatigue criterion up to crack initiation emerges and therefore a local approach has to be developed and validated. Accordingly, Meneghetti and Quaresimin (MEN11) predicted the fatigue behavior of PA66-GF35 notched specimens by locally measuring the heat dissipation at the most critical sites (i.e. notch root).

In the literature, the attention on the modeling activity of SFRTs has been mainly emphasized with regard to plain specimens, developing criteria usually capturing the fiber orientation effect, without comprehensively taking into account the damage mechanisms occurring at the microscale. Accordingly, in BEL17_2 the stages previous to the crack onset in sharply notched specimens undergoing cyclic fatigue loading were analyzed. The authors showed indeed that damage mainly occurs at the matrix level within highly stressed matrix regions surrounding the fibers themselves. Accordingly, Arif et al. (ARI14) tracked the damage evolution within the matrix of a fiber reinforced thermoplastic and observed a diffused damage along fibers and at their tips by means of CT scans.

Being aware of the aforementioned factors affecting the fatigue life of a SFRT, particularly in the presence of notches, the thesis work aims at developing a multiscale fatigue criterion accounting for the relevant observed damage mechanisms evolving at the micro-scale. Analogously to the section about the plain specimens' model, the proposed model will cover the effect of local fiber orientation and fiber volume fraction by computing a matrix stress distribution based effective stress. Additionally, the notch geometry is here taken into account by applying an averaging concept inside a critical material volume, i.e. around the peak value of the defined effective stress. Within the next paragraphs, more details regarding the choice of the critical volume responsible for the crack initiation will be given.

5.2 Multiscale model

In this paragraph, the complete description of the fatigue model formulation and implementation is provided. As mentioned in the introduction, the aim of the present work concerns the development of a multiscale model enabling to capture the combined effect of local fiber orientation, fiber volume fraction and notch geometry. This will be done by computing the mean value of a matrix stress-based effective stress (σ_{eff}) in a critical volume, to which the crack initiation phase is attributed.

For the sake of clarity, the complete workflow that must be followed (Fig. 5.1) to compute the abovementioned average effective stress can be summarized through the following steps:

- Generation and solution of a homogenized and anisotropic macro-scale model, to which the proper external load has to be applied. This step can be performed by means of the sub-modeling technique. It must be reminded that, throughout this work, only linear elastic analyses will be carried out. Therefore, the computation of the proper driving forces responsible for the crack initiation can be referred to a normalized external load, i.e. to a unit external nominal stress.
- Solution of a micro-scale model for each element, by means of which a matrix-based effective stress is obtained and subsequent mapping of the carried out field onto the finite element (FE) model. In this step, the carried out homogenized stress tensors evaluated at the macro-level are used as boundary conditions to the micro-model, in combination with the FOT and fiber volume fraction information.
- Fatigue criterion formulation, i.e. application of an averaging concept within a critical volume surrounding the effective stress peak and computation of a mean effective stress, responsible for the crack initiation phase.

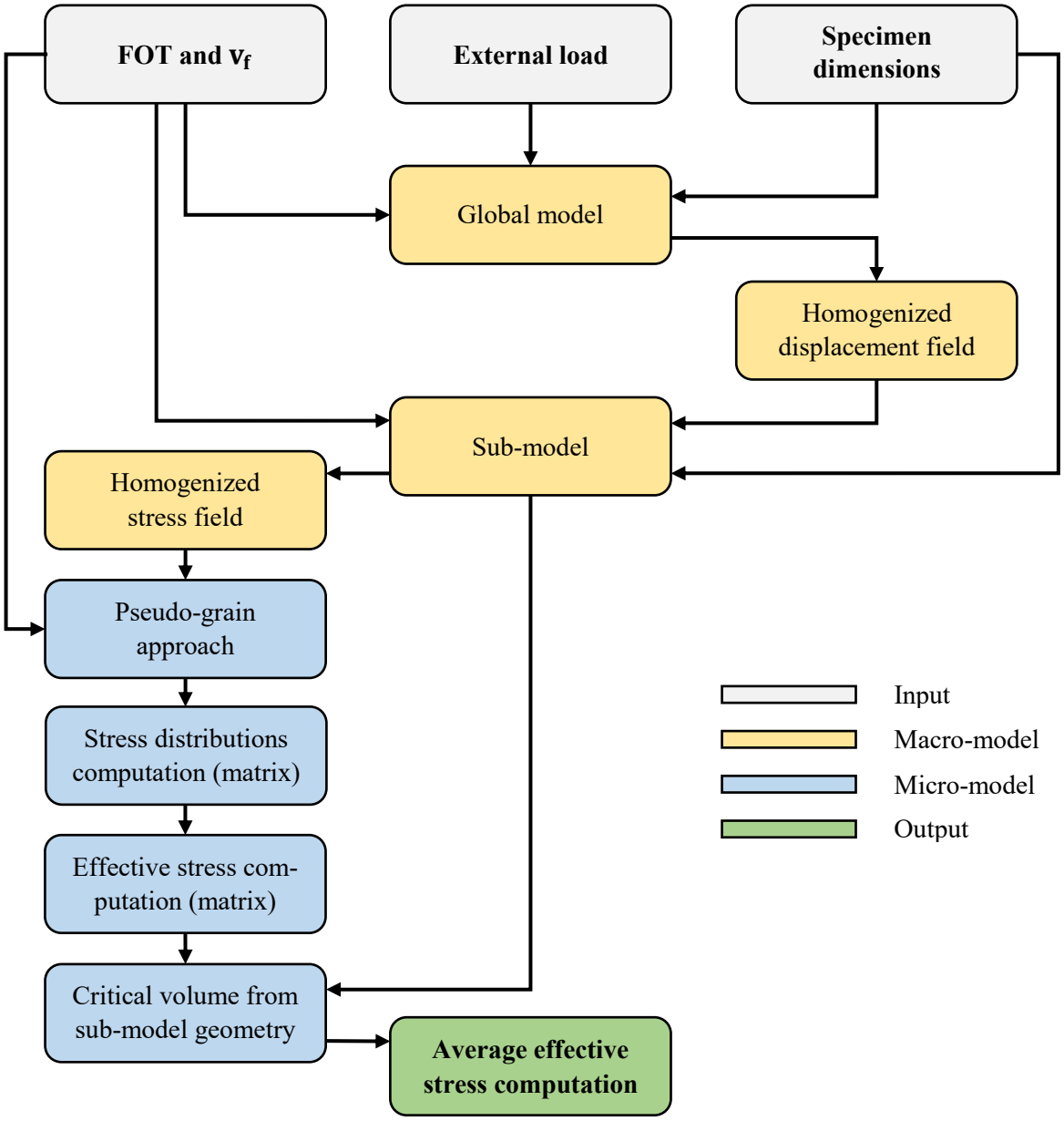

Figure 5.1. Flow-chart for the computation of the average effective stress responsible for the crack onset in SFRT notched specimens.

5.2.1 Macro-scale model

In this paragraph the formulation of the macro-model is described. The latter provides the inputs to the micro-model, which in turn permits the formalization of the fatigue criterion based on the micro-mechanical damage mechanisms.

The proposed macro-model can be subdivided into the following steps:

a) Generation and solution of a homogenized global model;
b) Generation and solution of a homogenized sub-model which inherits the boundary nodal displacement from global model solution;
c) Reading of the homogeneous macro-stresses.

Concerning point a), the entire specimen geometry has to be reproduced according to its actual dimensions (chapter 2). This operation is performed within the software Abaqus®, which will be also used for the model numerical solution.

As it was highlighted in the aforementioned points, the first step to carry out is the generation of the global model. Because of the strong anisotropy characterizing the considered specimens, the elastic properties have to be applied properly to the global model. In the most generic case, every element has its own elastic constants. The fourth-order stiffness tensor (Eq. 5.1) of a single mesh-element depends on the element's fiber orientation tensor (that may be derived from CT analyses or Moldflow® simulations) and fiber volume fraction.

$$\mathbb{C}_{el} = f(FOT, v_f) \tag{5.1}$$

The term $\mathbb{C}_{el}$ of Eq. (5.1) stands for the stiffness tensor of the single finite element.

Similarly to chapter 4, the fiber volume fraction is assumed not to vary within the specimen geometry and is set equal to the nominal one, which in turn is calculated by means of the constituents' density and weight fraction.

The process of assigning the proper stiffness tensor to each element is depicted in Fig. 5.2.

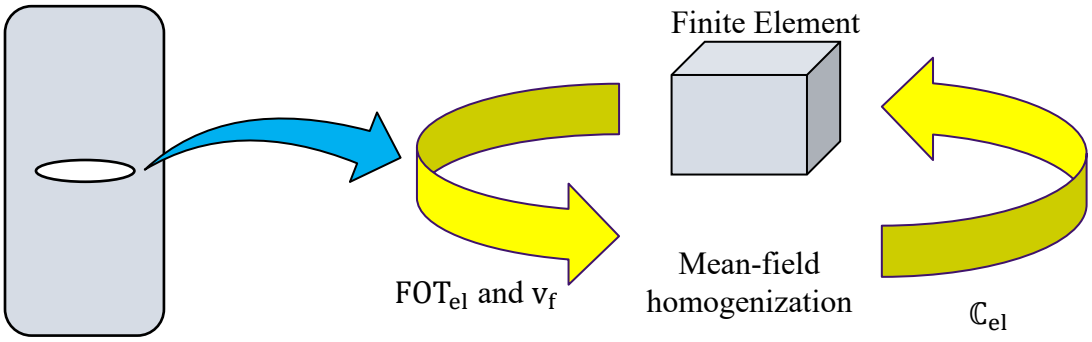

Figure 5.2. Homogenized elastic properties assignment to SFRT notched FE models.

From Fig. 5.2 it is clear that, once the single element that must receive the elastic constants is isolated, homogenization methods (TIA16, KAI14, MÜL15, BAB18, PIE18) have to be applied according to Eq. (5.1) in order to evaluate all entries of the anisotropic stiffness tensor. Term FOT_{el} of Fig. 5.2 identifies the fiber orientation tensor that has been attributed to the single FE element of interest. The same operation will be also repeated for the sub-model. As already mentioned, the global model undergoes a unit external nominal stress in order to obtained normalized results and once it is solve, the resulting displacement field computed in the region surrounding the notch root can be used as boundary condition to a sub-model (Fig. 5.3).

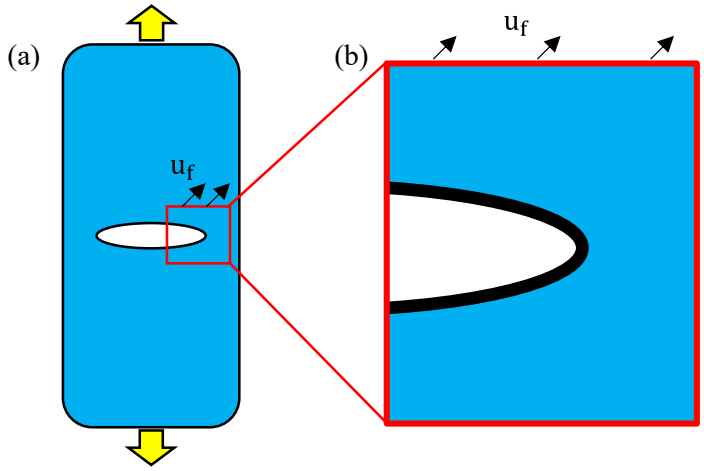

Figure 5.3. Schematic global model (a) and sub-model (b).

In Fig. 5.3, symbol u_f indicates the displacement field that is computed on the surfaces (in case of a 3D model) of the sub-model, depicted by the red square.

The motivation of generating a sub-model stems from the need of performing a finer mesh close to the notch tip, in order to better solve the stress field in the most critical homogenized volumes. With this technique, a finer mesh can be applied to the sub-model, still keeping acceptable computational times.

At this stage, the sub-model can be solved and the resulting homogenized stress tensors read for each element and used as inputs to the micro-model, the formulation of which will be detailed within the next paragraphs. It is worth remarking that the solved homogenous stress field does not distinguish between fiber and matrix, but is comprehensive of both. This aspect

differs from the micro-model definition, where only information carried out at the matrix level will be considered as relevant to the fatigue criterion formulation.

Nonetheless, Fig. 5.4 reports an example of a solved sub-model (geometry N/A of chapter 2), from which the stress tensor and the FOT can be read for the micro-model solution.

In Fig. 5.4, symbol $\boldsymbol{\sigma}_{el}$ represent the homogenized stress tensor of a single element.

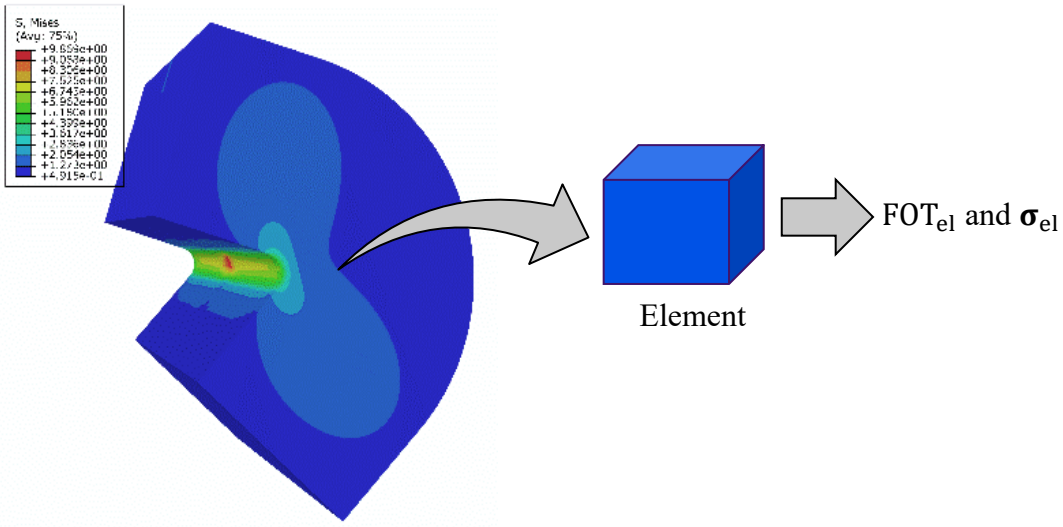

Figure 5.4. Example of a solved sub-model generated around the tip of a V-notch.

5.2.2 Micro-scale model

Once the solution of the homogenous model is obtained, the formulation of the micro-scale model can be now presented, which aims at providing information related to the matrix stresses relevant to the multiscale fatigue criterion formulation. With this step, the matrix stress distributions are computed at the micro-scale and will be later used to formulate the micro-mechanically based fatigue criterion. As mentioned above, the latter must take into account the effect of fiber volume fraction, local fiber orientation and notch geometry.

Analogously to the model for plain specimens, the solution of the macro-scale model is now used as boundary conditions to the micro-scale model. Nevertheless, differently from the plain specimens' model formulation where a schematic macro-geometry was created in form of RVE, the computation of the matrix stress distribution is now carried out for each mesh-

element. The reason of such a choice stems from the fact that stress concentrations, and therefore localized fatigue damages induced by the notch geometry must be accounted for. This step was not needed in case of plain specimens, where the fatigue damage was assumed to be equally distributed on the specimen plane and thence the specimen failure was attributed to the most critical section.

In the absence of the pseudo-grain (PG) approach previously presented, the computation of the matrix stress distribution for a generic element of the sub-model might be performed by generating an equivalent microstructure fulfilling the requirements of FOT and v_f. In Fig. 5.5, an example of the conceptual derivation of an equivalent microstructure is shown.

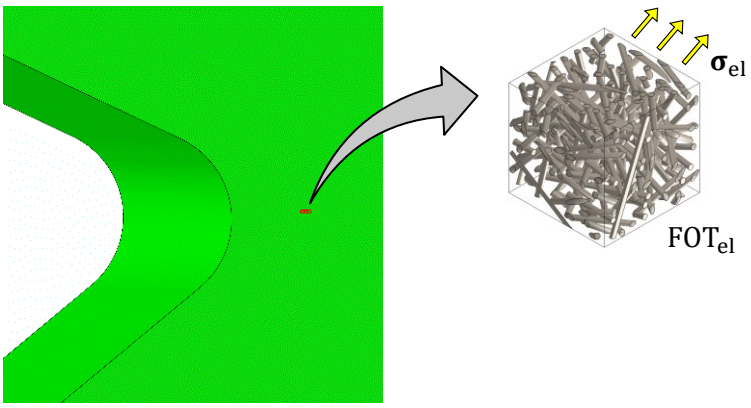

Figure 5.5. Schematic representation of multiscale modeling for notched specimens.

At this stage, the matrix stress distribution computation should be carried out at the matrix level of the equivalent microstructure (Fig. 5.5) of each finite element of the sub-model. Nevertheless, because of different issues related to the generation and solution of a generic heterogeneous volume element, the pseudo-grain methodology developed in the chapter 3 is hereby applied once again to compute the stress distributions for each element. More details about the stress components that will considered are reported within the next paragraphs while developing the fatigue criterion.

According to chapter 3, the pseudo-grain methodology requires the same inputs as the heterogeneous volume element shown in Fig. 5.5, i.e. FOT and v_f.

In particular, the attention will be payed to the computation of the matrix cumulative stress distributions, from which the effective stress (Fig. 5.1) is computed. In Fig. 5.6, the steps that

must be followed elementwise to compute the aforementioned cumulative functions are depicted.

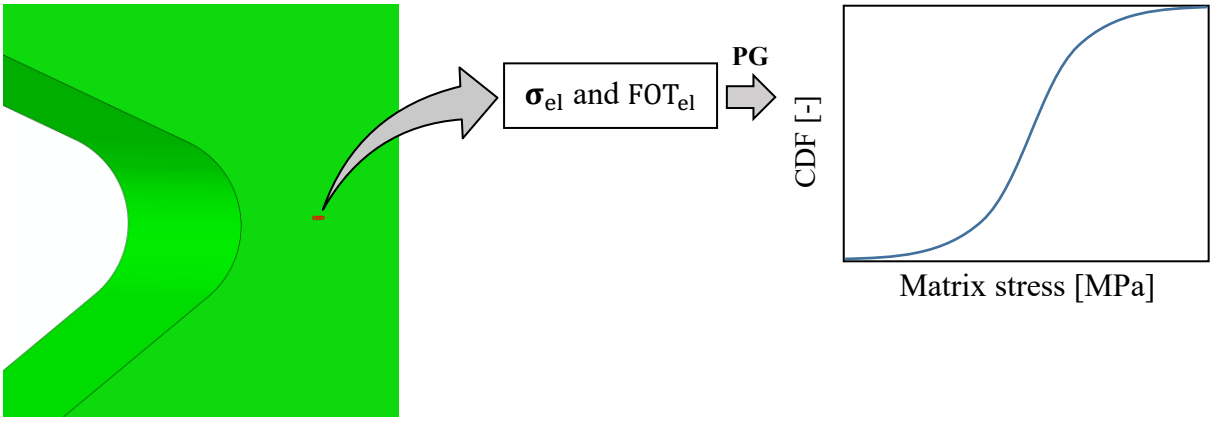

Figure 5.6. Schematic application of the PG approach to notched FE models.

5.3 Fatigue criterion formulation

In this section, the complete formulation of the fatigue criterion, which will applied to specimens with a generic notch geometry, fiber orientation distribution and fiber volume fraction, is presented. Particularly, the complete workflow that must be followed in order to carry out an average value of the effective stress responsible for the crack initiation in case of fatigue loading is hereinafter detailed. Eventually, the choice of the critical volume in which the crack initiation is assumed to occur is discussed.

Firstly, some assumption have to been done before formally formulating the procedure to follow:

- The damage mechanisms responsible for the crack onset are univocally attributed to the matrix level, therefore possible fiber failures are not considered;
- The abovementioned mechanisms do not affect the fatigue curves' slope. This means that non-linear effect causing a slope change are hereby not taken into account;

- The micromechanical damage nature only depends on the matrix properties and is independent of the local fiber orientation, fiber volume fraction and local stress state. Therefore, the effect of these three parameters is automatically taken into account while computing the matrix stress distributions.

Being aware of the points listed above, the choice of the effective stress based on the matrix stress distributions can be done. Similarly to chapter 4, a Beltrami stress (σ_B) is chosen in order to formulate the micro-mechanical fatigue criterion.

The reason of adopting such a stress component derives from the fact that it is closely related to the expression of the total strain energy. Indeed, the Beltrami stress carried out in the matrix reads:

$$\sigma_{B,m} = \sqrt{W_{tot,m} \cdot E_m} \tag{5.2}$$

Analogously to chapter 4, subscript m of Eq. (5.2) indicates that the calculation is done at the matrix level and terms W_{tot} and E respectively denote the total strain energy and the elastic of the considered constituent. Further details concerning the analytical formulation of the terms in Eq. (5.2) can be found in chapter 4.

According to Eq. (5.2), the Beltrami stress contains both dilatational and deviatoric contributions. This makes the proposed approach suitable to the case of short fiber-reinforced composites, the matrix of which undergoes a strongly multiaxial stress state as a consequence of the complex local orientation of the fibers, combined to the generically multiaxial macro-stress state deriving from the strong material anisotropy. The idea of describing the fatigue strength of a composite by means of the matrix stress state was also used in the work of Carraro et al. (CAR14) who correlated micromechanical stress components to the formation of macroscopic cracks in a continuous fiber lamina. Differently from that work, in the present section the fiber orientation cannot be considered as uniform within a certain region of interest and, furthermore, the effect of the fiber tip onto the local stress state perturbation is not negligible. For such a reasons, a fatigue criterion is hereby formulated in the most generic manner, considering the total energy contribution as responsible for the complex damage mechanisms occurring at the micro-scale level, among fibers.

Different authors observed that the fatigue damage mainly evolves within the SFRT matrix and, in particular, within volumes surrounding fibers (HOR97, KAB06, DEM10_3, KLI11, ARI14), i.e. along the fibers' wall and close the fibers' tip. The work of Belmonte at al. (BEL17) refers to the specimens geometry N/B. The authors focused on microscopic observation of damage mechanisms for a sharply notched specimen and they observed that the damage anticipating the crack onset can be considered as distributed around the aforementioned critical regions. For a better understanding, the mostly damaged regions are schematically shown in Fig. 5.7.

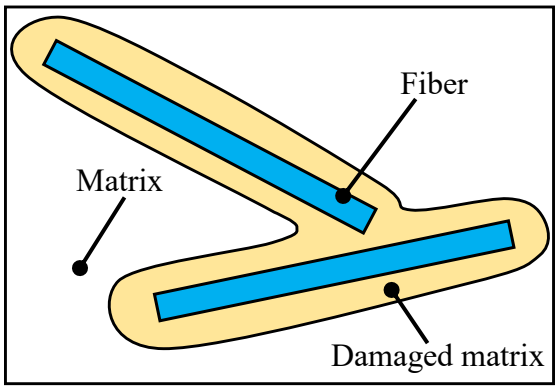

Figure 5.7. Schematic representation of damage evolution zones around fibers.

Assuming the schematic damage representation of Fig. 5.7 to be valid, a criterion can now be defined in order to carry out the effective stress involved in the matrix fatigue damage. It is thus decided to isolate the highly stress matrix volumes of Fig. 5.7 by considering the Beltrami stress distributions at the matrix level. Especially, the attention is focused on the cumulative distribution functions. Accordingly, the highly stressed matrix volumes can be identified by means of the tails of the Beltrami stress distributions, as it is depicted in Fig. 5.8.

By defining a threshold value of the cumulative stress distribution function, a method for isolating the most stressed region is thus defined.

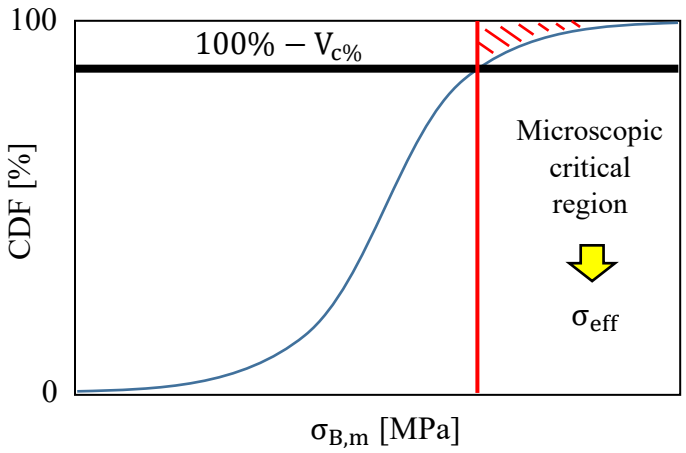

Figure 5.8. Matrix stress cumulative function and critical matrix regions identification.

After properly choosing the CDF threshold, the effective stress, responsible for the crack onset, is now calculated as the weighted average matrix Beltrami stress computed within the micro-scale critical regions identified by the CDF upper tail.

Referring once again to Fig. 5.6, the previously mentioned effective stress can now be evaluated for each mesh-element thanks to the stress state, FOT and v_f. The resulting σ_{eff} field can be displayed for the entire FE model (sub-model) and used for further developments of the fatigue approach.

According to Fig. 5.9, the complete workflow describing the achievement of the effective stress field is depicted. Nonetheless, it must be reminded that linear elastic stress components are computed.

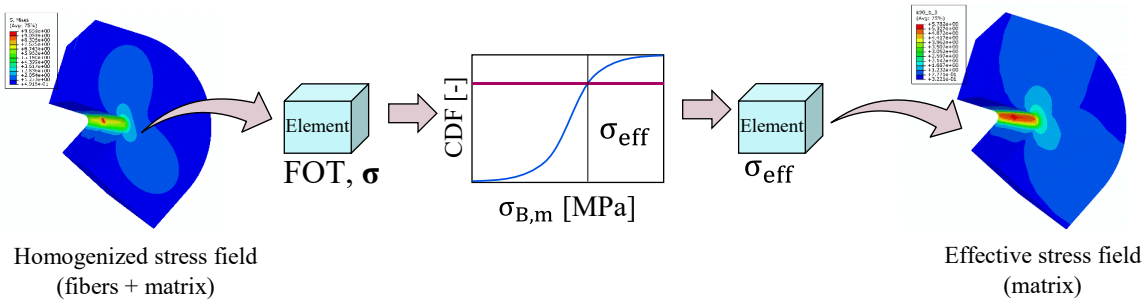

Figure 5.9. Effective stress computation workflow for notched specimens.

All treated fatigue data fall within the high cycle fatigue (HCF) range (between 10^3 and 10^6 cycles), this implying that high local plasticization is avoided.

Nevertheless, the presence of a notch concentrates the fatigue damage within a limited macroscopic volume around the notch tip, or alternatively, around the most critical mesh-element. In this context, the following assumptions are reasonably formulated:

- The crack initiation site is controlled the peak value of the effective stress;
- The crack onset phase is controlled by the average value of the effective stress, calculated in a critical macro-scale volume surrounding the most critical element.

According to the two listed assumptions, the shape of the critical volume is defined as spherical and is assumed to be centered on the effective stress peak computed at the notch tip.

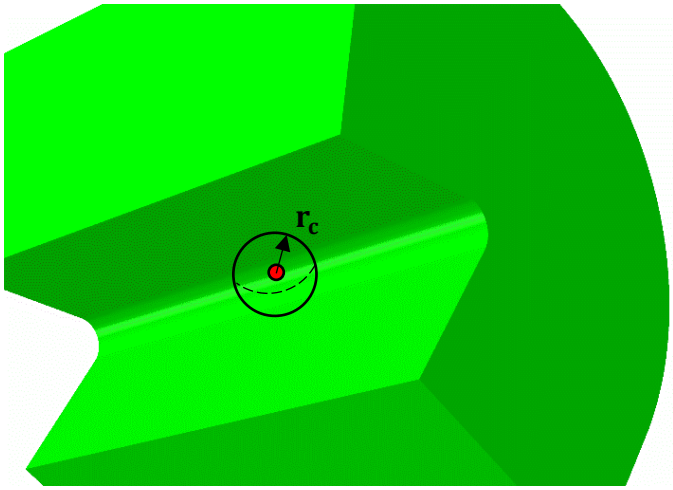

Figure 5.10. Example of spherical critical macroscopic volume at the notch tip of SFRT models.

Symbol r_c of Fig. 5.10 denotes the radius of the sphere isolating the macroscopic critical volume.

5.4 Definition of the critical radius

In this paragraph, the determination of the radius of the critical volume identified by the sphere of Fig. 5.10 is described.

Because of the complex nature of SFRTs, the determination of the critical radius as a material parameter could be an issue due to the difficulties of controlling the testing input parameters,

namely the local fiber orientation distribution. As it will be shown, the critical radius can be carried out by performing a model calibration with the aid of two specimens with different notch geometries or, alternatively, by means of a plain a notched specimen.

Before proceeding with the description of the algorithm that has to be followed for the obtaining the critical radius value, some parameters formulations need firstly to be explained. Symbol r will be hereinafter used to indicate a genetic radius of a sphere centered on the effective stress peak.

Be symbol $\langle\overline{\sigma}_{eff}\rangle_r$ the average value of the effective stress, computed within the volume identified by a sphere of radius r for an applied unit nominal tensile stress. With regard to the FE model, it reads:

$$\langle\overline{\sigma}_{eff,cycles}\rangle_r = \sum_{i=1}^{K_{el,r}} \sigma_{eff,i}\, V_i \tag{5.3}$$

where $\sigma_{eff,i}$ and V_i respectively denote the effective stress and volume associated to the i-th element of the mesh. Symbol $K_{el.r}$ indicates the amount of elements contained in the considered spherical volume of radius r.

As already anticipated, since only linear analyses are performed, the computation of the average effective stress is done only once per specimen. Thence, the calculation of the actual average σ_{eff} yields:

$$\langle\sigma_{eff,cycles}\rangle_r = \sigma_a \cdot \langle\overline{\sigma}_{eff,cycles}\rangle_r \tag{5.4}$$

Term σ_a of Eq. (5.4) indicates the nominal stress amplitude, typical of a Wöhler-curve.

Now considering the value of Eq. (5.4) for two generic different specimens (A and B), possibly with different notch geometries, the following error estimator can be defined:

$$\Delta_{AB}(r) = \left|\langle\sigma^{A}_{eff,cycles}\rangle_r - \langle\sigma^{B}_{eff,cycles}\rangle_r\right| \tag{5.5}$$

In Eq. (5.5), the subscript r is once again recalled to indicate that the computation of the terms is carried out within the volume of radius r.

The choice of the r_c is performed through a loop, the formalization of which is shown in Fig. 5.11.

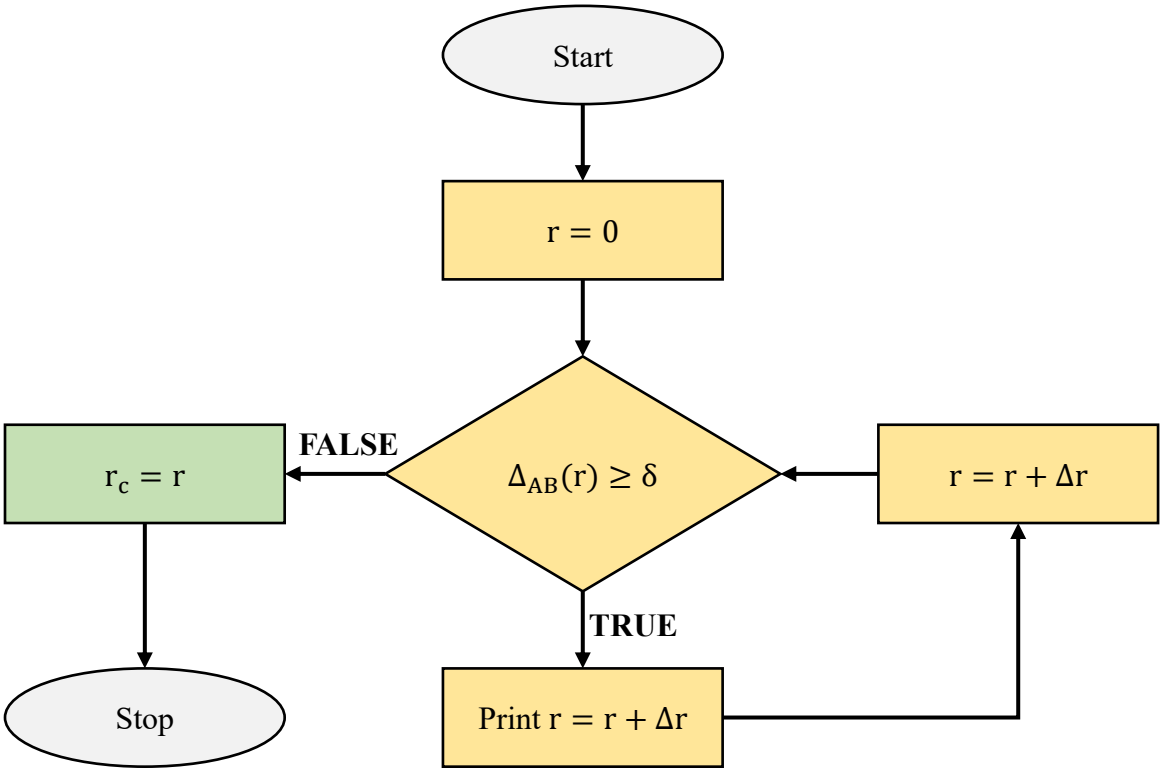

Figure 5.11. Calibration process and determination of the critical radius for notched specimens.

Eventually, Δr is used to indicate a small incremental value of r and δ is an error estimator. Once the critical radius r_c is carried out through the calibration process reported in Fig. 5.11, the carried out value can be used for other notch geometries, fiber volume fraction and local fiber orientation distributions.

It must be observed that the proposed methodology may be adopted not only to predict the fatigue curves of coupons, but also to estimate the fatigue lifetime of real parts undergoing similar conditions to the ones treated in this thesis work.

5.5 Case studies

At this stage, more information concerning the analyzed specimens is provided.
As it was already reported within the previous paragraphs, the proposed approach is suitable for the prediction of the fatigue lifetime of notched specimens, in particular for those undergoing fatigue loadings up to crack initiation. Indeed, fatigue data reported in chapter 2 are hereby used for the sake of validation and the corresponding FOTs adopted in order to properly assign the elastic properties to the developed FE models. Additionally, data presented by Belmonte et al. (BEL17) are employed to extend the model validation to other fiber weight fractions and notch-geometries.
In Tab. 5.1, a summary of the used data set is shown, reporting details regarding the specimens' dimensions and fiber content. Symbols FO, r_{notch}, T and R of Tab. 5.1 respectively denote the main fiber orientation, the notch radius, the temperature at which tests have been conducted and the load ratio.
More information related to the specimen geometries and fatigue strength has been reported in chapter 2.
The elastic properties' assignment has been differentiated between coupons that were machined out of injection-molded plates (geometries N/A and N/C) and those obtained by shaping the notch geometry with a metallic insert (N/B and N/D).
With reference to the geometries listed in Tab.1, the procedure that has been followed for obtaining the macro-model is hereinafter presented.

Table 5.1. Summary of the considered notched specimens for the model validation.

Name	Material	FO	r_{notch}	Mold	Machined	T	R	Source
N/A1	PA66-GF15	0°	0.1 mm	120x80x2 mm³	✓	RT	0	Chap. 2
N/A2	PA66-GF35	0°	0.1 mm	120x80x2 mm³	✓	RT	0	Chap. 2
N/A3	PA66-GF50	0°	0.1 mm	120x80x2 mm³	✓	RT	0	Chap. 2
N/A4	PA66-GF15	90°	0.1 mm	120x80x2 mm³	✓	RT	0	Chap. 2
N/A5	PA66-GF35	90°	0.1 mm	120x80x2 mm³	✓	RT	0	Chap. 2
N/A6	PA66-GF50	90°	0.1 mm	120x80x2 mm³	✓	RT	0	Chap. 2
N/B1	PA66-GF15	0°	0.2 mm	250x40x3 mm³	✗	RT	0	BEL17
N/B2	PA66-GF25	0°	0.2 mm	250x40x3 mm³	✗	RT	0	BEL17
N/B3	PA66-GF35	0°	0.2 mm	250x40x3 mm³	✗	RT	0	BEL17
N/B4	PA66-GF50	0°	0.2 mm	250x40x3 mm³	✗	RT	0	BEL17
N/C1	PA66-GF35	0°	2 mm	80x80x2 mm³	✓	RT	0	Chap. 2
N/D1	PA66-GF35	0°	5 mm	250x40x3 mm³	✗	RT	0	DEM08

5.5.1 Global model generation

According to Fig. 5.1, before solving the sub-model to which the fatigue criterion is applied, the solution of the global model has to be achieved. In this section, two different techniques are presented:

1) Concerning those specimens the shape of which corresponds to the mold shape and where the notch is not obtained by removing material, the workflow described in Tab. 5.12 is adopted. The generation and solution of the global model takes place within different environments. Indeed, different software are involved, namely Moldflow® for process simulations, Digimat® for assigning material properties to the model and Abaqus® to obtain the model solution in terms of homogenized stress fields. With

regard to the first steps of Fig. 5.12, the proper process parameters (pressure, temperature, material velocity, etc.) must be properly defined according to the actual ones adopted for injecting the molds. Subsequently, once the solution of the software Moldflow® is reached, the fiber orientation tensors, i.e. the process simulation outputs, are provided to Digimat® in order to carry out the elastic properties that are later attributed to the Abaqus® model. Once the proper loading conditions are defined and given to the FE solver, the solved file containing the complete stress field is obtained. It must be highlighted that, because of the fully 3D process simulation, the resulting model has elastic properties generally varying along all directions. With reference to Tab. 5.1, the procedure described in Fig. 5.12 can be therefore applied to specimens N/B and N/D.

2) The second adopted technique can be used for specimens extracted from injection-molded plates, in which the variation of the FOT component on the xy plane can be neglected with regards to the through-the-thickness one.

   The generation and solution of the global model is detailed in the flow-chart of Fig. 5.14. Since no particular FOT gradients are present, the specimen geometry can be reproduced by means of a layered model (Fig. 5.15).

   According to Fig. 5.14, once the through-the-thickness FOT components are identified, homogenization schemes can be used to properly assign the elastic constants to the modeled geometry. In this step, the use of other external software (Digimat®) useful for attributing the elastic properties to the FE model is not required anymore. Indeed, the analytical homogenization formulations have been simply implemented through Python® scripting.

   Eventually, the layered FE model can be solved and the homogenized stress field can be read from the Abaqus® .odb file.

   As already mentioned, the detailed model generation and solution can be employed for those specimens that are extracted from plates and, therefore, for the specimens geometries N/A and N/C listed in Tab.5.1.

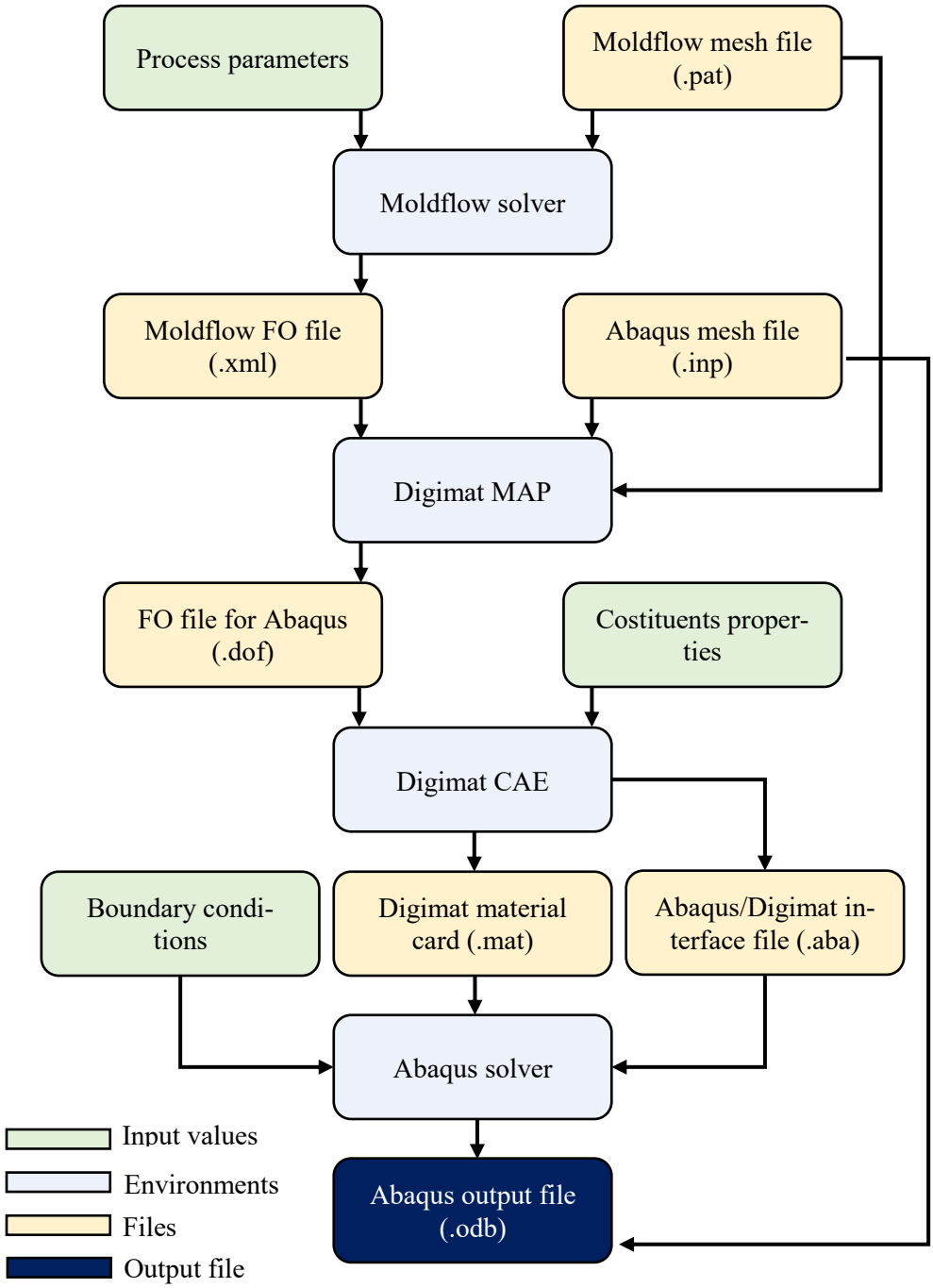

Figure 5.12. Macro-model solution workflow for notched specimens, estimating FOTs with Moldlfow®.

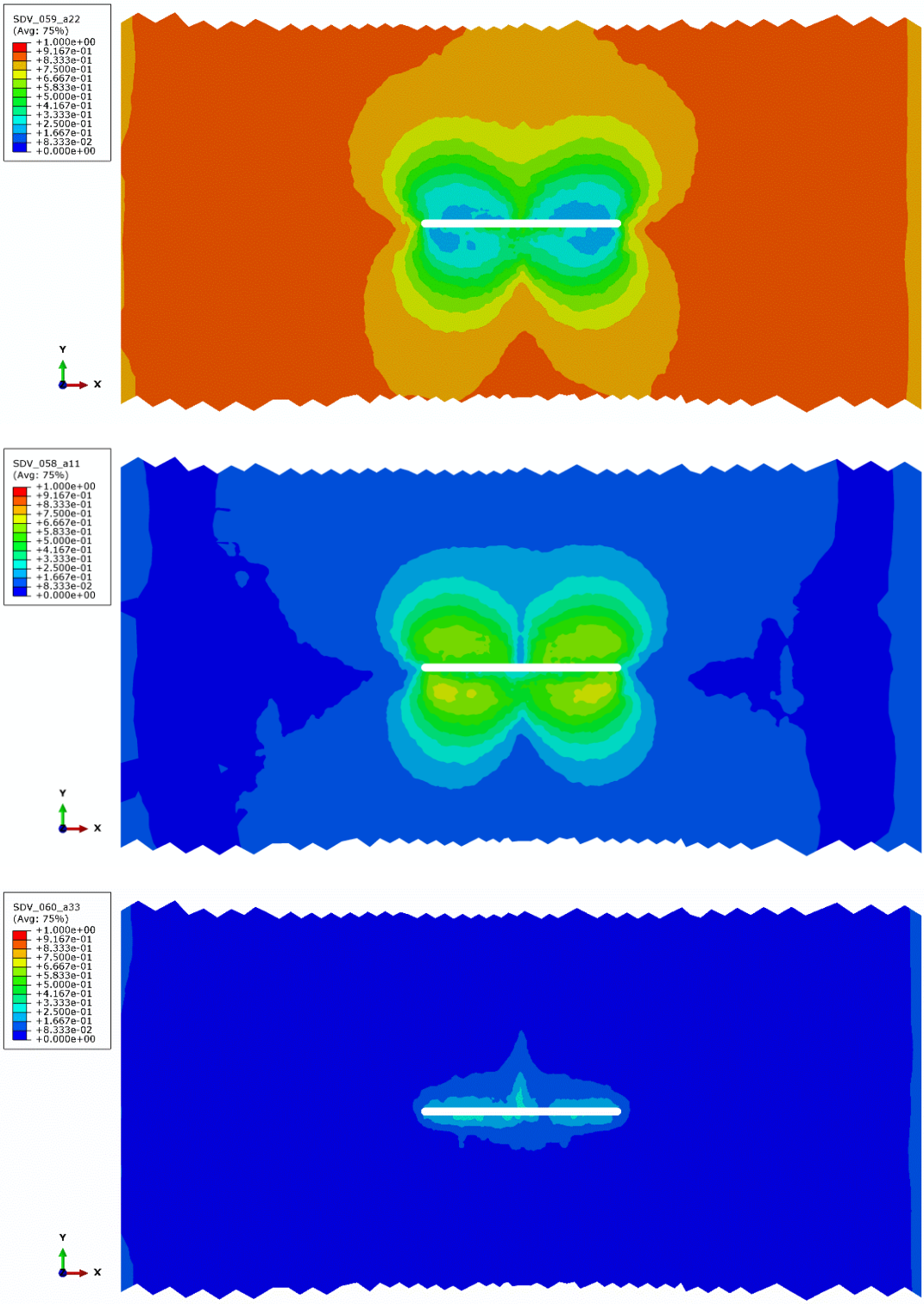

Figure 5.13. Example of FOT components resulting from Moldflow® near the notch of specimen N/B3 of Tab. 5.1**.**

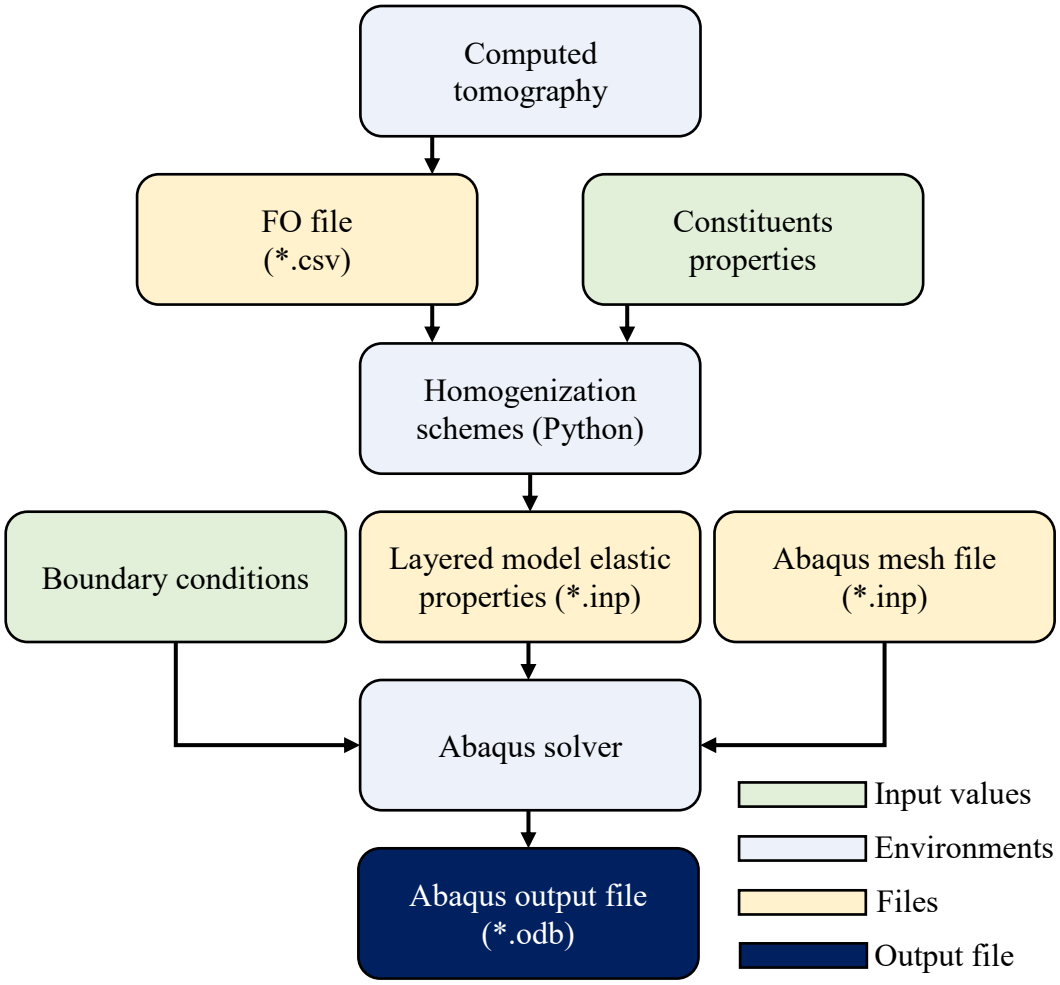

Figure 5.14. Layered macro-model solution workflow for notched specimens, evaluating FOTs with CT scans.

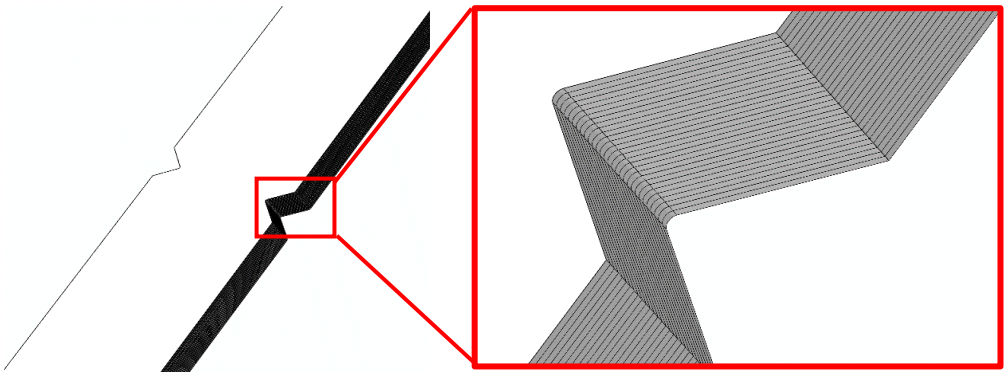

Figure 5.15. Layered FE model generated in Abaqus®.

5.5.2 Sub-model generation

With regard to the generation and solution of the sub-models, the geometries reported in Fig. 5.16 have been created and subsequently solved by applying the nodal displacements derived from the global models' solution as boundary conditions.

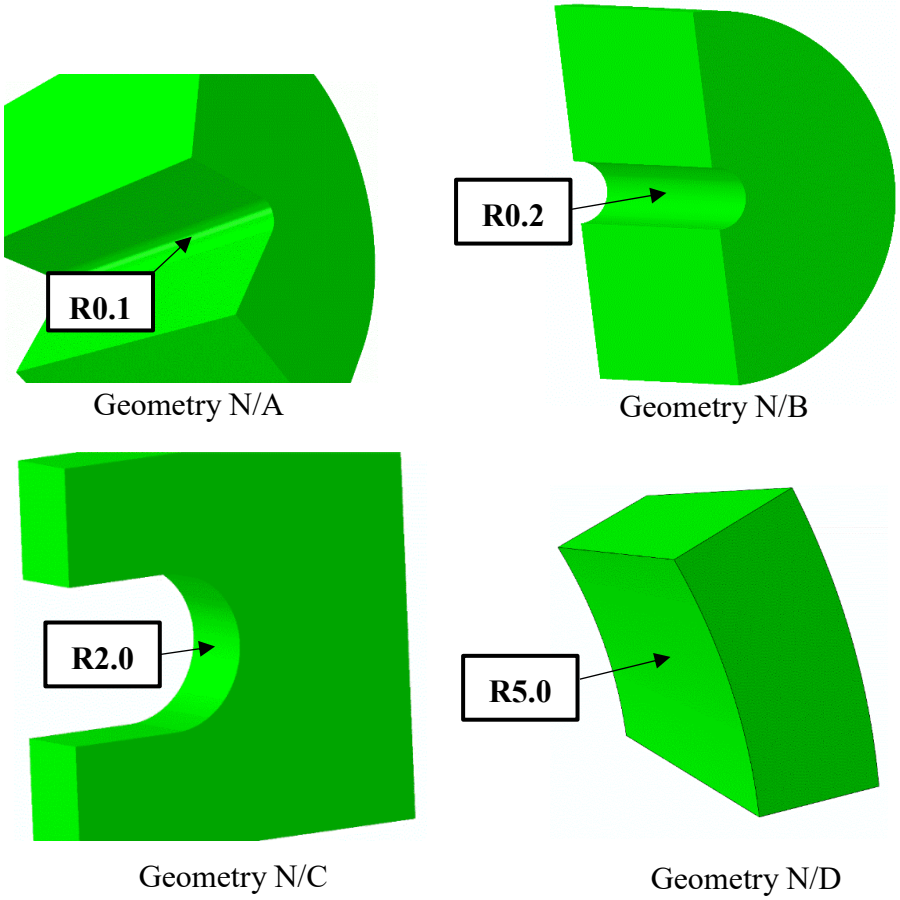

Figure 5.16. Sub-models for notched specimens listed in Tab. 5.1.

In this section, three type of sub-model properties and boundary conditions assignments are presented:

a) The first case regards specimens of geometries N/B and N/D. The same procedure as the one detailed in Fig. 5.11 is adopted. Namely, the FOTs are estimated through process simulations. Concerning the application of the boundary conditions, the

nodal displacements obtained from the global model described at point (1) of section 5.5.1 (Fig. 5.12) are used.

b) The second case, that will be employed only for geometry N/B, consists in using the FOTs obtained through CT scans at the notch root of the specimens of interest. On the other hand, the nodal boundary displacements still derive from the global model type described at point (1) of section 5.5.1 (Fig. 5.12). The procedure to solve such a model is depicted in Fig. 5.17. Furthermore, a comparison between the CT observation grid and the structural FE model is shown in Fig. 5.18.

c) The third procedure will be exclusively adopted for specimen type N/A and N/C. In this case, the coupons have been extracted from injection-molded plates and no significant fiber orientation gradients are expected on the xy plane. Therefore a layered sub-model is created according to the method described at point (2) of section 5.5.1 (Fig. 5.14). The boundary conditions are obtained from the solution of a global model, the properties of which are assigned in the same manner (Fig. 5.14).

Before proceeding with the application of the developed fatigue criterion, some considerations must be done with regards to the presented sub-modeling techniques (a, b and c).

For method (a), the following considerations can be done:

- A reduced effort is required in order to detect the complex fiber orientation around the tip of notches shaped by means of a metallic insert;
- Less accuracy on the FOT prediction in the elements close to the notch edge is achieved.

Concerning method (b), it can be stated that:

- High accuracy on the FOT assignment is encountered;
- There might be errors induced by the nodal displacements discontinuities between the global model (whose properties derive from Moldflow® FOTs) and the sub-model (whose properties derive from the FOT evaluated through CT scans).

Instead, with regards to method (b):

- The elastic properties assignment relies on a simple method, since the stiffness matrix has to be computed only for few layers (Fig. 5.15).
- Information related to FOT variation on the xy plane is lost.

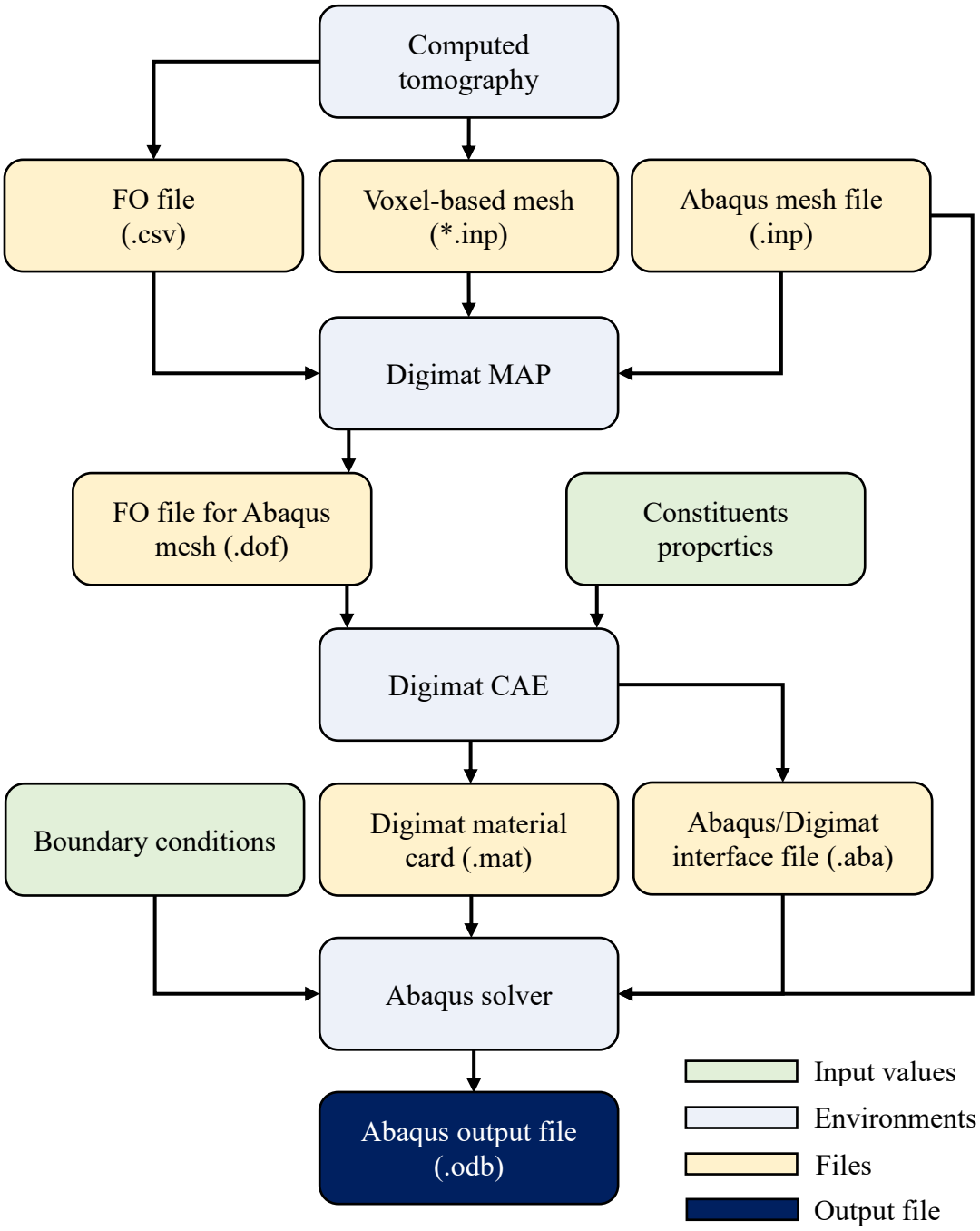

Figure 5.17. Macro-Model solution starting from CT scans, considering three-dimensional FOT variations.

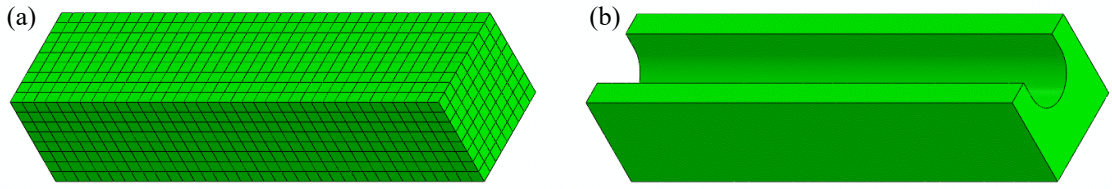

Figure 5.18. CT scans' grid (a) and Abaqus® sub-model (b) for geometry N/B.

Once the sub-model is numerically solved, it is possible to proceed with the application of the multiscale fatigue criterion according to workflow shown in Fig. 5.9 and with the identification of the critical radius of the macroscopic spherical volume centered on the peak of the effective stress (Fig. 5.10 and 5.11).

5.6 Results and discussion

In this paragraph, the results deriving from the application of the proposed fatigue criterion to specimens characterized by different notch geometries, fiber volume fractions and fiber orientation distributions are reported. According to chapter 3, $V_{c\%}$ is set to 10%.
Three examples of validations are reported in this section. Firstly, the fatigue raw data of the considered notched specimens are reported in Fig. 5.19.

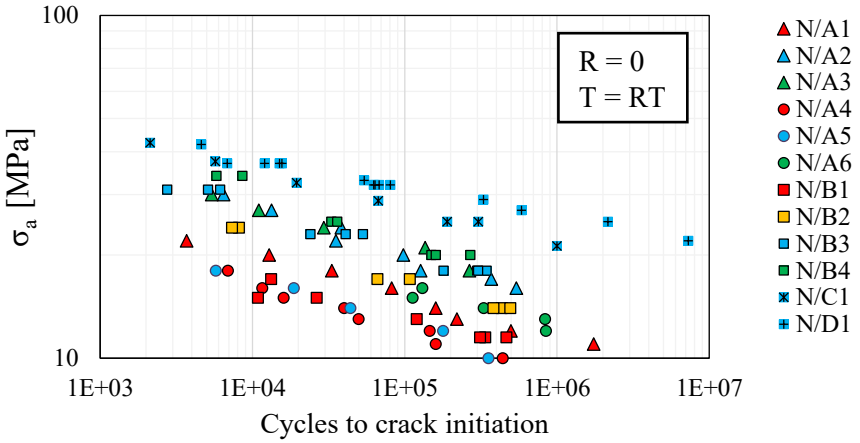

Figure 5.19. Collection of considered fatigue raw data for notched specimens (Tab. 5.1).

5.6.1 Example 1

For this first example of model validation, the following methods have been adopted for the considered specimen notched geometries:

- Geometries N/A and N/C: the fiber orientation tensor components have been obtained through CT scans. Therefore procedure of Fig. 5.14 has been adopted both for the global and the sub-model;
- Geometries N/B and N/D: FOTs have been obtained by means of Moldflow® simulations either for the global model either for the sub-model (Fig. 5.12).

The calibration process is shown in Fig. 5.20 and the obtained critical radius is equal to 0.15 mm. The specimens used for the calibration are two notched specimens, i.e. N/B3 and N/C1. Fatigue data expressed in terms of the average effective stress responsible for crack onset are shown in Fig. 5.21.

As it can be observed in Fig. 5.21, the fatigue strength of the considered specimens is predicted correctly. It is worth mentioning that the calibration phase has been performed by considering specimens with the same fiber volume fraction, with different geometries and that they are now sufficient to predict the fatigue response of other fiber volume fractions and notch shapes (milder and sharper).

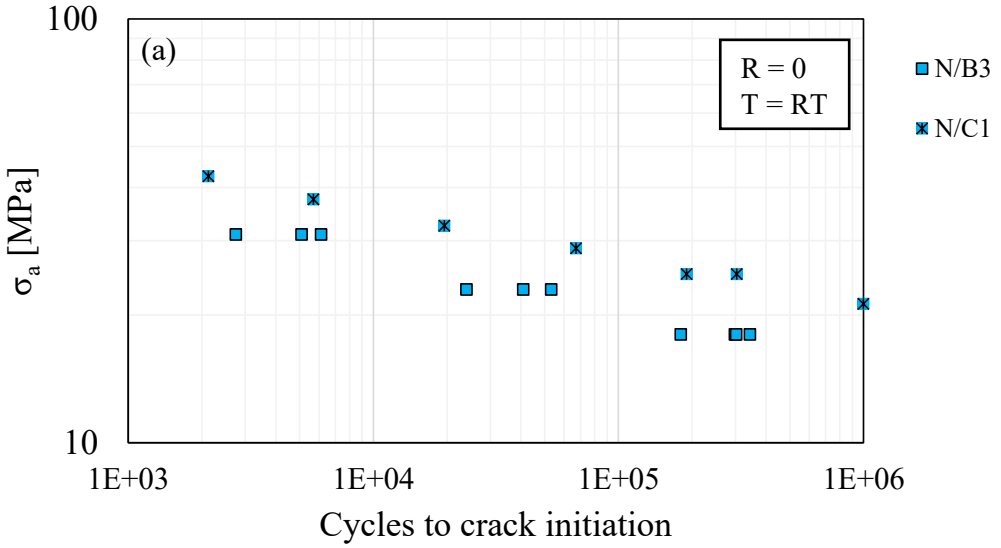

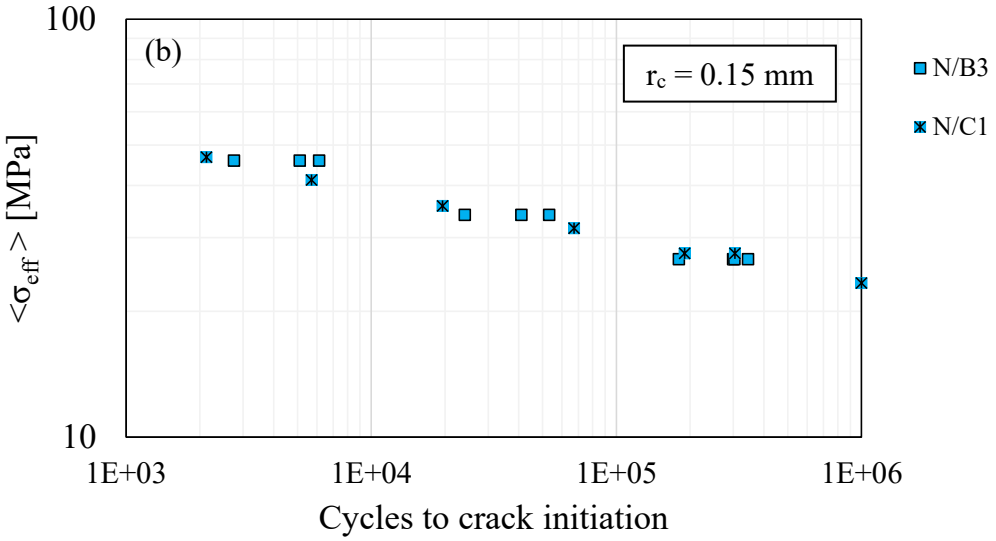

Figure 5.20. Calibration fatigue curves expressed in terms of nominal stress (a) and average effective stress (b), according to Eq. (5.4).

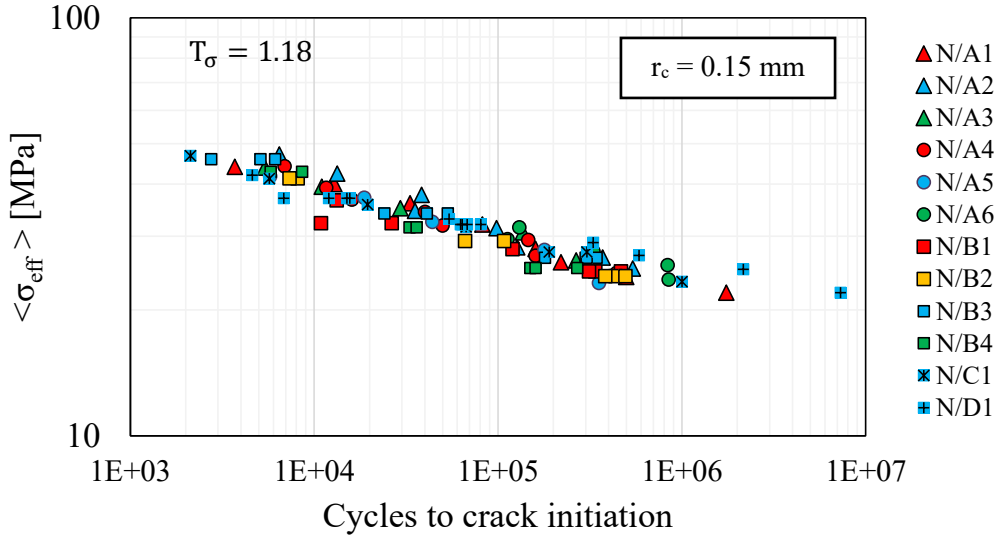

Figure 5.21. Fatigue data expressed in terms of $\langle\sigma_{eff}\rangle$.

5.6.2 Example 2

In this example the following model procedures have been adopted:

- Geometries N/A and N/C: the fiber orientation tensor components have been obtained through CT scans. Therefore procedure of Fig. 5.14 has been adopted both for the global and the sub-model;
- Geometries N/B and N/D: FOTs have been obtained from Moldflow® in case of the global model (Fig. 5.12), while the sub-model has inherited the FOTs from CT scans, according to Fig. 5.17 and 5.18.

In this case, no calibration curves are reported, since a procedure similar to Fig. 5.20 is obtained, yielding a critical radius of 0.13 mm.

Fatigue data expressed in terms of average effective stress responsible for crack onset are shown in Fig. 5.22.

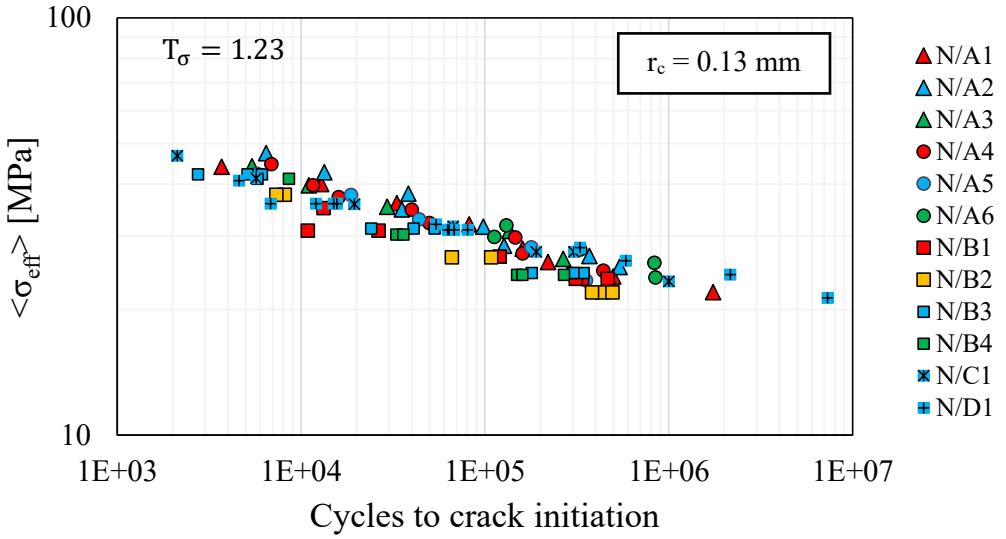

Figure 5.22. Fatigue data expressed in terms of $\langle\sigma_{eff}\rangle$.

5.6.3 Example 3

With regard to the property assignment to notched specimens, the same considerations as example 1 can be done. Nonetheless, the model calibration (Fig. 5.23) has been carried out by means of a notched specimen (N/B3) and a plain coupon (P/C3 of chapter 4). The prediction of the fatigue strength of the other notched specimens is shown in Fig. 5.24.

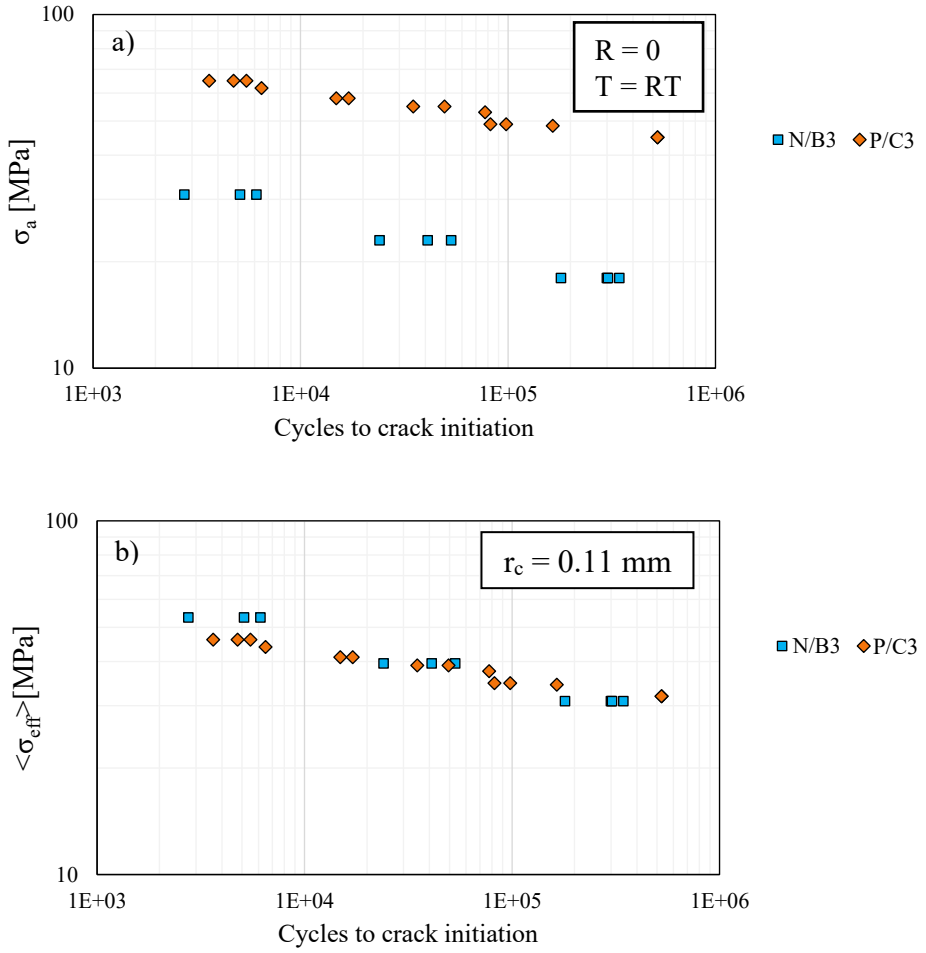

Figure 5.23. Fatigue data for specimens N/B3 and P/C3 before (a) and after (b) calibration.

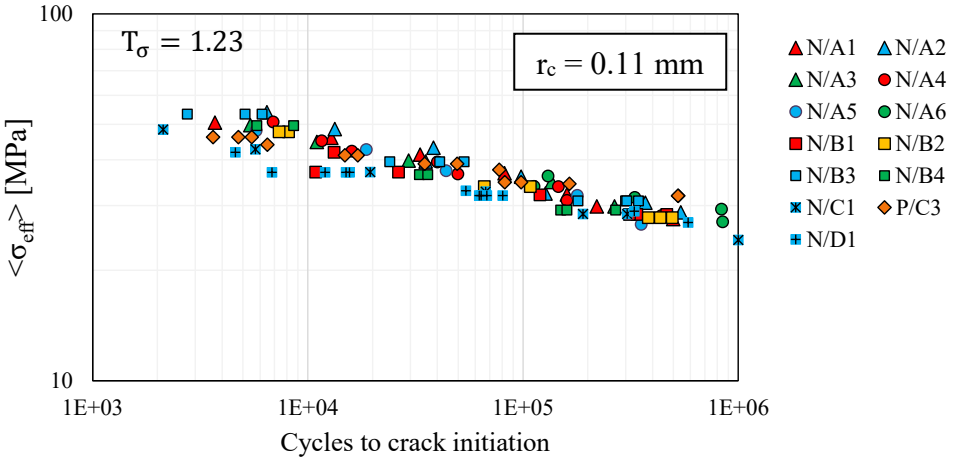

Figure 5.24. Fatigue curve prediction by means of one plain and one notched specimen.

This time, the carried out critical radius is equal to 0.11 mm, the value of which is not much different from the other validations.

5.7 Schematic application to a real component

In this paragraph, the possible application of the proposed fatigue to a real part is discussed. The full procedure for a possible application to a real component is detailed in Fig.5.25.
It must firstly clear that the reported procedure has to be considered as an example, since no studies on the actual material and mechanical behavior of the component of Fig. 5.25 have been done in this thesis work.
To sum up, once the component dimensions are known, the process simulation model can be generated and solved. The latter requires some inputs, such as parameters related to fibers (fiber diameter, length and volume fraction) and others about the production process (pressure, temperature, etc.). This type of simulation leads to the estimation of the FOT components within the modeled geometry. The latter are then fed into analytical homogenization schemes to compute the spatially varying anisotropic stiffness matrices that have to be assigned to the FE model. The structural simulation can subsequently performed, yielding the complete homogenized stress field characterizing the solved model, after applying the external load (in this case, in the form of distributed pressure on the surface highlighted in Fig. 5.25). The carried out stress tensors (or alternatively, strain tensors) can be used as inputs to the pseudo-grain approach (chapter 3 and PIE18). This numerical analytical model can be applied to each element of the solved FE model, enabling the computation of the effective stress field for the whole geometry. Before proceeding with the estimation of the fatigue cycles to crack initiation, the size of the critical radius of the spherical critical volume (responsible for the crack onset), a calibration has to be performed on tested specimens. Accordingly, two coupons with different geometries must be tested under fatigue loadings and, after properly assigning the elastic properties (thanks to the specimens' FOTs), the critical radius dimension is reached. At this stage, the critical spherical volume (whose radius derived from the calibration process) can be placed onto the effective stress peak.

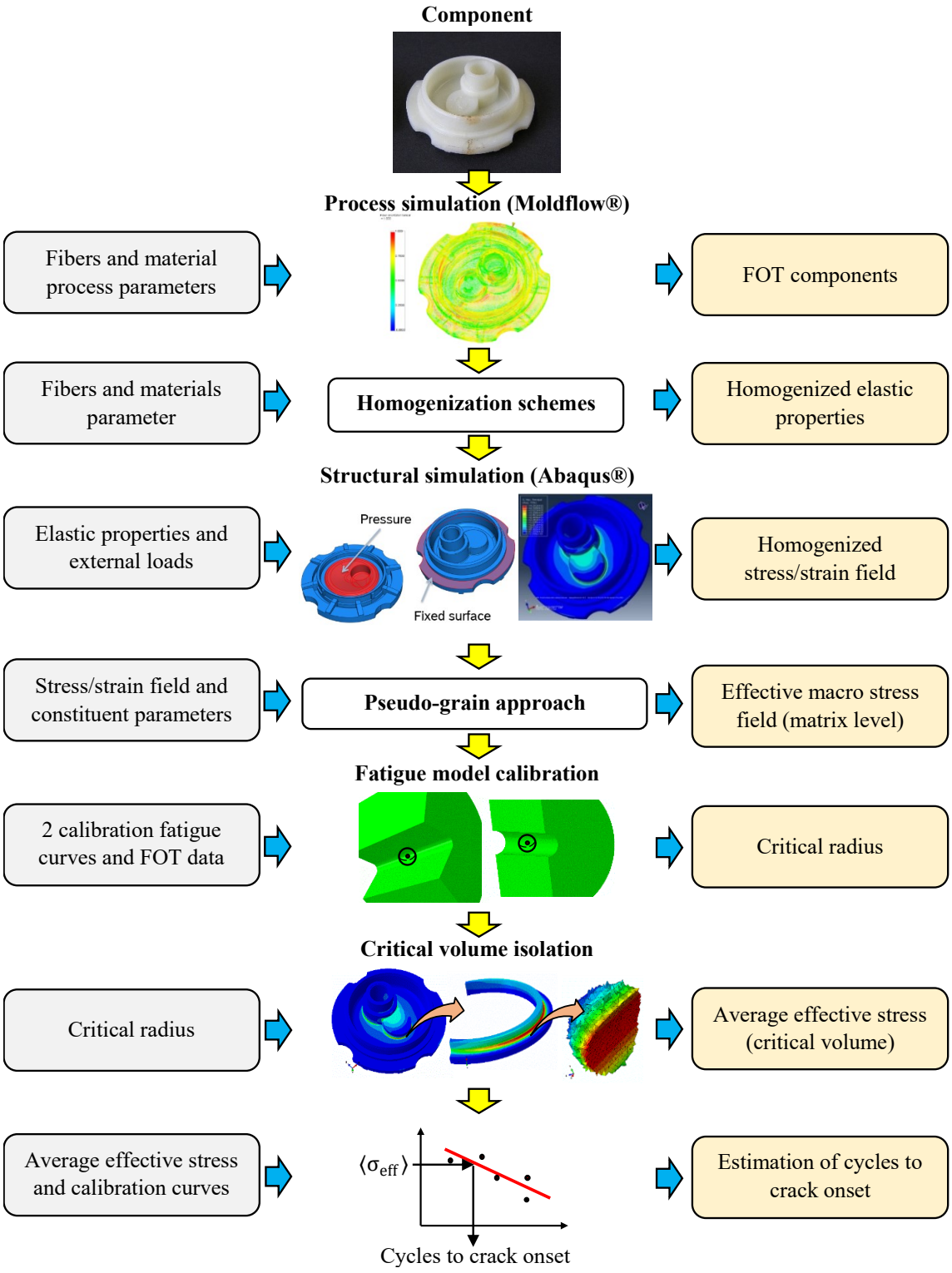

Figure 5.25. Schematic application of the proposed fatigue criterion to real parts.

The average value of the effective stress, computed in the critical macroscopic value, can now be entered in the calibration curve (carried out on specimens) to estimate the amount of cycles spent up to crack initiation.

5.8 Conclusions

In the present chapter, an innovative criterion for the estimation of the lifetime duration of SFRTs in the presence of notches has been proposed.

Until now, no model in the literature capable of combining the effect of fiber contents, local fiber orientations and notch geometry onto the fatigue strength of SFRTs has been available. Indeed, the aim of the present chapter was to take all the aforementioned effects into account, this enabling to significantly reduce the amount of experimental tests (i.e. fatigue data) that are needed to comprehensively characterize the fatigue behavior of the considered materials. The complete workflow that must be followed to evaluate the fatigue life of notch specimens has been defined.

The formulation of such an approach has been possible thanks to the models that have been previously presented in this thesis. As a matter of fact, a multiscale approach has been developed and validated, which makes use of the matrix stress distribution functions. The computation of the latter has been enabled by the pseudo-grain methodology described in chapter 3. Subsequently, based on the micromechanical information inherited from the model for plain specimens presented in chapter 4**,** the definition of an effective stress responsible for the damage of the matrix while undergoing fatigue loadings has been possible.

Firstly, the generation of the macro-scale model has been done by using the FOTs, either from CT scans either from process simulations (Moldflow®), and the resulting stress fields have been used as inputs for the micro-scale model generation and solution. Secondly, the effective stresses (carried out at the micro-scale level) have been computed for different notch radii (0.1 mm, 0.2 mm, 2.0 mm and 5.0 mm), different fiber weight fractions (15 wt%, 25 wt%,35 wt% and 50 wt%,) and different nominal fiber orientations (0° and 90°).

Once the complete effective stress field has been displayed around the notch root, an averaging method has been defined in order to correlate the fatigue strength of specimens with different notch geometries. In this context, a critical volume shape has been chosen, namely a spherical region, the center of which has to be placed onto the effective stress peak.
Fatigue data up to crack initiation that have been discussed in chapter 2 have been here employed to validate the fatigue criterion: firstly, a calibration based on the fatigue curves of two different notch geometries (R0.2 and R2.0) and, secondly, the same model has been calibrated by means of a plain and a notched specimen (R0.2). Subsequently, once the radius of a critical spherical macroscopic volume (responsible for the crack initiation phase) has been identified, the fatigue criterion has been applied to other notched geometries showing a good agreement between the predicted fatigue strength and the experimental ones.
Eventually, it must be pointed out that very different geometries have been employed for the calibration/validation of the proposed multiscale fatigue criterion, still yielding good results in terms of fatigue strength prediction. This means that the assumptions made, concerning the use of a multiscale model common to all types of specimens without considering the differences in terms of notch generation process (with metallic slits or by machining plates), are acceptable.

.

Concluding remarks

The present thesis' work has faced some design issues still present in the industry and in the literature, regarding the use of short fiber-reinforced thermoplastics for the fabrication of injection-molded parts. The advantage of using such materials can be summed up as the reduction of components' weight, the achievement of mechanical properties similar to those of metals and high production rates.

On the other hand, while the production process of such materials has reached advanced results, the design efficiency is still encountering obstacles because of the complexity of the materials morphology and of the various factors affecting the mechanical response of such composites.

In this thesis, the attention has been payed to the mechanical behavior of SFRTs undergoing fatigue loadings. In this context, the present work has aimed at deeply investigating and predicting the effect of morphology (fiber content and local fiber orientation distributions) and specimen geometry (presence of notches) on the fatigue strength of short fiber-reinforced thermoplastics.

In the literature, different authors reported that the onset of a macroscopic crack in a SFRT part undergoing fatigue loadings can be attributed to the nucleation and coalescence of microscopic cracks evolving at the matrix level. The latter are mainly diffused around fibers, within highly stressed regions. On the other hand, only few works have proposed multiscale models comprehensively taking into account the actual fatigue damage occurring at the matrix level.

In this thesis, experimental studies (chapter 2) have been firstly presented, aiming to analyze the specimens' local fiber orientation distributions (with computer tomography analyses) and characterizing the fatigue response of short glass fiber-reinforced PA66-coupons.

Being aware of the multiscale nature of the fatigue damage occurring in such materials, it has been chosen to reproduce the micro-scale matrix cracking by relying on the local stress distributions interesting the composite matrix. In this context, an analytical numerical pseudo-

grain approach (chapter 3) has been secondly formulated and validated, in order to compute the stress distributions to which the thermoplastic matrix is subjected.
The latter innovatively enables the computation of matrix stress cumulative distribution functions in microstructures with misaligned short fibers, without dealing with the generation and solution of complex finite element models.
Thirdly, a criterion that makes use of the abovementioned matrix stress distributions (obtained with the pseudo-grain approach) has been formulated (chapter 4). The presented criterion has been furthermore validated by means of the experimental data reported in chapter 2. Namely, fiber orientation tensors have been used for properly assigning the elastic properties to the finite element models and the fatigue curves for assessing whether the fatigue strength is correctly predicted. The developed model permits now to estimate the fatigue strength of a generic plain specimen characterized by its fiber orientations and volume fraction, by only relying on one calibration Wöhler-curve.
Eventually, the model developed for plain specimens has been extended for capturing the influence of notch geometries (chapter 5). Also in this case, a comprehensive validation has been performed by using data on notched specimens reported in chapter 2. Thanks to the formulated criterion, it is possible to efficiently predict the fatigue curves of a generic notched specimen, by carrying out only two calibration fatigue curves (two notched specimens or one plain and one notched).
Concerning possible future activities, the proposed methodology for predicting the fatigue strength of SFRTs should be applied to specimens undergoing different multiaxial external fatigue loads causing the crack onset under mode II, III and mode mixity. This step would be essential to understand the limitations of the formulated fatigue criterion and to have a better insight on the damage mechanisms caused by the entity of the external load. Furthermore, a required extension of the proposed fatigue model concerns the application to specimens undergoing different load ratios (positive and negative) and the necessity of predicting the effect of them. Similar model enhancements might also be performed to predict the fatigue strength of SFRTs being loaded under different temperatures (e.g. -40°C and 130°C). Nonetheless, the effect of the matrix relative humidity should also be taken into account.
Further improvements of the fatigue criterion could derive from the capability of predicting the fatigue lifetime of a SFRT undergoing variable amplitude load histories.

Eventually, the aforementioned variants should be implemented into one single code in order to be estimate the lifetime of a generic part undergoing real loading and environmental conditions.

Appendix A

A.1 Fiber orientation tensor components of geometry N/B

In this appendix, the out-of-diagonal components referring to the same FOTs as in Fig. 2.20-2.22 are reported for geometry N/B. The following figures are respectively related to PA66-GF15 (Fig. A.1), PA66-GF25 (Fig. A.2) and PA66-GF50 (Fig. A.3).

-0.03	-0.01	0.25	0.32	0.34	0.2	0.02	-0.03	0.03
0.05	0.13	0.16	0.16	-0.04	-0.07	0.05	0.18	0.08
0.08	-0.02	0.03	0.03	0.06	0.05	0.05	0.04	0.14
0.08	0.01	-0.04	-0.08	-0.05	0.08	0	0.07	0.01
0.22	0.09	-0.03	-0.11	0.35	-0.11	-0.11	-0.02	0.07
0.05	0.1	0.04				-0.1	-0.12	0.04
-0.06	0	0.04		$\mathbf{a_{xy}}$		-0.08	-0.02	0.08
-0.06	-0.02	0.01				0	-0.05	0.04

-0.36	-0.35	-0.31	-0.26	-0.22	-0.04	0.16	0.36	0.39
-0.32	-0.32	-0.19	-0.19	-0.28	-0.2	-0.1	0.19	0.25
-0.33	-0.35	-0.16	-0.04	0.05	0.17	0.25	0.26	0.28
-0.26	-0.28	-0.23	-0.02	0.06	0.21	0.36	0.35	0.29
-0.21	-0.4	-0.19	-0.04	0.08	0.14	0.22	0.44	0.37
-0.12	-0.24	-0.21				0.03	0.16	0.42
-0.01	-0.13	-0.03		$\mathbf{a_{xz}}$		0.1	0.08	0.34
-0.16	-0.06	-0.01				0	0.07	0.18

0.03	0.01	-0.15	-0.12	-0.12	-0.03	0.07	-0.03	-0.01
-0.02	-0.06	-0.04	-0.05	0.04	0.03	-0.02	0.04	0
-0.04	0.01	-0.03	0.03	0	-0.01	0.04	0.02	0.06
-0.15	-0.09	-0.09	-0.02	0.01	0.02	0	0.05	0.05
-0.04	-0.08	0.04	0.02	0.11	-0.08	-0.08	-0.02	0.06
-0.03	-0.3	-0.04				-0.19	-0.24	0.05
0.1	-0.02	-0.44		$\mathbf{a_{yz}}$		-0.35	-0.03	0.17
0.21	0.03	-0.33				0.33	-0.1	0.07

Figure A.1. Out-of-diagonal FOT components for geometry N/B1 (PA66-GF15).

-0.15	-0.13	-0.02	-0.09	-0.07	-0.12	0.02	0.06	0.12
-0.1	-0.04	0	0.07	0.06	0.02	-0.02	-0.06	0
0.06	-0.13	0.07	0.04	0.04	-0.01	0.01	0.08	0.05
0.03	0.01	0.04	0.15	-0.16	-0.03	-0.01	-0.02	0.07
-0.02	0.06	0.13	0.39	-0.43	0.11	-0.05	-0.02	-0.06
0.16	-0.02	-0.07				-0.03	-0.14	-0.01
0.02	0.02	-0.05				-0.03	-0.04	0
0	0.01	-0.03		$\mathbf{a_{xy}}$		0.07	0.03	0.01

-0.25	-0.15	-0.08	-0.12	-0.14	-0.1	0.13	0.22	0.31
-0.21	-0.05	-0.14	-0.18	-0.21	0.02	0.08	0.25	0.37
-0.03	-0.1	-0.32	-0.26	0.04	0.25	0.32	0.31	0.33
0.05	-0.08	-0.22	-0.17	0.02	0.24	0.39	0.38	0.37
-0.12	-0.35	-0.29	-0.2	0.06	0.13	0.19	0.43	0.4
-0.16	-0.22	-0.07				0.23	0.25	0.41
-0.2	-0.21	-0.03				0.05	0.1	0.27
-0.2	-0.06	0		$\mathbf{a_{xz}}$		0.08	0.08	0.16

0.03	0.01	-0.02	-0.01	0.02	0.01	0.02	-0.01	0.06
-0.03	-0.09	0.01	-0.01	-0.02	-0.01	0	-0.02	-0.01
-0.16	-0.14	-0.07	-0.01	0	-0.01	-0.02	0.04	0.05
-0.09	-0.06	-0.05	-0.03	0	0	-0.01	-0.05	0.06
-0.12	-0.04	-0.1	-0.18	-0.1	0.08	-0.06	-0.02	-0.1
-0.13	0.16	0.1				-0.1	-0.27	-0.04
-0.03	-0.01	0.41				0.15	-0.08	0.08
0.05	0.08	-0.09		$\mathbf{a_{yz}}$		0.45	0.1	0.04

Figure A.2. Out-of-diagonal FOT components for geometry N/B2 (PA66-GF25).

0	0.13	0.12	0.09	0.06	0.05	0.11	0.04	0.02
0	-0.04	-0.04	-0.02	0.01	0.03	0.06	0.11	0.1
-0.01	0	0.01	0.05	0	-0.02	-0.06	-0.02	0.04
-0.02	-0.01	0.02	0.02	0.08	0.08	0.11	0.04	0.03
-0.11	-0.07	-0.04	-0.05	0.11	-0.02	0.09	0.04	0.01
-0.09	-0.05	-0.05				-0.03	0.04	0.03
-0.06	-0.03	-0.03				0.04	0.02	0.04
-0.03	-0.01	0		$\mathbf{a_{xy}}$		0	-0.01	0.01

-0.32	-0.25	-0.18	-0.08	0.04	0.17	0.24	0.28	0.33
-0.37	-0.3	-0.2	-0.04	0.05	0.14	0.21	0.24	0.31
-0.31	-0.33	-0.29	-0.19	-0.08	0.03	0.24	0.37	0.36
-0.33	-0.32	-0.29	-0.21	0.06	0.21	0.27	0.35	0.43
-0.35	-0.36	-0.39	-0.32	-0.03	0.36	0.4	0.36	0.42
-0.32	-0.28	-0.21				0.29	0.32	0.41
-0.19	-0.12	-0.15				0.08	0.16	0.35
-0.23	-0.06	-0.01		$\mathbf{a_{xz}}$		-0.12	0.09	0.2

0.01	-0.06	-0.04	0	0.01	0.01	0.03	0.01	0.01
0	0.04	0.01	-0.01	-0.01	-0.01	0.01	0.04	0.04
-0.01	0.01	0	-0.01	-0.01	0	-0.02	-0.01	0
0.05	0.04	0	0	0.01	0.03	0.04	0.03	0.01
0.14	0.07	0.02	0.01	-0.01	0	0.07	0.06	0.01
0.1	0.08	0.18				-0.02	0.06	0.02
0.03	0.12	0.26				0.07	0.1	0.06
0.03	0.08	0.13		$\mathbf{a_{yz}}$		-0.09	0.09	0.02

Figure A.3. Out-of-diagonal FOT components for geometry N/B4 (PA66-GF50).

Appendix B

B.1 Periodic boundary conditions' formulation

In this section, the application of 3D periodic boundary conditions to a generic element cell is formulated in a manner suitable to the software Abaqus®, but the hereinafter presented methodology may be easily transferred to other commercial FE codes.
Periodic boundary conditions are hereby expressed in terms of strains and, in particular, they will be applied to the considered models as node displacements. Before formulating the complete set of equations which the volume cell external nodes undergo, it is worth depicting the normal (Fig. B.1) and shear (Fig. B.2) deformations of a generic cell, in order to better understand the meaning of the employed strain tensor components.

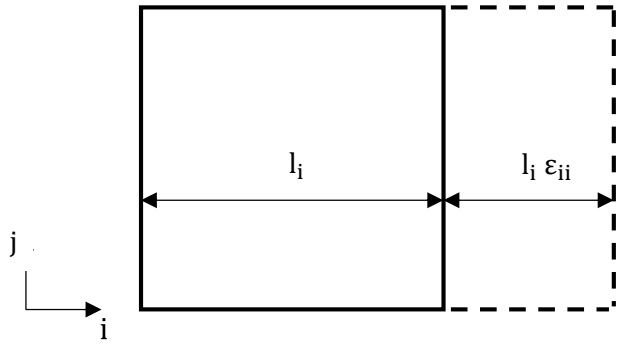

Figure B.1. Schematic representation of a normal deformation.

Indices i and j of Fig. B.1 and B.2 can be substituted by the axes' name (x, y, z) in the 3D case. In order to better interpret the indices, it is here assumed that $x < y < z$.

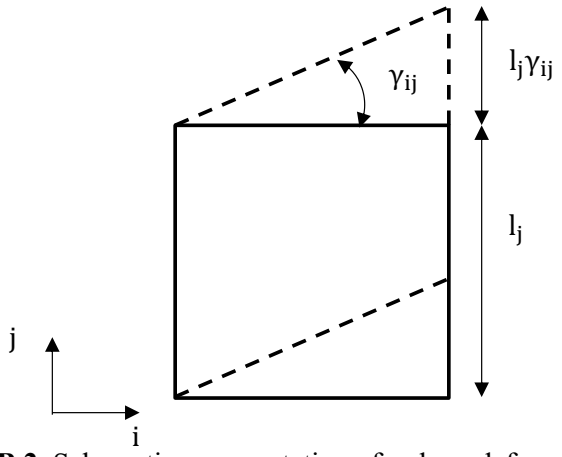

Figure B.2. Schematic representation of a shear deformation.

Term γ_{ij} of Fig. B.2 denotes the strain components expressed in the Voigt notation and it is defined as follows:

$$\gamma_{ij} = \varepsilon_{ij} + \varepsilon_{ji} \qquad \forall i \in [x,y]\ ;\ \forall j \in [y,z] \ \text{ with } \ i \neq j \ \text{ and } \ i < j \qquad \text{(B.1)}$$

Considering the strain tensor **ε** as symmetric, the following equation is therefore valid:

$$\gamma_{ij} = 2\,\varepsilon_{ij} \qquad \forall i \in [x,y]\ ;\ \forall j \in [y,z] \ \text{ with } \ i \neq j \ \text{ and } \ i < j \qquad \text{(B.2)}$$

It is furthermore assumed that the shear deformation is univocally represented by Fig. B.2 and

$$\gamma_{ji} = 0 \qquad \forall i \in [x,y]\ ;\ \forall j \in [y,z] \ \text{ with } i \neq j \ \text{ and } \ i > j \qquad \text{(B.3)}$$

The formulation of the PBC equations will be hereinafter subdivided into three steps:

1. Formulation of the equations for the cell faces;
2. Formulation of the equations for the cell edges;
3. Formulation of the equations for the cell vertices.

Moreover, the notation of faces, edges and vertices is reported in Fig. B.3 and the relevant cell dimensions in Fig. B.4.

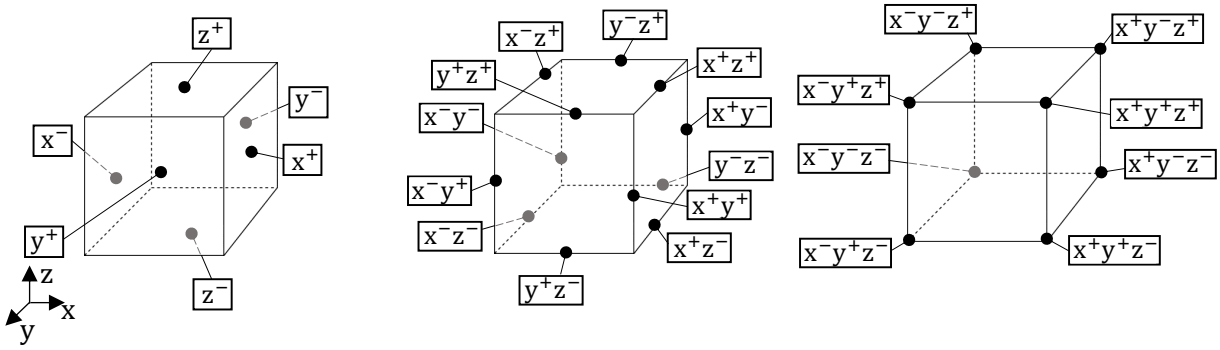

Figure B.3. Notation of faces, edges and vertices.

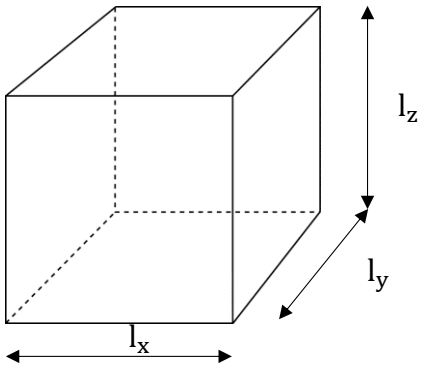

Figure B.4. Relevant dimensions of a representative element.

B.1.1 Faces' equations

According to Fig. B.3 and B.4, the set of equations governing the normal deformations of the faces is formulated in the following manner:

$$u_i^{i^+} - u_i^{i^-} = -l_i \varepsilon_{ii} \qquad \forall i \in [x, y, z] \tag{B.4}$$

With regard to the shear-related equations of the faces, Eq. (B.5) and (B.6) are therefore valid:

$$u_j^{i^+} - u_j^{i^-} = -l_i \gamma_{ij} = -2\,\varepsilon_{ij} \qquad \forall i,j \in [x,y,z]\ ;\ i \neq j \text{ and } i < j \tag{B.5}$$

$$u_i^{j^+} - u_i^{j^-} = -l_l \gamma_{ji} = 0 \qquad \forall i,j \in [x,y,z]\ ;\ i \neq j \text{ and } i < j \tag{B.6}$$

B.1.2 Edges' equations

After some algebraic manipulations, the equations expressing the edge deformations can be thus formulated:

$$u_i^{i^-j^-} - u_i^{i^+j^+} = l_i \varepsilon_{ii} + l_j \gamma_{ij} = -l_i \varepsilon_{ii} - 2\, l_j \varepsilon_{ij} \tag{B.7}$$

$$u_j^{i^-j^-} - u_j^{i^+j^+} = -l_j \varepsilon_{jj} - l_i \gamma_{ji} = -l_j \varepsilon_{jj} \tag{B.8}$$

$$u_i^{i^+j^+} - u_i^{i^+j^-} = -2\, l_j \varepsilon_{ij} \tag{B.9}$$

Eq. (B.7)-(B.9) must be valid for the following conditions:

$$\forall i \in [x,y]\ ;\ \forall j \in [y,z] \quad \text{with}\ \ i \neq j \text{ and } i < j \tag{B.10}$$

Whether indices i, j and k are substituted in Eq. (B.4)-(B.9), a set of 27 equations is therefore obtained for the edges' nodes. It has to be noticed that Eq. (B.7) and (B.8) contain either normal either shear terms, as a consequence of the fact that each edge must simultaneously fulfill the constraints imposed by two adjacent faces.

B.1.3 Vertices' equations

Analogously, the expressions related to the vertex displacements are expressed as follows:

$$u_i^{x^-y^-z^-} - u_i^{x^+y^+z^+} = -l_i\left[\varepsilon_{ii} + \gamma_{ji} + \gamma_{jk}\right] \tag{B.11}$$

$$u_i^{x^-y^+z^+} - u_i^{x^+y^-z^-} = -l_i\left[\varepsilon_{ii} + \gamma_{ji} + \gamma_{jk}\right] \tag{B.12}$$

$$u_i^{x^-y^+z^-} - u_i^{x^+y^-z^+} = -l_i\left[\varepsilon_{ii} + \gamma_{ji} + \gamma_{jk}\right] \tag{B.13}$$

$$u_i^{x^-y^-z^+} - u_i^{x^+y^+z^-} = -l_i\left[\varepsilon_{ii} + \gamma_{ji} + \gamma_{jk}\right] \tag{B.14}$$

In order to correctly interpret Eq. (B.11)-(B.14), the indices must respect the following conditions:

$$\forall i, j \in [x, y, z] \quad \text{with} \quad i \neq j \tag{B.15}$$

It is reminded that whether $i < j$ and $j < k$, terms γ_{ji} and γ_{jk} of Eq. (B.11)-(B.14) are set to 0 and in case $i > j$ and $j > k$, they respectively equal $2\varepsilon_{ji}$ and $2\varepsilon_{jk}$.
Eventually, the last set of equations for vertices reads:

$$u_i^{x^+y^-z^+} - u_i^{x^+y^-z^-} = -l_x\, a_{ix} \qquad \forall i \in [x, y, z] \tag{B.16}$$

$$u_i^{x^+y^-z^-} - u_i^{x^+y^+z^-} = -l_y\, a_{iy} \qquad \forall i \in [x, y, z] \tag{B.17}$$

$$u_i^{x^+y^+z^-} - u_i^{x^+y^+z^+} = -l_z\, a_{iz} \qquad \forall i \in [x, y, z] \tag{B.18}$$

where:

$$a_{ii} = \varepsilon_{ii} \qquad \forall i \in [x, y, z] \tag{B.19}$$

$$a_{ij} = \gamma_{ij} = 2\varepsilon_{ij} \qquad \forall i, j \in [x, y, z] \quad \text{if} \quad i < j \ \text{and} \ i \neq j \tag{B.20}$$

$$a_{ij} = \gamma_{ij} = 0 \qquad \forall i, j \in [x, y, z] \quad \text{if} \quad i > j \ \text{and} \ i \neq j \tag{B.21}$$

B.1.4 Mixed PBCs

By replacing the indices of Eq. (B.11)-(B.14) and Eq. (B.16)-(B.21), a set of 21 equations is therefore obtained.
In order to get the formulation of the *mixed* PBCs for the cell faces, it is firstly sufficient not to include the term $i = z$ of Eq. (B.4) and to add the following equations:

$$u_z^{i^+} = u_z^{i^-} \qquad \forall i \in [x, y] \tag{B.22}$$

Subsequently, the edges' displacement equation can be obtained by using Eq. (B.7) and (B.9) and excluding again $i = z$. Here again, the set can be completed by means of these expressions:

$$u_z^{i^- j^+} = u_z^{i^+ j^+} \qquad \forall i, j \in [x, y] \;\; \text{with} \;\; i < j \tag{B.23}$$

$$u_z^{i^- j^-} = u_z^{i^+ j^-} \qquad \forall i, j \in [x, y] \;\; \text{with} \;\; i < j \tag{B.24}$$

$$u_z^{i^+ j^-} = u_z^{i^+ j^+} \qquad \forall i, j \in [x, y] \;\; \text{with} \;\; i < j \tag{B.25}$$

Also in case of vertices, Eq. (B.11)-(B.14) and Eq. (B.16)-(B.21) are valid whether $i = z$ is removed and the completing formulations read:

$$u_z^{x^- y^+ z^+} = u_z^{x^- y^- z^+} \tag{B.26}$$

$$u_z^{x^- y^- z^+} = u_z^{x^+ y^- z^+} \tag{B.27}$$

$$u_z^{x^+ y^- z^+} = u_z^{x^- y^- z^-} \tag{B.28}$$

$$u_i^{x^- y^- z^-} = u_i^{x^+ y^- z^-} \tag{B.29}$$

$$u_i^{x^+ y^- z^-} = u_i^{x^+ y^+ z^-} \tag{B.30}$$

B.2 Numerical implementation in Abaqus®

In this section, further details related to the PBC equations' implementation within the software Abaqus® are treated.

It must be reminded that the previously formulated equations refer to nodal displacements. Nevertheless, while identifying the nodes of faces, edges and vertices, it has to be highlighted that they are belonging only to one of these entities. This means in turn that face nodes exclude the edge and vertex nodes and edge nodes do not contain the vertex nodes.

Concerning the implementation of the PBC equations, all expressions can be written within an Abaqus® input file (.inp) and, either displacements either the constant terms defined by the strain tensor components and by the cell dimension, have to be handled as variables. This issue is hereby overcome by defining floating nodes (not belonging to the model geometry), to the degrees of freedom (DOF) of which constant values can be assigned in the form of boundary conditions. The generation of such floating nodes takes place after defining reference points outside of the geometry (Fig.B.5).

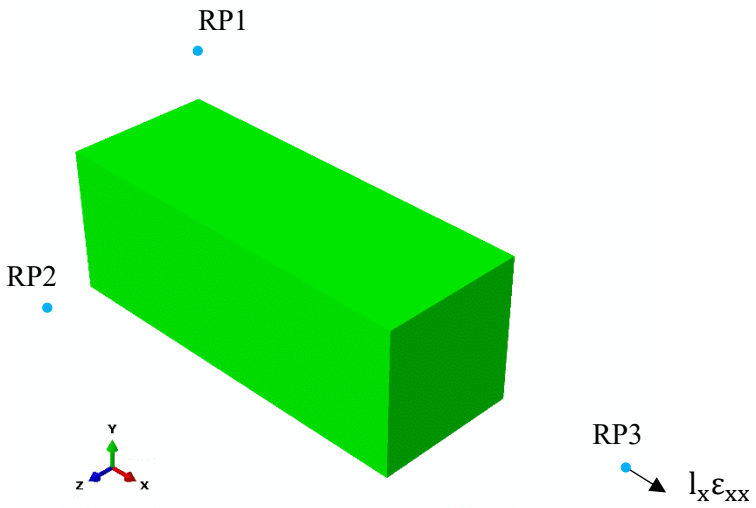

Figure B.5. Example of FE model with reference points (RP1, RP2 and RP3) and assignment of a constant value $l_x\varepsilon_{xx}$ to RP3.

Some problems may occur during the meshing activity as a consequence of the non-periodic node location on opposite faces and edges. In this work, this problem has been overcome by

utilizing the *tie* option of Abaqus®. Namely, the following steps must be followed in order to apply the PBCs to opposite faces and edges' nodes:

- Copying the nodes from one reference face/edge to the opposite one identified as target, as it is depicted in Fig. B.6;
- Constraining the new node set to the nodes belonging to the target face/edge. The new node set is now identical to the reference one, but shifted by the cell length;
- Application of the displacement equations between the new node set and the reference one.

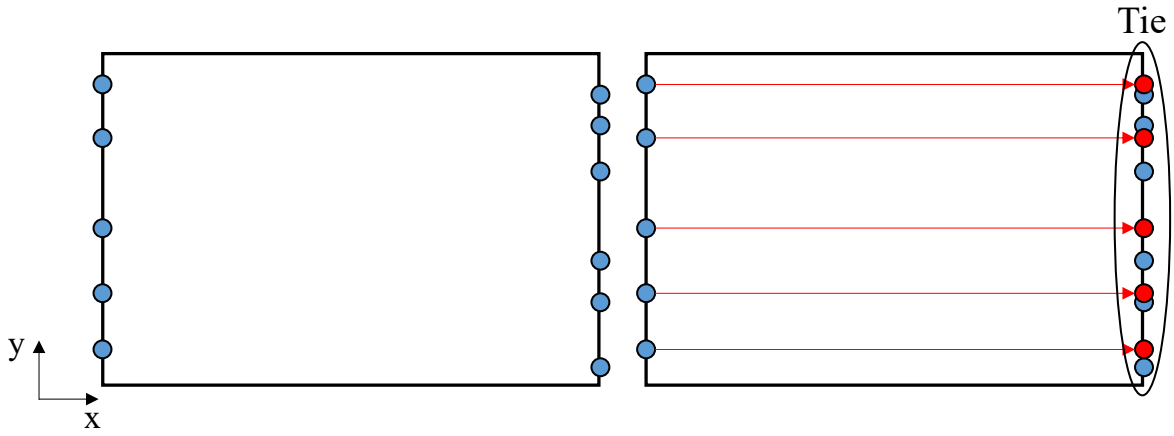

Figure B.6. Schematic 2D representation of the *tie* operation. In (a) the blue dots represent the original nodes. In (b) the reference nodes (left) are copied to the target face (red dots) and constrained to the original ones (blue dot on the right).

Appendix C

C.1 .Fatigue criterion based on the UTS

In this section, the limitation of applying a fatigue approach based on the normalization of the fatigue strength by means of the ultimate tensile strength is shown. The aforementioned criterion is a phenomenological approach and has been often used in the literature by different authors.

According to DEM10_2, the robustness of the approach is demonstrated whether fatigue curves collapse within a narrow scatter band, when expressed in terms of the following stress:

$$\sigma_{eff,UTS} = \frac{\sigma_a}{UTS} \tag{C.1}$$

where σ_a is the nominal stress amplitude of the considered specimen and UTS it its ultimate strength.

The UTS of some plain and notched specimens are respectively reported in Tab. C.1 and C.2.

Table C.1. UTS values of the considered plain specimens.

Specimen	P/A1	P/A2	P/A3	P/B1	P/B2	P/B3	P/B4	P/C1	P/C2	P/C3	P/C4
UTS [MPa]	160	127	88	94	96	95	121	119	160	181	194

Table C.2. UTS value of the considered notched specimens.

Specimen	N/B1	N/B2	N/B3	N/B4
UTS [MPa]	37	71	116	170

This fatigue criterion is firstly applied to plain specimens. The adopted fatigue model has been already presented in the literature by many authors (e.g. DEM10_2) and its validation is reported in Fig. C.1, yielding good results.

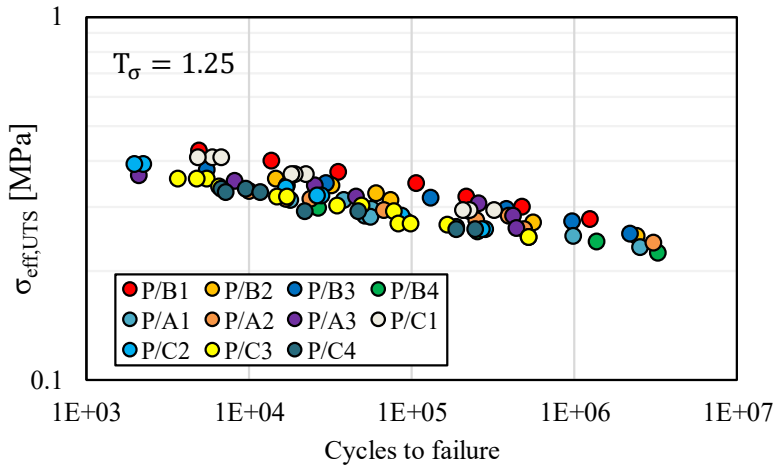

Figure C.1. Fatigue strength prediction by means of UTS values, for plain specimens.

Nevertheless, the main aim of the work is to give the possibility of embedding the thesis fatigue criterion into geometries that are more complex than those of plain specimens. For the sake of comparison, the UTS approach is also applied to notched specimens (geometry N/B of chapter 2 and results are plotted in Fig. C.2.

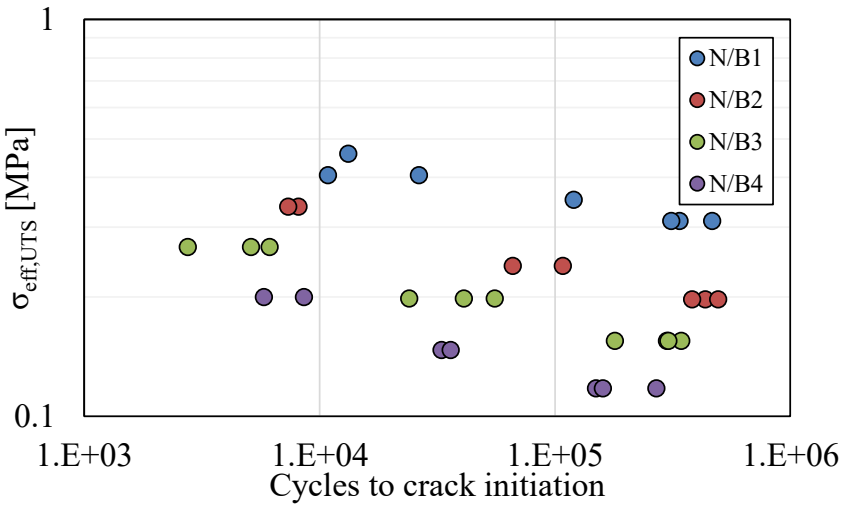

Figure C.2. Fatigue strength prediction by means of specimens UTS values, for notched specimens.

From Fig. C.2, it can be stated that such an approach is not sufficient to efficiently predict the fatigue behavior of a generic SFRT part, that may be characterized by the presence of stress concentrations caused by notches.

Appendix D

D.1 Considerations on the matrix stress threshold

In this section, some considerations about the choice of the threshold of the matrix Beltrami CDF are made. In chapter 4 and 5, this threshold has been denoted by $V_{c\%}$. It has been demonstrated in chapter 4, that in case of plain specimens, the application of the fatigue criterion yield good results while setting $V_{c\%}$ to values smaller then 10%. This is also experimentally justified by the fact that the most critical regions are around the fibers, i.e. in those sites where the matrix is stressed at the most. This statement agrees indeed with the choice of a small $V_{c\%}$.

With reference to the results obtained for plain specimens, it is clear that, by adopting $V_{c\%}$ values higher that 10%, the application of the fatigue criterion would bring to poor quality results. Nevertheless, it could be an interesting operation to investigate the application of the proposed fatigue criterion in case of notched coupons, by considering the matrix average effective stress, without setting any threshold. The reason of this alternative procedure can be attributed to the ease of computing the average matrix stress by means of commercial software, such as Digimat®.

For simplicity, the calibration procedure is performed by means of specimens N/B3 and N/D1 (chapter 5), which are both made of PA66-GF35. Once the calibration radius is carried out, the approach is applied to a third specimen geometry (N/C1) to assess whether the choice of the average matrix Beltrami stress as effective stress is acceptable.

The results deriving from the application of the proposed fatigue approach, after choosing the mean Beltrami stress, are reported in Fig. D.1. The obtained critical radius is equal to 0.20 mm. By focusing on the curve associated with specimen N/C1, it can be easily stated that the fatigue strength of the latter cannot be properly predicted. This supports the necessity of the computing the matrix effective stress determined by the choice of a low $V_{c\%}$ value, in

order to identify the most stressed matrix volumes, which are responsible for the fatigue micro-damage evolution.

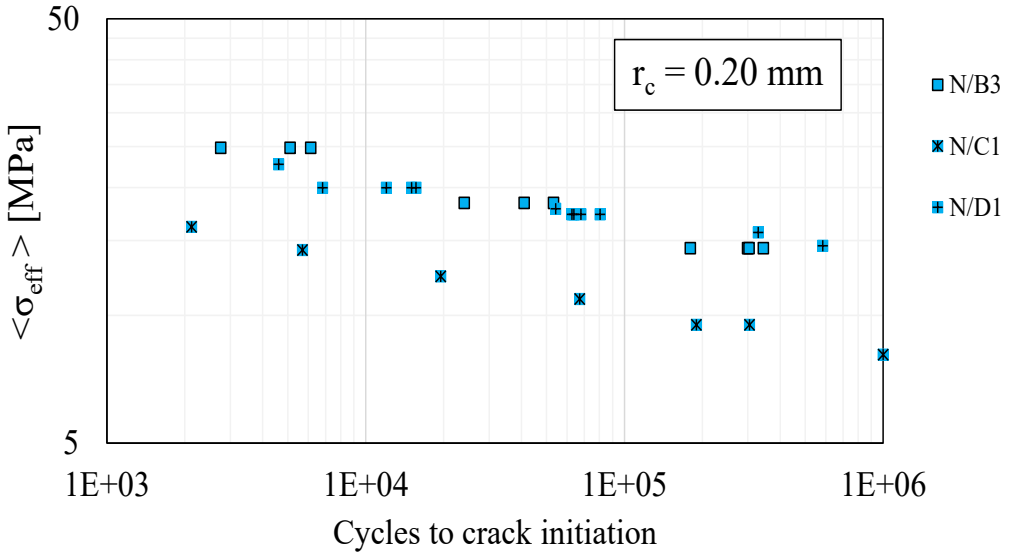

Figure D.1. Application of the fatigue criterion to notched specimens by adopting the matrix average Beltrami stress as σ_{eff}.

Nevertheless, further observations can be done with regard to the proposed threshold of the effective cumulative stress ($V_{c\%} \leq 10\%$). In this context, some quantitative analyses are herby reported in order to understand the entity of the expected matrix plasticization, by comparing the nominal matrix elastic limit with the carried out effective stress values.

As shown above, the use of the matrix average Beltrami stress does not yield good results. It is however interesting to compare the obtained matrix effective stress (corresponding to $V_{c\%}$ = 10%) with the matrix elastic limit. According to reference BAS1, the matrix yield stress ($\sigma_{y,m}$) is equal to 85 MPa for an unreinforced PA66 material. Assuming that the maximum principal stress coincides with $\sigma_{y,m}$ and setting all other stress components to 0 MPa, the Beltrami stress associated with the elastic limit can be obtained by means Eq. (4.1) and it reads:

$$\sigma_{B,y,m} = \frac{\sigma_{y,m}}{\sqrt{2}} = \frac{85}{\sqrt{2}}\ \text{MPa} = 60\ \text{MPa} \tag{D.1}$$

By taking specimen N/B3 as a reference and using the critical radius of 0.15 mm (chapter 5), the maximum tested nominal stress amplitude can be expressed in terms of average effective stress $\langle\sigma_{eff}\rangle$ computed in the critical sphere, resulting in a value of 30 MPa. The latter is associated with a stress amplitude and therefore, by doubling it, the maximum average effective stress (to be intended as the stress peak over the constant amplitude load history) equals 60 MPa. By comparing this value with $\sigma_{y,m}$, it can be stated that no significant plasticization is expected, in average, within the critical spherical volume. On the other hand, by considering the effective stress deriving from $V_{c\%}$ = 10%, the yield Beltrami stress would be significantly exceeded by it. Indeed, the doubled average effective stress computed within the critical sphere (r_c = 0.15 mm) reads 82 MPa (whilst the peak of effective stress at the notch tip is 102 MPa). This agrees with some experimental observations (BEL17_2).stating that micro-plasticization phenomena mainly occur around fibers.

Eventually, it is worth investigating the value of $V_{c\%}$ at which the elastic limit is overcome in a plain specimen. In this context and according to section 5.6.3, the specimen type P/C3 (PA66-GF35) is taken as a reference. Tab. D.1 reports the matrix effective stresses evaluated for different thresholds of the cumulative function of the Beltrami stress.

Table D.1. Effective stress values evaluated for different $V_{c\%}$ values.

$\mathbf{V_{c\%}}$	10%	20%	30%	40%	50%
$\mathbf{2 \cdot \sigma_{eff}}$	67 MPa	54 MPa	47 MPa	43 MPa	41 MPa

From Tab. D.1, it can be seen that the elastic limit ($\sigma_{B,y,m} = 60$ MPa) is exceeded between $V_{c\%}$= 10% and $V_{c\%}$= 20%. More precisely, the limit is reached at $V_{c\%}$= 15%.

Eventually, the same observations can be done with reference to the plain specimen P/C3 in the presence of humidity. In this case, the matrix elastic modulus is set to 1000 MPa. After some algebraic manipulation, the Beltrami elastic limit is found to be 35 MPa. By applying

the same load as in case of dry matrix, the effective stress results to overcome the elastic limit for $V_{c\%}$ equal to 15%. Nevertheless, the damage mechanisms interesting a conditioned matrix are generally different from those of dry matrices, i.e. higher plasticization is encountered. For this reason, some limitations deriving from the use of linear elastic laws for humid matrices may be not valid any more and more accurate models might be required.

References

ADV87 S. G. Advani and C. L. Tucker, Closure approximations for three-dimensional structure tensors, Journal of Rheology, vol. 34, pp. 367-386, 1990

ADV90 S. G. Advani, C. L. Tucker, *A numerical simulation of short fiber orientation in compression molding,* Polymer Composites, vol. 11, pp. 164-173, 1990

ADV90_2 S. G. Advani, C. L. Tucker, *The use of tensors to describe and predict fiber orientation in short fiber composites*, Journal of Rheology, vol. 31, pp. 751-784, 1987

ARI14 M. F. Arif, N. Saintier, F. Meraghni, J. Fitoussi, Y, Chemiscky, G. Robert, *Multiscale fatigue damage characterization in short glass fiber reinforced polyamide-66,* Composites Part B, vol. 61, pp. 55-65, 2014

BAB18 K. P. Babu, P. M. Mohite, C. S. Upadhyay, *Development of an RVE and its stiffness predictions based on mathematical homogenization theory for short fibre composites,* International Journal of Solids and Structures, vol. 130-131, pp. 80-104

BAR07 S. Barbouchi, V. Bellenger, A. Tcharkhtchi, Ph. Castaing, T. Jollivet, *Effect of water on the fatigue behaviour of a pa66/glass fibers composite material,* Journal of Materials Science, 2007

BAS1 BASF, *CAMPUS® Datasheet, Ultramid® A3W - PA6*6, 2018

BAS2 BASF, *CAMPUS® Datasheet, Ultramid® A3WG3- PA66-GF15*, 2018

BAS3 BASF, *CAMPUS® Datasheet, Ultramid® A3WG5 - PA66-GF25*, 2018

BAS4 BASF, *CAMPUS® Datasheet, Ultramid® A3WG7 - PA66-GF35*, 2018

BAS5 BASF, *CAMPUS® Datasheet, Ultramid® A3WG10 - PA66-GF50*, 2018

BAS90 C. Bastioli, I. Guanella, G. Romano, *Effects of water sorption on the physical properties of PET, PBT, and their long fibers composites*, Polymer Composites, vol. 11, pp. 1-9, 1990

BEL16 E. Belmonte, M. De Monte, T. Riedel, M. Quaresimin, *Local microstructure and stress distributions at the crack initiation site in a short fiber reinforced polyamide under fatigue loading,* Polymer Testing, vol. 54, pp. 250-259, 2016

BEL17 E. Belmonte, M. De Monte, C.-J Hoffmann, M. Quaresimin, *Damage initiation and evolution in short fiber reinforced polyamide under fatigue loading: Influence of fiber volume fraction,* Composites Part B, vol. 113, pp. 331-341, 2017

BEL17_2 E. Belmonte, M. De Monte, C.-J Hoffmann, M. Quaresimin, *Damage mechanisms in a short glass fiber reinforced polyamide under fatigue loading*, vol. 94, pp. 145-157, 2017

BER07 A. Bernasconi, P. Davoli, A. Basile, A. Filippi, *Effect of fibre orientation on the fatigue behaviour of a short glass fibre reinforced polyamide-6*, International Journal of Fatigue, vol. 29, pp. 199-208, 2006

BER12 A. Bernasconi, F. Cosmi, P. J. Hine, *Analysis of fibre orientation distribution in short fibre reinforced polymers: A comparison between optical and tomographic methods,* Composite Science and Technology, vol. 72, pp. 2002-2008, 2012

BER15 A. Bernasconi, E. Conrado, P. Hine, *An experimental investigation of the combined influence of notch size and fibre orientation on the fatigue strength of a short glass fibre reinforced polyamide 6,* polymer Testing, vol. 47, pp. 12-21, 2015

BIE16 D. Biermann, L. Laperrière, G. Reinhart, CIRP Encyclopedia of Production Engineering, Springer Berlin Heidelberg, 2016

BIR12 M. Biron, Thermoplastics and Thermoplastic Composites, William Andrew 2013 , 2012

CAM90 C. W. Camacho, C. L. Tucker, S. Yalvaç, L. McGee, *Stiffness and thermal expansion predictions for hybrid short fiber composites*, Polymer Composites, vol. 11, p. 229–239, 1990

CAS17 J. A. Casado, F. Gutiérrez-Solana, I. Carrascal, S. Diego, D. Ferreño, *Analysis of fatigue behaviour of notched specimens made of fibreglass reinforced polyamide by means of a cohesive model*, vol. 64, pp. 337-344, 2017

CAR14 P. A. Carraro, M. Quaresimin, *A damage based model for crack initiation in unidirectional composites under multiaxial cyclic loadings,* Composites Science and Technology, vol. 99, pp. 154-163, 2014

CHU02 D. H. Chung, T. H. Kwon, *Fiber orientation in the processing of polymer composites*, Korea Australia Rheology Journal, vol. 14, pp. 175-188, 2002

DEA17 A. Dean, S. Sahraee, J. Reinoso, R. Rolfes, *A new invariant-based thermo-plastic model for finite deformation analysis of short fibre reinforced composites: Development and numerical aspects*, Composites Part B, vol. 125, pp. 241-258, 2017

DEM08 M. De Monte, Multiaxial fatigue behaviour of short fibre reinforced thermoplastics, PhD-Thesis, 2008

DEM10 M. De Monte, E. Moosbrugger, M. Quaresimin, *Influence of temperature and thickness on the off-axis behaviour of short glass fibre reinforced polyamide 6.6 – Quasi-static loading*, Composites Part A, vol. 41, pp. 859-871, 2010

DEM10_2 M. De Monte, E. Moosbrugger, M. Quaresimin, *Influence of temperature and thickness on the off-axis behaviour of short glass fibre reinforced polyamide 6.6 – Cyclic loading*, Composites Part A, vol. 41, pp.1368-1379, 2010

DEM10_3 M. De Monte, E. Moosbrugger, K. Jaschek and M. Quaresimin, *Multiaxial fatigue of a short glass fibre reinforced polyamide 6.6, Fatigue and fracture behaviour*, International Journal of Fatigue, vol. 32, p. 17–28, 2010

DIG17 Digimat User's manual - Release 2018.0, 2017

DOG05 I. Doghri, L. Tinel, *Micromechanical modeling and computation of elasto-plastic materials reinforced with distributed-orientation fibers*, International Journal of Plasticity., vol. 21, p. 1919–1940, 2005

DOG06 I. Doghri, L. Tinel, *Micromechanics of inelastic composites with misaligned inclusions: Numerical treatment of orientation*, Computational Methods in Applied Mechanics and Engineering, vol. 195, p. 1387–1406, 2006

DRA07 D. Dray, P. Gilormini and G. Regnier, *Comparison of several closure approximations for evaluating the thermoelastic properties of an injection molded short-fiber composite*, Composites Science and Technology, vol. 67, p. 1601–1610, 2007

EFT16 M. Eftekhari, A. Fatemi, *Creep-fatigue interaction and thermo-mechanical fatigue behaviors of thermoplastics and their composites,* International Journal of Fatigue, vol. 91, pp. 136-148, 2016

FAT15 A. Fatemi, S. Mortazavian, A. Khosrovaneh, *Fatigue Behavior and Predictive Modeling of Short Fiber Thermoplastic Composites,* Procedia Engineering, vol. 133, pp. 5-20, 2015

FOS14 P. H. Foss, H. -C. Tseng, J. Snawerdt, Y.-J. Chang, W. -H. Yang, C. -H. Hsu, *Prediction of fiber orientation distribution in injection molded parts using Moldex3D simulation*, Polymer Composites, vol. 35, p. 671–680, 2014.

FU00 S.-Y Fu, B. Lauke, E. Mäder, C.-Y Yue, X. Hu, *Tensile properties of short-glass-fiber- and short-carbon-fiber-reinforced polypropylene composite,* Composite Part A, vol. 31, pp. 1117-1125, 2000

FU01 S. -Y Fu, C.-Y Yue, X. Hu, *Characterization of fiber length distribution of short-fiber reinforced thermoplastic,* Journals of Materials Science Letters, vol. 20, pp.31-33, 2001

GOL17 N. Goldberg, F. Ospald, M. Schneider, *A fiber orientation-adapted integration scheme for computing the hyperelastic Tucker average for short fiber reinforced composites*, Computational Mechanics, vol. 60, pp. 595-611, 2017

GOO07 J. W. Gooch, Encyclopedic Dictionary of Polymers, 2007

HAS12 A. Hassan, N. A. Rahman, R. Yahya, *Moisture absorption effect on thermal, dynamic mechanical and mechanical properties of injection-molded short glass-fiber/polyamide 6,6 composites,* Fibers and polymers, vol. 13, pp. 899-906, 2012

HOP92 C. P. Hoppel, *The effect of tension-tension fatigue on the mechanical behavior of short fiber reinforced thermoplastics, Proceedings-American Society for Composites*, TECHNOMIC PUBLISHING AG, p509-509, 1992

HOR97 J. J. Horst, J. L. Spoormaker, *Fatigue fracture mechanisms and fractography of short-glassfibre-reinforced polyamide 6,* Journal of Materials Science, vol. 32, pp. 3641-3651, 1997

HSI09 J. Hsieh, Computed Tomography: Principles, Design, Artifacts and Recent Advances, 2009

JAI13 A. Jain, S. V. Lomov, Y. Abdin, I. Verpoest, W. Van Paepegem, *Pseudo-grain discretization and full Mori Tanaka formulation for random heterogeneous media: Predictive abilities for stresses in individual inclusions and the matrix*, Composites Sciences and Technology, vol. 87, p. 86–93, 2013

JAI16 A. Jain, W. Van Paepegem, I. Verpoest, S. V. Lomov, *A feasibility study of the Master SN curve approach for short fiber reinforced composites,* International Journal of Fatigue, vol. 91, pp. 264-274, 2016

JAI16_2 A. Jain, J. M. Veas, S. Straesser, W. Van Paepegem, I. Verpoest, S. V. Lomov, *The Master SN curve approach – A hybrid multi-scale fatigue simulation of short fiber reinforced composites,* Composites Part A, vol. 91, pp. 510-518, 2016

KAB06 M. R. Kabir, W. Lutz, K. Zhu, S. Scmauder, Fatigue modeling of short fiber reinforced composites with ductile matrix under cyclic loading, Computational Materials Science, vol. 36, pp.361-366, 2006

KAM11 S. Kammoun, I. Doghri, L. Adam, G. Robert, L. Delannay, *First pseudo-grain failure model for inelastic composites with misaligned short fibers,* Composite Part A, vol. 42, pp. 1892-1902, 2011

KAW17 M. Kawai, H. Takeuchi, I. Taketa, A. Tsuchiya, *Effects of temperature and stress ratio on fatigue life of injection molded short carbon fiber-reinforced polyamide composite*, Composites Part A, vol. 98, pp. 9-24, 2017

KAI14 J.-M. Kaiser, M. Stommel, *Modified mean-field formulations for the improved simulation of short fiber reinforced thermoplastics*, vol. 99, pp. 75-81

KLI11 B. Klimkeit, Y. Nadot, S. Castagnet, C. Nadot-Martin, C. Dumas, S. Bergamo, C. M. Sonsino, A. Büter, *Multiaxial fatigue life assessment for reinforced polymers,* International Journal of Fatigue*,* vol. 33, pp. 766-780, 2011

KÖP13 T. Köpplmayr, I. Milosavljevic, M. Aigner, R. Hasslacher, B. Plank, D. Salaberger, J. Miethlinger, *Influence of fiber orientation and length distribution on the rheological characterization of glass-fiber-filled polypropylene,* Polymer Testing, vol. 32, pp. 535-544, 2013

KRA16 A. Krairi, I. Doghri, G. Robert, *Multiscale high cycle fatigue models for neat and short fiber reinforced thermoplastic polymers,* International Journal of Fatigue, vol. 92, pp. 179-192, 2016

KRE17 J Kreutzer, J. DeLuca, B. Caplan, Encyclopedia of Clinical Neuropsychology, Springer New York, 2011

LAP16 L. Laperrière, G. Reinhart, CIRP Encyclopedia of Production Engineering, Springer Berlin Heidelberg, 2016

LAR18 M. Laribi, S. Tamboura, J. Fitoussi, R. Tié Bi, A. Tcharkhtchi, H. Ben Dali, *Fast fatigue life prediction of shor fiber reinforced composites using a new hybrid damage approach: Application to SMC,* Composites Part B, vol. 139, pp. 155-162, 2018

LEE18 D. Lee, *Local anisotropy analysis based on the Mori-Tanaka model for multiphase composites with fiber length and orientation distributions*, Composites Part B, vol. 148, pp. 227-234, 2018

LUN13 A. Lunay, M. H. Maitournam, Y. Marco, I. Raoult, *Multiaxial fatigue models for short glass fiber reinforced polyamide – Part I: Nonlinear anisotropic constitutive behavior for cyclic response,* International Journal of Fatigue, vol. 47, pp. 382-389, 2013

LUN13_2 A. Launay, M. H. Maitournam, Y. Marco and I. Raoult, *Multiaxial fatigue models for short glass fibre reinforced polyamide. Part II: Fatigue life estimation*, International Journal of Fatigue*,* vol. 47, pp. 390-406, 2013

MAL04 P. K. Mallick, Y. Zhou, *Effect of mean stress on the stress-controlled fatigue of a short E-glass fiber reinforced polyamide-6,6,* International Journal of Fatigue, vol. 26, pp. 941, 946, 2004

MAS16 Y. Masumuchi, M. Terada, A. Yamanaka, T. Yamamoto, T. Ishikawa, *Distribution function of fiber length in thermoplastic composites,* Composites Science and Technology, vol. 134, pp.43-48, 2016

MEN11 G. Meneghetti, M. Quaresimin, *Fatigue strength assessment of a short fiber composite based on the specific heat dissipation,* Composites Part B, vol. 42, pp. 217-225,2011

MOO11 A. Moosaie, A. Le Duc, M. Manhart, *A priori analysis of a closure model using the reconstruction of the orientation distribution function in flow of fiber suspensions,* Computational Mechanics, vol. 48, pp. 451-459, 2011

MOR15 S. Mortazavian, A. Fatemi, *Effects of fiber orientation and anisotropy on tensile strength and elastic modulus of short fiber reinforced polymer composite,* Composite Part B, vol. 72, pp. 116-129, 2015

MOR15_2 S. Mortazavian, A. Fatemi, A. Khosrovaneh, *Effect of Water Absorption on Tensile and Fatigue Behaviors of Two Short Glass Fiber Reinforced Thermoplastics,* SAE Int. J. Materi. Manf., vol. 8, pp. 435-443, 2015

MOR15_3 S. Mortazavian, A. Fatemi, *Fatigue behavior and modeling of short fiber reinforced polymer composites: A literature review*, International Journal of Fatigue, vol. 70, pp. 297-321, 2015

MOR15_4 S. Mortazavian, A. Fatemi, *Fatigue behavior and modeling of short fiber reinforced polymer composites including anisotropy and temperature effects*, *International Journal of Fatigue,* vol. 77, pp. 12-27, 2015

MOR17 S. Mortazavian and A. Fatemi, *Fatigue of short fiber thermoplastic composites: A review of recent experimental results and analysis*, *International Journal of Fatigue,* vol. 102, pp. 171-183, 2017

MOU06 B. Mouhmid, A. Imad, N. Benseddiq, S. Benmedakhène, A. Maazuouz, *A study of the mechanical behaviour of a glass fibre reinforced polyamide 6,6: Experimental investigation,* Polymer Testing, vol. 25, pp. 544-552, 2006

MÜL15 V. Müller, M. Kabel, H. Andrä, T. Böhlke, *Homogenization of linear elastic properties of short-fiber reinforced composites – A comparison of mean field and voxel-based methods,* International Journal of Solids and Structures, vol. 67-68, pp. 56-70, 2015

NGU12 V. -D. Nguyen, E. Béchet, C. Geuzaine, L. Noels, *Imposing periodic boundary condition on arbitrary meshes by polynomial interpolation*, Computational Materials Science, vol. 55, p. 390–406, 2012

NOT14 D. Notta-Cuvier, F. Lauro, B. Bennani, R. Balieu, *Damage of short-fibre reinforced materials with anisotropy induced by complex fibres orientations*, Mechanics of Matererials, vol. 68, p. 193–206, 2014

OGI17 W. Ogierman and G. Kokot, *Homogenization of inelastic composites with misaligned inclusions by using the optimal pseudo-grain discretization*, International Journal of Solids and Structures,vol. 113-114, pp. 230-240, 2017

ONA88 E. T. Onat, F. A. Leckie, *Representation of Mechanical Behavior in the Presence of Changing Internal Structure*, Journal of Applied Mechanics, vol. 55, pp. 1-10, 1988

OSS12 T. A. Osswald, G. Menges, Materials Science of Polymers for Engineers, 2012

PAT06 S. Patcharaphun, *Characterization and Simulation of Material Distribution and Fiber Orientation in Sandwich Injection Molded Parts,* Dissertation, Technische Universität Chemnitz, 2006

PIE04 O. Pierard, C. Friebel, I. Doghri, *Mean-field homogenization of multi-phase thermo-elastic composites: a general framework and its validation*, Composites Science and Technology, vol. 64, p. 1587–1603, 2004

PIE18 R. Pietrogrande, P. A. Carraro, M. De Monte and M. Quaresimin, *A novel pseudo-grain approach for the estimation of the elastic stress distributions within the matrix of Short Fiber-Reinforced Polymers,* Composite Part B, vol. 150, pp. 115-123, 2018

PON15 A. Pontefisso, M. Zappalorto, M. Quaresimin, *An efficient RVE formulation for the analysis of the elastic properties,* Computational Materials Science, vol. 96, pp. 319-326, 2015

QUA16 M. Quaresimin, P. A. Carraro, L. Maragoni, *Early stage damage in off-axis plies under fatigue loading,* Composites Science and Technology, vol. 128, pp. 147-154, 2016

ROL16 H. Rolland, N. Saintier, G. Robert, *Damage mechanisms in short glass fibre reinforced thermoplastic during in situ microtomography tensile tests,* Composites Part B, vol. 90, pp. 365-377, 2016

ROL18 H. Rolland, N. Saintier, I. Raphael, N. Lenoir, A. King, G. Robert, *Fatigue damage mechanisms of short fiber reinforced PA66 as observed by in-situ synchrotron X-ray microtomography,* Composites Part B, vol. 143, pp. 217-229, 2018

ROS12 D. V. Rosato, M. G. Rosato, Injection Molding Handbook, Springer Science and Business Media, 2012

SCH17 M. Schneider, *The sequential addition and migration method to generate representative volume elements for the homogenization of short fiber reinforced plastics,* Computational Mechanics, vol. 59, pp. 247-263, 2017

SCH14 A. Schaaf, M. De Monte, C. -J. Hoffmann, M. Vormwald and M. Quaresimin, *Damage mechanisms in PBT-GF30 under thermo-mechanical cyclic loading*, AIP (American Institute of Physics) Conference Proceedings, vol. 1593, p. 600, 2014. loading, AIP (American Institute of Physics) Conference Proceedings, vol. 1593, p. 600, 2014

SON08 C. M. Sonsino, E. Moosbrugger, *Fatigue design of highly loaded short-glass-fibre reinforced polyamide parts in engine compartments,* International Journal of Fatigue, vol. 30, pp. 1279-1288, 2008

TAN14 K. Tanaka, T. Kitano, N. Egami, *Effect of fiber orientation on fatigue crack propagation in short-fiber reinforced plastics,* Engineering Fracture Mechanics, vol. 123. pp.44-58, 2014

TIA14 W. Tian, L. Qi, J. Zhou, J. Guan, *Effects of the fiber orientation and fiber aspect ratio on the tensile strength of Csf/Mg composites,* Computational Materials Science, vol. 89, pp. 6-11, 2014

TIA15 W. Tian, L. Qi, J. Zhou, J. Liang, Y. Ma, *Representative volume element for composites reinforced by spatially randomly distributed discontinuous fibers and its applications,* Composite Structures, vol. 131, pp. 366-373, 2015

TIA16 W. Tian, L. Qi, J. Liang, X. Chao and J. Zhou, *Evaluation for elastic properties of metal matrix composites with randomly distributed fibers: Two-step mean-field homogenization procedure versus FE homogenization method*, Journal of Alloys and Compounds, vol. 658, pp. 241-247, 2016

TSA80 S. Tsai, H. T. Hahn, Introduction to Composite Materials, TECHNOMIC Publishing Co. Inc. 1980, 1980

WEB1 https://www.epa.gov

WEB2 http://www.custompartnet.com/wu/InjectionMolding

WEB3 https://www.geodict.com

WIL15 A. Wilmes and K. Hornberger, *Influence of Fiber Orientation and Multiaxiality on the Fatigue Strength of Unnotched Specimens – Lifetime Estimation*, Procedia Engineering, vol. 133, pp. 148-160, 2015

WIL16 A. Wilmes, M. Vormwald, K. Hornberger, *Fatigue Lifetime Estimation Concept for Short Fiber Reinforced Thermoplastics,* ICMFF11 Proceedings, 2016

ZAG01 A. Zago, G. S. Springer, *Constant Amplitude Fatigue of Short Glass and Carbon Fiber Reinforced Thermoplastics,* Journal of Reinforced Plastics and Composites, vol. 20, pp. 564-595, 2001

ZHO06 Y. Zhou, P. K. Mallick, *Fatigue performance of an injection-molded short E-glass fiber-reinforced polyamide 6,6. I. Effects of orientation, holes, and weld line,* Polymer Composites, vol. 27, pp. 230-237, 2006